Structural and functional characterisation of the *Pseudomonas aeruginosa* lipid-modifying translocase MprF



Matthew T.K. Hankins

Trinity College

University of Oxford

A thesis submitted for the degree of Doctor of Philosophy

Trinity Term 2024

Abstract

The multiple peptide resistance factor (MprF) is a bifunctional membrane protein found in the cytosolic membrane of many Gram-positive and Gram-negative bacteria, including pathogens such as *Pseudomonas aeruginosa* and *Staphylococcus aureus*. MprF modifies inner leaflet lipid headgroups through aminoacylation, and translocates modified lipid to the outer leaflet, resulting in a reduction in anionic character of the bacterial surface. The altered surface charge provides resistance to cationic antimicrobial peptides (CAMPs) and commercial positively charged antimicrobials. MprF presents a novel target to combat antimicrobial resistance, but structural information is limited, especially for MprF from common clinical pathogens. Moreover, the substrate specificity and energisation of lipid transport by MprF are yet to be characterised.

In this thesis, I structurally and functionally characterised the *P. aeruginosa* MprF (*Pa*MprF). I determined the structure of *Pa*MprF by cryo-electron microscopy (cryo-EM) to 3.28 Å using a nanobody to increase particle size and improve sample behaviour. Comparison of *Pa*MprF to a known MprF structure from *Rhizobium tropici* (*Rt*MprF) reveals significant structural differences and suggests novel routes of lipid transport. Furthermore, I established an *in vitro* lipid transport assay to probe the mechanism of *Pa*MprF-mediated lipid translocation. With this assay - the first application of a direct *in vitro* lipid transport assay to the MprF family - I demonstrated that *Pa*MprF does not require an external energy source and can transport a wide range of different lipid species. My data indicate that *Pa*MprF is a lipid scramblase, which is contrary to previous suggestions. By combining the lipid transport assay with site-directed mutagenesis, I investigated possible lipid transport pathways through *Pa*MprF, resulting in novel hypotheses for its mechanism of action.

Acknowledgements

I would like to thank Associate Professor Maike Bublitz for her invaluable supervision and guidance over the course of my studies, as well as for sparking my initial interest in bacterial lipid transport systems, an area I hope to continue exploring in the future. I would also like to thank Dr Alex Bullock for his support as my co-supervisor, as well as the Wellcome trust for their generous funding of my research.

I am grateful for the guidance and support I have received over the course of my studies from all members of both the Bublitz group in the Department of Biochemistry and the IMP group in the Centre for Medicines Discovery. From the IMP group, I am especially grateful to Dr Roslin Adamson for providing my initial hands-on training in cryo-EM sample preparation, and Dr Ashley Pike for his expert knowledge and support in cryo-EM data collection and analysis, as well as his patience with my early attempts at data processing. From the Bublitz group, I would like to thank Dr Margaret Young for all of her assistance with cryo-EM data collection and for providing optimism while on the microscope, something that was sorely needed towards the end of my degree.

The success of the structural component of this thesis would not have been possible without collaboration from Professor Markus Seeger. I would like to thank all of the Seeger group for welcoming me to their lab, from which the beautiful alpine view made it difficult to return to a basement lab in Oxford. I am especially grateful to Dr Alisa Garaeva and Jennifer Earp who provided day-to-day supervision for the duration of my stay.

Finally, I am most grateful for the endless encouragement, support and love I have received from my friends and family. To my partner Hannah, who had the unenviable task of teaching me how to use simple functions in R, and who had to endure the brunt of my daily ramblings as I grew increasingly untethered from my sanity. To my brother Joshua, my sister Laura, and my parents Mark and Jane, whose constant support throughout my life, but especially in these final months of my degree, has been invaluable. This thesis would not have been possible without all of your efforts, and I will always remember that.

Authorship Declaration

The work presented in this thesis was carried out in the Department of Biochemistry, University of Oxford, between November 2019 and December 2023 under the supervision of Associate Professor Maike Bublitz. Sybody selections were carried out during a secondment in the Institute of Medical Microbiology, University of Zurich, under the supervision of Dr Alisa Garaeva, Jennifer Earp, and Professor Markus Seeger.

Mass spectrometry (MS) analysis of the synthesised DSPE-PEG2000-NBD lipid was conducted by Dr Abraham Oluwole (Kavli Institute for Nanoscience Discovery, Oxford). Tryptic digestion and MS analysis of purified and biotinylated *Pa*MprF was conducted by Dr Aygul Malone (Advanced Proteomics Facility, Department of Biochemistry, Oxford). Cryo-EM datasets were collected and analysed with assistance from Dr Ashley Pike (Centre for Medicines Discovery, Nuffield Department of Medicine, University of Oxford), Dr Margaret Young (Bublitz group), and Dr Teige Matthews-Palmer (COSMIC Cryo-EM facility, University of Oxford). Initial *Pa*MprF mutants (E295Q/R, R319A/E) were cloned with assistance from Theodore Osmond (Bublitz group). Previous contributions prior to the start of the work in this thesis are clearly stated in the text.

Publications resulting from this thesis

The results from this thesis are currently being prepared for publication, supplemented with data from molecular dynamics simulations by collaborators Matyas Parrag and Professor Phillip Stansfeld, University of Warwick.

Hankins M.T.K., Parrag M., Seeger M.A., Stansfeld P.J., Bublitz M. "MprF from *Pseudomonas aeruginosa* is a promiscuous lipid scramblase with broad substrate specificity." (*Manuscript in preparation*).

Part of the work described in this thesis was presented at the following occasion:

Hankins, M.T.K., Osmond, T., Bublitz M. "Structure-function studies of the *Pseudomonas aeruginosa* Multiple Peptide Resistance Factor, MprF" (*Poster*). Molecular Mechanism of Membrane Proteins Conference, Biochemical Society, Birmingham (April 2023).

List of Abbreviations

ABC	ATP binding cassette
ADP	Adenosine diphosphate
AEBSF	Aminoethylbenzenesulfonyl fluoride
AlaPG	Alanyl-phosphatidylglycerol
AlaRS	Alanyl tRNA synthetase
Amp	Ampicillin
APS	Ammonium persulfate
ATP	Adenosine triphosphate
AU	Absorbance unit
A_X	Absorbance at X nm
BME	2-mercaptoethanol
*Bl*MprF	*Bacillus licheniformis* MprF
BPA	p-benzoyl-l-phenylalanine
BSA	Bovine serum albumin
CaCC	Calcium activated chloride channel
Cam	Chloramphenicol
CAMP	Cationic antimicrobial peptide
CC	Correlation coefficient
CCCP	Carbonyl cyanide 3-chlorophenylhydrazone
CDR	Complementarity determining region
CPD	Cysteine protease domain
Cryo-EM	Cryo-electron microscopy
CTD	C-terminal domain
CTF	Contrast transfer function
Ctrl	Control
Da	Dalton
DAG	Diacylglycerol
DDM	n-dodecyl β-D-maltoside
DNA	Deoxyribonucleic acid
DSPE	Distearoyl-sn-glycero-3-phosphoethanolamine
EDTA	Ethylenediamine tetraacetic acid
EF-Tu	Elongation factor thermo unstable
ELISA	Enzyme linked immunosorbent assay
ER	Endoplasmic reticulum
FPLC	Fast protein liquid chromatography
FX	Fragment exchange
F_X	Fluorescence at X nm excitation wavelength
Glc_2DAG	Diglucosyl-diacylglycerol
GlcN6P	Glucosamine-6-phosphate
GNAT	GCN5-related *N*-acteyltransferase
GPCR	G-protein coupled receptor
GSFSC	Gold standard Fourier shell correlation
HEPES	4-(2-hydroxyethyl)-1-piperazineethanesulfonic acid
HPTS	8-hydroxypyrene-1,3,6-trisulfonic acid

HRP	Horseradish peroxidase
IEX	Ion exchange chromatography
IMAC	Immobilised metal ion affinity chromatography
$InsP_6$	Inositol-6-phosphate
IPTG	Isopropyl-β-D-thiogalactopyranoside
IVT	*In vitro* transcription
Kan	Kanamycin
K_D	Affinity constant
kpsi	Kilopounds per square inch
LB	Lysogeny broth
LPS	Lipopolysaccharide
LTA	Lipoteichoic acid
LysPG	Lysyl-phosphatidylglycerol
MD	Molecular dynamics
MFS	Major facilitator superfamily
MOP	Multidrug/Oligosaccharidyl-lipid/Polysaccharide
MprF	Multiple peptide resistance factor
mRNA	Messenger ribonucleic acid
MRSA	Methicillin resistant *Staphylococcus aureus*
MS	Mass spectrometry
MSP	Membrane scaffold protein
MurNAc	*N*-acetylmuramic acid
MW	Molecular weight
MWCO	Molcular weight cut-off
NBD	Nitrobenzoxadiazole
NBD-SE	Succinimidyl 6-(*N*-(7-nitrobenz-2-oxa-1,3-diazol-4-yl)amino)hexanoate
NBDG	Nitrobenzoxadiazol-amino-D-glucose
NHS	N-Hydroxysuccinimide
NTA	Nitrilotriacetic acid
NTD	N-terminal domain
NU	Non-uniform
OD_{600}	Optical density at 600 nm
PaMprF	*Pseudomonas aeruginosa* MprF
PBP	Penicillin binding protein
PBS	Phosphate buffered saline
PC	Phosphatidylcholine
PCR	Polymerase chain reaction
PDB	Protein data bank
PE	Phosphatidylethanolamine
PEG	Polyethylene glycol
PG	Phosphatidylglycerol
PI	Phosphatidylinositol
PMF	Proton motive force
PMSF	Phenylmethylsulfonyl fluoride
POPC	1-palmitoyl-2-oleoyl-glycero-3-phosphocholine
POPG	1-palmitoyl-2-oleoyl-sn-glycero-3-phospho-(1'-rac-glycerol)
ProtK	Proteinase K

PS	Phosphatidylserine
PVDF	Polyvinylidene fluoride
qPCR	Quantitative polymerase chain reaction
RMSD	Root-mean-square deviation
RT	Room temperature
*Rt*MprF	*Rhizobium tropici* MprF
*Sa*MprF	*Staphylococcus aureus* MprF
SapA	SaposinA
SapNP	SapA nanoparticle
SAXS	Small-angle X-ray scattering
SDS	Sodium dodecyl-sulfate
SDS-PAGE	Sodium dodecyl-sulfate polyacrylamide gel electrophoresis
SEC	Size exclusion chromatography
SOC	Super optimal broth with catabolite repression
SPR	Surface plasmon resonance
TB	Terrific broth
TBS	Tris buffered saline
TBST	Tris buffered saline + tween 20
TCEP	Tris(2-carboxyethyl)phosphine
TEMED	Tetramethylethylenediamine
Tet	Tetracycline
TEV	Tobacco etch virus
TLC	Thin layer chromatography
TM	Transmembrane
TMB	3,3′,5,5′-Tetramethylbenzidine
tRNA	Transfer ribonucleic acid
UDP	Uridine diphosphate
UDP-MurNAc	UDP-*N*-acetylmuramic Acid
UndP	Undecaprenyl-phosphate
UndPP	Undecaprenyl-diphosphate
UV	Ultraviolet
WT	Wildtype
WTA	Wall teichoic acid

Table of Contents

ABSTRACT ..... **I**

ACKNOWLEDGEMENTS ..... **II**

AUTHORSHIP DECLARATION ..... **III**

PUBLICATIONS RESULTING FROM THIS THESIS ..... **IV**

LIST OF ABBREVIATIONS ..... **V**

CHAPTER 1: INTRODUCTION **1**

1.1. LIPID TRANSPORT WITHIN BIOLOGICAL MEMBRANES 1
1.1.1. Scramblases *4*
1.1.2. P4-ATPases *7*
1.1.3. ABC transporters *9*
1.1.4. ATP-independent flippases *12*
1.2. LIPID MODIFICATION AND TRANSPORT IN BACTERIA AS A TARGET FOR ANTIMICROBIALS 15
1.2.1. Lipopolysaccharide and O-antigen synthesis *15*
1.2.2. Teichoic acid synthesis *17*
1.2.3. Modification of bacterial cellular surface charge *19*
1.3. THE MULTIPLE PEPTIDE RESISTANCE FACTOR, MPRF 21
1.3.1. Identification of MprF as a lipid-modifying flippase *21*
1.3.2. The MprF soluble domain aminoacylates PG headgroups *24*
1.3.3. MprF flippase domain activity *32*
1.3.4. Regulation of MprF expression and aminoacyl-PG levels *38*
1.3.5. The MprF flippase architecture is more widespread than initially thought *42*
1.3.6. Wider roles of MprF in virulence and as a target in multi-resistant bacteria *45*
1.4. A STRATEGY TO STUDY MPRF 48
1.4.1. Structural characterisation with cryo-EM *48*
1.4.2. In vitro assessment of lipid transport activity *50*
1.4.3. Previous work on MprF in the Bublitz group *53*
1.5. AIMS AND SCOPE 54

CHAPTER 2: MATERIALS AND METHODS **55**

2.1. DNA METHODS 55
2.1.1. Bacterial transformation *55*
2.1.2. Fragment Exchange (FX) cloning *55*
2.1.3. AlaRS cloning *56*
2.1.4. Site-directed mutagenesis *57*
2.2. RNA METHODS 57
2.2.1. Gel electrophoresis *57*
2.2.2. $tRNA^{Ala}$ in vitro transcription (IVT) and purification *57*
2.3. LIPID METHODS 58
2.3.1. Lipid extraction *58*
2.3.2. Thin layer chromatography (TLC) *58*
2.3.3. PEG2000-NBD lipid synthesis *59*
2.4. PROTEIN METHODS 61
2.4.1. Sodium dodecyl-sulfate polyacrylamide gel electrophoresis (SDS-PAGE) *61*
2.4.2. Western blotting *61*
2.4.3. Large-scale expression and purification of PaMprF *62*
2.4.4. Expression and purification of SaposinA (SapA) *65*
2.4.5. Reconstitution of PaMprF into SapA nanoparticles *66*
2.4.6. Large-scale expression, purification and biotinylation of PaMprF for sybody selections *67*
2.4.7. Attempted large-scale expression and purification of PaMprF transmembrane construct for sybody selections *70*
2.4.8. Small-scale expression testing p-benzoyl-l-phenylalanine (BPA) mutants *72*

2.4.9. Large-scale expression and purification of PaMprF mutants ... *73*
2.4.10. Large-scale expression and purification of BPA mutants ... *74*
2.4.11. Alanine tRNA synthetase (AlaRS) expression and purification ... *74*
2.4.12. AlaRS^{440} expression and purification ... *75*
2.5. *IN VITRO PA*MPRF SYNTHASE ASSAY ... 77
2.6. *IN VITRO PA*MPRF LIPID TRANSLOCATION ASSAY ... 77
2.6.1. Reconstitution of PaMprF into liposomes containing NBD-labelled lipid ... *77*
2.6.2. Liposome transport assay ... *78*
2.6.3. Deriving the three-state model for analysis ... *79*
2.6.4. Analysis of fluorescence time-course data using the three-state model ... *86*
2.6.5. PaMprF orientation assay ... *87*
2.7. SELECTION OF SYNTHETIC NANOBODIES (SYBODIES) ... 87
2.8. ALARS-*PA*MPRF INTERACTION STUDIES ... 87
2.8.1. Pull-down assay ... *87*
2.8.2. SEC co-elution ... *88*
2.8.3. Surface plasmon resonance (SPR) ... *88*
2.9. CRYO-ELECTRON MICROSCOPY ... 89
2.9.1. Preparation of cryo-EM grids ... *89*
2.9.2. PaMprF Cryo-EM data collection ... *89*
2.9.3. PaMprF Cryo-EM data processing ... *89*
2.9.4. PaMprF-Sybody29 complex Cryo-EM data collection ... *90*
2.9.5. PaMprF-Sybody29 complex Cryo-EM data processing ... *90*
2.9.6. Model building and refinement ... *91*

CHAPTER 3: STRUCTURAL CHARACTERISATION OF *PSEUDOMONAS AERUGINOSA* MPRF ... 92

3.1. INTRODUCTION ... 92
3.2. *PA*MPRF-SAPNP CRYO-ELECTRON MICROSCOPY ... 93
3.2.1. Optimisation of PaMprF-SapNP cryo-EM grid preparation ... *93*
3.2.2. PaMprF is purified as a monomer ... *95*
3.2.3. PaMprF adopts a novel conformation ... *96*
3.3. GENERATION OF SYBODY BINDERS ... 99
3.3.1. Outline of sybody selection pipeline ... *100*
3.3.2. Ribosome display ... *102*
3.3.3. Phage display ... *103*
3.3.4. Assessment of sybody binders by ELISA ... *105*
3.3.5. Purification of selected sybodies ... *108*
3.3.6. Sybody selection yielded two unique TM binders ... *109*
3.4. CRYO-EM STUDIES OF *PA*MPRF-SYBODY COMPLEXES ... 112
3.4.1. Optimisation of PaMprF-Sybody29 complex grid preparation ... *112*
3.4.2. Sybody29 binding significantly improves PaMprF-SapNP sample for Cryo-EM ... *113*
3.4.3. High-resolution characterisation of PaMprF-Sybody29 complex to 3.28 Å ... *116*
3.5. STRUCTURAL ANALYSIS OF *PA*MPRF ... 119
3.5.1. PaMprF architecture ... *119*
3.5.2. Cryo-EM density indicates PaMprF is bound to multiple lipid molecules ... *124*
3.5.3. The Soluble Domain of PaMprF is significantly displaced compared to RtMprF ... *127*
3.5.4. The TM domains of PaMprF separate to open a deep cleft ... *129*
3.5.5. Structural analysis reveals a possible alternate lipid translocation pathway ... *133*
3.6. CHAPTER DISCUSSION ... 137
3.6.1. Sybody29 significantly improved sample behaviour of PaMprF ... *137*
3.6.2. PaMprF exhibits major structural changes compared to RtMprF ... *138*
3.6.3. PaMprF structural data suggests possible alternate lipid transport routes ... *142*

CHAPTER 4: *IN VITRO* ASSESSMENT OF *PA*MPRF FUNCTION AND INTERACTIONS .. 145

4.1. INTRODUCTION ... 145
4.2. *PA*MPRF AND ALARS FORM A COMPLEX *IN VITRO* ... 147
4.2.1. Purification of AlaRS ... *147*

4.2.2. PaMprF is enriched on affinity resin bound to AlaRS *148*
4.2.3. PaMprF and AlaRS co-elute on SEC *149*
4.2.4. PaMprF does not co-elute with a catalytic fragment of AlaRS, AlaRS^{440} *150*
4.2.5. SPR suggests a 7 μM K_D for the PaMprF-AlaRS interaction *153*
4.3. PURIFIED *PA*MPRF CAN MODIFY NBD-PG *IN VITRO* 155
4.3.1. tRNA^{Ala} synthesis and purification by modified IVT *155*
4.3.2. Purified PaMprF is catalytically active *158*
4.4. ESTABLISHMENT OF A LIPOSOME-BASED LIPID TRANSPORT ASSAY 159
4.4.1. PaMprF can be successfully reconstituted into liposomes *159*
4.4.2. Initial trials suggest PaMprF can translocate NBD-AlaPG in vitro *161*
4.4.3. Fluorescence decrease is not a result of dithionite transport into liposomes *166*
4.4.4. Fluorescence decrease is specific to PaMprF *169*
4.4.5. Fluorescence decrease is not a result of lipid asymmetry on reconstitution *170*
4.5. CHAPTER DISCUSSION 173
4.5.1. PaMprF and AlaRS form a complex *173*
4.5.2. Purified PaMprF is catalytically active, but requires tRNA derived from E. coli *174*
4.5.3. PaMprF can transport NBD-labelled lipid in vitro *175*

CHAPTER 5: CHARACTERISING THE MECHANISM OF LIPID TRANSLOCATION BY *PA*MPRF 176

5.1. INTRODUCTION 176
5.2. ENERGETICS OF *PA*MPRF-MEDIATED LIPID TRANSPORT 177
5.2.1. Characterisation of PaMprF by fitting to three-state model *177*
5.2.2. PaMprF lipid transport rates are unaffected by Sybody29 ..... *182*
5.2.3. PaMprF lipid transport rates are unaffected by common activators *183*
5.2.4. PaMprF lipid transport does not require the PMF *186*
5.3. SPECIFICITY OF *PA*MPRF-MEDIATED LIPID TRANSPORT 189
5.3.1. PaMprF exhibits broad substrate specificity *189*
5.3.2. PaMprF can transport the "giant" lipid NBD-PEG2000PE *193*
5.4. INVESTIGATING *PA*MPRF-MEDIATED LIPID TRANSPORT VIA MUTAGENESIS 196
5.4.1. PaMprF is resistant to mutations at the cytoplasmic lipid binding site *196*
5.4.2. PaMprF is resistant to mutations at the TM domain interface *206*
5.4.3. Targeted UV crosslinking of PaMprF does not inhibit lipid transport *210*
5.5. CHAPTER DISCUSSION 214
5.5.1. PaMprF behaves like a passive lipid scramblase *214*
5.5.2. PaMprF is highly promiscuous *214*
5.5.3. No PaMprF mutation reduced lipid transport *215*
5.5.4. PaMprF lipid transport is stimulated by the introduction of positive charge *217*

CHAPTER 6: DISCUSSION 218

6.1. COLLECTIVE EVIDENCE SUGGESTS THAT *PA*MPRF ACTS AS A LIPID SCRAMBLASE 218
6.2. NOVEL INSIGHT INTO THE PUTATIVE LIPID TRANSPORT PATHWAY 221
6.3. CONSIDERATIONS ON THE OLIGOMERIC STATE OF *PA*MPRF 229
6.4. SUBSTRATE BINDING AT THE SOLUBLE DOMAIN 229
6.5. MPRF'S POTENTIAL AS AN ANTIMICROBIAL TARGET 231
6.6. CONCLUDING REMARKS 233

APPENDICES **248**

A1. MPRF ALIGNMENT 248
A2. POLYMERASE CHAIN REACTION 249
A3. SYBODY SELECTION PROTOCOL 252
A4. SYBODY ALIGNMENTS AND PHYLOGENETIC TREE 260
A5. *PA*MPRF MODEL TM HELIX FIT TO MAP 262
A6. ISOLATION OF *P. AERUGINOSA* PA0919 AND ASSESSMENT OF FUNCTION 263
A7. *PA*MPRF MUTANT PURIFICATIONS 268
A8. *PA*MPRF DISULFIDE MUTANT LIPID TRANSPORT DATA 271

Chapter 1: Introduction

1.1. Lipid transport within biological membranes

Organic membranes of bacteria and eukaryotes are composed of two leaflets of lipids. Lipid transport between inner and outer membrane leaflets is essential for many critical cell processes in prokaryotes and eukaryotes. Synthesis of common lipid species occurs within the inner leaflets of membranes, and so cellular expansion requires export of these lipids to the outer leaflets to ensure uniform growth (Pomorski *et al.* 2001). In addition, many individual lipid species have specific functions within cells and require their distributions within membrane leaflets to be regulated. For example, the distribution of phosphatidylserine (PS), a proapoptotic signalling factor in eukaryotic cells (Fadok *et al.* 1992), is tightly controlled such that it remains in the cytoplasmic leaflet of membranes in healthy cells. In cells undergoing rapid cell death, PS is rapidly exposed to the cell surface, where it acts as a marker for phagocytosis. Lipids can also be conjugated to certain molecules that need to be transported from the interior of the cell to the exterior. Isoprenyl lipids such as undecaprenyl-phosphate (UndP) are widely used for this purpose (Workman and Strynadka 2020), acting as carriers to facilitate the transport of sugar repeat unit structures in bacteria for the building of cell walls and outer membranes.

The transport of lipids within membranes is a highly energetically unfavourable process, as the hydrophilic lipid headgroup needs to be translocated through the hydrophobic core of the membrane composed of lipid acyl tails. As a result of this, spontaneous flip-flop of lipids between bilayers is a rare event, occurring on the timescale of hours to days (Kornberg and McConnell 1971, Pomorski and Menon 2016). This led to the suggestion that membrane proteins facilitate the translocation of lipids between bilayers of the membrane (Bretscher 1973). Some of these potential lipid transporters were then characterised through genetic

screens (Feldman *et al.* 1999, Helenius *et al.* 2002, Suzuki *et al.* 2010) and *in vitro* assessments of lipid transport (Romsicki and Sharom 2001, Rick *et al.* 2003, Menon *et al.* 2011).

Following this early work, lipid transporting proteins in eukaryotes were broadly classified based on energetics and directionality of transport as either flippases, floppases or scramblases (**Figure 1.1**). Flippases and floppases were classified as proteins that transport lipid in an ATP-dependent manner unidirectionally to produce or maintain lipid asymmetry in a membrane, with flippases predominantly comprising P4-ATPases that transport lipid from the outer leaflet of the cytoplasmic membrane to the inner leaflet, and floppases comprising ATP binding cassette (ABC) transporters operating in the opposite direction (Coleman *et al.* 2013). However, ABC transporters that act as flippases under this classification have also been identified (Quazi *et al.* 2012). Scramblases, in contrast, collapse membrane lipid asymmetry, transporting lipid bidirectionally down a concentration gradient, independently of ATP (Sahu *et al.* 2007). Such scrambling activity can be important for facilitating the rapid disruption of membrane asymmetry, as observed in the PS example above, but is also required in biogenic membranes (e.g. the bacterial inner membrane or the eukaryotic endoplasmic reticulum (ER) membrane) where lipids can only be synthesised in the cytoplasmic leaflet and need to be transported to the opposite leaflet to facilitate membrane expansion (Chauhan *et al.* 2016).

Whilst several scramblase proteins in eukaryotes have been identified that are involved in the bidirectional transport of phospholipid species, there are currently no characterised bacterial phospholipid scramblases (Bogdanov *et al.* 2020). The best characterised eukaryotic scramblases belong to the TMEM16 family which are activated by calcium (Suzuki *et al.* 2010), but the Xk-family, activated by proteolysis, have also been identified (Suzuki *et al.* 2013). Interestingly, the first protein with scramblase activity to be characterised via *in vitro* functional assessment was opsin, the apoprotein of the G-protein coupled receptor (GPCR)

rhodopsin (Menon *et al.* 2011), which raises questions as to how widespread such lipid scrambling activity is in proteins with other assigned functionality.

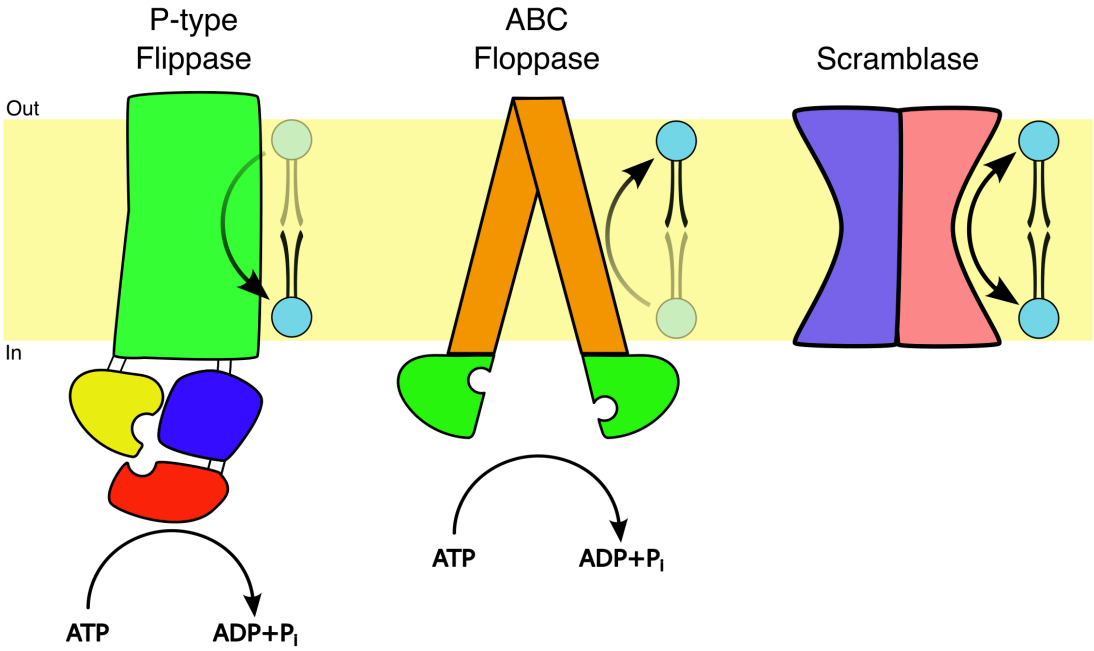

Figure 1.1: Eukaryotic lipid transporter categories. Schematic showing the initial categorisation of P-type flippases, ABC floppases, and scramblases in eukaryotes. A general lipid species is shown (light blue), with arrows indicating the direction of lipid transport for each transporter class.

There are, however, many lipid transporters that have been identified that do not fit neatly into these broad categories. Some Major Facilitator Superfamily (MFS) transporters couple lipid transport to cellular ion gradients: LtaA in bacteria is energised by the proton motive force (PMF) (Zhang *et al.* 2020), and Mfsd2A in humans is sodium-dependent (Chua *et al.* 2023). In addition, the Multidrug/Oligosaccharidyl-lipid/Polysaccharide (MOP) family contains lipid transporters including bacterial MurJ and Wzx; neither transporter is fully characterised, but MurJ activity has been shown to be dependent on the presence of a membrane potential (Rubino *et al.* 2018), whereas Wzx is thought to transport lipid in the absence of an external energy source via facilitated diffusion (Rick *et al.* 2003). Together, these examples highlight the existence of lipid transporters that are thought to transport lipid in one direction, but utilise an energy source for this transport that is distinct from ATP. As such, the term "flippase" has been used more broadly in the literature to describe proteins that transport lipid unidirectionally.

In some cases of passive lipid transport, lipid specificity has been shown to be somewhat relaxed; for example, fluorescently labelled phospholipids with choline (PC) and ethanolamine (PE) headgroups in *Escherichia coli* were both rapidly transported between leaflets of inner membrane vesicles (Kubelt *et al.* 2002), and transport of phosphatidylinositol (PI) across the ER occurred irrespective of substrate stereochemistry (Vishwakarma *et al.* 2005). These findings, together with the consideration of the amphipathic nature of the lipid substrate being transported, led to the suggestion of a general mechanism of lipid transporter activity called the "credit-card" model (Pomorski and Menon 2006). In this model, lipid transport proteins contain a hydrophilic groove which shields the headgroup of transported lipid from the hydrophobic core of the membrane as it moves between leaflets. The hydrophobic tails of the lipid remain in the bilayer during lipid transport (**Figure 1.2**).

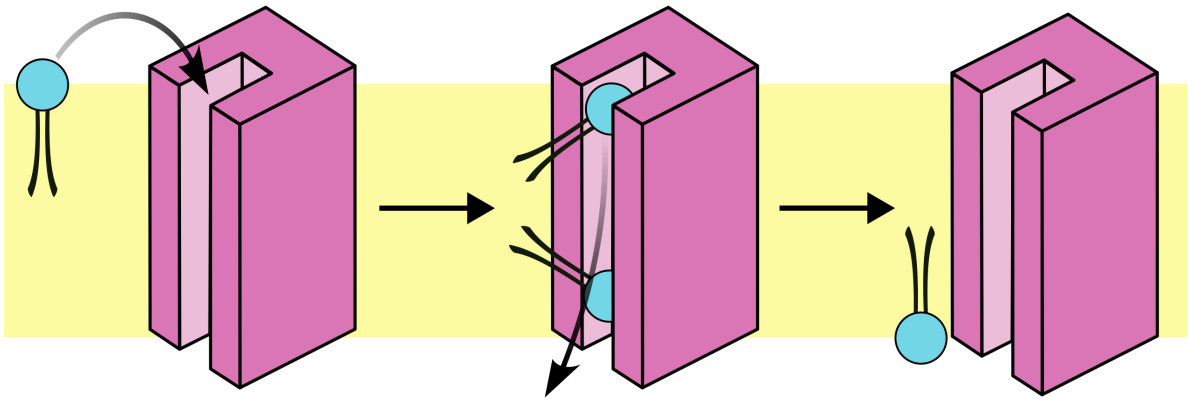

Figure 1.2: Proposed credit-card mechanism of lipid transport. Schematic outlining the credit-card mechanism (Pomorski and Menon 2006). A hydrophilic groove in a lipid transporter (pink) provides the pathway for a lipid headgroup (blue) to move through the hydrophobic bilayer while its tails (black lines) remain in the bulk membrane (yellow).

The following sections briefly discuss the salient features of the currently characterised classes of lipid transporters, and how applicable the credit-card model is to each.

1.1.1. Scramblases

The eukaryotic scramblases are best represented by the TMEM16 family, the majority of which function as calcium-dependent lipid scramblases (Suzuki *et al.* 2013). The first TMEM16 structure solved was from *Nectria haematococca* (*nh*TMEM16) (Brunner *et al.* 2014), but more

recently structures of TMEM16 from the fungus *Aspergillus fumigatus* (*af*TMEM16) (Falzone *et al.* 2019), as well as the human scramblases TMEM16K (Bushell *et al.* 2019) and TMEM16F (Alvadia *et al.* 2019) have been elucidated, all of which display the general features highlighted in **Figure 1.3**.

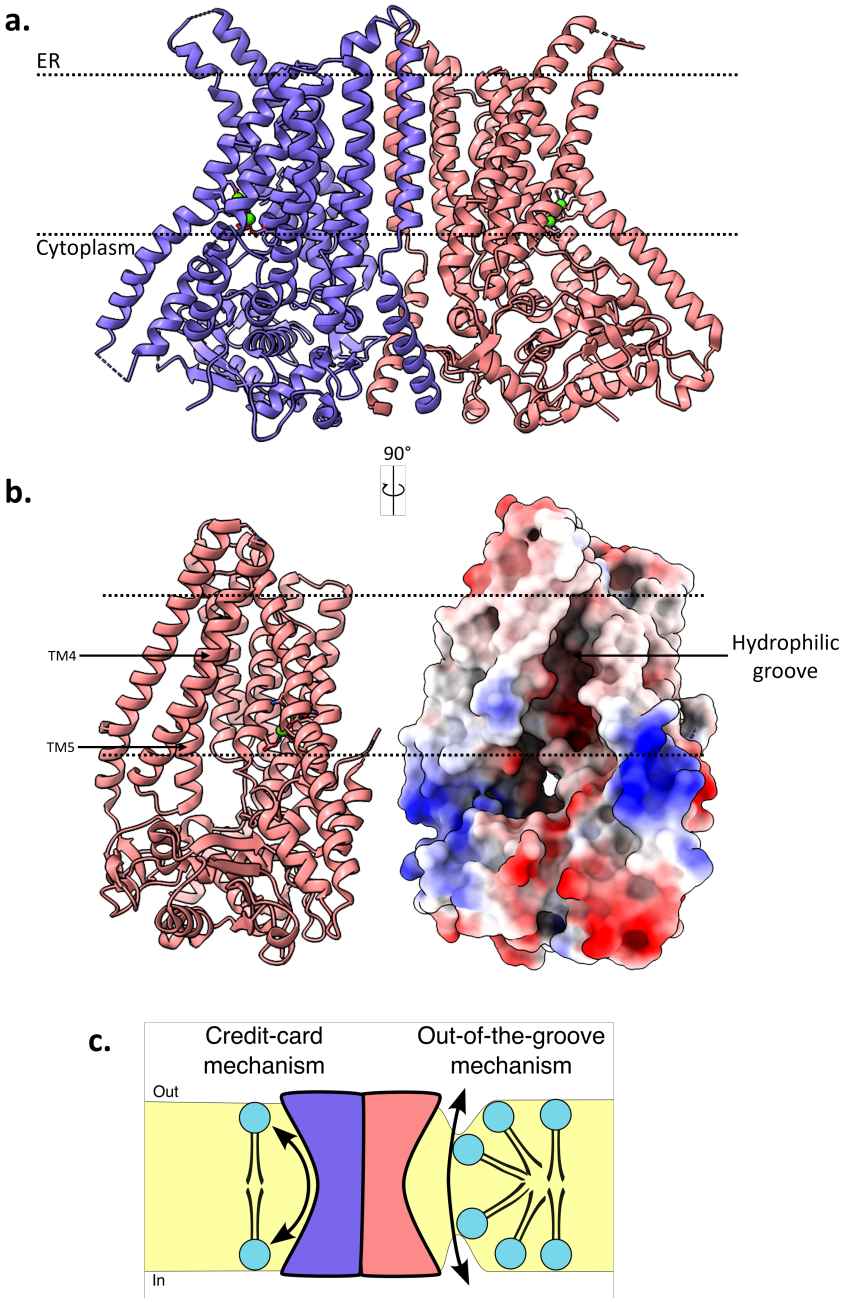

Figure 1.3: Human TMEM16K scramblase structure. a. Cartoon representation of hTMEM16K (PDB:5OC9) (Bushell *et al.* 2019). Monomers are coloured purple and pink, bound calcium ions are coloured green. **b.** Rotated view of **a.** showing the cartoon model (left) and electrostatic surface (right) of one TMEM16K monomer. **c.** Schematic of proposed mechanisms for TMEM16 lipid scrambling.

TMEM16 structures are dimeric, with each monomer made up of 10 transmembrane (TM) helices. In hTMEM16K, *nh*TMEM and *af*TMEM, the external face of each monomer contains an open hydrophilic groove that extends the width of the membrane (**Figure 1.3b**). This groove is closed in the current structures of TMEM16F, although molecular dynamics (MD) simulations of this protein have demonstrated structural transitions to an open conformation (Khelashvili *et al.* 2022). Such a hydrophilic groove is consistent with the predicted credit-card mechanism of lipid transport, with MD studies showing lipid headgroups accessing this groove while moving between membrane leaflets (Stansfeld *et al.* 2015, Bushell *et al.* 2019). Indeed, mutation of residues lining this groove in *nh*TMEM16 reduces scrambling activity (Lee *et al.* 2018), further supporting the notion of lipid headgroups contacting these residues during transport.

However, an increasing body of evidence suggests TMEM16 family scrambling occurs by a different mechanism. Early characterisation of TMEM16 family members had demonstrated that transport is non-specific (Malvezzi *et al.* 2013, Brunner *et al.* 2014), but *nh*TMEM16 was subsequently found to be capable of transporting a phosphatidylethanolamine (PE) lipid with polyethylene glycol (PEG) polymers of up to 5000 Dalton molecular weight (MW) attached to its headgroup (Malvezzi *et al.* 2018). Such lipid species are significantly larger than biological phospholipids and would not be accommodated by the hydrophilic groove present in the TMEM16 structures. Furthermore, mutation of groove-lining residues did not impair transport of these large lipid species, suggesting they are scrambled by a different mechanism. It was also demonstrated that opsin is capable of scrambling these large lipid species, which is consistent with previous work that showed opsin scrambling large glycolipids *in vitro* (Menon *et al.* 2011). This led to the proposal of a more general "out-of-the-groove" model for lipid scrambling (**Figure 1.3c**), whereby scramblases induce a thinning of the membrane around them and lower the energy barrier for lipid translocation between leaflets.

Recent cryo-electron microscopy (cryo-EM) maps of TMEM16F and *af*TMEM16 reconstituted into lipid nanodiscs further support this out-of-the-groove model, with maps of both proteins demonstrating deformation and thinning of the nanodisc in the vicinity of the hydrophilic groove (Feng *et al.* 2019, Falzone *et al.* 2022). In addition, structures of *af*TMEM16 in thicker nanodiscs exhibited open hydrophilic grooves but reduced *in vitro* scramblase activity, whilst structures in thinner nanodiscs in the absence of calcium displayed closed grooves but preserved *in vitro* scramblase activity (Falzone *et al.* 2022). This suggests that an open groove alone is not sufficient for scrambling, and that a closed groove state can still scramble lipid if the membrane is sufficiently thin. Taken together, these results suggest that opening of the hydrophilic groove contributes towards local thinning of the membrane to promote scrambling, rather than facilitating lipid scrambling via specific interactions between lipid headgroups and groove-lining residues.

1.1.2. P4-ATPases

P-type ATPases couple ATP hydrolysis to the transport of substrates across membranes against their concentration gradients (Montigny *et al.* 2016). There are six subfamilies of P-type ATPases named P1-P6 (Palmgren 2023), all containing a well-conserved architecture (**Figure 1.4a**) of a transmembrane domain of 6-12 TM helices, and three distinct soluble domains termed the N (**N**ucleotide binding), P (**P**hosphorylation) and A (**A**ctuator) domains. The well-characterised P2 class transports small ions via an alternating access mechanism, where a substrate binding site is alternately exposed to each side of the membrane via conformational change of the transporter, with certain states in the transport cycle occluding ions at the centre of the membrane (Bublitz *et al.* 2011). The P4-ATPase subfamily have been characterised as phospholipid and ceramide flippases, transporting their lipid substrates from the outer leaflet of the membrane to the cytoplasmic leaflet. P4-ATPases are generally more selective than scramblases regarding the identity of lipid headgroup that can be transported (e.g. yeast Dnf1 preferentially flips PC and PE, whereas Drs2p flips PS (Baldridge and Graham

2012)). The conserved architecture of the P-type flippases raised the "giant substrate problem" (López-Marqués *et al.* 2010): given that lipid substrates are much larger than the ions transported by the other well-characterised P-type ATPase classes, how can lipid transport occur by the same mechanism of alternating access that features an occluded state with such a small substrate binding site?

Cryo-EM structures of the *Saccharomyces cerevisiae* P4-ATPase Drs2p revealed a potential entry site for the headgroup of outer leaflet lipid at a hydrophilic groove formed from TM helices (Timcenko *et al.* 2019). Such an entry site was consistent with previous mutagenesis work that identified key residues for transport in this area (Vestergaard *et al.* 2014). Cryo-EM structures of the human P4-ATPase ATP8A1 identified a groove at the same location, and could resolve a bound lipid at this site (yellow spheres in **Figure 1.4a**) with its headgroup accessing the groove and its acyl tails oriented toward the bulk lipid of the membrane, making contact with the membrane-exposed hydrophobic surface of the TM region (Hiraizumi *et al.* 2019). However, the groove in this structure was not continuous but closed at the outer leaflet of the membrane, likely representing a partially occluded state in the lipid transport cycle. This suggests that transport in P4-ATPases occurs in a similar manner to the credit-card mechanism, but with alternate opening and closing of the substrate groove to the relevant face of the membrane. In this "central-cavity-model" (Palmgren 2023), the headgroup of the lipid being transported is accommodated in a hydrophilic transport groove that runs to the centre of the membrane, while the lipid acyl tails remain in the bulk membrane (**Figure 1.4b**).

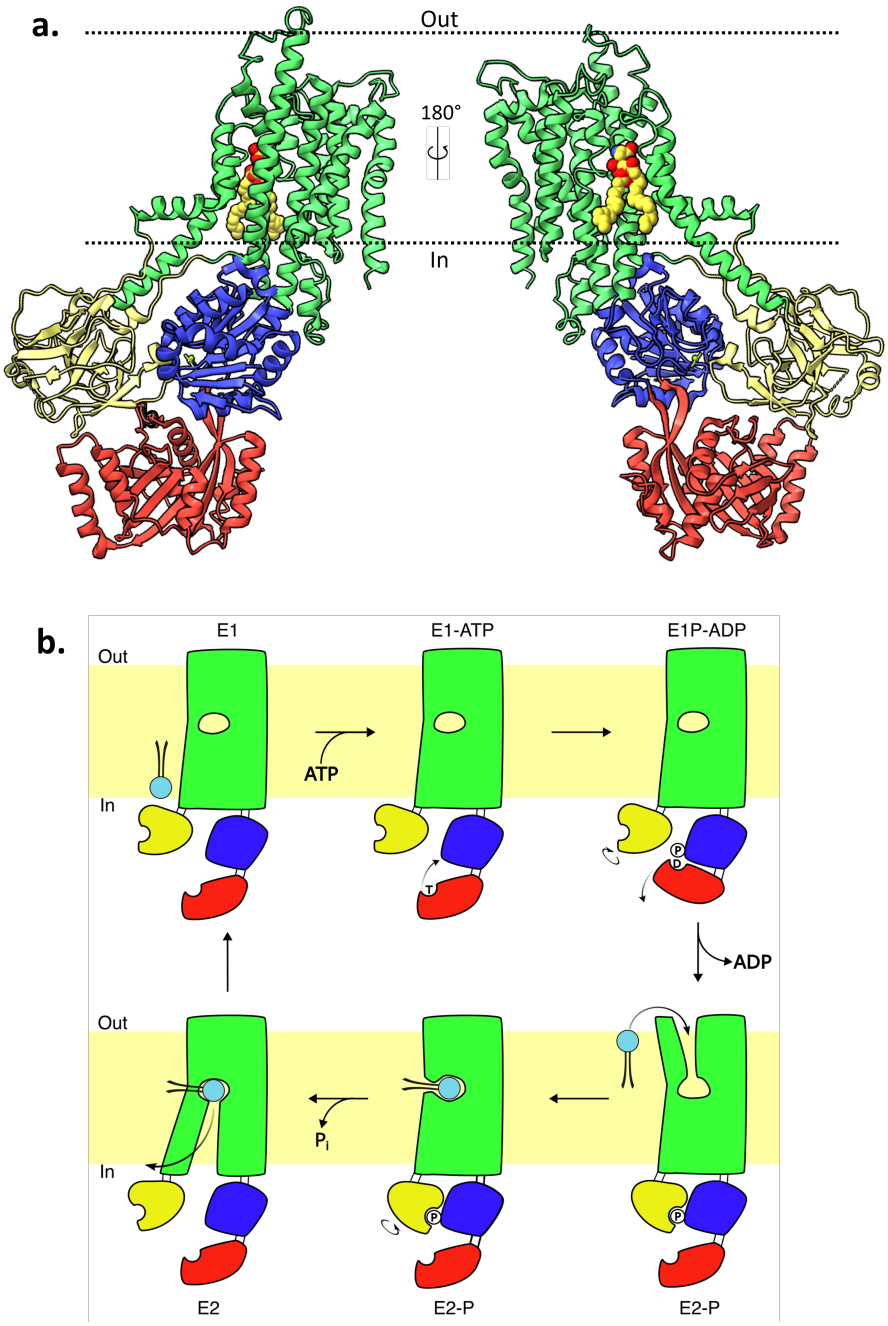

Figure 1.4: P4-ATPase structure and proposed mechanism. a. Cartoon representation of the structure of human ATP8A1 (PDB:6K7M) (Hiraizumi *et al.* 2019), demonstrating the general P-type architecture. Green = TM domain, blue = P domain, red = N domain, yellow = A domain. A bound PS lipid at the proposed transport pathway is shown as yellow spheres. **b.** Schematic outlining the proposed central-cavity model of lipid (light blue) transport for P4-ATPases. Domains are coloured as in **a.**, D = ADP, T = ATP, P = phosphate.

1.1.3. ABC transporters

ATP-binding cassette (ABC) transporters, similar to P-type ATPases, couple substrate transport to ATP hydrolysis. ABC transporters structurally comprise two nucleotide binding domains and two TM domains (**Figure 1.5a**) (Thomas and Tampé 2018). As with P4 flippases,

ABC floppases are generally more selective than scramblases (e.g. ABCA4 has been shown to transport fluorescently labelled PE *in vitro* but not PS or PC (Quazi *et al.* 2012)). ABC transporters transport non-lipid substrates via an alternating access mechanism, with a substrate binding site formed at the TM domain interface (**Figure 1.5b**). Such an alternating access could be consistent with the credit-card mechanism for lipid-transporting ABC proteins, with the headgroup of the lipid accessing alternately exposed grooves at the surface of the protein while the acyl tail-groups protrude into the bulk membrane.

The existence of a combined credit-card/alternating access model in ABC lipid transporters was supported by the structural characterisation of PglK, a bacterial floppase that exports glycolipid in the bacterial *N*-glycosylation pathway (Perez *et al.* 2015). A PglK crystal structure was determined in an occluded state and showed the presence of a short, surface-exposed amphipathic helix at the TM domains (**Figure 1.5a**) that is involved in lipid substrate binding. The surface underneath each amphipathic helix formed a hydrophobic groove in the outer leaflet of the membrane (**Figure 1.5c**). PgIK cannot bind lipids whose polyprenyl tails have been shortened, suggesting that a long prenyl tail is required to reach this binding site. Furthermore, introducing bulky tryptophan residues to the substrate binding cavity at the TM domain interface did not interfere with lipid transport rates, suggesting that the full lipid is not accommodated at the substrate binding pocket. Taken together, this supported an "outward-only" transport model (**Figure 1.5d**), where lipid binds at that outer surface of PglK while in its ADP-bound occluded state. Subsequent opening of the PgIK complex to an ATP-bound outward-open conformation would then enable the lipid headgroup of the substrate in the cytoplasmic leaflet to enter the outward-open cavity, and reorient into the outer leaflet. During this reorientation, the prenyl tail remains bound to the transporter outer surface, consistent with the credit-card mechanism.

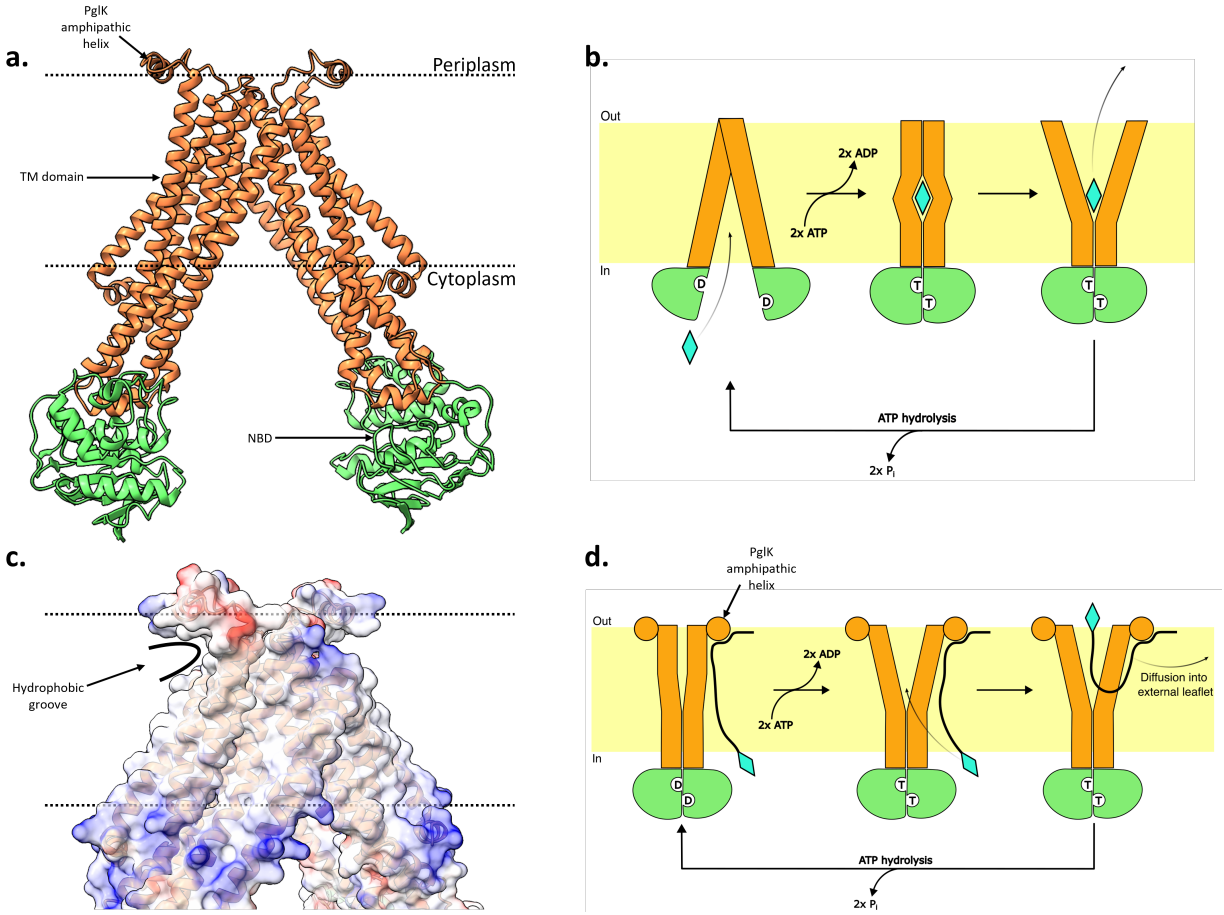

Figure 1.5: ABC transporter structure and mechanism. a. General architecture of ABC transporters, demonstrated with the cartoon structure of PglK (PDB:5C78) (Perez *et al.* 2015). Nucleotide binding domains are coloured green and TM domains orange. The amphipathic helix present in PglK is also highlighted on one TM domain. **b.** Schematic of general "trap-and-flip" mechanism for an ABC transporter (coloured as in **a.,** D = ADP, T = ATP) of soluble substrate (blue). **c.** Cartoon structure of PglK with transparent electrostatic surface. The hydrophobic groove formed from the amphipathic helix is highlighted. **d.** Schematic of proposed "outwards-only" mechanism of PglK-mediated lipid transport (prenyl lipid headgroup coloured blue).

However, more recent cryo-EM structures of other lipid-transporting ABC proteins suggest that lipid transport can also occur by an alternating access mechanism where the full lipid molecule is accommodated at the interface between the two TM domains, termed a "trap-and-flip" mechanism. Such a mechanism was demonstrated from a substrate bound cryo-EM structure of the bacterial floppase MsbA, where its lipid substrate could be clearly resolved in the inward-open MsbA conformation at the TM domain interface (Mi *et al.* 2017). Such a trap-and-flip mechanism was also shown to be relevant for the eukaryotic PC floppase ABCB4, since a PC-bound occluded structure was captured in which the full PC molecule was accommodated (Nosol *et al.* 2021). This evidence demonstrates the presence of both credit-card and trap-and-flip lipid transport mechanisms within a family of highly structurally related transporters and

highlights the importance of structural characterisation for the elucidation of mechanistic details.

1.1.4. ATP-independent flippases

Several flippases have been characterised that do not couple lipid transport to ATP hydrolysis, instead relying on ion gradients or substrate binding energy to promote unidirectional transport of lipids between leaflets of a membrane. LtaA is found in Gram-positive bacteria and transports the lipid anchor used in lipoteichoic acid (LTA) synthesis from the cytoplasmic leaflet of the cell membrane to the cell surface (discussed further in **section 1.2.2**). LtaA is part of the Major Facilitator Superfamily (MFS) of membrane proteins, one of the largest families of transporters (Reddy *et al.* 2012). MFS transporters typically contain 12 TM helices comprising two 6 TM helix bundles, the N-terminal domain (NTD) and the C-terminal domain (CTD) (**Figure 1.6a**). Transport of substrate is achieved through an alternating access mechanism, whereby a cavity for substrate is formed at the interface of NTD and CTD, and structural rearrangement of the transporter alternately exposes this cavity to each side of the membrane (**Figure 1.6b**). Substrate transport is often coupled to co/anti transport of an ion down its electrochemical gradient. In the case of LtaA, transport of lipid across the bilayer has been shown to be dependent on the PMF (Zhang *et al.* 2020). Similar to the ATP-dependent flippases, LtaA has also been shown to be highly selective toward the identity of the sugar headgroup of the lipid substrate being transported (Zhang *et al.* 2020).

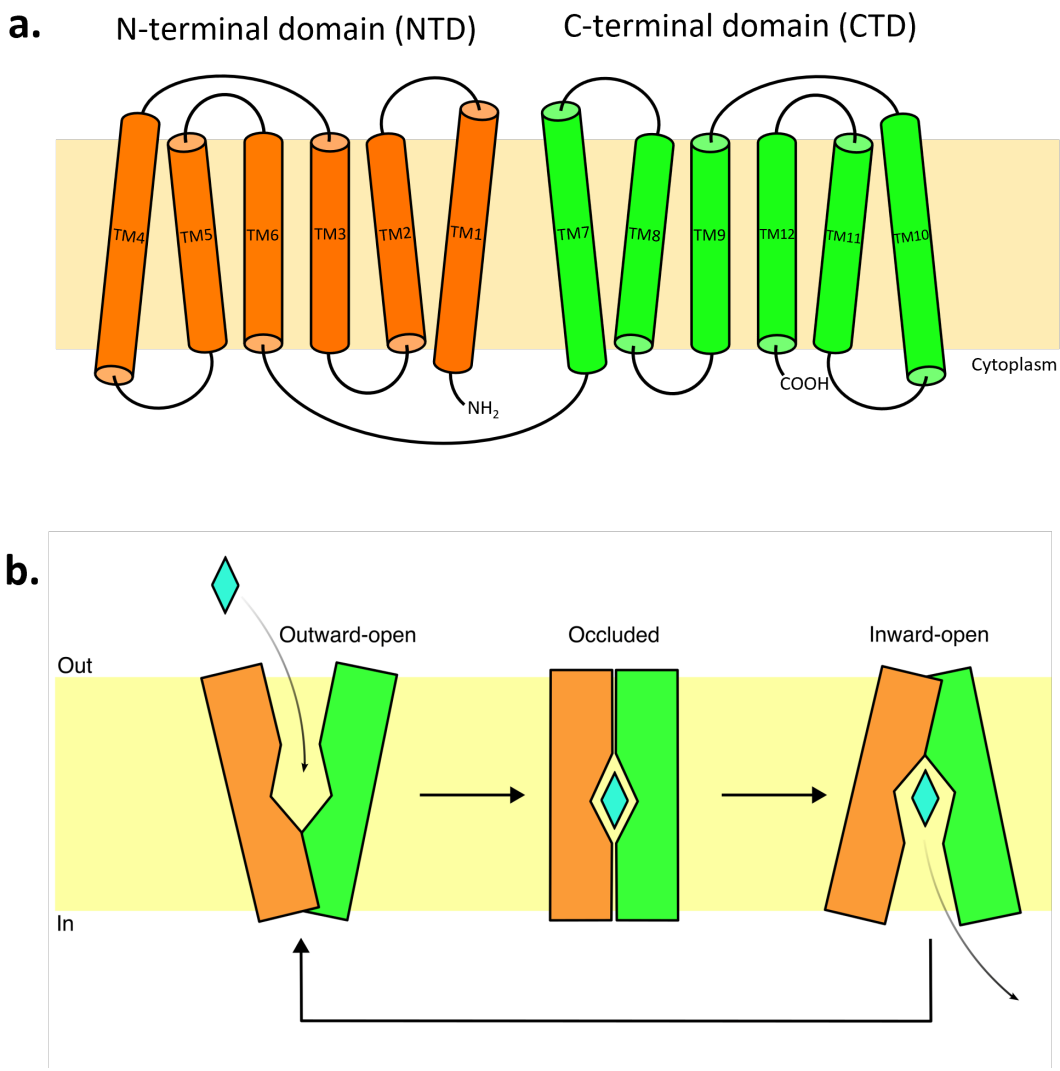

Figure 1.6: MFS topology and mechanism of transport. a. Topology diagram of the general MFS family fold. The NTD is coloured orange and the CTD coloured green. **b.** Alternating access mechanism of MFS transporters. NTD = orange, CTD = green, soluble substrate = blue.

Recent structural characterisation captured an outward-open conformation of LtaA and revealed a substrate cavity with an amphipathic binding surface, something which was absent from previously characterised MFS transporters (Zhang *et al.* 2020). The lipid substrate of LtaA could be docked into this pocket, suggesting that the full lipid molecule is accommodated by LtaA during transport. Such a mechanism would be consistent with the trap-and-flip mechanism discussed in **section 1.1.3**. Subsequent experiments demonstrated that mutation of the hydrophobic residues lining half of the substrate cavity significantly reduced lipid transport (Lambert *et al.* 2022), further supporting the trap-and-flip model over the credit card mechanism for this transporter.

This trap-and-flip mechanism has also been proposed for the lipid transporter MurJ, a member of the MOP exporter family, which exports large peptidoglycan subunits for cell wall synthesis in bacteria. MurJ was the first MOP transporter to be structurally characterised (Kuk *et al.* 2017); it comprises 14 TM helices, with a hydrophobic groove running the length of helices 13 and 14. This groove was suggested as the binding site for the acyl tails of the lipid substrate it transports. MurJ is essential in *E. coli,* and truncation of helices 13 and 14 is lethal, further supporting their importance in lipid transport and the notion that the full lipid molecule is accommodated by MurJ during transport (Zheng *et al.* 2018). However, many members of the MOP family lack TM helices 13 and 14, including homologues of the predicted O-antigen flippase Wzx in Gram-negative bacteria (Marolda *et al.* 2010). As such, it is unclear whether the trap-and-flip mechanism is also utilised by other lipid transporters of the MOP family.

A summary of the key features of each class of lipid transporter discussed above is provided in **Table 1.1**.

Table 1.1: Summary of key features of characterised lipid transporter classes.

Transporter class	**Energy source**	**Directionality *in vivo***	**Substrate specificity**	**Proposed transport mechanisms**
Scramblase	None	Bidirectional	Broad	• Credit-card • Out-of-the-groove
P-type flippase	ATP	Unidirectional	Narrow	• Credit-card (central-cavity model)
ABC floppase	ATP	Unidirectional	Narrow	• Credit-card (always-open model) • Trap-and-flip
ATP-independent flippase	Variable (PMF, ion gradient, substrate binding energy)	Unidirectional	Narrow	• Trap-and-flip

1.2. Lipid modification and transport in bacteria as a target for antimicrobials

Bacteria are reliant on lipid modification and transport systems to produce structures essential for their growth. In pathogenic bacteria, these transporters also promote increased resistance to antimicrobials and therefore represent appealing targets in the development of novel antimicrobials that could either inhibit bacterial growth or sensitise bacteria to existing antimicrobials. A brief overview of some of the key lipid transport systems in Gram-negative and Gram-positive bacteria is given below, along with examples of how such systems can be inhibited therapeutically.

1.2.1. Lipopolysaccharide and O-antigen synthesis

In Gram-negative bacteria, the presence of an outer membrane provides a barrier to many antimicrobials, making Gram-negative bacteria especially difficult to treat clinically. The outer leaflet of the outer membrane is packed with lipopolysaccharide (LPS) lipids that are often covalently linked to O-antigen sugar polymers; these sugar polymers form a dense barrier to many hydrophobic small molecules, limiting antimicrobial access to the cell itself (Delcour 2009). However, synthesis of LPS occurs at the bacterial inner membrane, and so effective antimicrobial resistance is dependent upon efficient LPS transport both between leaflets of bilayers and from the inner to the outer membrane. Synthesis of LPS begins at the inner leaflet of the inner bacterial membrane, involving the prenyl carrier lipid UndP. The O-antigen polymer attached to LPS is made up of repeating units of 3-5 sugars, the identities of which are variable depending on the species and strain of bacteria (Lerouge and Vanderleyden 2002). These individual O-antigen repeat units are synthesised in the cytoplasm and attached onto the headgroup of UndP in the inner leaflet of the inner membrane (**Figure 1.7**). The majority of O-antigen synthesis in Gram-negative bacteria occurs via the Wzx/Wzy pathway, in which these single O-antigen repeats attached to UndP are translocated to the outer leaflet of the

bilayer by Wzx (Islam and Lam 2014). Once in the periplasm, O-antigen polymers are formed from these units by Wzy.

The core of the LPS molecule, Lipid-A, is also synthesised at the inner leaflet of the membrane (Raetz *et al.* 2009) before being transported by the ABC transporter MsbA to the outer leaflet (Zhou *et al.* 1998). Once the O-antigen polymers have been synthesised by Wzy, they are transferred from UndP to Lipid-A by the ligase WaaL to form the full LPS molecule (Abeyrathne *et al.* 2005). LPS is then transported from the inner to the outer bacterial membrane by the Lpt transport system, a macromolecular complex that extends between both membranes and forms a hydrophobic groove to protect the lipid tails of LPS from the bulk solvent of the periplasm (Luo *et al.* 2017).

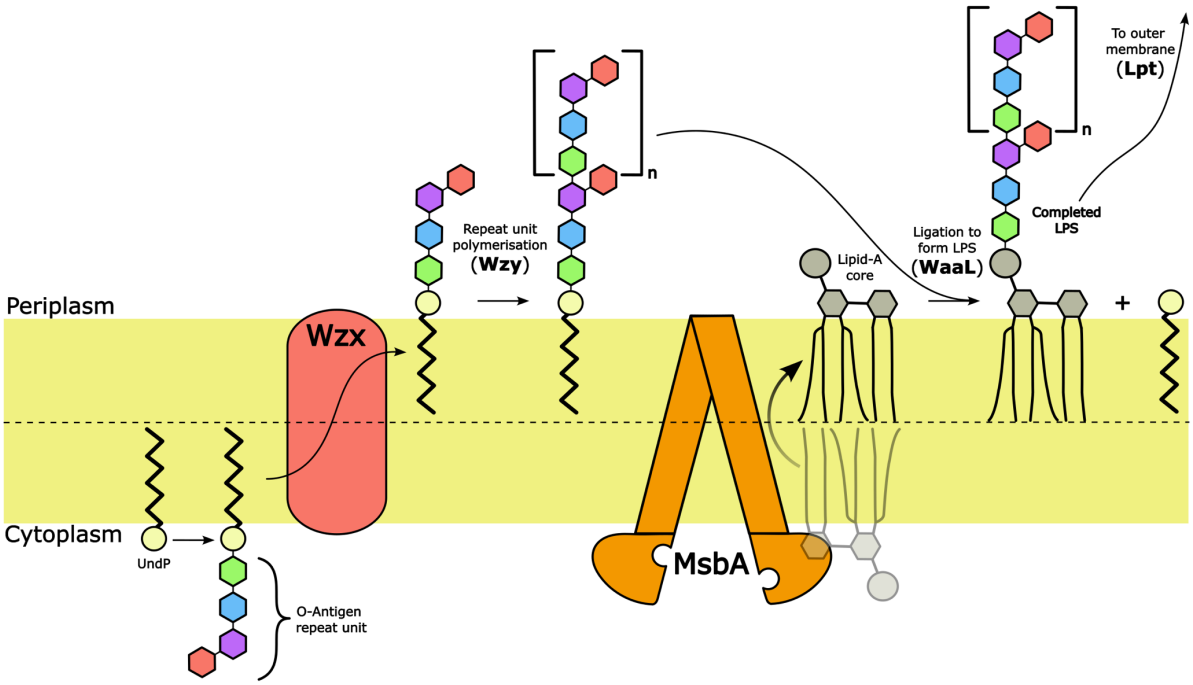

Figure 1.7: O-antigen synthesis pathway in Gram-negative bacteria. Schematic outlining the lipid transport steps involved in the Wzx/Wzy O-antigen synthesis pathway in Gram-negative bacteria.

Recently, a novel class of antimicrobials has been identified that acts against *Acinetobacter* infections (Zampaloni *et al.* 2024) by targeting the Lpt transport system in Gram-negative bacteria (Pahil *et al.* 2024). This highlights the validity of targeting lipid transport systems in

the development of novel antimicrobials, and the importance of their study. MsbA is also a target of interest, and two classes of MsbA inhibitors that lock the transporter in different states of its lipid transport cycle have been identified (Ho *et al.* 2018, Zhang *et al.* 2018). These compounds inhibit the growth of *E. coli* cells, and so hold promise for future clinical applications.

The carrier lipid UndP is utilised by both Gram-positive and Gram-negative bacteria for a variety of other processes, including cell wall synthesis (Garde *et al.* 2021) and glycosylation (Nothaft and Szymanski 2010). As such, bacteria rely on lipid transport systems to recycle UndP back to the inner leaflet of the inner membrane to ensure a constant supply of carrier lipid for these processes. Indeed, some antibiotics kill cells by binding to UndP at the cell surface, thus preventing this recycling (Rubinchik *et al.* 2011). The transporters responsible for UndP recycling could therefore also function as targets for novel antimicrobials. Recently, a member of the DedA family, UptA, was implicated in the retrograde transport of UndP (Roney and Rudner 2023). The DedA family are widely conserved across all domains of life, yet remain poorly characterised (see **section 1.3.5**).

1.2.2. Teichoic acid synthesis

One cellular process reliant on lipid transport that is unique to Gram-positive bacteria is teichoic acid synthesis. Teichoic acids are negatively charged carbohydrate polymers at the surface of Gram-positive bacteria. They provide cells with additional structural integrity, and have also been implicated in processes such as cell division and interaction with eukaryotic host cells (Weidenmaier and Peschel 2008). These teichoic acid polymers are either attached to the cell wall (Wall teichoic acid, WTA) or to lipid headgroups in the outer leaflet of the bacterial membrane (Lipid teichoic acid, LTA), as shown in **Figure 1.8**. WTA synthesis occurs in the cytoplasm, with repeat units (typically ribitol phosphate or glycerol phosphate (Brown *et al.* 2013)) being assembled onto UndP in the inner leaflet before being flipped to the cell

surface by an ABC transporter (e.g. TarGH in *Staphylococcus aureus*) (Lazarevic and Karamata 1995). The WTA polymer is then transferred from UndP to an *N*-acetylmuramic acid (MurNAc) residue in the peptidoglycan cell wall. Some bacteria also synthesise LTAs via the WTA synthesis pathway (so-called Type IV LTA synthesis (Denapaite *et al.* 2012)), but the more commonly occurring LTAs (Type I) are synthesised directly at the cell surface (Percy and Gründling 2014). Type I LTAs are polymers of glycerol phosphate derived from phosphatidylglycerol (PG) in the outer leaflet of the membrane. LtaS catalyses the formation of these polymers (Gründling and Schneewind 2007) onto a glycolipid base, such as diglucosyl-diacylglycerol (Glc_2-DAG) in *S. aureus* (Kiriukhin *et al.* 2001). This glycolipid base is synthesised in the cytoplasm using UDP-glucose, and must then be transported from the inner leaflet of the membrane to the outer leaflet by the flippase LtaA, which is energised by the PMF (Zhang *et al.* 2020).

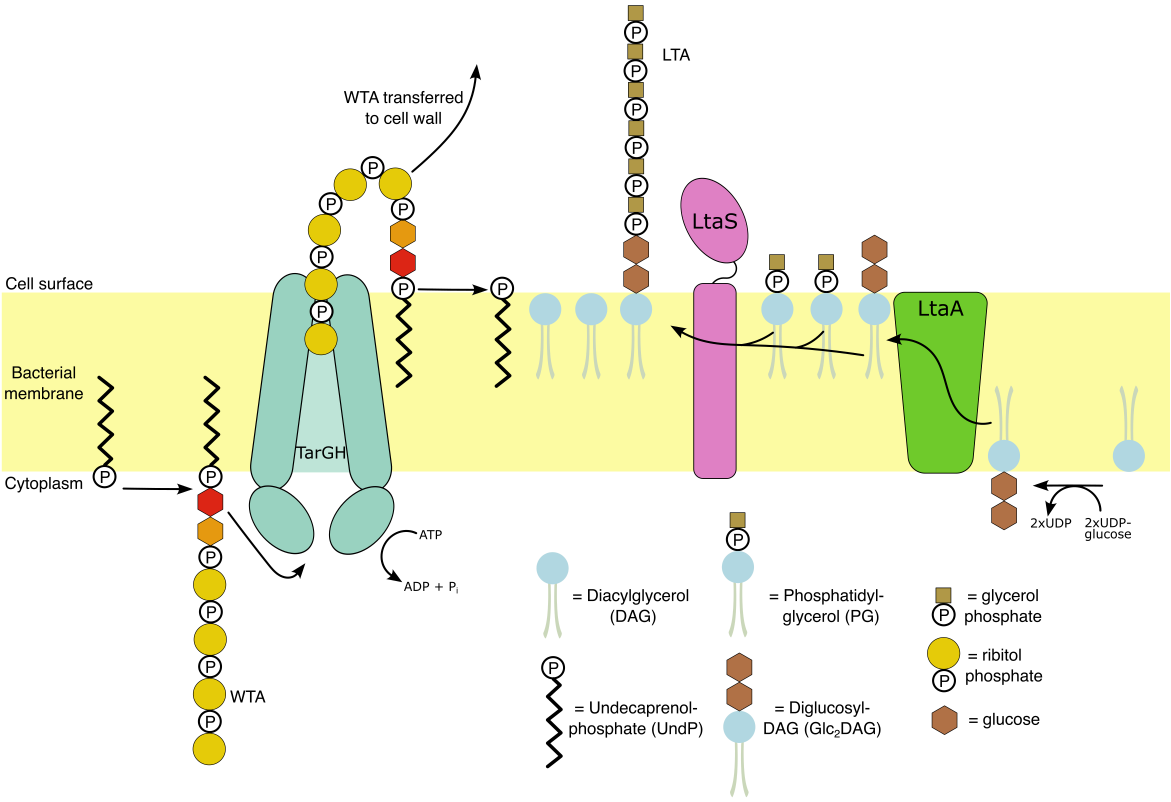

Figure 1.8: WTA and LTA synthesis pathways in Gram-positive bacteria. The synthesis of WTA involves the ATP-dependent transporter TarGH, and LTA precursors are transported and extended by LtaA and LtaS, respectively.

Both WTA and LTA synthesis pathways are appealing systems to target therapeutically in Gram-positive bacterial infections. Disruption of WTA synthesis *in vivo* reduces *S. aureus* host colonization (Misawa *et al.* 2015) and sensitises Methicillin-resistant *S. aureus* (MRSA) to β-lactam antibiotics that target cell wall synthesis (Wang *et al.* 2013). As such, WTA inhibitors targeting TarGH-mediated lipid transport have been identified (Matano *et al.* 2017) which hold promise in the combinatorial treatment of MRSA infections. Similarly, disruption of LTA synthesis in *S. aureus* severely impacts cell growth and division (Gründling and Schneewind 2007). Recent structure-based drug development has produced compounds that target LtaS and inhibit *S. aureus* growth (Chee Wezen *et al.* 2022), suggesting that the lipid transporter LtaA could also be an effective target in the future development of novel antimicrobials.

1.2.3. Modification of bacterial cellular surface charge

Many bacteria are able to modify their surface charge to provide resistance to antimicrobials. For Gram-positive bacteria, this can involve modifying teichoic acid polymers with D-alanine residues (Heaton and Neuhaus 1992). Such modification reduces the negative charge of these polymers and so provides enhanced resistance to cationic antimicrobial peptides (CAMPs) (Kingston *et al.* 2013), positively charged compounds produced by host immune systems to combat infection (Jenssen *et al.* 2006). This process is catalysed by the proteins of the *dlt* operon (Peschel *et al.* 1999).

Gram-positive bacteria can also aminoacylate phospholipids which are transported to the cell surface to reduce surface negative charge. The presence of aminoacyl phosphatidylglycerol (aminoacyl-PG) in Gram-positive bacteria was first demonstrated in *S. aureus*, which can attach L-lysine to PG in their membranes (Macfarlane 1962). The extent of this modification is significant, with Lysyl-PG (LysPG) comprising ~40% of *S. aureus* membrane lipid when grown at pH 7 (Dennison *et al.* 2016). This modification is not unique to Gram-positive species, with some Gram-negative bacteria such as *Pseudomonas aeruginosa* and *Rhizobium tropici* able to

also synthesise aminoacyl-PG (Kenward *et al.* 1979, Sohlenkamp *et al.* 2007). The protein responsible for this aminoacylation was later identified as the Multiple Peptide Resistance Factor (MprF) which is the focus of this thesis. The following section describes the MprF protein and its potential as an antimicrobial target in further detail.

1.3. The Multiple Peptide Resistance Factor, MprF

1.3.1. Identification of MprF as a lipid-modifying flippase

The *mprF* gene was first identified in a transposon mutagenesis screen of *Staphylococcus xylosus* to identify mutants with increased sensitivity to the positively charged antimicrobial gallidermin (Peschel *et al.* 2001). The gene was predicted to encode an ~800 amino acid membrane protein with a substantial C-terminal soluble domain (~300 residues). When *mprF* was knocked out in *S. aureus*, cells were unable to produce the lysinylated-PG typically found in the wildtype (WT) bacterial membrane. Therefore, it was hypothesised that MprF was the protein responsible for the aminoacylation of PG with L-lysine in *Staphylococcus.* This study identified homologous sequences in a number of other bacterial species, both Gram-positive and Gram-negative, and noted that whilst there was limited conservation in the N-terminal predicted transmembrane region of the protein sequences, the C-terminal soluble region exhibited much greater sequence homology.

Investigation into the other bacterial species that possess an MprF homologue highlighted variation in the identity of the amino acid that is esterified to PG; for example *P. aeruginosa* utilises only L-alanine (Klein *et al.* 2009), whereas *Clostridium perfringens* encodes two MprF homologues; one homologue produces alanyl-PG and the other produces lysyl-PG (Roy and Ibba 2008). In this latter example, the two *Clostridium* MprF homologues exhibit strict substrate preference, but there are some MprF homologues with more relaxed aminoacylation activity. For example, *Bacillus subtilis* MprF can utilise L-alanine or L-lysine, and *Enterococcus faecalis* MprF can utilise L-alanine, L-lysine, and even L-arginine (Roy and Ibba 2009). Despite this variation, the broad activity of MprF remains the same across all species: the reduction in negative charge of PG by the esterification of a positively charged amino acid to its glycerol headgroup.

Topology predictions suggested that MprF comprised 14 N-terminal transmembrane (TM) helices, with a highly hydrophobic α-helix at the very C-terminal end of the soluble domain that was predicted to insert into the membrane (Roy and Ibba 2009). Further investigation suggested that some predicted TM helices do not fully pass through the membrane (Ernst *et al.* 2015), resulting in the predicted topology diagram shown in **Figure 1.9.**

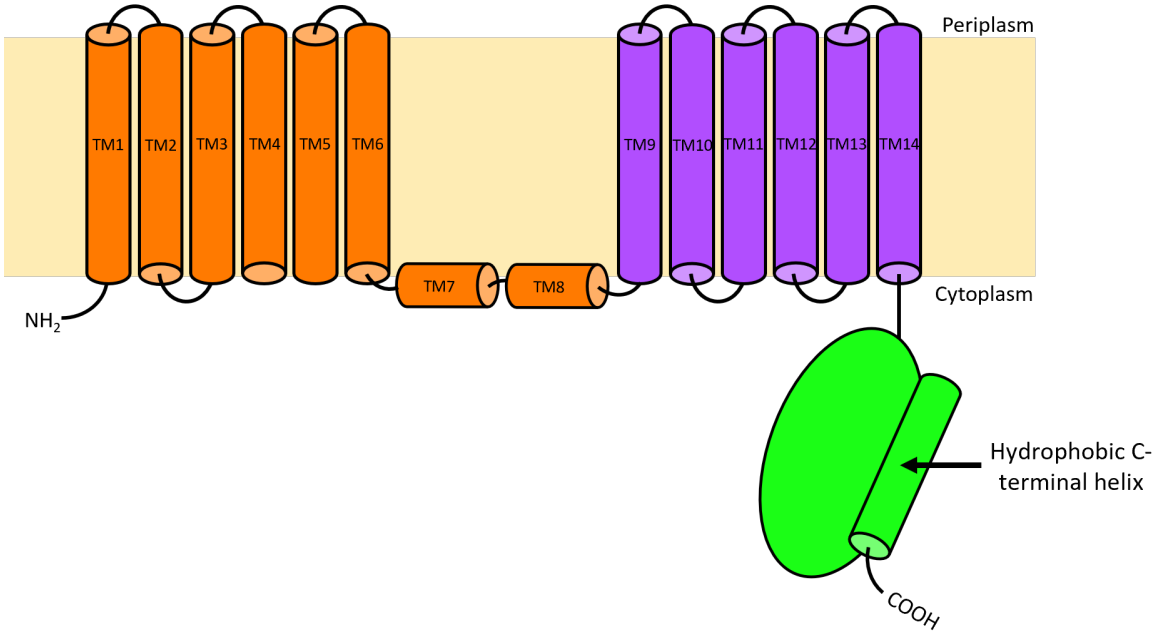

Figure 1.9: Predicted MprF topology. Early topology prediction for MprF (Ernst *et al.* 2015). The "Flippase" domain of MprF is coloured orange, the remaining TM helices are coloured purple, and the soluble domain is coloured green.

Given the soluble C-terminal domain was more conserved than the predicted transmembrane N-terminal region, further investigation into MprF's aminoacylation activity used truncations of the *S. aureus* homologue recombinantly expressed in *E. coli* (Ernst *et al.* 2009). Analysis of cell lipid content found that LysPG was still produced in cells expressing a construct of MprF that lacked its first eight predicted N-terminal TM helices, highlighting that the majority of the TM region is not required for aminoacylation activity. However, *S. aureus* Δ*mprF* cells expressing this truncated MprF construct were significantly more susceptible to daptomycin (a cyclic lipopeptide antibiotic that associates with calcium to form a cationic complex that targets the bacterial cytoplasmic membrane (Jung *et al.* 2004)) than WT cells, despite still producing LysPG, indicating that the N-terminal TM region of MprF is still required for

antimicrobial resistance to be conferred. Indeed, co-expression of these separate domains *in trans* confirmed this, with cells then exhibiting the same level of daptomycin resistance as WT, whilst also suggesting that these two domains act independently from each other.

The role of the MprF TM domain was elucidated further by treating cells with the membrane-impermeable dye fluorescamine, which can be used to probe the level of surface-exposed LysPG in cells. Cells expressing the soluble domain of MprF alone had very little surface-exposed LysPG, whereas cells expressing both domains had a similar level of surface-exposed LysPG as in their inner leaflets (Ernst *et al.* 2009). This suggested that the N-terminal TM region of MprF was acting as a flippase, transporting the aminoacyl-PG synthesised by the soluble domain from the inner to the outer leaflet of the bacterial membrane (**Figure 1.10**). This MprF-dependent accumulation of LysPG on the cell surface is suggested to confer antimicrobial resistance by reducing the electrostatic attraction between CAMPs and the bacterial surface (Ernst *et al.* 2009). This model is supported by coarse-grain MD simulations showing that CAMPs exhibit reduced binding to bilayers containing increasing concentrations of AlaPG or LysPG (Simcock *et al.* 2021).

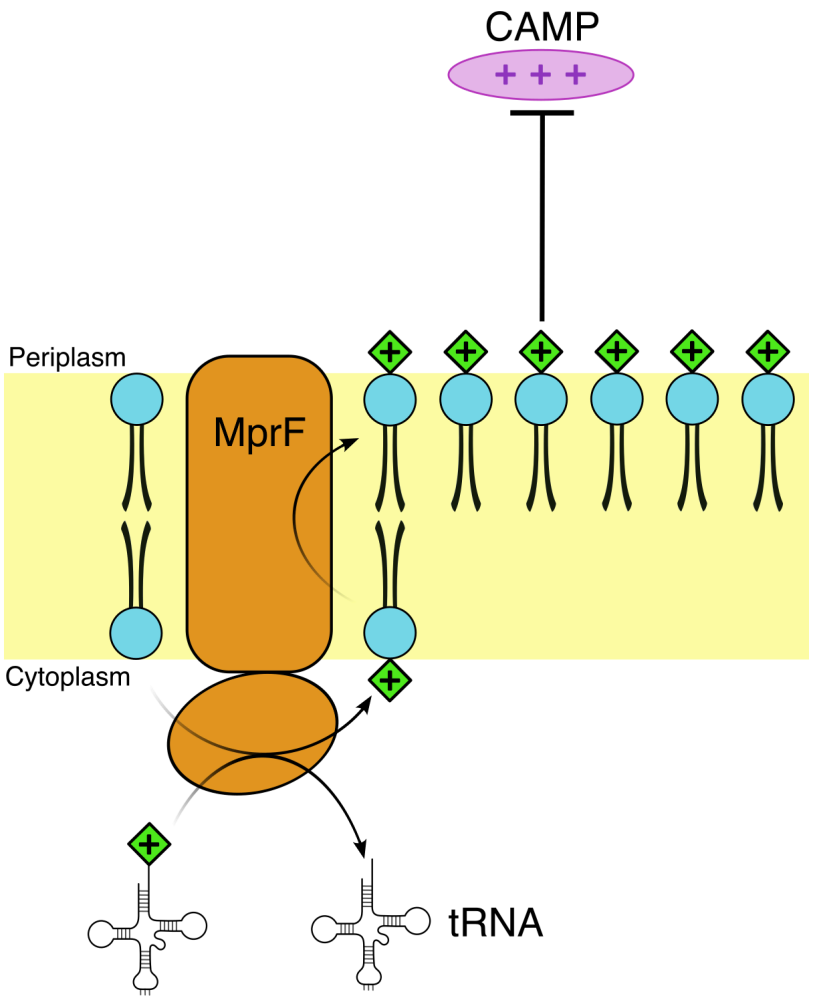

Figure 1.10: Schematic of MprF activity. MprF (orange) attaches an amino acid (green) from a charged-tRNA to the headgroup of PG (blue) in the inner leaflet of the bilayer, and transports it to the outer leaflet, where it electrostatically repels positively charged antimicrobials (pink).

1.3.2. The MprF soluble domain aminoacylates PG headgroups

The best characterised domain of MprF is the soluble domain responsible for aminoacylation of PG. Prior to the identification of MprF, it was known that the presence of aminoacylated PG in bacterial membranes was dependent on tRNA (Lennarz *et al.* 1966, Nesbitt and Lennarz 1968), so it was assumed that the substrate for MprF-mediated aminoacylation would be charged-tRNA. This was demonstrated experimentally *in vitro* using *C. perfringens* MprF, which synthesised radioactive ^{14}C-AlaPG when provided with charged ^{14}C-alanyl-tRNA^{Ala} (Roy and Ibba 2008). Furthermore, *in vitro* synthesis of ^{14}C-AlaPG using crude *P. aeruginosa* cell extract was abolished by application of RNase A (Klein *et al.* 2009). Similar *in vitro* assays using just the soluble domain of MprF demonstrated that no TM helices were required for

aminoacylation of PG (Hebecker *et al.* 2011). This contrasted the previously described truncation experiments of Ernst *et al.* (2009), which suggested that synthesis of LysPG *in vivo* requires the soluble domain of MprF to be expressed alongside the last 4 C-terminal TM helices. As such, these TM helices likely localise the soluble domain of MprF to the membrane surface so it is in close proximity to its PG substrate in a cellular context.

Subsequent studies investigated the recognition of tRNA substrate and found that near-maximal MprF-mediated aminoacylation of PG could be achieved *in vitro* using a tRNA microhelix that contained only the first 5 base pairs at the acceptor stem region (Hebecker *et al.* 2011). These first 5 bases contain a G-U wobble pair that is the basis of recognition of $tRNA^{Ala}$ by its cognate tRNA synthetase, AlaRS (Hou and Schimmel 1988, Naganuma *et al.* 2014). Chemical labelling also showed that MprF activity was not dependent on activated nucleophile residues within the protein, and that no metal ions were involved in catalysis as aminoacylation occurred in the presence of chelating agents (Hebecker *et al.* 2011). However, mutation of several acidic and basic residues did result in decreased MprF activity, leading to the hypothesis that aminoacylation occurs by direct nucleophilic attack from one of the PG hydroxyl groups onto the carbonyl group of the esterified Ala-$tRNA^{Ala}$, aided by acid-base catalysis from MprF residues (**Figure 1.11**).

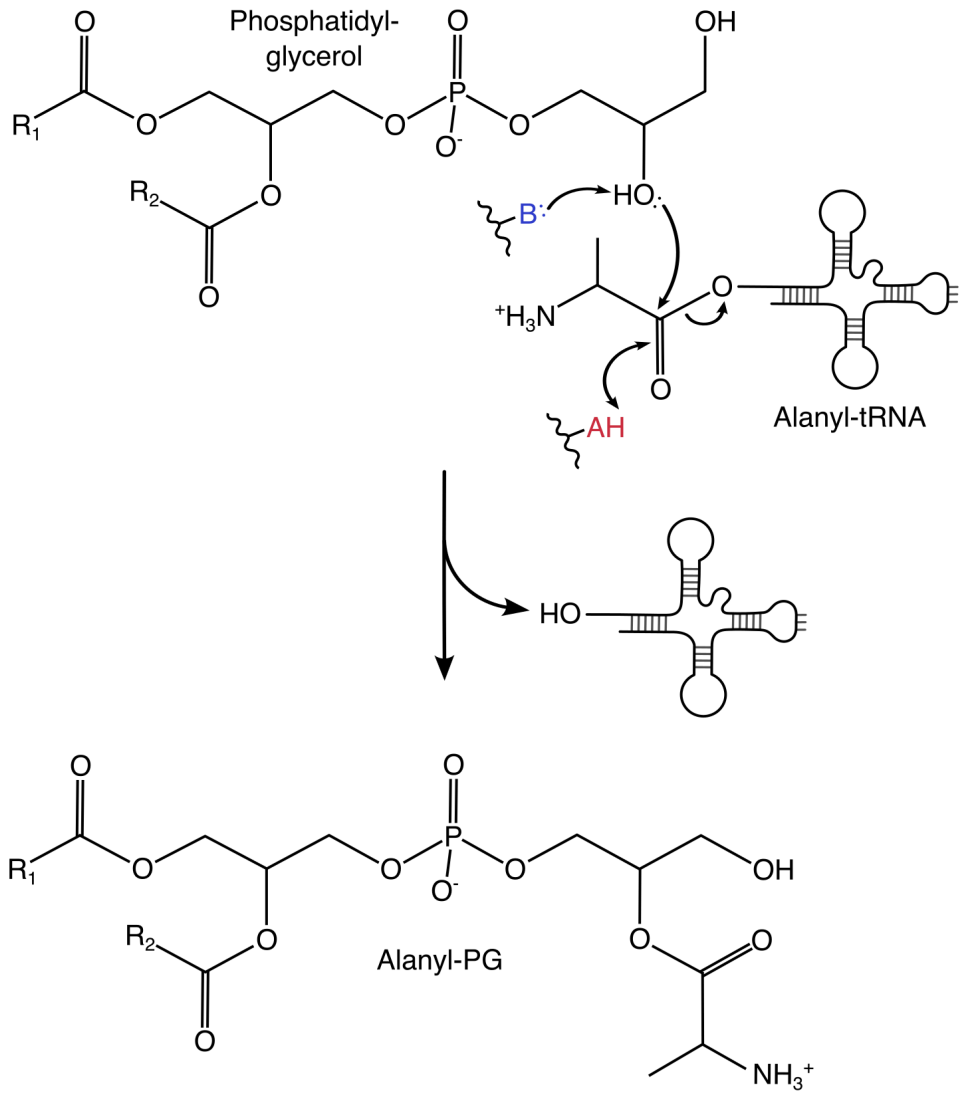

Figure 1.11: Proposed mechanism of MprF-mediated alanylation of PG. Basic (B, blue) and acidic (A, red) residues in MprF suggested to facilitate the nucleophilic attack are shown.

In addition, it was shown that the highly hydrophobic predicted α-helix at the C-terminus of the MprF soluble domain was essential for aminoacylation activity (Hebecker *et al.* 2011).

Following this work, the structures of soluble domains from two MprF homologues, *P. aeruginosa* (*Pa*MprF) and *Bacillus licheniformis* (*Bl*MprF), were solved by X-ray crystallography (Hebecker *et al.* 2015). Despite *Pa*MprF synthesising AlaPG and *Bl*MprF synthesising LysPG, the two soluble domains display significant structural conservation, with a root-mean-square deviation (RMSD) of only 1.1 Å. The key structural features of the soluble domain of MprF are shown in **Figure 1.12** with the structure from *Pa*MprF:

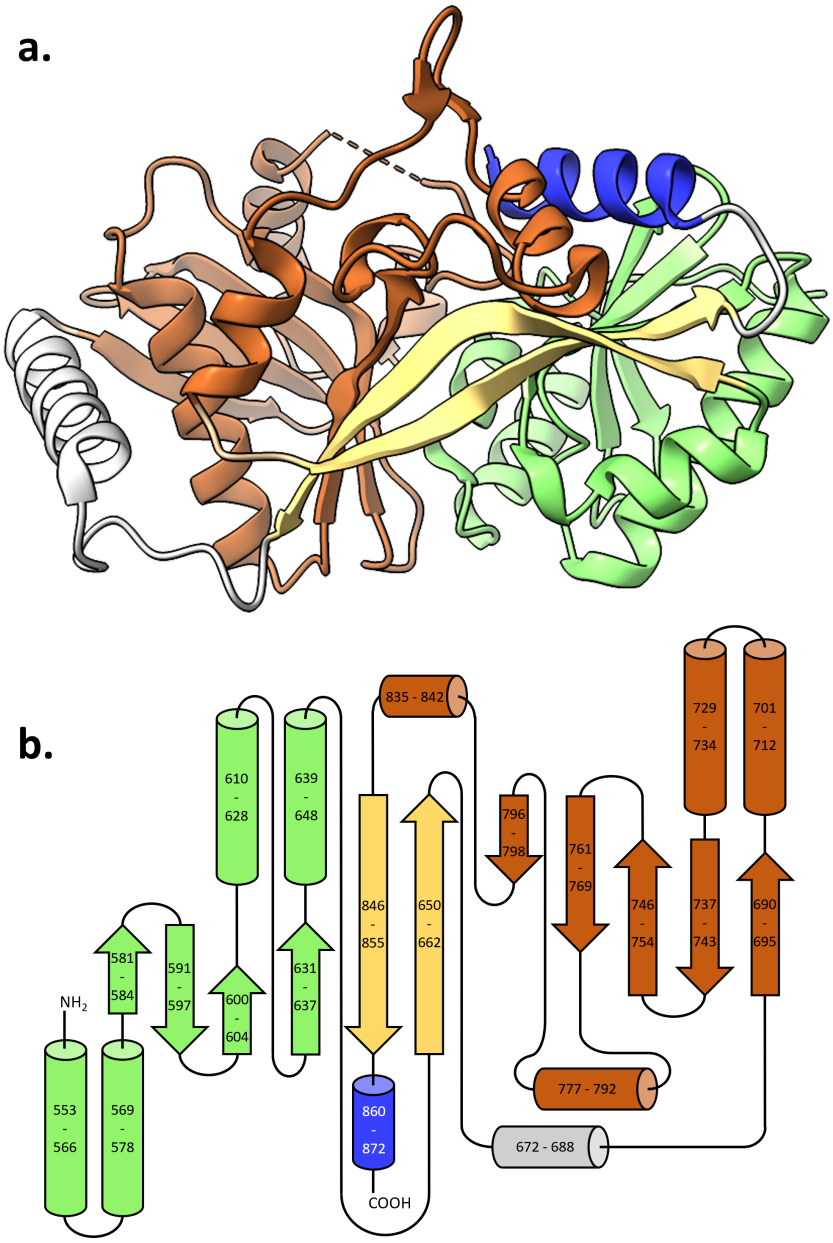

Figure 1.12: *Pa*MprF soluble domain structure. a. Cartoon structure (PDB: 4v35) and **b.** topology diagram of *Pa*MprF soluble domain. GNAT domains 1 and 2 are coloured green and brown respectively. Two β-strands (yellow) contribute to both GNAT domains. The hydrophobic C-terminal helix is coloured blue.

The soluble domain structures both contain two GNAT folds (GCN5-related *N*-acteyltransferase) (Dyda *et al.* 2000). GNAT folds are present in enzymes that catalyse the transfer of acetyl groups from coenzyme A to substrates. Two long β-strands (yellow in **Figure 1.12**) contribute to the β-sheets of both GNAT domains. The soluble domain structures of MprF resemble FemX (**Figure 1.13a**), a bacterial protein that catalyses the transfer of amino acids to UDP-MurNAc to form the pentapeptide subunits used for cell wall synthesis (Salah Ud-Din

et al. 2016). Like MprF, FemX utilises a charged-tRNA for its reaction mechanism. Using substrate analogues, a crystal structure of FemX was determined showing the locations of the substrate and donor tRNA binding sites (Fonvielle *et al.* 2013). F304 and K305 in FemX are highly conserved and interact with the ribose groups of the tRNA CCA acceptor stem. Mutation of the residues occupying the same positions in *Pa*MprF (F839, K840) abolishes aminoacylation activity (Hebecker *et al.* 2015), suggesting that recognition of the tRNA acceptor stem also occurs at this location in MprF. The *Bl*MprF soluble domain was co-crystallised with L-lysine amide, which binds in proximity to the 3'OH of the predicted tRNA CCA acceptor stem binding site (**Figure 1.13c**), providing further evidence that the tRNA binding site is conserved between the two structures.

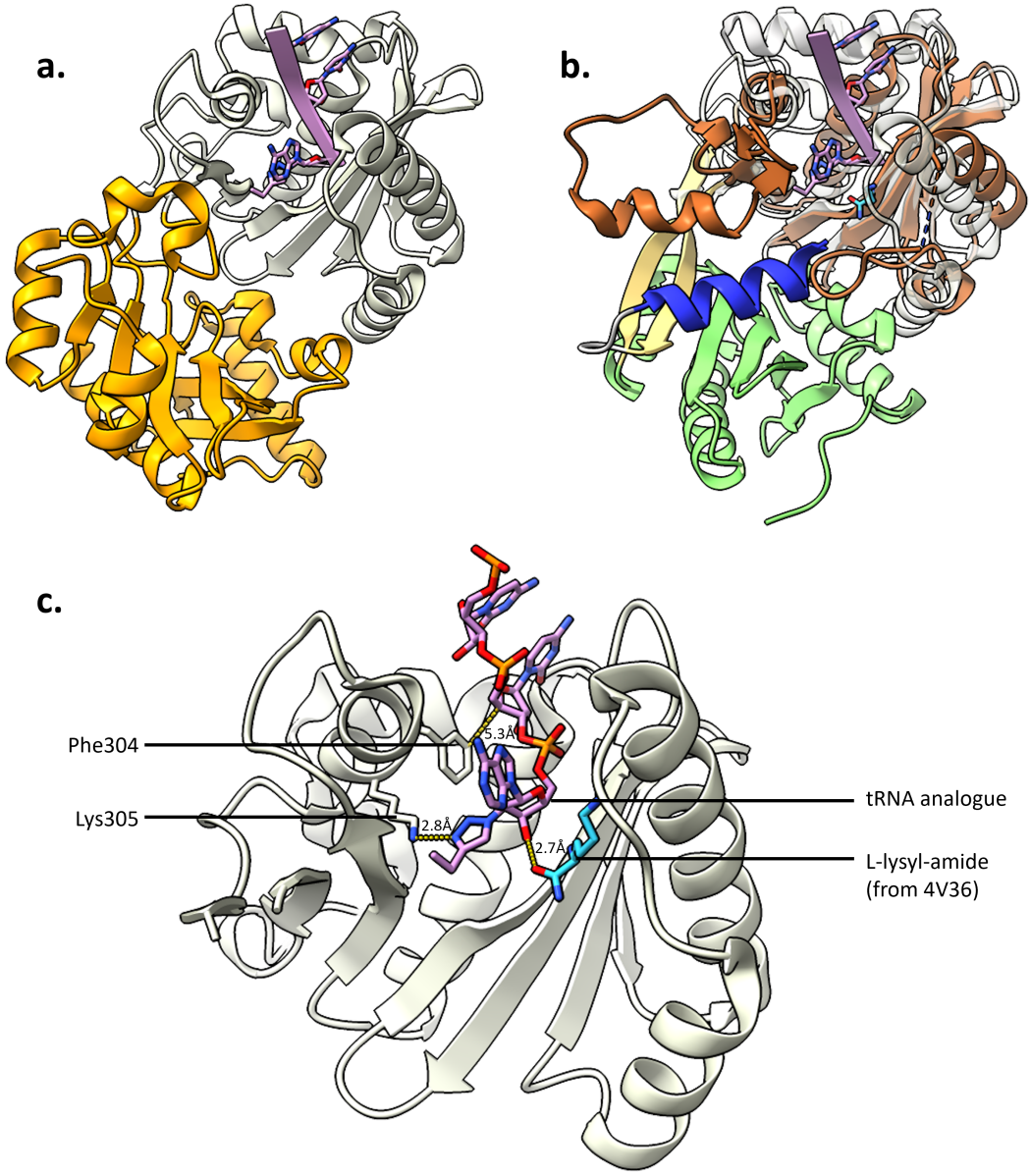

Figure 1.13: FemX *Pa*MprF structural comparison. a. FemX cartoon structure (PDB: 4ii9) showing GNAT domains 1 and 2 in orange and white respectively. Co-crystallised tRNA analogue is shown in pink. **b.** Alignment of GNAT domain 2 of FemX (white transparent) to *Pa*MprF soluble domain (GNAT domain 1 = green, GNAT domain 2 = brown), RMSD = 1.2 Å. L-lysyl-amide (co-crystallised in *Bl*MprF, PDB:4v36) is overlaid in cyan. **c.** FemX tRNA binding site at GNAT domain 2, showing key tRNA binding residues. L-lysyl-amide from *Bl*MprF is overlaid (cyan), with the close proximity to the 3' OH of the tRNA analogue highlighted.

However, whilst the FemX UDP-MurNAc binding site is adjacent to the bound CCA acceptor stem in a groove running along the face of the protein, this groove is closed in the MprF soluble domain structures (**Figure 1.14**). This led Hebecker *et al.* (2015) to hypothesise that PG accesses the active site for aminoacylation via a tunnel on the opposite face of the protein (**Figure 1.14c**). Whilst a PG molecule could be computationally docked into this proposed

substrate tunnel, there are no substrate-bound structures of MprF homologues to experimentally confirm the suggested soluble domain binding site for PG.

The C-terminal helix of the soluble domain is essential for aminoacylation activity, but in the published crystal structures it is not extended as if inserting into the membrane. Instead, it is folding back towards the core of the protein (residues 860-872 in *Pa*MprF, blue helix in **Figure 1.14a**). However, the solvent-exposed face of this helix is highly hydrophobic, suggesting that in a physiological context it could interact with the membrane plane in order to access PG substrate. This would explain the necessity of this helix in *Pa*MprF, but would be at odds with the PG substrate tunnel suggested by Hebecker *et al.* (2015) as this tunnel is on the opposite face of the protein. For the PG binding site to be in proximity to this C-terminal helix (near the corresponding substrate binding site in FemX), significant structural rearrangement to open the substrate groove would have to occur.

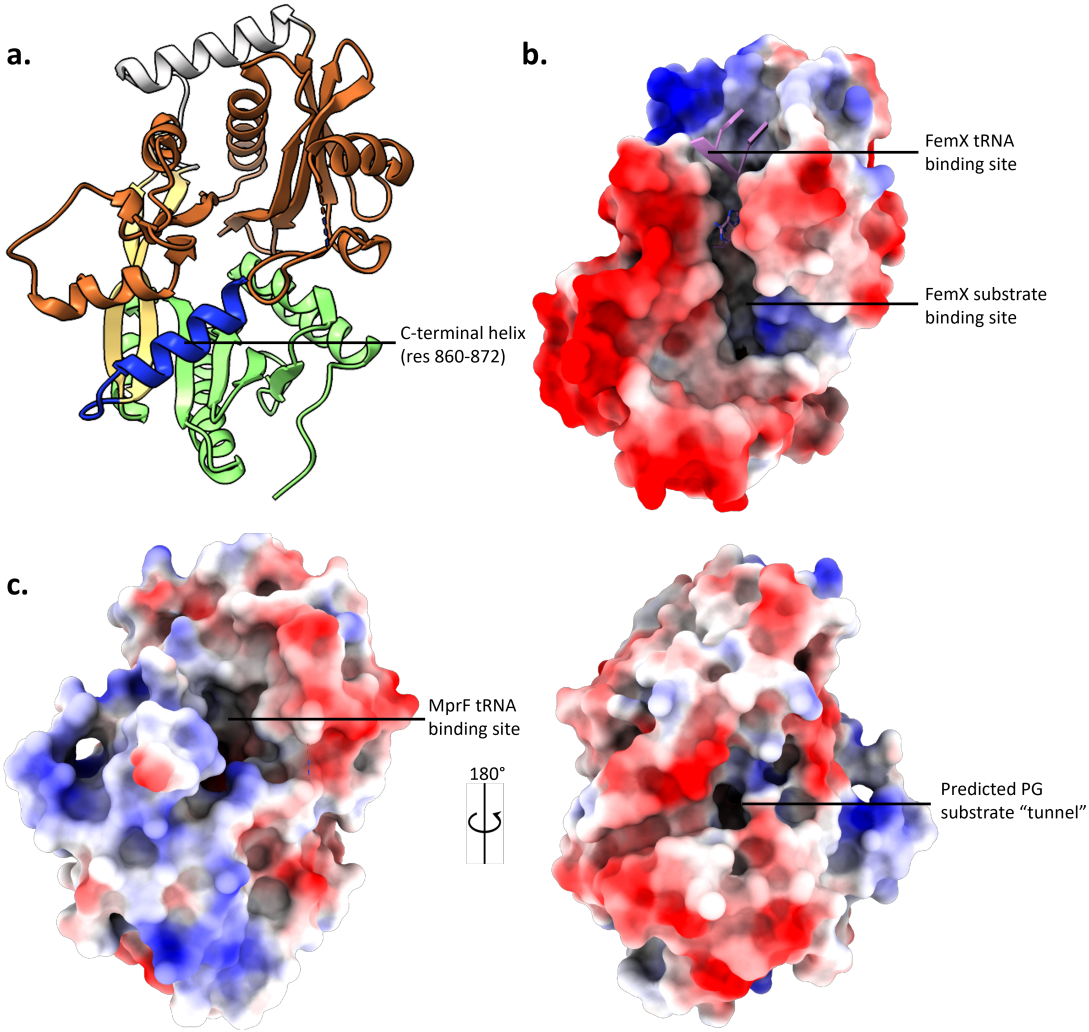

Figure 1.14: *Pa*MprF FemX substrate binding site comparison. a. Cartoon model of *Pa*MprF soluble domain showing orientation of electrostatic surfaces. The essential C-terminal helix is coloured blue. **b.** Electrostatic surface of FemX from same view as panel *a.*, showing a continuous tRNA-substrate groove. The bound tRNA analogue is coloured pink. **c.** Electrostatic surface of *Pa*MprF soluble domain from same view as panel *a.*, then rotated through 180° to show the PG substrate tunnel suggested by Hebecker *et al.*

An additional mechanistic unknown is how MprF accesses tRNA from the cytoplasm. Following aminoacylation, charged-tRNAs are typically bound by EF-Tu, a transcription factor that protects the tRNA from degradation and shuttles it to the site of protein synthesis at the ribosome (Louie *et al.* 1984). EF-Tu is highly abundant in the cytoplasm (Neidhardt *et al.* 1977) and binds to aminoacyl-tRNA with high affinity (Louie *et al.* 1984). As such, it is likely that MprF would only be able to utilise tRNA before it is sequestered by EF-Tu. Previous kinetic analysis suggests that EF-Tu and MprF would have similar affinities for charged-tRNA (Roy and Ibba 2008), but does not take into account the partitioning of the two proteins in the cell,

since MprF is restricted to the cell membrane so would presumably have less access to newly charged tRNA than EF-Tu does. Other bacterial pathways also utilise charged-tRNAs as substrates; the previously discussed FemX in *S. aureus* uses $tRNA^{Gly}$, and the *S. aureus* genome encodes five possible acceptor $tRNA^{Gly}$ species. Of these five tRNAs, three are expected to display weak binding to EF-Tu (Giannouli *et al.* 2009) and so are thought to be the mechanism by which aminoacylated-$tRNA^{Gly}$ can "escape" the protein synthesis pathway. It is unknown if a similar mechanism is employed to ensure tRNA availability for MprF activity, or if another protein carries tRNA to the membrane to deliver substrate directly to MprF and away from the protein synthesis pathway. One appealing candidate for this would be the tRNA synthetase itself, which could pass on newly charged tRNA to MprF, if a direct interaction between the two proteins existed.

1.3.3. MprF flippase domain activity

MprF was one of the first bacterial phospholipid flippases to be identified, but the predicted flippase domain of MprF is not homologous with any other characterised lipid transporter. As such, truncation experiments were performed to provide insight into the activity of this domain (Ernst *et al.* 2015). It was demonstrated that only the first six TM helices of MprF are required to confer increased daptomycin resistance to cells, although this daptomycin resistance is increased further by extension to the first eight TM helices, suggesting these helices increase the efficiency of lipid transport (Ernst *et al.* 2015). Sequence alignment of the TM regions of fifteen MprF homologues identified several conserved motifs, including YRXXY and PGGXGXFD/E motifs in close proximity at the core of the flippase domain. For a protein with an overall very low conservation across homologues, the consistent presence of highly charged residues R and D/E at the core of the membrane was striking, as well as conserved proline and glycine residues implying regions of the protein where flexibility/kinked helix geometry is essential for protein function. Mutagenesis of these conserved residues to alanine in *S. aureus* MprF demonstrated that these residues were dispensable for LysPG synthesis, but

were required for increased daptomycin resistance, suggesting their involvement in lipid transport (Ernst *et al.* 2015).

The specificity of MprF flippase activity has also been investigated. By expressing different domains of MprF from different homologues in *S. aureus*, one study demonstrated that cells expressing *C. perfringens* MprF (AlaPG-producing) with the flippase domain of *S. aureus* MprF (LysPG-producing) had similar levels of daptomycin resistance as cells expressing full-length *S. aureus* MprF (Slavetinsky *et al.* 2012). This demonstrates that the *Sa*MprF flippase domain is able to translocate AlaPG as well as LysPG, and so exhibits at least some degree of relaxed specificity. Whether this extends further, with MprF being able to transport a broader range of lipids than AlaPG and LysPG, is unknown.

The use of cryo-EM to determine the first and only full-length structure of an MprF homologue from *R. tropici*, a non-pathogenic Gram-negative soil bacterium, provided more information about the TM domain of MprF (Song *et al.* 2021). The *Rt*MprF structure and topology model are displayed in **Figure 1.15:**

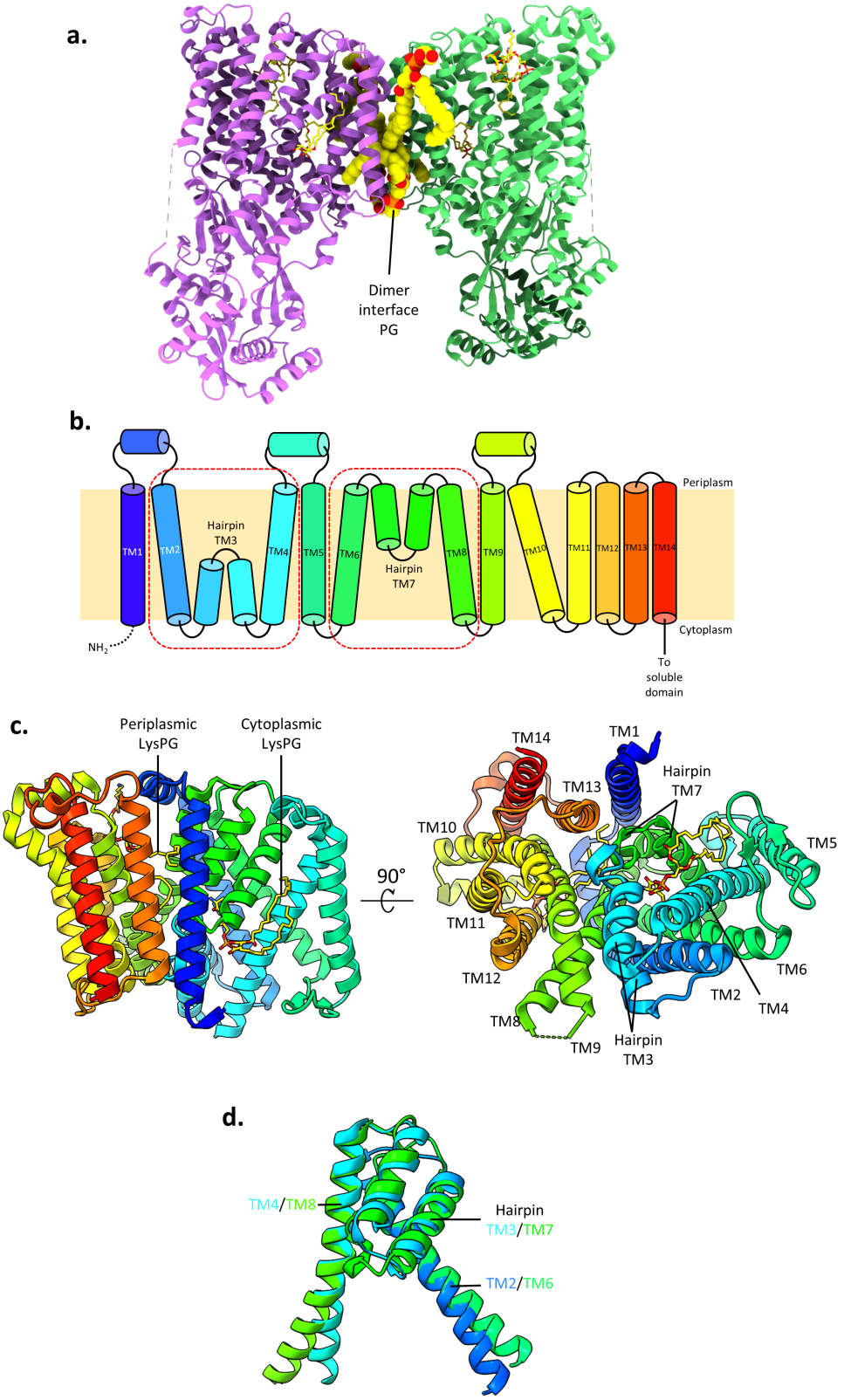

Figure 1.15: *Rt*MprF cryo-EM structure. a. Side view of the *Rt*MprF dimer (chains coloured purple and green, PDB 7DUW). PG molecules at the dimer interface are shown as yellow spheres, bound LysPG as yellow sticks. **b.** Topology diagram of the TM region of *Rt*MprF (coloured blue-red from N-C termini). The hairpin helices related by pseudosymmetry are highlighted with red dashed boxes. **c.** Side and top view of the TM region of a *Rt*MprF monomer, coloured as in the topology diagram. Top view is from the cytoplasmic face, with soluble domain removed for clarity. Bound LysPG molecules (yellow sticks) are highlighted. **d.** Alignment of hairpin helix repeats (RMSD = 1.27 Å).

*Rt*MprF is dimeric, with four PG molecules contributing to the dimer interface (**Figure 1.15a**). Consistent with sequence analysis of the TM region of MprF, the flippase fold comprising the first eight TM helices is novel and shares no similarities with the folds of other structurally characterised lipid transporters. The most striking feature of the *Rt*MprF flippase fold is the pair of re-entrant hairpin helices, which are oriented with hairpin loops positioned towards each other at the centre of the bilayer. These hairpin helices are related by a two-fold axis of pseudosymmetry (**Figure 1.15d**). The previously identified PGGXGXFD/E motif corresponds to the loop at the centre of hairpin TM7, providing an explanation for the conserved proline and glycine residues across homologues, and implying the involvement of these hairpin helices in lipid transport. Remarkably, the *Rt*MprF cryo-EM structure displays two bound molecules of LysPG, one in a cavity formed at the cytoplasmic side of the membrane, and the other in a cavity at the periplasmic side of the membrane. These lipid binding sites in the *Rt*MprF structure are highlighted in **Figure 1.16:**

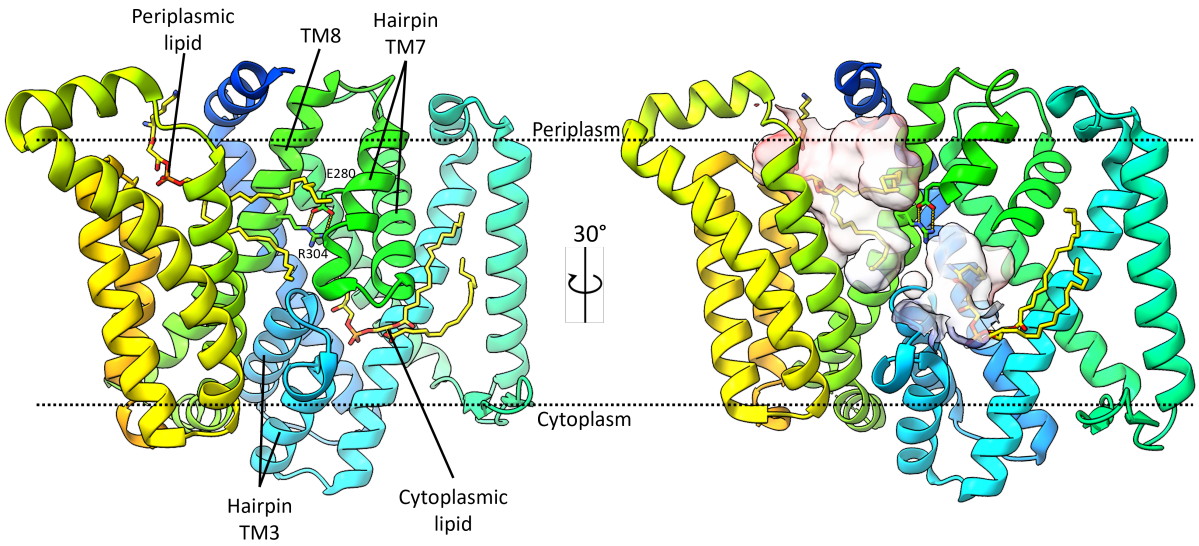

Figure 1.16: *Rt*MprF LysPG binding sites. *Left*: Side view of TM region of *Rt*MprF monomer (soluble domain removed, clipped through TM helices 1, 13 and 14 for clarity, coloured as in **Figure 1.15c**). Bound lipids and the E280-R304 salt bridge between hairpin TM7 and TM8 are shown as sticks. *Right*: Rotated view showing the electrostatic surface of the protein at the LysPG binding sites (transparent surface). The loop of hairpin TM7 is removed for clarity.

The bound LysPG molecules suggest a route of lipid translocation, as the headgroup of the cytoplasmic lipid is bent upwards into the core of the protein away from the cytoplasmic surface of the membrane. The two lipid binding cavities in *Rt*MprF are in close proximity,

suggesting that lipid at the cytoplasmic binding site translocates headgroup-first through MprF to the periplasmic lipid binding site, where it exits the protein. However, these sites are not continuous, but are separated by a glutamate-arginine salt bridge (E280-R304) between hairpin TM7 and TM8. This salt bridge corresponds to the conserved charged residues mutated by Ernst *et al.* (2015), and so had been previously implicated in MprF-mediated lipid transport. Their placement between these two lipid binding cavities led Song *et al.* to propose a model for lipid translocation distinct from the previously described models for other characterised lipid transporters. In this model, the entire aminoacyl-PG molecule moves through the core of MprF, from the cytoplasmic lipid binding site to the periplasmic exit cavity. This model suggests that the conserved D/E-R salt bridge functions as a gate between the two sites, and that breaking this salt bridge interaction would open the gate, allowing passage of the full lipid from cytoplasmic to periplasmic sites (**Figure 1.17**). This led to the suggestion that lipid transport is energised by the PMF, since protonation of the salt bridge by a periplasmic H^+ could disrupt the D/E-R interaction (Song *et al.* 2021). Subsequent release of H^+ into the cytoplasm would then allow the salt bridge to reform, closing the gate between the two sites. However, as there are no other MprF flippase structures, there is no structural evidence of this salt bridge adopting an "open" conformation, nor is there any functional data in the literature to support the hypothesis that the PMF energises lipid transport.

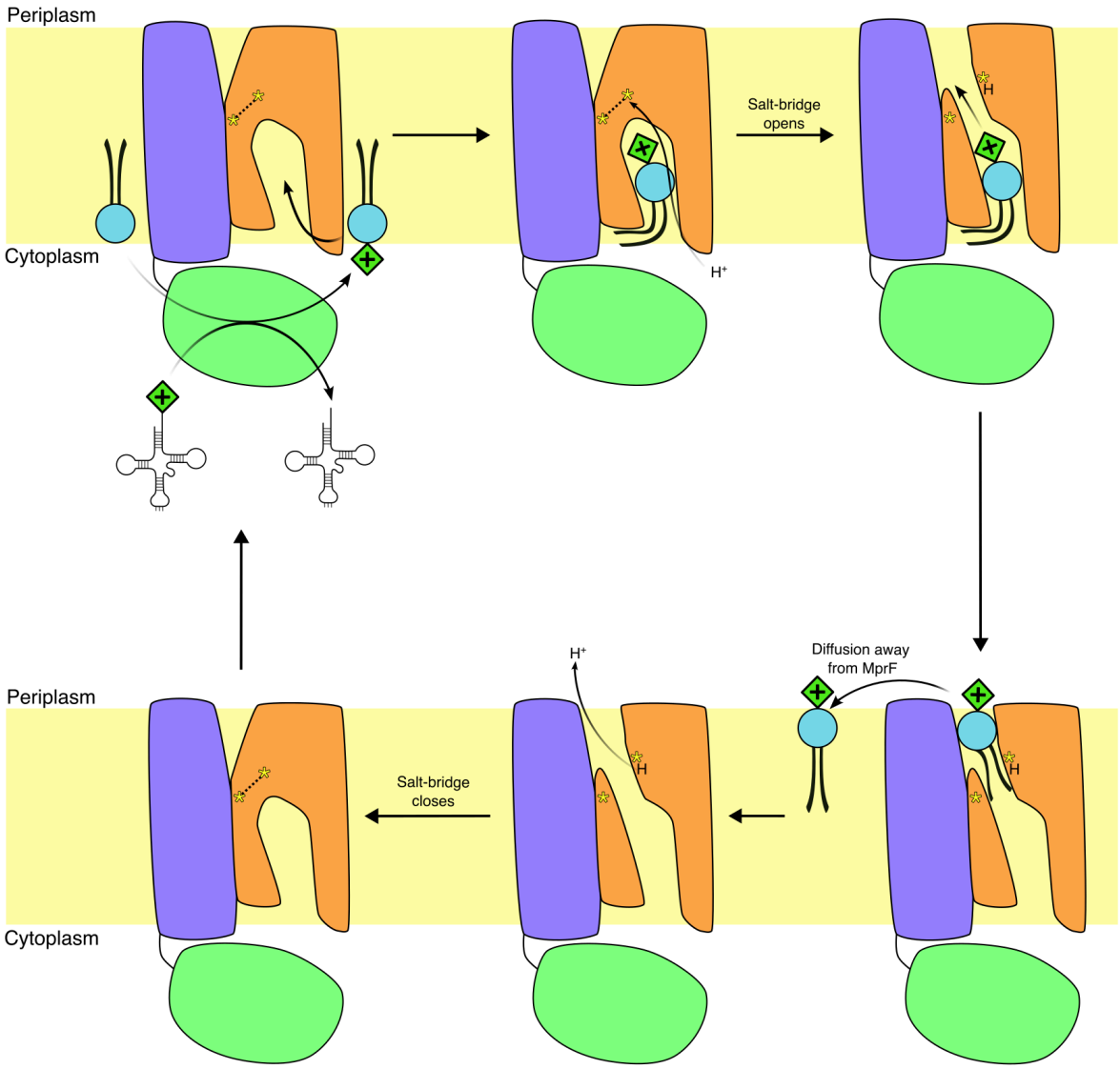

Figure 1.17: Proposed mechanism for MprF-mediated lipid transport. Schematic outlining a proposed PMF-energised MprF mechanism (Song *et al.* 2021). Flippase domain (TMs 1-8) = orange, TMs 9-14 = purple, soluble domain = green, salt bridge residues = yellow asterisks, PG = blue, amino acid residue = green diamonds.

To test their model, Song *et al.* mutated the conserved residues involved in lipid-binding interactions in the cytoplasmic cavity of *Rt*MprF (D234, Y303, Y307), as well as the salt bridge residues separating the lipid binding sites (E280, R304), and expressed these mutants in *E. coli*. Surprisingly, mutation of all lipid binding residues to alanine resulted in a 2- to 3-fold *increase* of both total and surface-exposed LysPG compared to WT. Furthermore, mutation of salt bridge residue R304 to alanine gave an 8-fold increase in LysPG, and charge reversal of E280 to lysine gave a >30-fold increase. For E280K MprF, this dramatic increase in LysPG content occurred despite the construct expressing at significantly lower levels than WT MprF.

This led to the suggestion that these mutations, especially E280K, increased the rate of lipid translocation between binding sites.

The residues mutated by Ernst *et al.* (2015) and Song *et al.* (2021), the effects of their mutation, and the corresponding residues in *P. aeruginosa* are summarised in **Table 1.2.** A full alignment of the *S. aureus, R. tropici,* and *P. aeruginosa* MprF sequences is given in **Appendix 1.**

Table 1.2: Effects of mutagenesis experiments on MprF homologues.

Ernst *et al.* (2015) mutants (*S. aureus* MprF)		
Mutant	***Pa*MprF equivalent**	**Effect**
P247A	P288	Moderate reduction in daptomycin resistance
D254A	E295	Complete reduction in daptomycin resistance
R279A	R319	Complete reduction in daptomycin resistance
P286A	P326	Mild reduction in daptomycin resistance
Song *et al.* (2021) mutants (*R. tropici* MprF)		
Mutant	***Pa*MprF equivalent**	**Effect**
E280K	E295	38-fold increase in surface LysPG content
E280Q	E295	30-fold increase in surface LysPG content
Y303A	Y318	4-fold increase in surface LysPG content
R304A	R319	8-fold increase in surface LysPG content
Y307A	Y322	3-fold increase in surface LysPG content

1.3.4. Regulation of MprF expression and aminoacyl-PG levels

In *S. aureus*, MprF is upregulated in response to CAMPs via a mechanism involving the two-component system GraRS (also known as ApsRS) (Li *et al.* 2007), and homologues of this sensing system have been identified in other Gram-positive bacteria (Mandin *et al.* 2005). In this system, CAMPs bind to a surface-exposed negatively charged loop of the transmembrane sensor GraS. GraS then auto-phosphorylates a conserved histidine residue, and this phosphate is transferred to the response regulator GraR (Cho *et al.* 2023). Activation of GraRS results in the upregulation of MprF, as well as the *dlt* operon involved in the alanylation of teichoic acids

(Li *et al.* 2007), which together function to reduce bacterial surface negative charge. In addition, expression of the ABC transporter VraFG is increased, but it has been shown that VraFG expression alone does not provide cells with increased CAMP resistance, suggesting that it does not act as an efflux pump but rather as an additional CAMP sensing unit in tandem with GraS (Falord *et al.* 2012). The *S. aureus* CAMP sensing system is summarised in **Figure 1.18**:

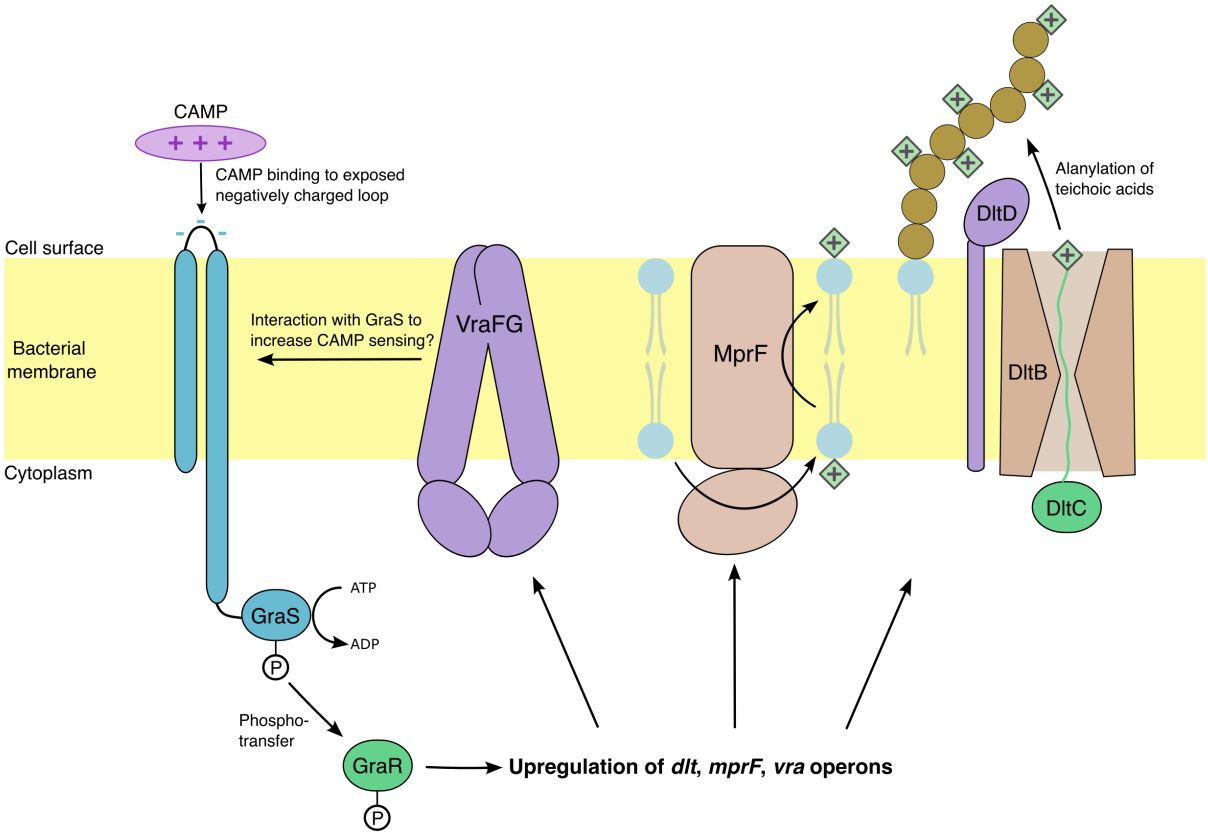

Figure 1.18: GraRS-mediated response to CAMPs in *S. aureus*.

The GraRS sensing system in *S. aureus* is also activated in low pH environments (Villanueva *et al.* 2018). *S. aureus* can survive within phagocytic cells such as macrophages (Schnaith *et al.* 2007, Kubica *et al.* 2008), where they replicate within the host phagolysosome before causing host cell death (Flannagan *et al.* 2016). Following engulfment of bacteria and the initial formation of the phagolysosome, the pH of the compartment is lowered through the activity of membrane proton pumps (Lukacs *et al.* 1990). It is therefore likely that activation of GraRS in response to low pH reflects adaptation of *S. aureus* to this invasive niche, as bacterial cells lacking GraRS are unable to replicate following phagolysosome formation and hence cannot

cause host cell death (Flannagan *et al.* 2018). The homologous two-component system (VirRS) in *Listeria monocytogenes*, another intracellular pathogen, is also upregulated in response to low pH (Dare *et al.* 2014). In addition, the presence of LysPG in *L. monocytogenes* may have additional benefits other than increased CAMP resistance, with MprF knockout *Listeria* cells exhibiting increased sensitivity to high salt concentrations and detergents, suggesting aminoacyl-PG more generally improves membrane integrity (Dare *et al.* 2014).

The mechanism of MprF regulation in Gram-negative bacteria is less well characterised than in *S. aureus.* Early genetic studies in *R. tropici,* which is resistant to low pH environments, found induction of MprF expression in acidic conditions (Vinuesa *et al.* 2003), and that *R. tropici* only produced LysPG when grown in such conditions (Sohlenkamp *et al.* 2007). The presence of LysPG was shown to increase *R. tropici* resistance to polymyxin B at low pH, but also to generally increase fitness of cells: MprF knockouts were less able to colonize root nodules than WT cells, again suggesting a role for aminoacyl-PG in Gram-negative bacteria beyond antimicrobial resistance (Sohlenkamp *et al.* 2007). pH-induced upregulation of MprF has also been characterised in the Gram-negative bacterium *P. aeruginosa* (Klein *et al.* 2009), the main pathogen that colonizes the lungs of patients with cystic fibrosis (Govan and Deretic 1996). The lungs of cystic fibrosis patients are typically acidified (Coakley *et al.* 2003), and so *P. aeruginosa* must be able to withstand acidic environments. The amount of membrane AlaPG produced by *P. aeruginosa* increases with decreasing pH (Klein *et al.* 2009), leading to the suggestion that aminoacyl-PG decreases the permeability of the inner membrane to protons. However, the proposal that aminoacyl-PG promotes a general increase in membrane integrity requires further characterisation, as do the exact sensing and regulatory systems involved in controlling MprF expression in Gram-negative bacteria.

In addition to controlling MprF expression in low pH, some bacteria regulate aminoacyl-PG levels in their membranes through the expression of aminoacyl-lipid hydrolases. Early studies

of the MprF operon in *R. tropici* identified a gene whose depletion made cells less tolerant to low pH, similar to knockouts of MprF (Vinuesa *et al.* 2003). Similar genes within the same operon as MprF are often found in other bacteria, and can be grouped into three families: α/β-hydrolases, esterases, and VirJ proteins (Smith *et al.* 2015). VirJ family proteins are only found in Gram-negative bacteria, α/β-hydrolases in both Gram-positive and negative bacteria, and esterases in actinobacteria and cyanobacteria. Characterisation of PA0919, a VirJ family member from *P. aeruginosa* (Arendt *et al.* 2013), and ahyD, an α/β-hydrolase from *Enterococcus faecium* (Smith *et al.* 2013), confirmed that they act as aminoacyl-lipid hydrolases localised in the periplasm, and remove the amino acid modifications from the headgroups of aminoacyl-PG in the outer leaflet of the inner membrane (**Figure 1.19**). Surprisingly, deletion of these proteins reduces the resistance of cells to positively charged antimicrobials, despite a significant increase in the total aminoacyl-PG content of the cell (Arendt *et al.* 2013). This suggests that the levels of aminoacyl-PG synthesised in the inner membrane of bacteria in response to external stimuli needs to be regulated. This finding also suggests that the mechanism by which modified lipids provide such resistance is more complex than the electrostatic repulsion model previously proposed, with supporting studies suggesting that the presence of aminoacyl-PG impacts membrane permeation by CAMPs rather than just membrane binding (Kilelee *et al.* 2010).

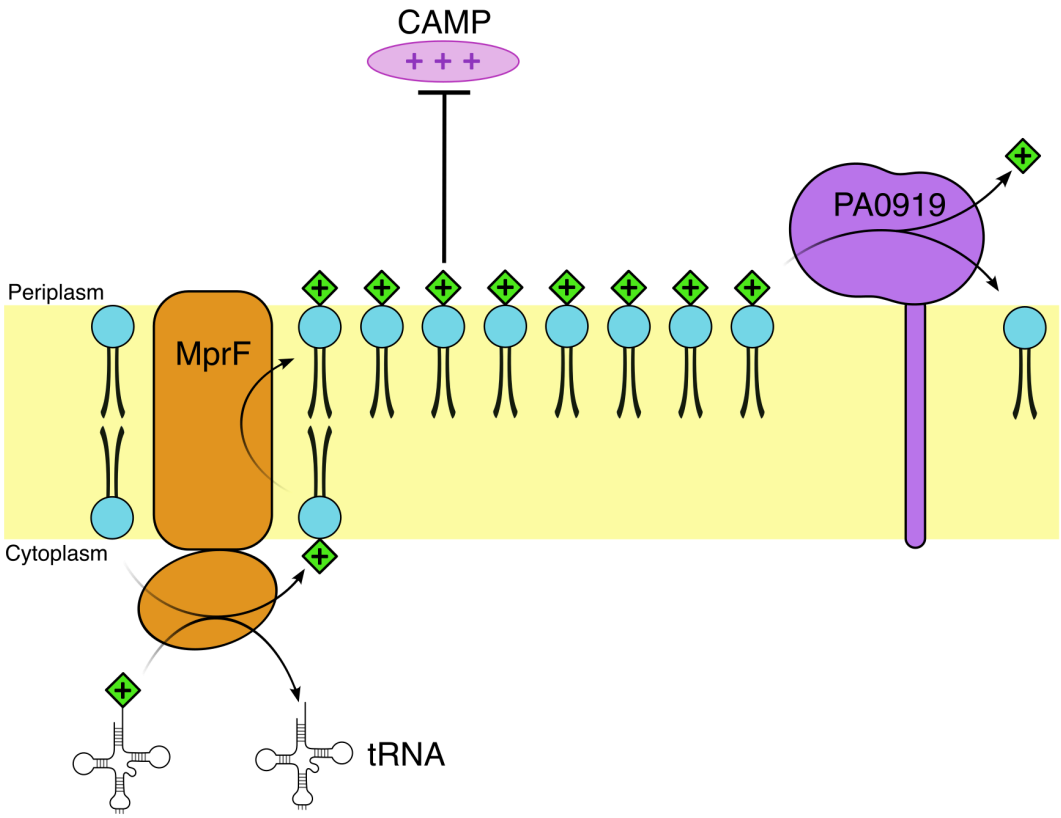

Figure 1.19: Combined activities of MprF and PA0919. Schematic of MprF and PA0919 activities in the *P. aeruginosa* inner membrane. PG = blue circles, amino acid modifications = green diamonds, CAMP = pink oval.

1.3.5. The MprF flippase architecture is more widespread than initially thought

A recent study found that the MprF flippase domain is more widespread than previously thought, being present in almost all bacterial phyla as well as many archaea (Hauser *et al.* 2022). Previous investigations into MprF homologues focused on gene products with both transmembrane and soluble domains, since the soluble synthase of MprF is more conserved than the flippase domain (e.g. between *Rt*MprF and *Sa*MprF, flippase domain sequence similarity = 37%, soluble domain sequence similarity = 49%). By contrast, novel work by Hauser *et al.* identified many examples of the MprF flippase fold occurring in bacterial genomes distinct from a soluble aminoacylation domain, for example YbhN in *E. coli*. The AlphaFold (Jumper *et al.* 2021) predicted structure of YbhN is shown in **Figure 1.20,** aligned to the core flippase domain from *Rt*MprF**:**

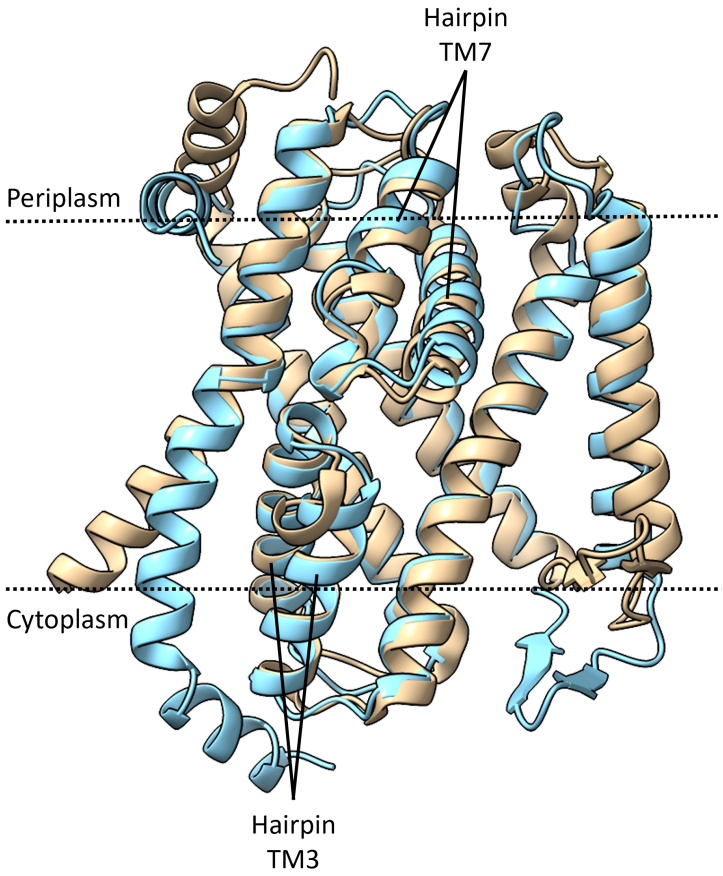

Figure 1.20: YbhN alignment to *Rt*MrpF flippase domain. Flippase domain of *Rt*MprF (TMs 1-8, brown) aligned to the AlphaFold model of YbhN (blue). RMSD of hairpin helix repeats = 1.12 Å. TM1 removed for clarity.

Despite YbhN having low sequence identity to MprF flippase folds (e.g. 28% identity with the *P. aeruginosa* MprF flippase domain), the predicted structure of YbhN displays the characteristic inverted hairpin helix repeats and is almost identical to the experimentally determined flippase fold of *Rt*MprF (RMSD between hairpin repeats = 1.12 Å), highlighting the broader presence of MprF-like transport domains in bacteria. Hauser *et al.* went on to knock out YbhN in *E. coli* and found that the growth of these mutants was compromised compared to WT (Hauser *et al.* 2022), suggesting that YbhN may contribute towards maintenance of membrane integrity. As *E. coli* do not naturally produce aminoacylated PG, the presence and importance of this MprF flippase fold suggests a broader substrate transport capacity, in line with previously described experiments that highlight the relaxed specificity of MprF for differently aminoacylated species.

In addition to MprF flippase folds expressed in isolation, Hauser *et al.* identified a number of MprF flippase homologues that are conjugated to soluble enzymes distinct from aminoacylation domains but implicated in the synthesis of different lipid species, such as glycosyl transferases and O-antigen ligases. Indeed, even flippase domains expressed alone are often organised in operons alongside lipid biosynthetic enzymes; YbhN is downstream of the cardiolipin synthase ClsB, and was shown by Hauser *et al.* to interact with ClsB and other PG synthesis enzymes in bacterial two-hybrid assays (Hauser *et al.* 2022). Together, this provides further evidence of the MprF flippase fold being duplicated and repurposed in many different bacteria and archaea, presumably to facilitate the transport of a broad range of differently modified lipid species across the inner membrane.

The re-entrant hairpin helices present in the MprF flippase homologues discussed here are a structural feature that has been previously described for lipid binding proteins, such as the undecaprenyl-diphosphate (UndPP) phosphatase BacA in *E. coli* (PDB: 5OON/6CB2) (El Ghachi *et al.* 2018, Workman *et al.* 2018). Recycling of UndPP following its use as a carrier lipid is dependent on its dephosphorylation to UndP and transport back to the inner leaflet of the inner membrane. BacA has been identified as one of the bacterial UndPP phosphatases (El Ghachi *et al.* 2004), but it is currently unclear which proteins are responsible for the transport of dephosphorylated UndP back into the cytoplasm. Comparison of the BacA structures to other characterised transporters identified similarities with a chloride transporter (Dutzler *et al.* 2002), and a sodium/citrate symporter (Wöhlert *et al.* 2015), both of which contain re-entrant hairpin helix pairs. These similarities led to the hypothesis that BacA could also act as a transporter, responsible for the recycling of UndP following dephosphorylation (Workman *et al.* 2018), but such flippase activity remains to be confirmed experimentally.

Another family of membrane proteins predicted to contain similar structural elements is the DedA family. DedA proteins, as discussed in **section 1.2.1**, are implicated in lipid transport in bacteria, but there are no experimentally determined structures of any family members.

Recent functional assessment of two eukaryotic DedA homologues, VMP1 and TMEM41B, demonstrated that these proteins act as non-specific lipid scramblases *in vitro* (Li *et al.* 2021, Wu *et al.* 2022). Furthermore, the *B. subtilis* DedA homologues UptA and PetA have been implicated in UndP transport (Roney and Rudner 2023) and PE transport (Roney and Rudner 2023) respectively. Together, this functional evidence suggests a role for DedA family members in lipid transport processes that is conserved across the domains of life. AlphaFold predictions of DedA family member structures consistently include the presence of two re-entrant hairpin helices, further suggesting that this architecture present in MprF may represent a more widespread general lipid transporting fold.

1.3.6. Wider roles of MprF in virulence and as a target in multi-resistant bacteria

In addition to the aminoacylation and PG-transport activities described above, recent studies have implicated MprF in other lipid modification and transport processes that provide bacteria with increased resistance to antimicrobial compounds or with increased virulence.

B. subtilis cells lacking the Penicillin Binding Proteins (PBPs, which are involved in cell wall synthesis) upregulate expression of enzymes involved in LTA synthesis, such as LtaS, when grown on glucose. They also upregulate the autolysin LytE, which is a cell wall hydrolase that regulates the shape of the cell wall during cell growth (Bisicchia *et al.* 2007). This overexpression of LytE in the absence of PBPs results in cell death due to unregulated LytE activity, but surprisingly this phenotype can be rescued by knockout of the MprF gene (Guyet *et al.* 2023). In PBP and MprF double knockout strains, LTA length and abundance is reduced compared to PBP single knockout strains. This suggests that LTAs are involved in regulating

the activity of autolysins, consistent with previous studies (Neuhaus and Baddiley 2003, Hanson and Neely 2012), and that MprF is involved in the regulation of LTA abundance and length. It was hypothesised that MprF activity could be increasing LTA synthesis indirectly, either by increasing the abundance of aminoacyl-PG in the outer leaflet of the inner membrane onto which LTAs can be polymerised by LtaS, or by altering the local electrostatic environment at the bacterial surface to increase LtaS processivity (Guyet *et al.* 2023). In any case, this work highlights the broader role MprF appears to play in the regulation of antimicrobial resistance systems employed by bacteria.

A more diverse functionality of MprF is also exhibited in *Streptococcus agalactiae*. Previous work has shown that resistance to CAMPs in *S. agalactiae* is predominantly a result of the alanylation of LTAs by *dlt* gene products, with MprF knockout in these bacteria having no effect on CAMP resistance (Saar-Dover *et al.* 2012). However, recent work by Joyce *et al.* has identified a novel aminoacylated lipid species in *S. agalactiae*, lysyl-glucosyl-diacylglycerol (LysGlcDAG), which is absent in cells not expressing MprF (Joyce *et al.* 2022), suggesting that MprF is responsible for the synthesis of this novel lipid, with LysPG being an additional minor product of MprF activity. *S. agalactiae* is a member of the Group B *Streptococci* which are one of the main causative agents of infections that impact new-born babies, and if they penetrate the blood-brain barrier, infections can cause meningitis (Maisey *et al.* 2008). This requires *S. agalactiae* to invade endothelial cells lining the blood-brain barrier, and Joyce *et al.* demonstrated that cells lacking MprF were less able to infect endothelial cells *in vitro.* These MprF knockout cells were also incapable of surviving in the low-pH environments which would be present in endothelial cells, potentially mirroring the previously described role of MprF in virulence of *S. aureus* in the phagolysosome of macrophages. Taken together, these studies highlight that in *S. agalactiae,* the role of MprF has specialised away from providing cells with CAMP resistance, instead being able to produce a novel lipid species that appears to aid these

bacteria in the virulent niche they occupy. The mechanism by which LysGlcDAG promotes endothelial cell invasion is unclear however, and requires further study to be fully elucidated.

Novel MprF activities have also been suggested to be present in bacteria expressing point mutants of MprF. Daptomycin is a last resort antibiotic used as an effective treatment of Gram-positive infections (Sauermann *et al.* 2008), most notably of MRSA which is a leading cause of infection and mortality worldwide (Fowler *et al.* 2005). Daptomycin is thought to act by binding to the bacterial cell surface and polymerising in the membrane to form a pore for potassium ions that depolarises the cell membrane (Straus and Hancock 2006). Despite being negatively charged, daptomycin only displays bactericidal activity in the presence of Ca^{2+} ions (Jung *et al.* 2004), resulting in its designation as a CAMP-like antibiotic. Whilst *S. aureus* expressing WT MprF exhibit increased resistance to daptomycin compared to MprF knockouts (Ernst *et al.* 2009), daptomycin is still potent enough to effectively treat *S. aureus* infections. However, MRSA strains have arisen that are resistant to daptomycin treatment, and many of these strains contain single point mutations in the *mprF* gene at the flippase domain (Friedman *et al.* 2006, Julian *et al.* 2007, Chen *et al.* 2018). Interestingly, some of these mutations do not result in elevated cellular LysPG membrane content (Ernst *et al.* 2018), or positive surface charge (Bayer *et al.* 2015), implying a charge-independent mechanism of daptomycin resistance provided by mutated MprF. Many of these gain-of-function point mutations at the flippase domain are concentrated at TM9, which forms part of the periplasmic exit cavity in the *Rt*MprF structure. Studies on one of these mutants, T345A, demonstrated that *S. aureus* strains with this mutation were resistant to daptomycin and a closely related antibiotic friulimicin B, but not other positively charged antimicrobials, further supporting the hypothesis of charge-independent mechanisms of increased resistance and suggesting that the mechanism of resistance was specific to daptomycin-like antimicrobials (Ernst *et al.* 2018). Following their determination of the *Rt*MprF structure, Song *et al.* produced a homology model of *S. aureus* MprF, and found that daptomycin could be docked into the periplasmic exit cavity

in proximity to TM9 (Song *et al.* 2021), suggesting that gain of function mutations at this region of the flippase domain increase resistance through binding of daptomycin to MprF. This proposed charge-independent mechanism of daptomycin resistance has yet to be confirmed experimentally, however.

1.4. A strategy to study MprF

The presence of antimicrobial-resistant strains of bacteria is a critical threat to global health (Murray *et al.* 2022), yet the number of novel antimicrobials developed yearly to combat this threat is decreasing (Ventola 2015). The studies described above highlight the validity of MprF as a novel antimicrobial target, as its prevalence in Gram-positive bacteria and gain-of-function mutation in MRSA suggests that inhibition of MprF would sensitise these bacteria to already existing positively charged antimicrobials, offering a promising path of co-therapy in difficult MRSA cases.

As discussed in **section 1.2**, there is already a precedent for targeting other bacterial lipid transport systems, with such work often requiring the structural characterisation of proteins for structure-based drug development, and *in vitro* transport assays probing protein function that can be used to identify inhibitor compounds. These techniques have been instrumental in much of the current understanding of lipid transporters discussed in **section 1.1**, and are described below.

1.4.1. Structural characterisation with cryo-EM

Structural characterisation of lipid transporters has been essential in elucidating transport mechanisms, with X-ray crystallography being a major method of high-resolution structural analysis. However, this technique requires high concentrations of homogenous protein, which can be difficult to obtain with low expressing and unstable membrane protein targets.

Furthermore, membrane proteins are purified in detergent which can cause issues with the formation of protein crystals (Loll 2003). Recent advances in cryo-EM have provided an alternate route to high resolution structural characterisation of membrane proteins (Cheng 2018). In single particle cryo-EM, the sample is flash frozen in a layer of vitreous ice and imaged with an electron microscope to obtain images of single particles in different orientations (Cheng *et al.* 2015). These particles are then classified based on orientation, averaged to improve signal-to-noise, and reconstructed to give a map of the Coulomb potential of the protein (i.e. the charges within a protein that influence the scattering of electrons that produces the recorded image) (Marques *et al.* 2019), which can be used to build a model of the 3D structure of the protein of interest.

As imaging is dependent upon the scattering of incident electrons from sample particles, larger particles that contain more atoms will scatter more electrons and so result in particle images with a higher signal-to-noise ratio. As such, cryo-EM excels at the determination of structures of proteins or complexes with higher MWs. Despite this, the development of direct electron detectors for data acquisition and the improvement of image processing algorithms has enabled high resolution structural characterisation of smaller proteins (Benjin and Ling 2020), with proteins ~100-150 kDa in size now routinely being characterised by this method. However, as structural determination is dependent upon the averaging of individual particle images, the resolution that can be obtained for small proteins can be limited by sample heterogeneity, or inherent flexibility. Particle alignment issues can be especially problematic for small membrane proteins; membrane proteins are typically imaged following purification in detergent or reconstitution into membrane-mimetic systems, and these micelles surround and obscure the transmembrane regions of small membrane-proteins (Lander and Glaeser 2021). If a large proportion of a small membrane protein is obscured by a micelle, with no significant protruding portion(s) this will reduce available recognisable structural features that aid particle alignment. Such issues can be compensated for during sample preparation, for

example, by using soluble nanobody binders to produce a complex with increased particle size and asymmetry (Zimmermann *et al.* 2018).

The MprF monomer is ~100 kDa in size and therefore a potentially challenging target for cryo-EM. Careful consideration of the potentially limiting aspects of sample preparation was therefore regarded as crucial when working towards the elucidation of a high-resolution structure by cryo-EM.

1.4.2. *In vitro* assessment of lipid transport activity

As demonstrated in **section 1.1**, there are a variety of mechanistic variations and energy sources that can be employed by proteins to facilitate lipid transport between membrane leaflets. In order to accurately characterise lipid transporters, *in vitro* assays have been used, where the protein of interest is purified and reconstituted into liposomes. Such an environment allows for the control of which lipid species are present, as well as what ions or energy sources are in solution to provide insight into substrate specificity and details of transporter mechanisms.

One powerful *in vitro* assay for lipid transporter activity utilises lipid probes containing fluorescent nitrobenzoxadiazole (NBD) labels. In this assay, the transporter of interest is reconstituted into liposomes containing a small fraction of NBD-labelled lipid. Liposome NBD fluorescence is monitored over time following addition of dithionite to samples. Dithionite bleaches NBD fluorescence but is membrane impermeable, so can only access NBD in the outer leaflet of liposomes. Therefore, the fraction of NBD that is bleached following dithionite addition reports on the distribution of the fluorescent probe between liposome leaflets, and when compared to liposomes that do not contain reconstituted protein can be used to assess whether the protein of interest is transporting lipid (**Figure 1.21a**).

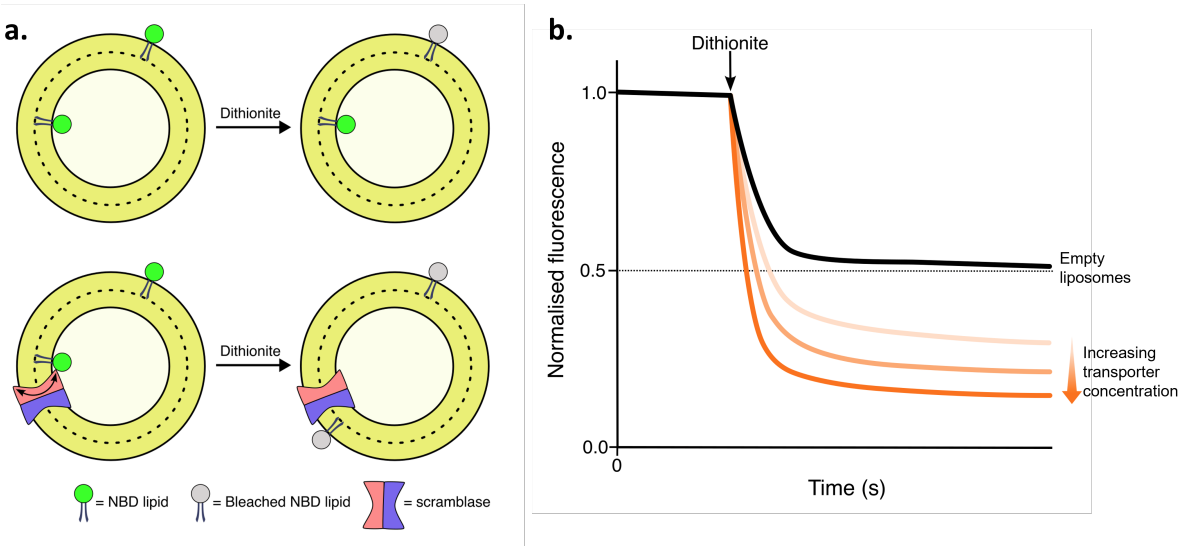

Figure 1.21: *In vitro* lipid transport assay. a. Schematic of liposome-based lipid transport assay, showing empty liposomes in top panels and proteoliposomes reconstituted with a scramblase in bottom panels. **b.** Representative normalized fluorescence time-course data for lipid transport assay. Empty liposomes = black, proteoliposomes = orange.

This assay is well suited to the characterisation of scramblases, which when active can continuously expose lipid from the inner leaflet of liposomes. This results in a fluorescence decay that occurs in two phases (Brunner and Schenck 2019, Falzone and Accardi 2020), with an initial rapid decrease as outer leaflet lipid is quickly bleached, followed by a slower decay from exposure of inner leaflet lipid over time until a plateau is reached which is lower than the ~50% plateau for empty liposomes (**Figure 1.21b**). The final plateau value for scramblase-reconstituted liposomes represents the fraction of liposomes that do not contain an active scramblase and so contain inner leaflet NBD lipid that cannot be exposed to dithionite. This empty fraction is dependent on the concentration of membrane protein used during reconstitution, with higher scramblase concentrations giving lower fluorescence plateau values (Goren *et al.* 2014, Li *et al.* 2021). At high protein concentrations however, the final plateau value does not reach zero, as there will typically be a fraction of liposomes that are refractory to protein insertion independently of protein concentration (Ploier and Menon 2016).

In addition to qualitative confirmation of lipid transport, this fluorescence decrease over time can be fitted to a mathematical model to estimate the rate constants for lipid transport

(Malvezzi *et al.* 2018, Falzone and Accardi 2020). Such quantitative fitting allows for comparison of rates when using different NBD-labelled lipid to assess scramblase specificity, and can be used to assess how rates of transport are affected when key residues are mutated (Lee *et al.* 2018).

Such a system can also be used for characterisation of flippases and floppases, although fluorescence decreases in these cases can be more subtle. During insertion into liposomes, membrane proteins are often not uniformly oriented, with the ratio of inward facing and outward facing units varying depending on protein identity and reconstitution conditions (Skrzypek *et al.* 2018). For flippases and floppases that require ATP for lipid transport, addition of ATP to solution following proteoliposome formation will only activate transporters with ATP binding domains at the external surface of liposomes since ATP is membrane impermeable. As such, if a flippase/floppase is preferentially oriented with ATP binding domains contained within liposomes, this will limit the number of activated transporter units and the magnitude of fluorescence decrease observed. Furthermore, unidirectional transport of lipid from one liposome leaflet to another increases membrane surface tension (Traïkia *et al.* 2002). This increase in surface tension can make further transport of lipid energetically unfavourable, which limits the maximum amount of NBD-labelled lipid transport that can be measured in these assays (Marek and Günther-Pomorski 2016).

In the case of ATP-dependent transporters, incubation of proteoliposomes with ATP can result in an increase/decrease in the final fluorescence plateau observed compared to proteoliposomes without ATP incubation, depending on whether lipid is transported into inner liposome leaflets (Huang *et al.* 2004, Eckford and Sharom 2005, Park *et al.* 2022) or exposed to the liposome surface (Coleman *et al.* 2009, Zhou *et al.* 2013). For flippases that are activated by the PMF, similar fluorescence plateau changes have been demonstrated when a proton gradient is established across liposome membranes (Zhang *et al.* 2020).

Taken together, the liposome-based NBD-lipid transport assay would be an ideal tool to characterise the lipid-transporting mechanism of MprF and would additionally be suitable to probe whether MprF is energised by the PMF as previously hypothesised. Of note, despite a considerable body of published work addressing various molecular aspects on MprF, no *in vitro* data of MprF-mediated lipid transport have as yet been described, indicative of the technical challenges associated with establishing such an assay for this protein.

1.4.3. Previous work on MprF in the Bublitz group

Previous work on MprF in the Bublitz group has focused on the structural characterisation of the full-length transporter. Fourteen full-length MprF homologues from different bacterial species were cloned and recombinantly expressed in *E. coli*, with MprF from *P. aeruginosa* expressing at the highest levels (Lorenz 2016). Large-scale purification of *Pa*MprF was optimised, and purified *Pa*MprF was used in vapour diffusion and lipidic cubic phase crystallisation trials, but this did not yield crystals of *Pa*MprF (Smilova 2017). More recent work has focused on reconstituting *Pa*MprF into membrane-mimetic systems for study by cryo-EM. Initial trials attempting reconstitution into SaposinA nanoparticles (SapNPs) (Frauenfeld *et al.* 2016) were unsuccessful (Lundie-Brown 2018). Prior to this DPhil thesis, I undertook an 18-week Master's project in the Bublitz group, and in this time successfully reconstituted *Pa*MprF into SapNPs (Hankins 2019). I subsequently optimised the reconstitution to maximise the incorporation of *Pa*MprF into SapNPs using a 7:3 (mol/mol) PC:PG lipid composition. I then collected a small angle X-ray scattering (SAXS) dataset for *Pa*MprF-SapNPs to obtain a low-resolution bead model of the sample. The reconstituted *Pa*MprF-SapNPs were also assessed via negative-stain electron microscopy, demonstrating that the sample was homogenous, of high-purity, and therefore suitable for future cryo-EM studies.

1.5. Aims and scope

Structural insight of MprF homologues is currently limited, with only one published full-length structure from a non-pathogenic bacterium (Song *et al.* 2021). Given the low sequence identity across MprF homologues, elucidation of a full-length structure from a pathogenic bacterium could provide valuable insight into the structure-function relationship and the structural conservation of MprF. Given the MprF transport fold is distinct from all other lipid transporter architectures characterised as yet, additional MprF structures could capture different conformational states of the protein which could provide further information about the mechanism of lipid transport, which is currently unclear. Furthermore, and importantly, no *in vitro* assessments of lipid transport by MprF have been carried out to date, so the extent of lipid specificity as well as the energy source for lipid transport are currently unknown.

In light of this, the aims of this thesis are:

1) To obtain a full-length structure of MprF from the Gram-negative human pathogen *P. aeruginosa* by cryo-electron microscopy.
2) To establish *in vitro* assays to assess MprF synthase and lipid transport activities using fluorescence-based methods.
3) To characterise the lipid specificity and energetics of MprF-mediated lipid transport using the *in vitro* assays established in (2).
4) To combine the insight gained in (1) and (3) to suggest a molecular mechanism of MprF.
5) To evaluate my findings in context of exploring MprF as a novel antimicrobial target.

Chapter 2: Materials and Methods

2.1. DNA methods

2.1.1. Bacterial transformation

Bacteria were transformed with plasmids by standard heat-shock technique. 50 µL of competent cells were incubated on ice with 1 µL of ~100-200 ng/µL plasmid of interest for 30 minutes. Cells were heat shocked at 42°C for 45 seconds, incubated on ice for a further 2 minutes, and then outgrown in 800 µL Super Optimal broth with Catabolite repression (SOC) medium (2 % (w/v) tryptone, 0.5 % (w/v) yeast extract, 10 mM NaCl, 2.5 mM KCl, 10 mM $MgCl_2$, 20 mM glucose) at 37°C for one hour. Cells were plated on Lysogeny Broth-agar (LB-agar) (1 % (w/v) tryptone, 0.5 % (w/v) yeast extract, 1 % (w/v) NaCl, 1.5 % (w/v) agar) containing the relevant antibiotic.

2.1.2. Fragment Exchange (FX) cloning

The FX cloning system (Geertsma and Dutzler 2011) was employed for cloning of the protein constructs used in this thesis. FX cloning utilises a cloning vector, pINIT, to facilitate rapid subcloning of genes of interest into a variety of expression vectors that are compatible with the FX system. The cloning and expression vectors contain a suicide gene (*ccdb*) flanked by recognition sites for the restriction enzyme SapI. Sequences of interest are amplified by polymerase chain reaction (PCR) with complementary flanking SapI sites, and then inserted into pINIT, replacing the suicide gene. Following sequence confirmation, similar SapI subcloning can transfer the gene into expression vectors containing SapI sites, except cleavage sites are reversed in expression vectors to ensure unidirectional insertion of target sequences and removal of the SapI sites after insertion. Cloning and expression vectors contain different

antibiotic resistance markers and, in addition, pINIT contains the *sacB* gene, which is lethal for cells when grown in 7 % (w/v) sucrose medium.

Genes of interest to be inserted into pINIT were first amplified by PCR (thermocycling details listed in **Appendix 2**) using primers that introduce SapI restriction sites either side of the gene. 100 ng of pINIT was mixed with a 5-fold molar excess of PCR product and 1 µL CutSmart® Buffer (NEB) and made up to 10 µL with ultrapure water. 1 µL of SapI (NEB) was added and the reaction incubated at 37°C for one hour, followed by 65°C for 20 minutes to heat inactivate SapI. 1 µL 10 mM ATP and 1 µL T4 DNA ligase (NEB) were added and incubated at room temperature (RT) for 1 hour, followed by 65°C for 20 minutes to heat inactivate T4 DNA ligase. 5 µL of this ligation mixture was then transformed into Mach1 *E. coli* and plated on LB-agar supplemented with 25 µg/mL chloramphenicol (LB-Cam). Colonies from transformation were grown in 5 mL LB-Cam overnight at 37°C and plasmid was isolated using a QIAprep Spin Miniprep Kit (Qiagen). The insertion of the correct sequence into pINIT was confirmed by Sanger sequencing (Source Bioscience) using sequencing primers listed in **Appendix 2.** Genes of interest were then subcloned into the desired expression vector by SapI digestion and ligation as described above (using a 1:5 molar ratio of expression vector:pINIT), transformed into *E. coli* and plated on LB-agar supplemented with 7 % (w/v) sucrose and the relevant antibiotic marker in the expression vector.

2.1.3. AlaRS cloning

The AlaRS coding sequence was amplified by PCR from *P. aeruginosa* PAO1 genomic DNA using primers detailed in **Appendix 2**. The PCR product was run on a 1 % agarose (w/v) gel at 100 V for 1 hour and visualised with ethidium bromide, followed by isolation with a GenElute Gel Extraction kit (Sigma Aldrich). The PCR fragment was inserted via FX cloning into the expression vector p7XNH3, which contains an isopropyl-β-D-thiogalactopyranoside (IPTG) inducible promoter and encodes an N-terminal 10xHis affinity tag.

2.1.4. Site-directed mutagenesis

*Pa*MprF mutants were generated using a QuikChange II Site-directed mutagenesis kit (Agilent). The primers and PCR conditions for mutagenesis are listed in **Appendix 2.** 1µL DpnI solution was added to PCR reactions to digest template DNA. 1 µL DpnI-treated DNA was then transformed into XL1-Blue supercompetent cells according to manufacturer's instructions. Cells were plated on LB-Cam. Colonies from mutagenesis were grown in 5 mL LB-Cam liquid culture overnight and plasmids isolated using a QIAprep Spin Miniprep Kit (QIAgen). Plasmids were sent for Sanger sequencing (Source Bioscience) to confirm successful mutagenesis. Mutant plasmids were subcloned into the expression p7XC3H as outlined in **section 2.1.2** for transformation and expression in *E. coli* C41 (effective at overexpressing toxic membrane proteins).

2.2. RNA methods

2.2.1. Gel electrophoresis

RNA products were analysed using gel electrophoresis on E-Gel™ EX 4 % Agarose Gels (Invitrogen). RNA samples were mixed with 2x RNA loading dye (Thermo Scientific) and denatured at 70°C for 10 minutes. Samples were then loaded and run against a RiboRuler Low Range RNA ladder (Thermo Scientific). Gels were run using an E-Gel® iBase™ Power System (Invitrogen) for 15 minutes before visualisation with UV light.

2.2.2. $tRNA^{Ala}$ *in vitro* transcription (IVT) and purification

A synthetic gene was ordered (Integrated DNA technologies) comprising the $tRNA^{Ala}$ gene from *P. aeruginosa* (PAO1, locus tag: PA4280.3) fused to a GlmS ribozyme sequence (Winkler *et al.* 2004). This gene was amplified by PCR using primers in **Appendix 2**. The PCR product was then used as a template for IVT (at 80 µg/mL) using a MEGAscript™ T7 Transcription Kit

(Invitrogen). The transcription was run for 4 hours at 37°C. 10 mM glucosamine-6-phosphate (GlcN6P) was added and the reaction incubated for 10 hours at 37°C to initiate GlmS cleavage. RNA fragments were separated using a 1 mL QHP HiTrap anion exchange chromatography (IEX) column (Cytiva). The column was equilibrated in 20 mM 4-(2-hydroxyethyl)-1-piperazineethanesulfonic acid (HEPES) pH 7.6, 10 mM $MgCl_2$, 200 mM KCl. The RNA sample was injected onto the column and then eluted over 60 mL using a linear gradient of 200-800 mM KCl. Peak fractions were analysed on 4 % agarose by gel electrophoresis to identify the tRNA species elution volume.

2.3. Lipid methods

2.3.1. Lipid extraction

Lipids were extracted from 100 µL reaction mixes following a modified method from Bligh & Dyer (Bligh and Dyer 1959). 375 µL methanol:chloroform 2:1 (v/v) was added to reactions and incubated for 5 minutes at 35°C. 250 µL chloroform:50 mM NaCl 1:1 (v/v) was added to induce phase separation, briefly mixed, and spun at 3000 g for 5 minutes. The top aqueous phase was discarded, and the lower chloroform phase containing solubilised lipid was dried under a nitrogen stream to give a lipid film. The film was resuspended in 500 µL chloroform:methanol 2:1 (v/v) and analysed by thin layer chromatography (TLC).

2.3.2. Thin layer chromatography (TLC)

Extracted lipid was spotted onto analytical 0.25 mm silica gel 60 plates (Merck Millipore) and separated using a mobile phase of 60:25:4 chloroform:methanol:water (v/v/v). NBD labelled lipids were visualised by illuminating plates with blue light (470 nm).

2.3.3. PEG2000-NBD lipid synthesis

9.8 mg DSPE-PEG2000-amine (Avanti) and 2.7 mg succinimidyl 6-(*N*-(7-nitrobenz-2-oxa-1,3-diazol-4-yl)amino)hexanoate (NBD-SE, Cambridge Bioscience) were dissolved in 1.5 mL dichloromethane. 10 µL triethylamine was added and the reaction mix stirred at RT in the dark for 2 hours. Samples of the reaction mix before and after incubation were taken and run on an analytical 1D TLC (mobile phase of 85:15 chloroform:methanol (v/v)) to confirm the addition of the NBD label to the DSPE PEG-2000 lipid (**Figure 2.1**).

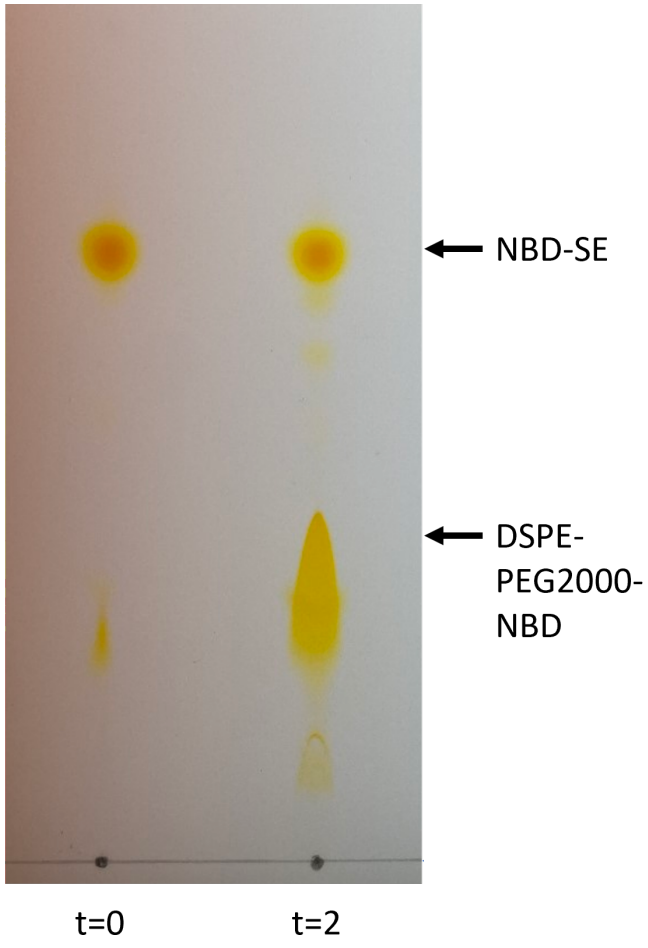

Figure 2.1: DSPE-PEG2000-NBD TLC. TLC showing reaction of DSPE-PEG2000-amine with NBD-SE at t = 0 hours and t = 2 hours.

The full reaction mixture was then separated by TLC in the same mobile phase. The band corresponding to DSPE-PEG2000-NBD was scraped from the plate and the mass of silica

scraped was weighed. Fluorescent lipid was isolated by incubation with 12 volumes of methanol and then filtration to remove silica. Methanol was evaporated under nitrogen stream and the resulting lipid film dried overnight in a vacuum desiccator to remove residual solvent. The film was then weighed and dissolved in chloroform to 5 mg/mL for use in liposome transport assays. A sample of the final product was kindly analysed by Dr Abraham Oluwole (Kavli Institute for Nanoscience Discovery, Oxford) by Mass Spectrometry (MS) to confirm the expected mass (**Figure 2.2**).

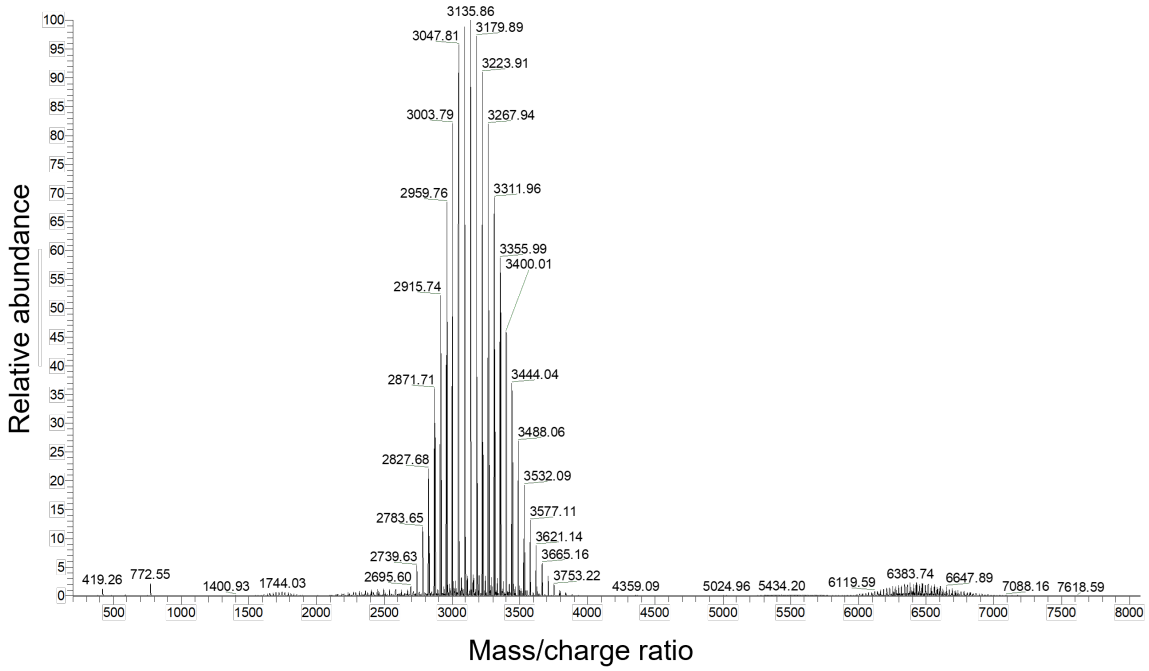

Figure 2.2: DSPE-PEG2000-NBD MS spectrum.

The resulting spectrum shows a broad peak of masses centring at ~3100 Da (expected MW of DSPE-PEG2000 is 3050 Da). The difference between each peak in the spectrum is 44 Da, corresponding to the MW of a single PEG unit, so the broad peak observed here is due to the polydispersity of PEG lengths in the original DSPE-PEG2000-amine compound used for synthesis.

2.4. Protein methods

2.4.1. Sodium dodecyl-sulfate polyacrylamide gel electrophoresis (SDS-PAGE)

SDS-PAGE was performed on self-cast gels of a fixed acrylamide percentage in the resolving phase using a Bio-Rad gel casting system. The resolving gel phase comprised 380 mM Tris/HCl pH 8.8, 10-16 % (v/v) (depending on size of proteins being separated) acrylamide/0.26-0.4 % bis-acrylamide, 0.1 % (w/v) SDS. The stacking gel phase comprised 120 mM Tris/HCl pH 6.8, 5 % (v/v) acrylamide/0.13 % (v/v) bis-acrylamide, 0.1 % (w/v) SDS. Acrylamide polymerisation of each phase was initiated by addition of 0.08 % (w/v) ammonium persulfate (APS) and 5 mM tetramethylethylenediamine (TEMED).

Membrane protein samples were incubated with 4x sample buffer (120 mM Tris-HCl pH 8, 20 % (v/v) glycerol, 8 % (w/v) SDS, 0.4 % (v/v) 2-mercaptoethanol (BME), 6 mM bromophenol-blue) at 35°C for 20 minutes to denature protein. Soluble protein samples were incubated with 4x sample buffer at 90°C for 5 minutes. Samples were separated on self-cast gels alongside a PageRuler Plus Prestained MW marker (ThermoFisher) at 40 mA per gel for 50 minutes in SDS-PAGE running buffer (25 mM Tris HCl pH 8.2, 190 mM glycine, 0.1 % (w/v) SDS). Gels were washed three times in distilled water and either stained with Coomassie brilliant blue G-250 (ThermoFisher) (80 mg/L), or used for western blotting.

2.4.2. Western blotting

Western blotting was performed using a Trans-Blot® SD Semi-Dry Transfer Cell (Bio-Rad). SDS-PAGE gels were equilibrated for 15 minutes in transfer buffer (48 mM Tris/HCl pH 8.2, 39 mM Glycine, 0.0375 % (w/v) SDS). The semi-dry western blot was assembled with a polyvinylidene fluoride (PVDF) membrane (activated for 1 minute in methanol and then equilibrated for 15 minutes in transfer buffer) beneath the gel at the cathode. The blot was run

at 1.6 mA/cm^2 gel area for 45 minutes. The PVDF membrane was rinsed three times in Tris Buffered Saline + Tween (TBST; 150 mM NaCl, 20 mM Tris/HCl pH 7.5, 0.05 % (v/v) Tween-20).

Western blots were imaged for His-tagged constructs by incubation with antibodies and visualisation with horseradish peroxidase (HRP). The blots were first blocked with Immobilon Signal Enhancer (Merck-Millipore) for 1 hour at RT to prevent non-specific antibody binding to the PVDF membrane. Blocking solution was removed and the primary antibody solution was added (Monoclonal Mouse anti-polyHistidine, Sigma-Aldrich, diluted 1:3000 in Immobilon Signal Enhancer). Blots were incubated with primary antibody for 1 hour at RT, and washed four times with TBST. Secondary antibody solution was added (Anti-Mouse HRP conjugate, Promega, diluted 1:2500 in Immobilon Signal Enhancer) and incubated for 1 hour at RT. Blots were washed four times with TBST followed by addition of Immobilon Classico Western HRP substrate (Merck-Millipore) for visualisation. Blot images were taken on a G:box Chemi HR 16 (Syngene).

2.4.3. Large-scale expression and purification of *Pa*MprF

Expression and purification of full-length *Pa*MprF was carried out according to the protocols established (Lorenz 2016) and optimised (Smilova 2017, Lundie-Brown 2018) by previous students of the Bublitz group. The *Pa*MprF sequence (PA0920 from PAO1) is expressed in a pET21a-CPD vector in C41 *E. coli.* pET21a-CPD is IPTG-inducible with an ampicillin (Amp) resistance marker, and fuses the *Pa*MprF sequence to a C-terminal 24 kDa cysteine protease domain (CPD) and 10x-histidine tag (His_{10}). CPD is a soluble domain that is activated by inositol-6-phosphate ($InsP_6$) and cleaves the linker region between *Pa*MprF and the CPD domain (**Figure 2.3**). This cleavage removes CPD-His_{10} from full-length *Pa*MprF.

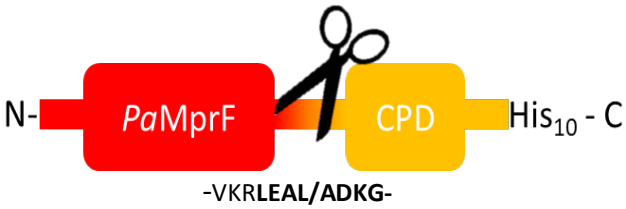

Figure 2.3: *Pa*MprF-CPD construct schematic. Schematic of the *Pa*MprF-CPD construct with the cleavage site shown below the linker between domains.

A starter culture of 250 mL TB-Amp was inoculated with a single colony of transformed C41 and grown overnight at 37°C. The next day, this culture was used to inoculate 6 L of TB-Amp to OD_{600} = 0.1. Cells were grown at 37°C until OD_{600} = 0.6 - 0.8, and then induced by the addition of 0.5 mM IPTG. Cells were grown overnight at 20°C for 15 hours before being pelleted at 4500 g for 20 minutes. Pelleted cells were resuspended in lysis buffer (50 mM Tris/HCl pH 7.6, 20 % (v/v) glycerol, 200 mM KCl, 1 mM $MgCl_2$, 5 mM BME) containing a spatula tip of DNAse I (bovine pancreas, Sigma-Aldrich) and one tablet of cOmplete™ Mini EDTA-free Protease Inhibitor Cocktail (Roche). Resuspended cells were passed through a cell disruptor (Constant Systems) twice at 30 kpsi and the cell debris pelleted at 17,000 g for 45 minutes. The supernatant was collected and ultracentrifuged at 200,000 g for 1 hour to pellet cell membranes. Membranes were weighed and resuspended in immobilised metal ion affinity chromatography (IMAC) buffer (20 mM HEPES pH 7.6, 20 % (v/v) glycerol, 200 mM KCl, 2 mM $MgCl_2$, 5 mM BME) to 6 mL/g for solubilisation and purification.

Membranes were solubilised by addition of 1.2 % n-dodecyl β-D-maltoside (DDM) (w/v) (low alpha, Generon), and were left rotating at 4°C for 1 hour. Membranes were ultracentrifuged at 200,000 g to pellet insoluble material, and the supernatant collected. 20 mM imidazole was added to the soluble supernatant and the supernatant loaded onto two 5 mL HisTrap FF affinity columns (Cytiva) connected in series using a peristaltic pump. Supernatant was passed over the columns three times, before being set on circular flow overnight at 4°C. Columns were washed with Wash Buffer (IMAC buffer + 0.0261 % (w/v) DDM) + 75 mM imidazole until the

A_{280} of flowthrough was constant, then *Pa*MprF eluted with 50 mL Wash Buffer + 400 mM imidazole in 1 mL fractions. Peak fractions were pooled and dialysed overnight at 4°C against 1 L of Wash Buffer in 10 kDa molecular weight cut-off (MWCO) snakeskin dialysis tubing (ThermoFisher). 0.1 mM $InsP_6$ was added to the dialysate to initiate CPD autocleavage, and this was incubated for 1 hour at RT followed by 3 hours at 4°C. Dialysate was passed over the affinity columns and the flow-through concentrated with 50 kDa MWCO Vivaspin 20 concentrators (Sartorius). This sample was then loaded onto a HiLoad 16/600 Superdex 200pg column (Cytiva), equilibrated in 20 mM HEPES pH 7.6, 20 % (v/v) glycerol, 80 mM KCl, 2 mM $MgCl_2$, 5 mM BME, 0.017 % (w/v) DDM) on an ÄKTA Pure fast protein liquid chromatography (FPLC) system (Cytiva) operated at 4°C. A typical size exclusion chromatography (SEC) chromatogram of *Pa*MprF is shown in **Figure 2.4:**

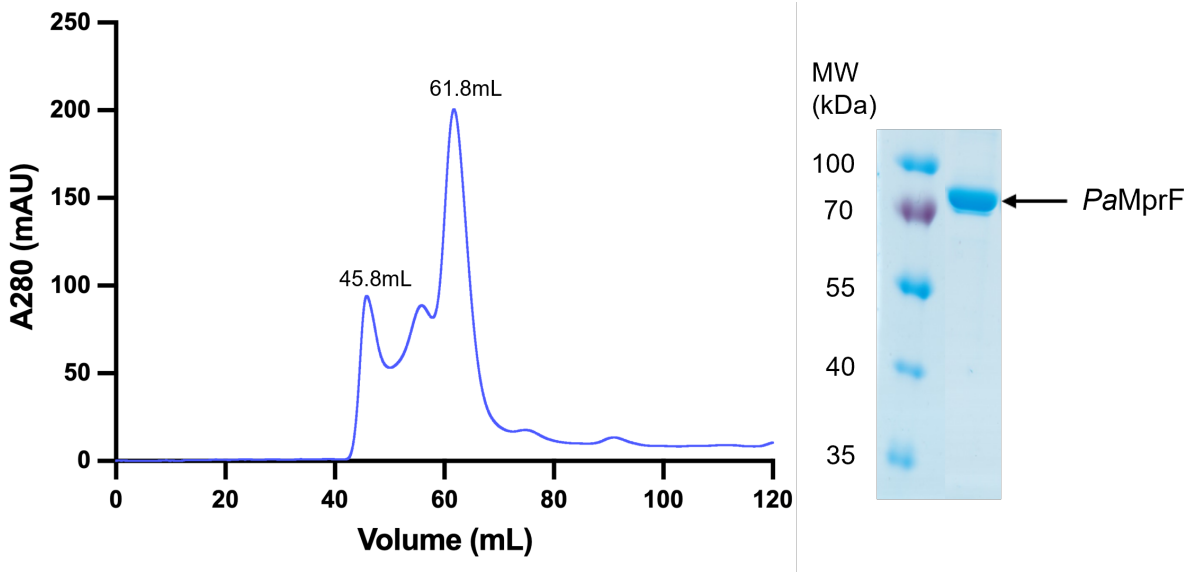

Figure 2.4: Full-length *Pa*MprF purification. *Left:* SEC chromatogram of full-length *Pa*MprF purification. *Right*: SDS-PAGE gel (12 %, Coomassie stain) of sample eluting at 61.8 mL.

*Pa*MprF elutes predominantly at 61.8 mL at >95% purity. The fractions corresponding to the 61.8 mL peak were pooled and concentrated in 100 kDa MWCO Vivaspin 6 concentrators (Sartorius) to ~5 mg/mL, flash frozen in liquid nitrogen and stored at -80°C.

2.4.4. Expression and purification of SaposinA (SapA)

The sequence for human SapA was expressed in a pNIC-Bsa4 vector (kindly provided by Dr Jens Frauenfeld, Salipro Biotech AB, Sweden) under an IPTG inducible promotor and adding an N-terminal 6x-His tag with a Tobacco Etch Virus (TEV) cleavage site. Expression and purification of SapA was performed as described by Frauenfeld *et al.* (2016). The SapA expression plasmid was transformed into Rosetta gami-2 (DE3) *E. coli.* A 90 mL starter culture of TB supplemented with 15 µg/mL Kanamycin, 12.5 µg/mL Tetracycline, and 34 µg/mL Chloramphenicol (TB-Kan/Tet/Cam) was inoculated with a single transformant and grown overnight at 37°C. The following day 3 L of TB-Kan/Tet/Cam was inoculated with this starter culture to OD_{600} = 0.1 and grown at 37°C until OD_{600} = 1.2. Cells were cooled to 25°C and induced with 0.7 mM IPTG. Cells were grown for 20 hours shaking at 25°C.

Cells were harvested at 4,500 g for 20 minutes, and cell pellets resuspended to 5 mL/g wet cell mass in 20 mM HEPES pH 7.5, 150 mM NaCl, 20 mM imidazole, 2 U/mL DNase I, EDTA-free protease inhibitors. Cells were lysed by 2 passes through a cell disruptor (Constant Systems) operated at 30 kpsi. Lysate was incubated at 85°C in a water bath for 10 minutes and centrifuged at 40,000 g for 1 hour to pellet precipitated proteins. The supernatant containing SapA was collected and incubated with 6 mL Ni Sepharose 6 Fast Flow resin (Cytiva) for 1 hour at RT. Affinity resin was washed with 100 mL of 20 mM HEPES pH 7.5, 150 mM NaCl, 40 mM imidazole to remove non-specifically bound proteins, before elution with 30 mL of 20 mM HEPES pH 7.5, 150 mM NaCl, 400 mM imidazole. Eluate was supplemented with 1 mg TEV protease per 12.5 mg SapA, and dialysed against 1 L 20 mM HEPES pH 7.5, 150 mM NaCl overnight at RT. Dialysate was passed over re-equilibrated affinity resin and the flow-through collected. Flowthrough was concentrated in 3 kDa MWCO Vivaspin 20 concentrators (Sartorius) and loaded onto a HiLoad 16/600 Superdex 200pg column (Cytiva) equilibrated in 20 mM HEPES pH 7.5, 150 mM NaCl. A typical SEC chromatogram is shown in **Figure 2.5:**

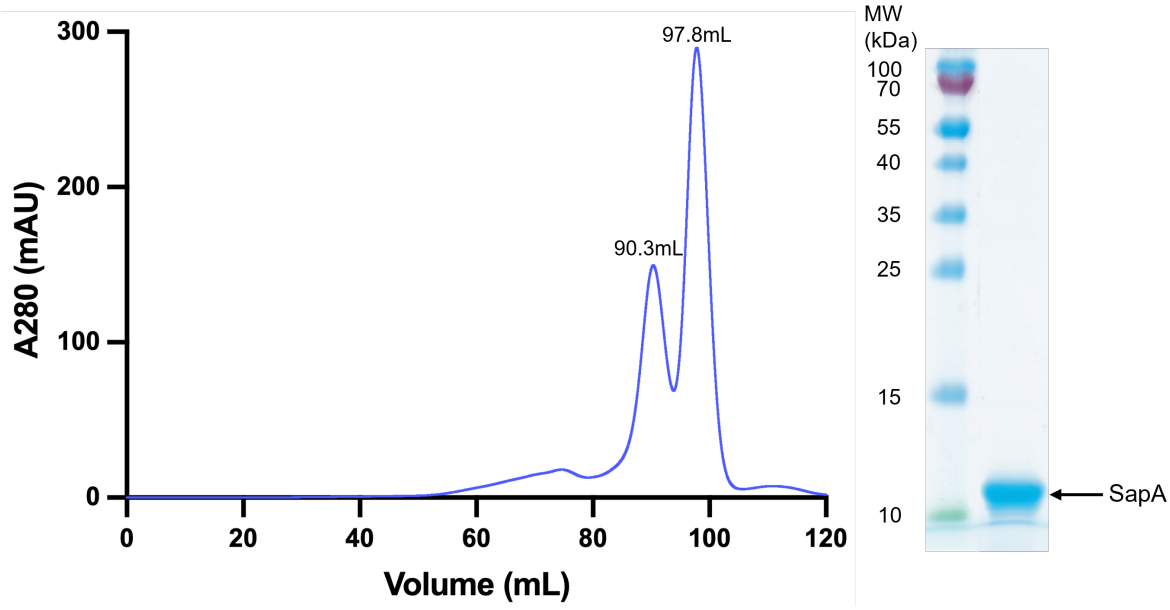

Figure 2.5: SapA purification. *Left:* SEC chromatogram of SapA purification. *Right*: SDS-PAGE gel (16 %, Coomassie stain) of sample eluting at 97.8 mL.

Peak fractions from the 97.8 mL peak corresponding to monomeric SapA (MW = 9 kDa) were pooled and concentrated to 1.2 mg/mL before being flash frozen in liquid nitrogen and stored at -80°C.

2.4.5. Reconstitution of *Pa*MprF into SapA nanoparticles

In all reconstitutions, lipid stocks were prepared by mixing the chloroform solubilised lipids in the desired ratio in a round bottom flask. Chloroform was evaporated in a fume hood under a nitrogen stream to form lipid films that were left overnight in a vacuum desiccator. Films were dissolved in buffer (50 mM HEPES pH 7.6, 20 mM NaCl) containing 100 mM sodium cholate to give a final lipid concentration of 50 mM.

*Pa*MprF was reconstituted into SapA nanoparticles (SapNPs) following the procedure described by Frauenfeld *et al.* (2016). *Pa*MprF, SapA and a 7:3 lipid mixture of POPC:POPG was mixed in a molar ratio of 1:25:40 respectively and incubated on ice for 1 hour. Detergent was removed by incubation with 50 mg activated Biobeads-SM2 (Bio-Rad) for 1 hour at 4°C,

followed by incubation overnight at 4°C with a further 100 mg Biobeads. The sample was loaded onto a Superdex 200 10/300 increase column (GE healthcare) equilibrated in 20 mM HEPES pH 7.6, 80 mM KCl, 2 mM $MgCl_2$ to separate *Pa*MprF-SapNPs from empty SapNPs. The peak corresponding to *Pa*MprF-SapNPs was pooled and concentrated for cryo-EM sample preparation as described in **section 2.9.1.**

2.4.6. Large-scale expression, purification and biotinylation of *Pa*MprF for sybody selections

The gene for the full-length sequence of *Pa*MprF (PA0920) was cloned via the FX cloning system into the expression plasmid pBXCA3H, putting the *Pa*MprF gene under an arabinose inducible araBAD promoter, and adding a C-terminal AviTag™, a 3C protease cleavage site and a 10x-His affinity tag. This plasmid was transformed into MC1061 *E. coli* (reduced arabinose metabolism) for large-scale expression.

250 mL of TB-Amp was inoculated with a colony of MC1061 containing the expression plasmid and grown overnight at 37°C. The next day, this culture was used to inoculate 6 L of TB-Amp to OD_{600} = 0.1. Cells were grown over the day at 37°C until OD_{600} = 0.6 - 0.8, and induced by the addition of 0.01 % L-arabinose. Cells were grown overnight at 20°C before being pelleted at 4500 g for 20 minutes. Pelleted cells were resuspended in lysis buffer (see **section 2.4.3.**) containing a spatula tip of DNAse I (bovine pancreas, Sigma-Aldrich) and three tablets of cOmplete™ Mini EDTA-free Protease Inhibitor Cocktail (Roche). Resuspended cells were passed through a cell disruptor (Constant Systems) twice at 30 kpsi, and cell debris pelleted at 17,000 g for 45 minutes. The supernatant was collected and ultracentrifuged at 200,000 g for 1 hour to pellet cell membranes. Membranes were weighed and resuspended in IMAC buffer (see **section 2.4.3.**) to 6 mL/g for solubilisation and purification.

Membranes were solubilised by addition of 1.2 % DDM (w/v) (low alpha, Generon), and were left rotating at 4°C for 1 hour. Membranes were ultracentrifuged at 200,000 g to pellet insoluble material, and the supernatant collected. 20 mM imidazole was added to the soluble supernatant and incubated with 2 mL Ni Sepharose 6 Fast Flow resin (Cytiva) for 1 hour at 4°C. Resin was washed with IMAC buffer containing 0.0261 % (w/v) DDM and 50 mM imidazole until A_{280} of flowthrough was constant. *Pa*MprF was eluted in 2 mL fractions with IMAC buffer containing 0.0261 % (w/v) DDM and 250 mM imidazole. Peak fractions were then pooled and dialysed overnight at 4°C against 20x volume of IMAC buffer containing 0.0261 % (w/v) DDM to remove imidazole. 3C protease was added during dialysis (at a molar ratio of 1:10 3C:MprF) to cleave the 10x-His tag from the construct. The next day, the dialysate was biotinylated by the addition of 0.4 mM biotin, 5 mM ATP, 1 M MgOAc, and recombinantly purified BirA (at a molar ratio of 1:15 BirA:MprF, BirA kindly provided by Abilasha Balakrishnan, Centre of Medicines Discovery, Oxford). This biotinylation reaction was incubated overnight at 4°C. 3C protease and BirA were removed the next day by incubation with 250 µL Ni Sepharose 6 Fast Flow resin (Cytiva). Flowthrough was collected, and loaded onto a Superdex 200 10/300 increase column for SEC. The chromatogram from this purification is shown in **Figure 2.6:**

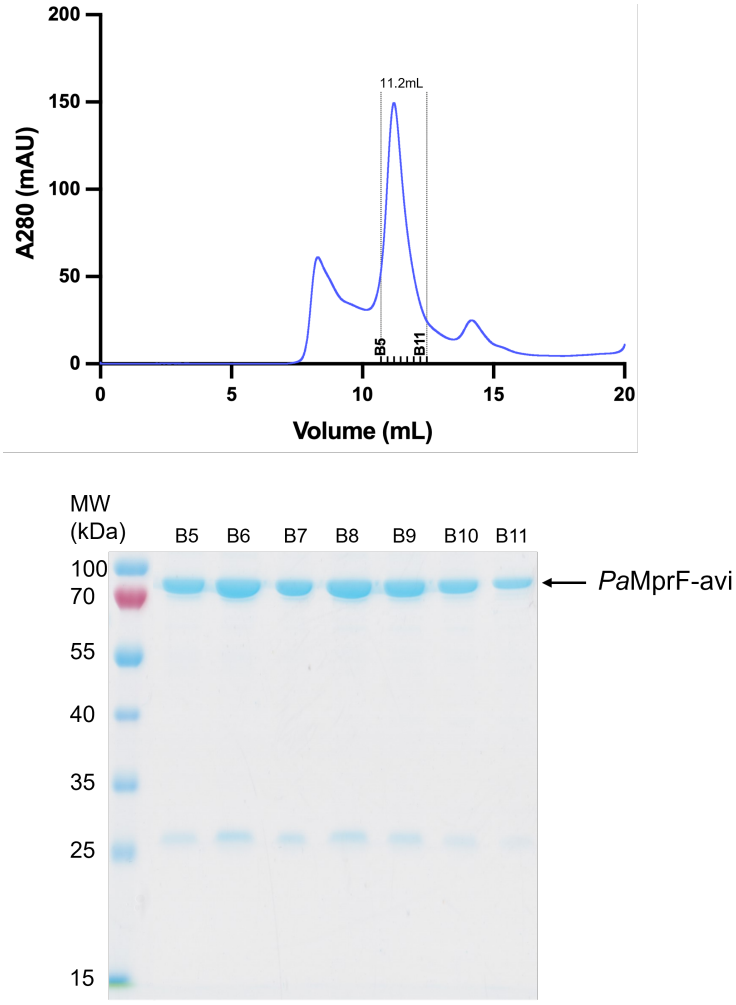

Figure 2.6: Purification of *Pa*MprF-avi. SEC chromatogram of *Pa*MprF-avi purification with peak fractions highlighted (***Top***) and SDS-PAGE gel (12 %, Coomassie stain) of peak fractions from SEC (***Bottom***).

Biotinylated *Pa*MprF-avi elutes at a similar volume to previously purified *Pa*MprF-avi, indicating that the construct is stable and folded correctly. SDS-PAGE shows the protein runs at the expected MW, with a high degree of purity.

For sybody selections, target protein must be >90 % biotinylated at the AviTag™. Biotinylation was assessed by SDS-PAGE band shift following incubation with excess streptavidin (**Figure 2.7**).

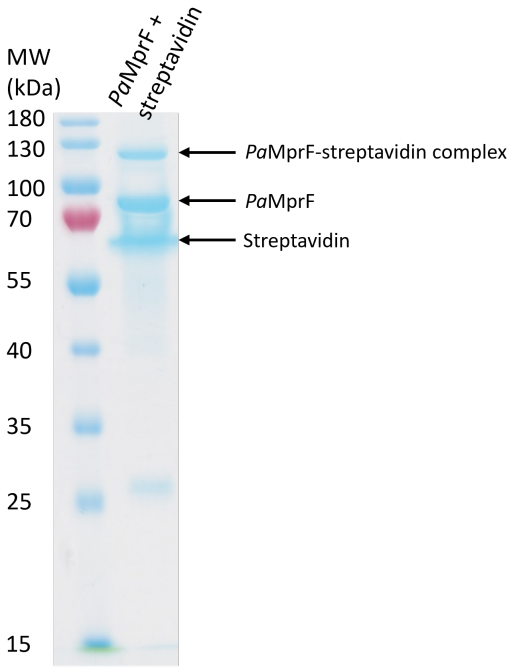

Figure 2.7: Band-shift assay. SDS-PAGE (12 %, Coomassie stain) showing band shift of *Pa*MprF-avi following incubation with streptavidin.

Figure 2.7 shows that incubation with streptavidin leads to the appearance of a higher MW band on SDS-PAGE, indicating that streptavidin is able to bind to *Pa*MprF and thus confirming the successful biotinylation of the AviTag™. The degree of biotinylation was quantified by tryptic digest Mass-Spectrometry by Dr Aygul Malone (Advance Proteomics Facility, Department of Biochemistry, Oxford), with >95 % of the detected AviTag™ peptides being biotinylated. This sample was therefore suitable for sybody selection.

2.4.7. Attempted large-scale expression and purification of *Pa*MprF transmembrane construct for sybody selections

The transmembrane region of *Pa*MprF (residues 1-545, construct hence referred to as *Pa*MprF^{545}) was cloned via the FX cloning system into the expression plasmid pBXCA3H. This plasmid was transformed into MC1061 *E. coli* for large-scale expression.

Expression and purification of *Pa*MprF^{545}-avi was performed as for full length *Pa*MprF-avi (**section 2.4.6.**). The yield was significantly lower than the full-length construct, so the peak

elution fractions were concentrated and run on a Superdex 200 10/300 increase column to assess the stability of the construct before biotinylation. SDS-PAGE samples of the elution fractions and the SEC chromatogram from *Pa*MprF^{545}-avi are shown in **Figure 2.8:**

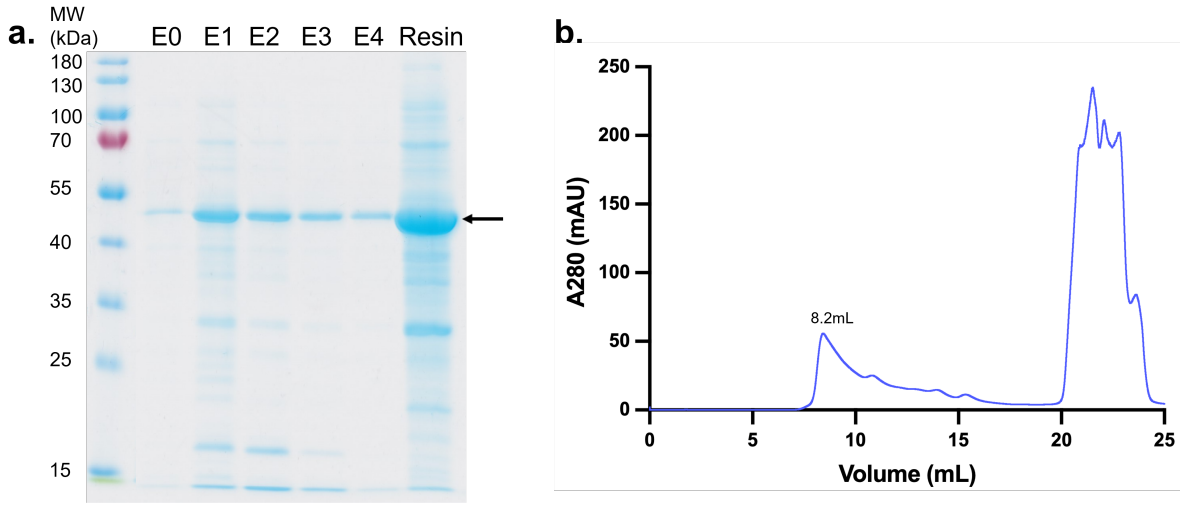

Figure 2.8: Purification of *Pa*MprF^{545}-avi. a. SDS-PAGE gel (12 %, Coomassie stain) of *Pa*MprF^{545}-avi elution fractions E0-E4, as well as a sample of the resin following elution. The band corresponding to *Pa*MprF^{545}-avi is highlighted with an arrow. **b.** SEC chromatogram of *Pa*MprF^{545}.

As evident from the SDS-PAGE gel, a significant proportion of the *Pa*MprF^{545}-avi remained bound to the affinity resin following elution and could not be removed even using imidazole concentrations of 1 M. This suggests the construct is aggregating on the resin and is significantly less stable than full-length *Pa*MprF. This is further supported by the SEC chromatogram, which shows that the majority of protein elutes at the void volume of the column (~8.2 mL), indicating aggregation. The high A_{280} after 20 mL elution volume corresponds to the imidazole present in the sample. As such, this sample is not suitable for biotinylation or sybody selection as it cannot be stably purified at sufficient quantities. The construct was instead used for pull-down assays following sybody selection to identify TM domain-binding sybodies.

2.4.8. Small-scale expression testing p-benzoyl-l-phenylalanine (BPA) mutants

*Pa*MprF mutants containing the artificial amino acid p-benzoyl-l-phenylalanine (BPA) were produced following the protocol of Isom *et al.* (2020). The amber stop codon TAG was introduced by site directed mutagenesis at amino acid sites to be replaced with BPA, and TAG mutant plasmids co-transformed into BL21 *E. coli* with pEVOL-pBpF (kindly provided by Dr Georgia Isom, Sir William Dunn School of Pathology, Oxford), a plasmid containing the $tRNA^{BPA}$ and tRNA-synthetase system for the incorporation of BPA at TAG codons (Chin *et al.* 2002). Small-scale expression testing of *Pa*MprF constructs containing the artificial amino acid BPA was carried out by inoculating 20 mL of TB-Kan/Cam and growing cells at 37°C to OD_{600} = 0.6 - 0.8 before inducing with 1 mM IPTG (to induce *Pa*MprF expression) and 0.2 % (w/v) L-arabinose (to induce pEVOL-pBpF). 0.5 mM BPA (Alfa Aesar) was also added to the medium. Cells were grown at 20°C overnight.

Cells were pelleted at 4000 g for 20 minutes, and cell pellets resuspended in lysis buffer (50 mM Tris pH 7.6, 200 mM KCl, 1 mM $MgCl_2$, 20 % (v/v) glycerol, 2 U/mL DNase I, EDTA-free protease inhibitors). Cells were lysed using a FastPrep-24 5G bead beater (MP Biomedicals) using 300 mg 0.1 mm glass beads per sample, with three cycles of 20 s lysis at 6 m/s (breaks on ice in between cycles). Unbroken cells were pelleted at 20,000 g for 1 minute, and the supernatant retrieved for small-scale purification.

1.2 % (w/v) DDM was added to each supernatant sample and samples were incubated, rotating end over end, at 4°C for 1 hour. 25 µL Ni Sepharose 6 FF (Cytiva) was added to each sample and samples were rotated end over end at 4°C for 1 hour. Affinity resin was pelleted by spinning at 500 g for 5 minutes. The supernatant was removed and the resin resuspended in 1 mL lysis buffer + 40 mM imidazole. This batch wash was repeated 3 times before eluting the

resin with 30 µL lysis buffer + 500 mM imidazole. Eluates were analysed by SDS-PAGE and western blot to identify well-expressing constructs.

2.4.9. Large-scale expression and purification of *Pa*MprF mutants

*Pa*MprF mutants were cloned by FX cloning into the expression plasmid p7XC3H, placing the *Pa*MprF gene under an IPTG inducible T7 promoter, and adding a C-terminal 10x-His affinity tag. Constructs were expressed in C41 *E. coli*. 100 mL of TB-Kan was inoculated with a colony of C41 containing the expression plasmid and grown overnight at 37°C. The next day, this culture was used to inoculate 2 L of TB to OD_{600} = 0.1. Cells were grown over the day until OD_{600} = 0.6 - 0.8, and then induced by the addition of 0.5 mM IPTG. Cells were grown overnight at 20°C before being pelleted at 4500 g for 20 minutes. Pelleted cells were resuspended in lysis buffer (see **section 2.4.3.**) containing a spatula tip of DNAse I (bovine pancreas, Sigma-Aldrich) and one tablet of cOmplete™ Mini EDTA-free Protease Inhibitor Cocktail (Roche). Resuspended cells were passed through a cell disruptor (Constant Systems) twice at 30 kpsi, and cell debris pelleted at 17,000 g for 45 minutes. The supernatant was collected and ultracentrifuged at 200,000 g for 1 hour to pellet cell membranes. Membranes were weighed and resuspended in IMAC buffer (see **section 2.4.3.**) to 6 mL/g for solubilisation and purification.

Membranes were solubilised by addition of 1.2 % DDM (w/v) (low alpha, Generon), and were left rotating at 4°C for 1 hour. Membranes were ultracentrifuged at 200,000 g to pellet insoluble material, and the supernatant collected. 20 mM imidazole was added to the soluble supernatant and incubated with 0.5 mL Ni Sepharose 6 Fast Flow resin (Cytiva) for 1 hour at 4°C. Resin was washed with IMAC buffer containing 0.0261 % (w/v) DDM and 50 mM imidazole until A_{280} of flowthrough was constant. *Pa*MprF was eluted in 0.5 mL fractions with IMAC buffer containing 0.0261 % (w/v) DDM and 400 mM imidazole. Peak fractions were then

pooled and loaded onto a Superdex 200 10/300 increase column equilibrated in 20 mM HEPES pH 7.6, 10 % (v/v) glycerol, 80 mM KCl, 2 mM $MgCl_2$, 5 mM BME, 0.017 % (w/v) DDM.

2.4.10. Large-scale expression and purification of BPA mutants

*Pa*MprF BPA mutants were expressed large-scale in BL21 *E. coli.* 100 mL TB-Kan/Cam was inoculated with a single colony of each mutant and grown overnight at 37°C. The next day, this culture was used to inoculate 2 L of TB-Kan/Cam to OD_{600} = 0.1 and grown at 37°C to OD_{600} = 0.6. Cultures were then induced by addition of 1 mM IPTG, 0.2 % (w/v) L-arabinose, and 0.5 mM BPA (Alfa Aesar), and grown overnight at 20°C. Cells were harvested the next day at 4,500 g for 20 minutes, and cell pellets resuspended to 5 mL/g wet cell mass in lysis buffer (see **section 2.4.3.**). Cells were processed and *Pa*MprF constructs purified as outlined in **section 2.4.9**.

2.4.11. Alanine tRNA synthetase (AlaRS) expression and purification

Full-length *Pa*AlaRS was expressed and purified according to Hebecker *et al.* (2011). 5 mL TB-Kan was inoculated with a colony of Rosetta pLysS *E. coli* transformed with the *Pa*AlaRS expression plasmid. This starter culture was incubated at 37°C, 220 rpm for 7 hours and then used to inoculate 200 mL TB-Kan which was grown overnight at 37°C. The overnight culture was used to inoculate 2 L TB-Kan to OD_{600} = 0.1, and cells were grown at 37°C, 220 rpm until OD_{600} = 0.8. Cells were induced with 200 µM IPTG for 4 hours at 30°C. Cells were pelleted at 4,500 g for 20 minutes, and cell pellets resuspended in AlaRS lysis buffer (35 mM Tris/HCl pH 7.4, 10 % (v/v) glycerol, 300 mM NaCl, 40 mM $MgCl_2$, 2 U/mL bovine pancreas DNAse I, EDTA-free protease inhibitors) to 5 mL/g wet mass of cells. Cells were lysed by passing twice through a cell disruptor (Constant Systems) operated at 30 kpsi. Lysate was ultracentrifuged at 250,000 g for 1 hour to pellet cell debris and membranes. The supernatant was collected,

mixed with 20 mM imidazole, and added to 2 mL Ni Sepharose 6 FF affinity resin (Cytiva). Affinity resin was incubated with lysate for 1 hour at 4°C before being batch washed 3 times with 50 mL AlaRS lysis buffer + 50 mM imidazole. AlaRS was then eluted in an imidazole gradient from 0-400 mM imidazole in 5 mL fractions.

Following elution, peak fractions were concentrated to 500 µL in a Vivaspin 20 100 kDa MWCO concentrator (Sartorius) and loaded onto a Superdex 200 10/300 increase column equilibrated in 35 mM Tris pH 7.2, 300 mM NaCl, 40 mM $MgCl_2$. Peak fractions following SEC were pooled and flash-frozen in liquid nitrogen for storage at -80°C.

2.4.12. AlaRS^{440} expression and purification

Residues 1-440 of AlaRS were cloned from PAO1 genomic DNA and inserted into the expression plasmid p7XNH3, as described for full-length AlaRS. AlaRS^{440}-p7XNH3 was transformed into Rosetta pLysS *E. coli.* Expression and purification of AlaRS^{440} was carried out as described for full-length AlaRS (**section 2.4.11.**). Peak fractions following affinity resin elution were pooled and concentrated in a Vivaspin 20 30 kDa MWCO concentrator (Sartorius) and loaded onto a Superdex 200 10/300 increase column equilibrated in 35 mM Tris pH 7.2, 300 mM NaCl, 40 mM $MgCl_2$. Results of this SEC step are shown in **Figure 2.9:**

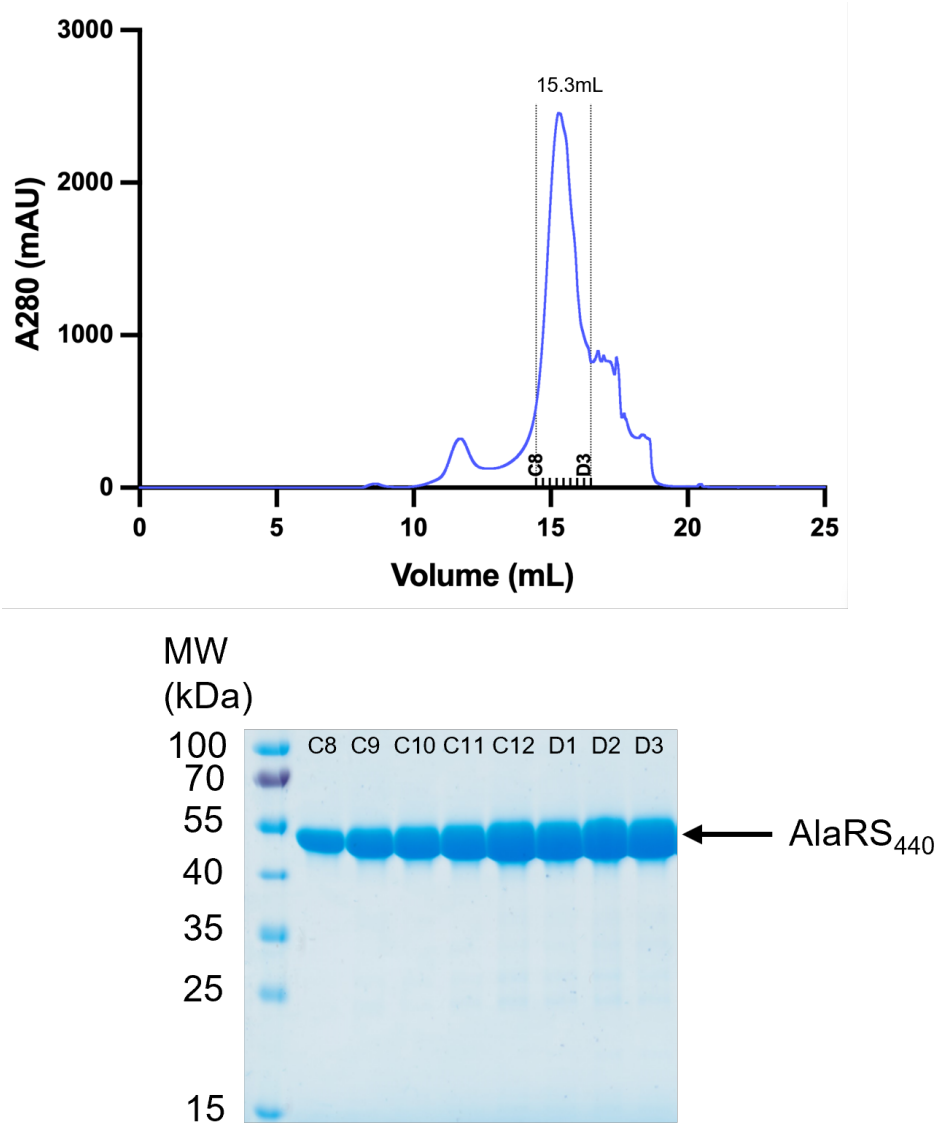

Figure 2.9: Purification of AlaRS^{440}. SEC chromatogram of AlaRS^{440} purification with peak fractions highlighted (***Top***) and SDS-PAGE gel (12 %, Coomassie stain) of peak fractions from SEC (***Bottom***).

AlaRS^{440} (MW = 52 kDa) elutes from the SEC column at 15.3 mL as a monomer, and SDS-PAGE demonstrates the high purity of the construct. Peak fractions were pooled and flash frozen in liquid nitrogen for storage at -80°C.

2.5. *In vitro Pa*MprF synthase assay

*Pa*MprF-mediated synthesis of alanyl-PG was assessed *in vitro* using NBD-PG and TLC. 2.5 mM POPG and 25 µM NBD-PG (1 mol% of bulk lipid to reduce NBD auto-quenching) dissolved in 0.1 % (w/v) DDM was incubated with 5 µM purified *Pa*MprF for one hour at RT. An aminoacylation mixture was then added to the lipid:*Pa*MprF reaction, comprising 5 µM tRNA (*in vitro* transcribed or *E. coli* extracted), 5 µM purified AlaRS/AlaRS^{440}, 0.05 % (w/v) DDM, 4 mM ATP, 6 mM L-alanine, and an ATP regenerating system of 36 µM creatine phosphate and 33 U/mL creatine phosphokinase (rabbit muscle, Sigma-Aldrich). Reactions were incubated overnight rotating at 4°C. The next day, lipids were extracted from samples as described in **section 2.3.1** and separated by TLC as described in **section 2.3.2**.

2.6. *In vitro Pa*MprF lipid translocation assay

2.6.1. Reconstitution of *Pa*MprF into liposomes containing NBD-labelled lipid

Proteoliposome formation was carried out using the technique developed by Rigaud *et al.* (Rigaud and Lévy 2003), in which empty liposomes are formed and destabilised by titration with a mild detergent to facilitate target protein insertion, followed by detergent removal. Chloroform solubilised lipid stocks of POPC and POPG were mixed in a 7:3 (mol:mol) ratio along with 0.4 mol% NBD-labelled reporter lipid. The lipid mixture was dried in a round bottom flask with a nitrogen stream to form a lipid film. Residual solvent was removed by drying overnight in a vacuum desiccator. The lipid film was rehydrated to 20 mg/mL total lipid concentration with liposome reconstitution buffer (100 mM HEPES pH 7.6, 100 mM KCl) for 2 hours at RT protected from light to limit NBD photobleaching. Rehydrated lipid was then extruded through a membrane filter (Merck Millipore, pore size 0.4 µm) using a mini-extruder (Avanti) 31 times to form liposomes. The resulting liposomes were titrated with DDM to

identify the concentration at which liposomes swell and are destabilised without fully solubilising, characterised by a peak in OD_{540} (Marek and Günther-Pomorski 2016, Brunner and Schenck 2019). For a POPC:POPG (7:3) bulk lipid mixture, this was determined as 0.4 % (w/v) DDM, which was then used for all liposome reconstitution experiments. Liposomes were incubated with 0.4 % (w/v) DDM for 3 hours at RT. *Pa*MprF at the desired *Pa*MprF:lipid (w/w) ratio was then added to the destabilised liposomes and incubated at 4°C for 30 minutes. DDM was removed by addition of Biobeads-SM2 (Bio-Rad); 80 mg Biobeads/mL liposomes were added and incubated at 4°C for 2 hours. This was repeated with a fresh 80 mg/mL Biobeads, and then a further 80 mg/mL Biobeads were added to samples for incubation overnight at 4°C. The next morning, one further 80 mg/mL Biobead incubation was performed to ensure complete DDM removal, and then Biobeads were removed and liposomes were either measured immediately in a fluorescence-based lipid transport assay described below, or frozen in liquid nitrogen and stored at -80°C for future use. When using stored liposomes, samples were thawed and subjected to extrusion as described above to ensure liposomes were unilamellar for fluorescence measurements. Variations in the recovery of lipid in the initial rehydration of lipid films meant that lipid transport measurements could not be directly compared across different batches of liposomes (Arndt *et al.* 2022), and so internal controls were included in all reconstitutions. For experiments using *Ilyobacter tartaricus* c-ring as a negative control, c-ring was kindly provided by Professor Thomas Meier, Liechtenstein Institute, Liechtenstein.

2.6.2. Liposome transport assay

NBD fluorescence of liposomes was monitored as a time-course in a 2 mL quartz cuvette using a LS55 fluorescence spectrometer (PerkinElmer). Measurements were taken at 25°C every three seconds at excitation = 460 nm, emission = 520 nm with 10 nm excitation and emission slit widths and a 0.5 s integration time. 40 µL of reconstituted liposomes were diluted in 2 mL of liposome buffer (100 mM HEPES pH 7.6, 100 mM KCl) and fluorescence monitored for an

initial two minutes to allow for sample equilibration with constant stirring. After two minutes, 20 µL 2 M sodium dithionite (dissolved in 1 M Tris) was added to the sample cuvette (20 mM final concentration), and the evolution of fluorescence over time measured for 10 minutes. After 10 minutes, 20 µL 10 % (v/v) Triton-X 100 was added (0.1 % (v/v) final concentration) to solubilise liposomes and expose any remaining protected NBD to dithionite.

For Bovine Serum Albumin (BSA) back extraction assay measurements, the assay was repeated as above, except 2 mg/mL fatty acid free BSA (Sigma Aldrich) was added at t = 120 s instead of 20 mM dithionite.

For NBD-glucose permeability control experiments and 8-hydroxypyrene-1,3,6-trisulfonic acid (HPTS) proton transport assays, liposomes were made as described above, but with NBD-labelled lipid removed from the bulk lipid and replaced with either 30 µM NBD-glucose or 40 mM HPTS. Following proteoliposome formation, liposomes were ultracentrifuged at 100,000 g for 2 hours and the supernatant removed. Pelleted liposomes were washed three times with 100 mM HEPES pH 7.6, 100 mM KCl, and then resuspended in 1 mL of the same buffer. This pelleting and wash step was repeated and the supernatant tested for fluorescence to confirm the removal of any NBD fluorophore not incorporated into liposomes.

2.6.3. Deriving the three-state model for analysis

A three-state model developed by Malvezzi *et al.* (Malvezzi *et al.* 2018) was used for the estimation of rate constants of *Pa*MprF-mediated lipid transport. The derivation of this three-state model is detailed below.

The fluorescent lipid populations within a single liposome can be described by the following three-state model:

$$L_i \underset{\beta}{\overset{\alpha}{\rightleftharpoons}} L_o \xrightarrow{\gamma} L_*$$

Where L_i is the fluorescent lipid in the inner leaflet of the liposome, L_o is fluorescent lipid in the outer leaflet, and L_* is fluorescent lipid that has been irreversibly bleached by dithionite. Conversion between L_i and L_o is mediated by *Pa*MprF activity, with α representing the forwards rate constant and β the reverse rate constant. γ represents the rate constant for bleaching of L_o lipid by dithionite, and depends on dithionite concentration. As such, dithionite concentration is kept constant across experimental measurements. The total fluorescence (F_{Scr}) in this liposome at any given time (t) is then the sum of L_i and L_o :

$$F_{Scr}(t) = L_i(t) + L_o(t)$$

The change in L_i over time is dependent on the lipid transported from L_o to L_i minus the lipid transported from L_i to L_o , such that:

$$\frac{dL_i(t)}{dt} = -\alpha L_i(t) + \beta L_o(t)$$

The change in L_o can be described similarly, with the additional consideration of lipid removed from L_o through irreversible dithionite bleaching:

$$\frac{dL_o(t)}{dt} = \alpha L_i(t) - (\beta + \gamma) L_o(t)$$

Writing these two equations in matrix form gives the following:

$$\frac{d}{dt}\begin{pmatrix} L_i(t) \\ L_o(t) \end{pmatrix} = \begin{pmatrix} -\alpha & \beta \\ \alpha & -(\beta+\gamma) \end{pmatrix}\begin{pmatrix} L_i(t) \\ L_o(t) \end{pmatrix} = M\bar{L}(t)$$

Where $M = \begin{pmatrix} -\alpha & \beta \\ \alpha & -(\beta+\gamma) \end{pmatrix}$ and $\bar{L}(t)$ is the vector $\begin{pmatrix} L_i(t) \\ L_o(t) \end{pmatrix}$. As these are first order differential equations, the solution is given as:

$$\bar{L}(t) = \hat{v}_1 A e^{\lambda_1 t} + \hat{v}_2 B e^{\lambda_2 t} \qquad \textbf{Equation 1}$$

Where A and B are two constants, $\hat{v}_{1,2}$ are the eigenvectors of M and $\lambda_{1,2}$ are the eigenvalues of M. The eigenvalues of M are values of λ for which the determinant of $M - \lambda I$ ($|M - \lambda I|$) is 0, where I is the identity matrix $\begin{pmatrix} 1 & 0 \\ 0 & 1 \end{pmatrix}$. Therefore:

$$|M - \lambda I| = \begin{vmatrix} -\alpha - \lambda & \beta \\ \alpha & -(\beta+\gamma) - \lambda \end{vmatrix} = \begin{vmatrix} -(\alpha+\lambda) & \beta \\ \alpha & -(\beta+\gamma+\lambda) \end{vmatrix} = 0$$

This gives the quadratic equation:

$$\lambda^2 - (\alpha + \beta + \gamma)\lambda + \alpha\gamma = 0$$

With the two solutions for λ:

$$\lambda_1 = \frac{(\alpha+\beta+\gamma) - \sqrt{(\alpha+\beta+\gamma)^2 - 4\alpha\gamma}}{2} \qquad \text{and} \qquad \lambda_2 = \frac{(\alpha+\beta+\gamma) + \sqrt{(\alpha+\beta+\gamma)^2 - 4\alpha\gamma}}{2}$$

By definition, the eigenvectors $\hat{v}_{1,2}$ satisfy the following:

$$M\hat{v}_1 = \lambda_1 \hat{v}_1 \quad \text{and} \quad M\hat{v}_2 = \lambda_2 \hat{v}_2$$

Which can be rearranged to:

$$(M - \lambda_1)\hat{v}_1 = 0 \quad \text{and} \quad (M - \lambda_2)\hat{v}_2 = 0$$

Therefore:

$$\begin{pmatrix} -\alpha - \lambda_{1,2} & \beta \\ \alpha & -(\beta + \gamma) - \lambda_{1,2} \end{pmatrix} \begin{pmatrix} x_{1,2} \\ y_{1,2} \end{pmatrix} = 0$$

Where $x_{1,2}$ and $y_{1,2}$ are the components of $\hat{v}_{1,2}$. Solving these equations gives $\hat{v}_{1,2}$ as:

$$\hat{v}_1 = \begin{pmatrix} \beta \\ \lambda_1 + \alpha \end{pmatrix} \quad \text{and} \quad \hat{v}_2 = \begin{pmatrix} \lambda_2 + \beta + \gamma \\ \alpha \end{pmatrix}$$

Substituting these values for $\hat{v}_{1,2}$ into **Equation 1** gives:

$$\begin{pmatrix} L_i(t) \\ L_o(t) \end{pmatrix} = \begin{pmatrix} \beta \\ \lambda_1 + \alpha \end{pmatrix} Ae^{\lambda_1 t} + \begin{pmatrix} \lambda_2 + \beta + \gamma \\ \alpha \end{pmatrix} Be^{\lambda_2 t}$$

This can be split into the two equations that represent the inner and outer leaflet fluorescent lipid populations at a given time, *t* :

$$L_i(t) = \beta Ae^{\lambda_1 t} + (\lambda_2 + \beta + \gamma)Be^{\lambda_2 t} \qquad \textbf{Equation 2}$$

and

$$L_o(t) = (\lambda_1 + \alpha)Ae^{\lambda_1 t} + \alpha Be^{\lambda_2 t} \qquad \textbf{Equation 3}$$

Where the total fluorescence of the liposome at a given time ($F_{Scr}(t)$) is the sum of these two populations:

$$F_{Scr}(t) = (\lambda_1 + \alpha + \beta)Ae^{\lambda_1 t} + (\lambda_2 + \alpha + \beta + \gamma)Be^{\lambda_2 t} \quad \textbf{Equation 4}$$

The values of the constants *A* and *B* can be determined by consideration of the system at *t=0*. At this time, no lipid has been irreversibly bleached, so the fraction of lipid in the inner leaflet ($L_i(0)$) and outer leaflet ($L_o(0)$) is equal to 1:

$$L_i(0) + L_o(0) = 1$$

When *t=0,* **Equations 2** and **3** become:

$$L_i(0) = \beta A + (\lambda_2 + \beta + \gamma)B \qquad \textbf{Equation 5}$$

and

$$L_o(0) = (\lambda_1 + \alpha)A + \alpha B \qquad \textbf{Equation 6}$$

Rearranging **Equation 5** for *A* and substituting into **Equation 6** gives:

$$L_o(0) = \frac{(\lambda_1 + \alpha)}{\beta} L_i(0) - \left(\frac{(\lambda_1 + \alpha)(\lambda_2 + \beta + \gamma) - \alpha\beta}{\beta}\right) B$$

Rearranging for B gives:

$$B = \frac{(\lambda_1 + \alpha)L_i(0) - \beta L_o(0)}{D}$$

Where:

$$D = (\lambda_1 + \alpha)(\lambda_2 + \beta + \gamma) - \alpha\beta$$

Substituting this expression for *B* back into **Equation 5** gives:

$$A = \frac{(\lambda_2 + \beta + \gamma) - (\lambda_2 + \alpha + \beta + \gamma)L_i(0)}{D}$$

Substituting these expressions for *A* and *B* back into **Equations 2, 3 and 4** gives:

$$L_i(t) = \frac{\beta\left((\lambda_2+\beta+\gamma)-(\lambda_2+\alpha+\beta+\gamma)L_i(0)\right)}{D} e^{\lambda_1 t} + \frac{(\lambda_2+\beta+\gamma)\left((\lambda_1+\alpha+\beta)L_i(0)-\beta\right)}{D} e^{\lambda_2 t} \quad \textbf{Equation 7}$$

$$L_o(t) = \frac{(\lambda_1+\alpha)\left((\lambda_2+\beta+\gamma)-(\lambda_2+\alpha+\beta+\gamma)L_i(0)\right)}{D} e^{\lambda_1 t} + \frac{\alpha\left((\lambda_1+\alpha+\beta)L_i(0)-\beta\right)}{D} e^{\lambda_2 t} \quad \textbf{Equation 8}$$

$$F_{Scr}(t) = \frac{(\lambda_1+\alpha+\beta)\left((\lambda_2+\beta+\gamma)-(\lambda_2+\alpha+\beta+\gamma)L_i(0)\right)}{D} e^{\lambda_1 t} + \frac{(\lambda_2+\alpha+\beta+\gamma)\left((\lambda_1+\alpha+\beta)L_i(0)-\beta\right)}{D} e^{\lambda_2 t} \quad \textbf{Equation 9}$$

Furthermore, before dithionite addition at *t=0* it is assumed that the distribution of lipid between inner and outer liposome leaflets is at equilibrium from *Pa*MprF activity. As such, it follows that before dithionite addition:

$$\frac{L_i(0)}{L_o(0)} = \frac{\beta}{\alpha} \quad \textbf{Equation 10}$$

And since $L_i(0) + L_o(0) = 1$, alternate substitution of this into **Equation 10** gives:

$$L_i(0) = \frac{\beta}{\alpha+\beta} \quad \text{and} \quad L_o(0) = \frac{\alpha}{\alpha+\beta}$$

Substitution of these expressions for $L_i(0)$ and $L_o(0)$ into **Equation 9** gives:

$$F_{Scr}(t) = \frac{\alpha(\lambda_2 + \gamma)(\lambda_1 + \alpha + \beta)e^{\lambda_1 t} + \lambda_1\beta(\lambda_2 + \alpha + \beta + \gamma)e^{\lambda_2 t}}{D(\alpha + \beta)}$$

Finally, this expression only accounts for liposomes that contain at least one active *Pa*MprF unit. In any reconstitution experiment there is a population of liposomes that do not contain any reconstituted protein, and the fluorescence of these protein-free (PF) liposomes ($F_{PF}(t)$) will also contribute to the fluorescence of the system at a given time ($F_{tot}(t)$). Since only outer leaflet lipid can be bleached in protein-free liposomes, their fluorescence at any time is given as:

$$F_{PF}(t) = L_i^{PF} + (1 - L_i^{PF})e^{-\gamma t} \qquad \textbf{Equation 11}$$

Where L_i^{PF} is the fraction of fluorescent lipid in the inner leaflet of protein-free liposomes. Letting f_0 represent the fraction of protein-free liposomes, the total fluorescence of the system is given as:

$$F_{tot}(t) = f_0 F_{PF}(t) + (1 - f_0)F_{Scr}(t) \qquad \textbf{Equation 12}$$

Substitution of **Equations 9** and **11** into **Equation 12** gives the full final equation used for fitting to experimental data:

$$F_{tot}(t) = f_0(L_i^{PF} + (1 - L_i^{PF})e^{-\gamma t}) + \frac{(1 - f_0)\left(\alpha(\lambda_2 + \gamma)(\lambda_1 + \alpha + \beta)e^{\lambda_1 t} + \lambda_1\beta(\lambda_2 + \alpha + \beta + \gamma)e^{\lambda_2 t}\right)}{D(\alpha + \beta)}$$

In this equation, the values of γ and L_i^{PF} can be determined experimentally by measuring the fluorescence over time of protein-free liposomes after dithionite addition, and fitting this fluorescence to the protein-free component of the final expression (**Equation 11**). These

values are then fixed when fitting experimental proteoliposome fluorescence data, such that the only variables to be solved for are f_0, α and β.

2.6.4. Analysis of fluorescence time-course data using the three-state model

Experimental data was fitted to the model above in R using the Nonlinear Least Squares function (nls). Protein-free liposomes were included in all reconstitution experiments and traces from protein-free liposomes fitted to **Equation 11** to obtain estimates of γ and L_i^{PF} that were fixed when fitting proteoliposome data to the full final model. In all liposomes, a slow linear decay in fluorescence can be observed that reflects the combined processes of NBD photobleaching and slow entry of dithionite into liposomes. The rate constant of this decay was determined in all reconstitutions to be of the order $\sim 10^{-5}$ s^{-1}, similar to other values reported in the literature (Lee *et al.* 2018, Malvezzi *et al.* 2018), and so was not included in proteoliposome analysis as it had a negligible effect on the determined rate constants from fitting.

Variations in f_0 affect the determined values of α and β. As the same concentration of WT and mutant *Pa*MprF was used in experiments investigating mutagenic effects on transport, the values of f_0 , α and β were determined for the most catalytically active construct (proteoliposomes that gave the greatest decrease in fluorescence on dithionite addition), and then this estimated value of f_0 was fixed for other proteoliposomes within the same reconstitution experiment, as is practice in previous studies (Lee *et al.* 2018, Falzone and Accardi 2020).

2.6.5. *Pa*MprF orientation assay

*Pa*MprF was labelled with a Cy5 derivative, DY-647P1 (Dyomics). An N-hydroxysuccinimide (NHS) ester of DY-647P1 was mixed with *Pa*MprF at a 1:10 (mol/mol) *Pa*MprF:DY-647P1 ratio and incubated overnight at 4°C. Labelled *Pa*MprF was separated from unreacted dye with SEC on a Superdex 200 10/300 increase column equilibrated in 20 mM HEPES pH 7.6, 10 % (v/v) glycerol, 80 mM KCl, 2 mM $MgCl_2$, 5 mM BME, 0.017 % (w/v) DDM. Peak labelled *Pa*MprF fractions were reconstituted into liposomes as described in **section 2.6.1.** Fluorescence of these liposomes was monitored in a 100 µL quartz cuvette using a LS55 fluorescence spectrometer (PerkinElmer, excitation = 639 nm, emission = 670 nm). Orientational distribution was assessed by addition of 1 µL 2 M Tris(2-carboxyethyl)phosphine (TCEP, 20 mM final concentration) followed by 1 µL 10 % (v/v) Triton X-100 (0.01 % (v/v) final concentration).

2.7. Selection of synthetic nanobodies (sybodies)

Selection of sybody binders was carried out following the protocol established by Zimmerman *et al.* (Zimmermann *et al.* 2020). An overview of the selection platform and the rationale behind each stage of selection is detailed in **Chapter 3**. The experimental details of each selection stage, along with sybody small-scale/large-scale purifications and pull-down assays with *Pa*MprF^{545} are given in **Appendix 3.**

2.8. AlaRS-*Pa*MprF interaction studies

2.8.1. Pull-down assay

25 µL of 2.6 mg/mL His-tagged AlaRS was incubated with 5 µL Ni Sepharose 6 FF resin (Cytiva) for 1 hour rotating at 4°C. Resin was washed with 1 mL Wash Buffer (20 mM HEPES pH 7.6,

100 mM KCl, 5 mM BME, 0.017 % (w/v) DDM, 75 mM imidazole). 5 µL of 4.6 mg/mL *Pa*MprF was then added and incubated for 1 hour rotating at 4°C. Resin was washed with 3 mL Wash Buffer and loaded onto an SDS-PAGE gel. In some experiments a different His-tagged protein – TEV protease – was added (200 µL at 1 mg/mL) to investigate *Pa*MprF binding to a non-specific control protein.

2.8.2. SEC co-elution

Samples of *Pa*MprF alone, AlaRS alone, and a 1:1 molar ratio of *Pa*MprF:AlaRS incubated for 1 hour at 4°C were loaded onto a Superdex 200 10/300 increase column (Cytiva) equilibrated in 20 mM HEPES pH 7.6, 80 mM KCl, 2 mM $MgCl_2$ to see if a shift in the elution volumes of the peaks could be observed, suggesting the formation of a complex with a higher MW.

2.8.3. Surface plasmon resonance (SPR)

SPR was performed using a BIAcore T200 (Cytiva) and a nitrilotriacetic acid (NTA) sensor chip (Cytiva) using a running buffer composed of 20 mM HEPES pH 7.5, 80 mM KCl, 3 mM $MgCl_2$, 5 mM BME, 0.017 % (w/v) DDM, 0.05 % (v/v) Tween-20 at a flow rate of 10 µL/minute. The sensor chip was first charged with 0.5 mM $NiCl_2$ solution, then His-tagged AlaRS at 50 µg/mL giving an increase in response of ~100 RU. Untagged *Pa*MprF at 1 µM - 24 µM was then injected over the chip and the response measured. The chip was regenerated with 6 M urea and 350 mM EDTA, with an additional wash of 2 M NaCl and 10 mM glycine/HCl pH 3 to remove non-specifically bound protein. The analysis cycle was then repeated with another *Pa*MprF concentration, starting with $NiCl_2$ charging again. One flow-cell was charged with nickel and AlaRS for measuring total *Pa*MprF binding, whilst a second flow-cell was uncharged to measure non-specific *Pa*MprF binding to the sensor chip surface. The resulting sensorgram shown in **Chapter 4** gives the signal difference between these two flow-cells, representing the binding of *Pa*MprF to AlaRS.

2.9. Cryo-Electron Microscopy

2.9.1. Preparation of cryo-EM grids

Grids were prepared by applying 3 µl of sample to glow-discharged holey carbon grids (Quantifoil R 1.2/1.3 Cu, either 200 or 300 mesh). Grids were then blotted at 100 % humidity and 4°C, before being plunge frozen in liquid ethane with a Vitrobot Mark IV (FEI). Optimisation of grid preparation for different samples is outlined in the relevant results sections of **Chapter 3**.

2.9.2. *Pa*MprF Cryo-EM data collection

Grids were assessed and initial datasets were collected using a Glacios Cryo-TEM (ThermoFisher) at Oxford Particle Imaging Centre (OPIC), Division of Structural Biology, Oxford, operated at 200 kV with a Falcon III direct electron detector. Movies were collected at 1.55 Å/pixel with a total dose of ~50 $e^-/Å^2$ and a defocus range of -3.0 to -1.5 µm.

A high-resolution dataset was collected using a Titan Krios Cryo-TEM (ThermoFisher) at the UK National Electron Bio-Imaging Centre (eBIC) at Diamond Light Source, Didcot, operated at 300 kV with a Falcon IV direct electron detector. Movies were collected at 0.723 Å/pixel with a total dose of ~50 $e^-/Å^2$ and a defocus range of -2.4 to -0.6 µm.

2.9.3. *Pa*MprF Cryo-EM data processing

Datasets were processed in CryoSPARC (Punjani *et al.* 2017) by the following general workflow. After motion correction and contrast transfer function (CTF) estimation of collected movies, particles were manually picked to produce initial templates for auto-picking. Auto-picked particles were subjected to multiple rounds of 2D classification to remove poor quality

particles. 2D classes with the best definition were used for *ab initio* 3D reconstruction to produce an initial model. For the high-resolution dataset, ~100k particles from micrographs with the thinnest ice and thus highest signal:noise ratio were used for *ab initio* reconstruction. Non-uniform and local refinements (using the starting *ab initio* model low-pass filtered to 12 Å and a focus mask with a 15-pixel soft edge that excluded the SapNP micelle) were then conducted with a larger ~700k particle set.

2.9.4. *Pa*MprF-Sybody29 complex Cryo-EM data collection

Grids were assessed and initial datasets were collected using a Talos Arctica Cryo-TEM (ThermoFisher) at the Central Oxford Structural Molecular Imaging Centre (COSMIC), Oxford, operated at 200 kV with a Falcon 4 direct electron detector. Movies were collected at 1.2 Å/pixel with a total dose of ~50 $e^-/Å^2$ and a defocus range of -2.25 to -0.75 μm.

A high-resolution dataset was collected using a Titan Krios Cryo-TEM (ThermoFisher) at COSMIC, Oxford, operated at 300 kV with a Gatan K3 direct electron detector. Movies were collected at 0.83 Å/pixel with a total dose of ~42 $e^-/Å^2$ and a defocus range of -2.25 to -0.75 μm.

2.9.5. *Pa*MprF-Sybody29 complex Cryo-EM data processing

Datasets were processed in CryoSPARC. Briefly, following motion correction and CTF estimation of collected movies, particles were picked using blob picker and 2D classified to produce initial templates that were used for template picking. Template picked particles were then subjected to multiple rounds of 2D classification before the best particle sets were used for *ab initio* 3D reconstruction. For the high-resolution dataset, these particles were then taken forward to heterogeneous refinement using the *ab initio* model low-pass filtered to 12 Å as three starting classes. The particle sets from the best two classes were subjected to a round of

3D classification (using three starting *ab initio* models low-pass filtered to 12 Å, and a focus mask with a 15-pixel soft edge that excluded the SapNP micelle). The particle set comprising the class with the best defined sybody map was taken forward to local CTF refinement and used for a final round of non-uniform refinement. This output was sharpened with a *B*-factor of -85 Å, producing the post-processed map used for model building.

2.9.6. Model building and refinement

The *Pa*MprF-Sybody29 model was built in Coot (Emsley and Cowtan 2004), using a homology model of *Pa*MprF and Sybody29 as an initial template. Homology models were generated from one chain of the *Rt*MprF cryo-EM structure (PDB:7DUW) (Song *et al.* 2021) and a loop-library sybody binder (PDB:3P0G) (Rasmussen *et al.* 2011) using SWISS-MODEL (Waterhouse *et al.* 2018). Model refinement was performed in PHENIX (Afonine *et al.* 2018) with iterative rounds of real-space refinement with rotamer and secondary structure restraints using the final map at 3.28 Å resolution.

Chapter 3: Structural characterisation of *Pseudomonas aeruginosa* MprF

3.1. Introduction

Structural data for a full-length homologue of MprF from a pathogen is currently lacking. A full-length structure of MprF from the non-pathogenic soil bacterium *R. tropici* has been determined (Song *et al.* 2021), but sequence conservation between MprF homologues is low (*Rt*MprF vs. *Pa*MprF = ~38% sequence identity). Therefore, obtaining a full-length structure of MprF from *P. aeruginosa* would allow a direct comparison to *Rt*MprF to see how structurally conserved the lipid transport core of the protein is between bacterial species. Structural data from another homologue may also provide insight into how the protein may function, as it is currently unclear how lipid is translocated from the inner to outer leaflets of the bacterial inner membrane.

As such, one key aim of this work has been obtaining a full-length structure of *Pa*MprF. Previous work in the Bublitz group resulted in the optimisation of *Pa*MprF purification from recombinant expression in *E. coli* (Lorenz 2016, Smilova 2017, Lundie-Brown 2018), and the reconstitution of *Pa*MprF into SaposinA nanoparticles (SapNPs) (Hankins 2019). Negative stain electron microscopy of these *Pa*MprF SapNPs suggested that the sample was homogeneous and suitable for cryo-EM studies, which is where the work described in this Chapter begins.

3.2. *Pa*MprF-SapNP Cryo-Electron Microscopy

3.2.1. Optimisation of *Pa*MprF-SapNP cryo-EM grid preparation

*Pa*MprF was reconstituted into SapNPs as described in **Methods (2.4.5.)**. The lipids used for reconstitution were 1-palmitoyl-2-oleoyl-glycero-3-phosphocholine (POPC) and 1-palmitoyl-2-oleoyl-sn-glycero-3-phospho-(1'-rac-glycerol) (POPG) at a 7:3 POPC:POPG molar ratio. *Pa*MprF, SapA and bulk lipid were mixed at a molar ratio of 1:25:40 *Pa*MprF:SapA:lipid, a ratio previously determined to maximise *Pa*MprF incorporation into nanoparticles (Hankins 2019). A mixture of 7:3 POPE:POPG was tested for reconstitution to better match the native *P. aeuriginosa* membrane composition, but resulted in significantly lower reconstitution efficiency, perhaps due to PE being charged yet having a smaller headgroup than PC and so resulting in tighter, less electrostatically favourable lipid packing. Indeed, previous studies have found membrane protein reconstitution efficiency is lower when using bulk PE lipid species (Li *et al.* 2019). *Pa*MprF loaded SapNPs were separated from empty SapNPs by SEC, as shown in **Figure 3.1:**

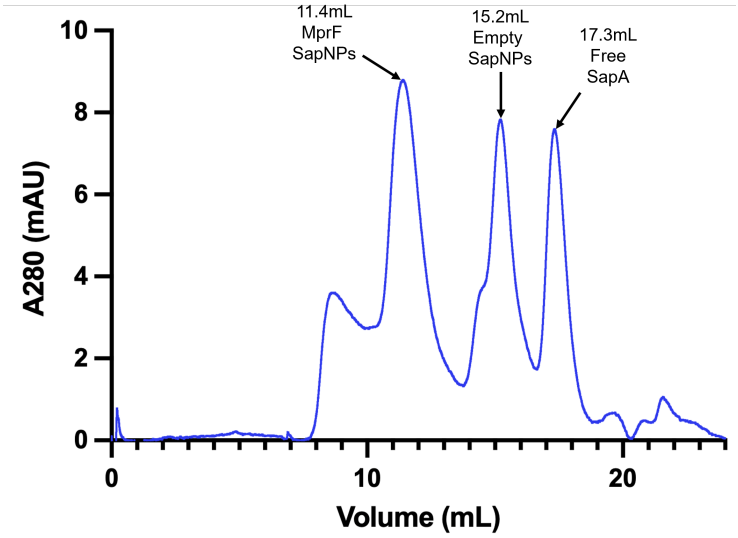

Figure 3.1: *Pa*MprF-SapNP SEC. SEC chromatogram of *Pa*MprF-SapNPs following reconstitution. *Pa*MprF-SapNPs elute at 11.4 mL, empty SapNPs at 15.2 mL and free SapA at 17.3 mL.

The peak at 11.4 mL corresponding to *Pa*MprF-SapNPs was concentrated for cryo-EM grid preparation. *Pa*MprF-SapNP cryo-EM grid preparation was optimised by altering blotting time, grid type and sample concentration parameters. Initial grids (1.5 second blot time, 300 mesh holey carbon grids, 0.5 mg/mL sample concentration) had issues with thick ice in holes which would hinder data collection, so longer blotting times (2.5 seconds) and 200 mesh holey carbon grids (Cu Quantifoil R1.2/1.3) were used to reduce ice thickness. A higher concentration of protein sample was also used (1 mg/mL) to increase sample viscosity and particle packing. An example of a grid produced from these optimisations is shown in **Figure 3.2:**

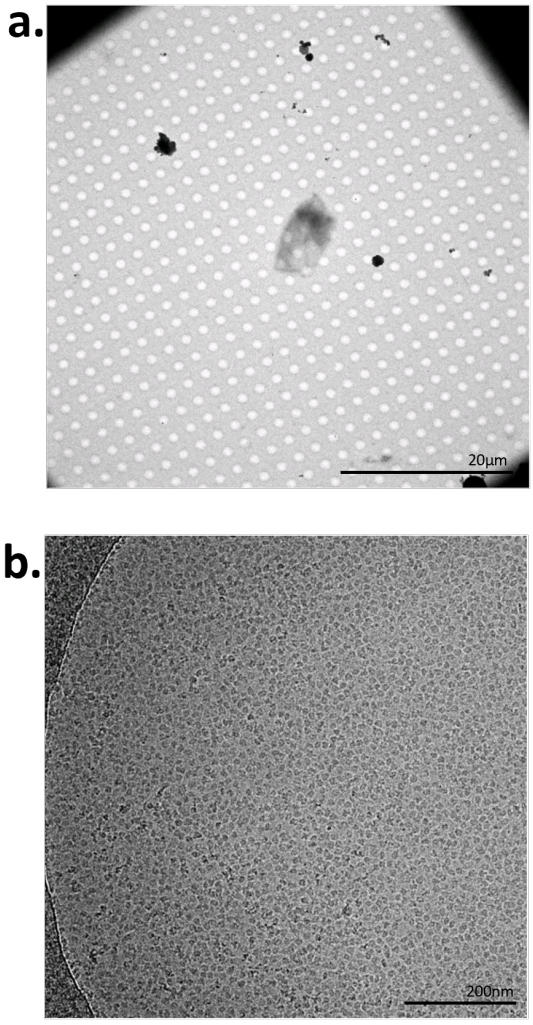

Figure 3.2: Screening images of *a.* example grid square and *b.* single hole of an optimised *Pa*MprF cryo-EM grid. The optimised *Pa*MprF grid was prepared with 2.5 s blotting time and 1 mg/mL sample concentration.

Panel **a.** in **Figure 3.2** shows the thin ice in grid square holes following optimisation. Panel **b.** shows a zoomed view of one of these holes. Particles are densely packed and therefore suitable for data collection, as many particles will be present in each image collected. These optimised grids were used to collect an initial small-scale dataset for sample characterisation prior to large-scale collection for higher resolution.

3.2.2. *Pa*MprF is purified as a monomer

The small-scale dataset collected at 1.55 Å/pixel was processed following the workflow outlined in **Methods (2.9.3.)**. 2D classes from these data are shown in **Figure 3.3** below:

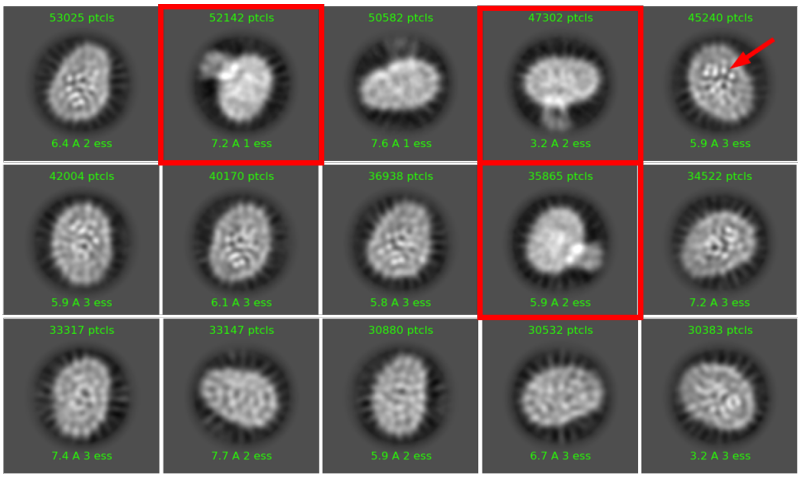

Figure 3.3: 2D classes of *Pa*MprF small-scale dataset. Best 2D classes of ~1.3 million particles (20 iterations, 130 Å circular mask diameter). The number of particles and resolution of each class is shown. Side view classes are highlighted with red boxes. An arrow points at visible secondary structure elements in a top view.

The 2D classes in **Figure 3.3** show the presence of top views of *Pa*MprF-SapNPs, as well as side views where the soluble domain is clearly visible. In addition, secondary structural elements can be seen in some of the higher definition top views. The a*b initio* reconstruction from the best classes (~400k particles) is shown in **Figure 3.4:**

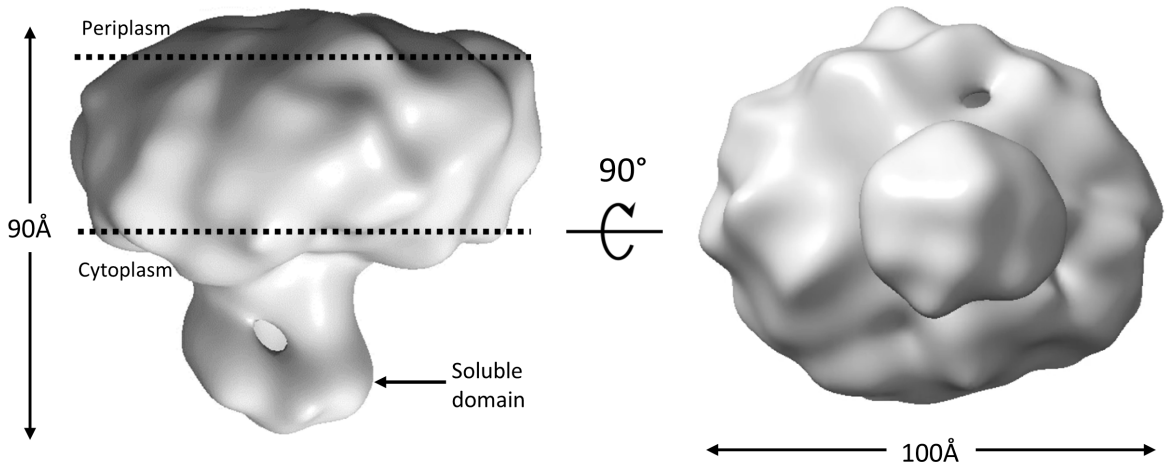

Figure 3.4: *ab initio Pa*MprF reconstruction. Density model for *Pa*MprF *ab initio* reconstruction. Membrane borders are marked with dotted lines.

The low-resolution reconstruction shown in **Figure 3.4** is a disc of 100 Å diameter with an additional globular structure on one side of the disc, corresponding to the soluble domain of *Pa*MprF. Consistently, the size of the soluble domain density in the model aligns well to a single molecule of the previously determined crystal structure of the *Pa*MprF soluble domain (PDB:4v35; (Hebecker *et al.* 2015)). This indicates that *Pa*MprF has been purified as a monomer, compared to the published *Rt*MprF structure which is dimeric (Song *et al.* 2021). Grids of this sample were used to collect a higher resolution dataset for further structural characterisation.

3.2.3. *Pa*MprF adopts a novel conformation

High-resolution data collected at 0.723 Å/pixel was processed as outlined in **Methods (2.9.3.)**. 2D classes from these data are shown in **Figure 3.5:**

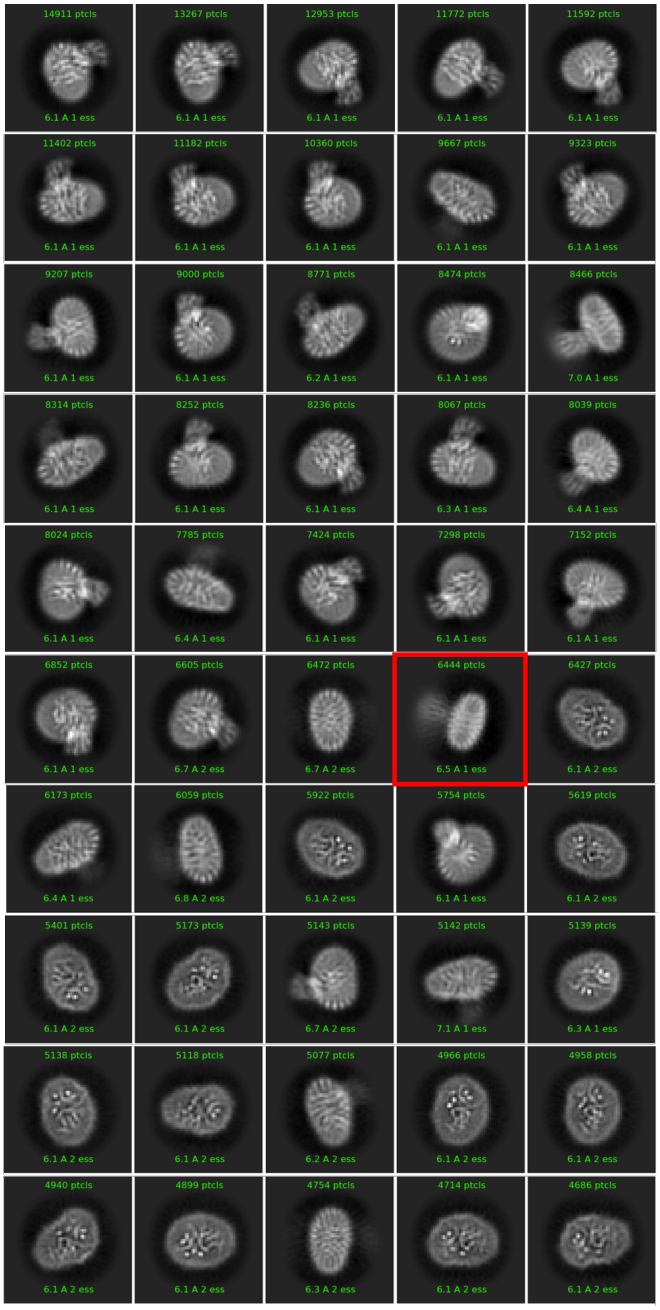

Figure 3.5: *Pa*MprF 2D classification from large-scale dataset. The best 50 2D classes of ~700k *Pa*MprF particles are shown, along with the number of particles and resolution per class. A class depicting a side view with a poorly resolved soluble domain is highlighted in red.

Clear secondary structure elements are present in most classes, but the majority of particles appear to be preferentially oriented, with a clear bias in the data towards top and oblique views with very low representation of side views. Of the few side view classes present (one representative class highlighted in red), there is a lack of clearly defined soluble domain density, indicating that there may be some degree of flexibility in this domain that is hindering

a consistent particle alignment. In addition, there appears to be some heterogeneity in SapNP size/shape that may have a similar effect. Taken together, these factors limit the obtainable resolution of the resulting structural model of *Pa*MprF.

Nevertheless, the best classes were used for *ab initio* reconstruction followed by non-uniform refinement with all particles to give a map with 4 Å resolution. All maps confirmed that *Pa*MprF had been purified as a monomer, compared to the published *R. tropici* structure which is a dimer (Song *et al.* 2021). This 4 Å map is shown in **Figure 3.6** aligned to one chain of *Rt*MprF:

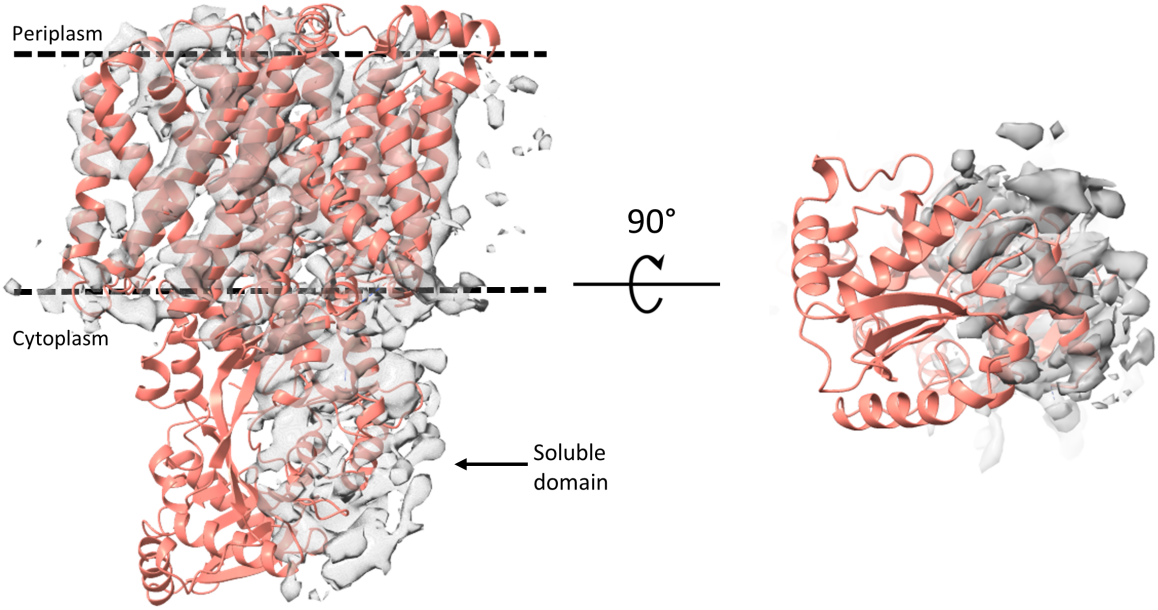

Figure 3.6: *Pa*MprF cryo-EM map at 4 Å resolution. The map of *Pa*MprF (grey) was fitted to one monomer of the published dimeric *Rt*MprF structure (PDB 7DUW; pink). Membrane borders are marked with dotted lines. Top view (*right*) from the cytosolic side is clipped to only show the soluble domain.

The transmembrane region of *Pa*MprF aligns well to the *R.tropici* structure, but the soluble domain is shifted significantly in this alignment by up to ~15 Å. This different conformation may represent a different state of the MprF catalytic cycle, but a higher resolution structure is required to confirm this.

3.3. Generation of sybody binders

In light of the issues with the previously collected data, it is clear that sample preparation must be further optimised to obtain a high-resolution structure of *Pa*MprF. The main barriers to this appear to be the small particle size, and the preferential orientation of particles. As a strategy to improve the sample, a 1-month research stay at Markus Seeger's group (University of Zurich, Switzerland) was carried out, with the aim to generate synthetic nanobody (sybody) binders for *Pa*MprF that would increase particle size and disrupt the preferential orientation of particles. Since previous cryo-EM data suggested that the soluble domain of *Pa*MprF is flexible, the focus was on obtaining binders specifically to the less mobile transmembrane region of the protein. The platform for sybody selection requires the biotinylation of the target protein via an AviTag™ for immobilisation on streptavidin/neutravidin coated surfaces (see **Appendix 3** for details). Purification of a transmembrane region (TM) construct of *Pa*MprF (residues 1-545, *Pa*MprF^{545}) fused to an AviTag™ was attempted for subsequent rounds of selection in the sybody platform, but the construct expressed poorly and appeared unstable after SEC (see **Methods – 2.4.7.**), resulting in insufficient quantities of the construct for sybody selections. Therefore, this TM construct was instead used in pull-down assays following the sybody selections to assess which of the selected sybodies bound to the transmembrane region of *Pa*MprF.

Sybodies were selected against biotinylated full-length *Pa*MprF following the protocol detailed by Zimmerman *et al.* (2020). A summary of the results specific to *Pa*MprF selections is outlined below.

3.3.1. Outline of sybody selection pipeline

The selection platform utilises a set of three single-domain sybody libraries which contain three complementarity determining regions (CDRs) and vary based on the length of CDR3 (Zimmermann *et al.* 2018). This produces three distinct binding modes for which the libraries are named: Concave, Loop, and Convex. Example structures of these sybody libraries are shown in **Figure 3.7**:

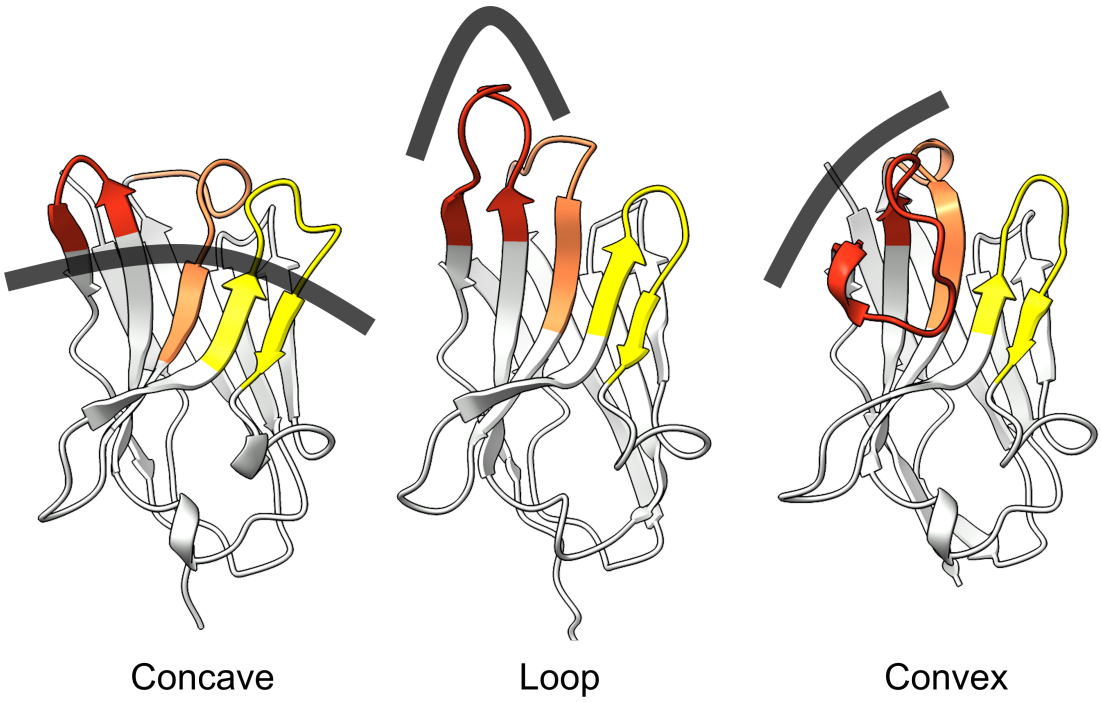

Figure 3.7: Structural basis of sybody binding: Depictions of the three sybody library types: concave (PDB:3K1K; (Kirchhofer *et al.* 2010)), loop (PDB:3P0G; (Rasmussen *et al.* 2011)), and convex (PDB:1ZVH; (De Genst *et al.* 2006)). CDR1 = orange, CDR2 = yellow, CDR3 = red. The binding mode of each library is indicated with a black line.

The use of three libraries with differently shaped binding surfaces increases the diversity of available epitopes that can be targeted, increasing the likelihood that binders can be produced for difficult membrane protein targets.

The sybody selection pipeline uses three rounds of selection (**Figure 3.8**). The first round utilises ribosome display: mRNA sequences for each sybody binder in the library are used as an input, all containing a stem loop at the 3' end of each transcript. Translation of these

transcripts by ribosomes produces the corresponding sybody but the 3' stem loop stalls translation, so the ribosome, mRNA and nascent sybody remain in complex. Therefore, sybodies which are pulled down with the target protein are also pulled down with their corresponding mRNA, which can then be reverse transcribed to form a cDNA library for the next round of selection. The second and third rounds of selection utilise phage display: previously enriched sybody sequences are transformed into a phagemid vector and phages are produced that each present a single unique sybody at their surface. Sybodies that are pulled down with the target protein are then separated from the phage body by trypsin digestion to isolate the phagemids containing the enriched sybody sequences.

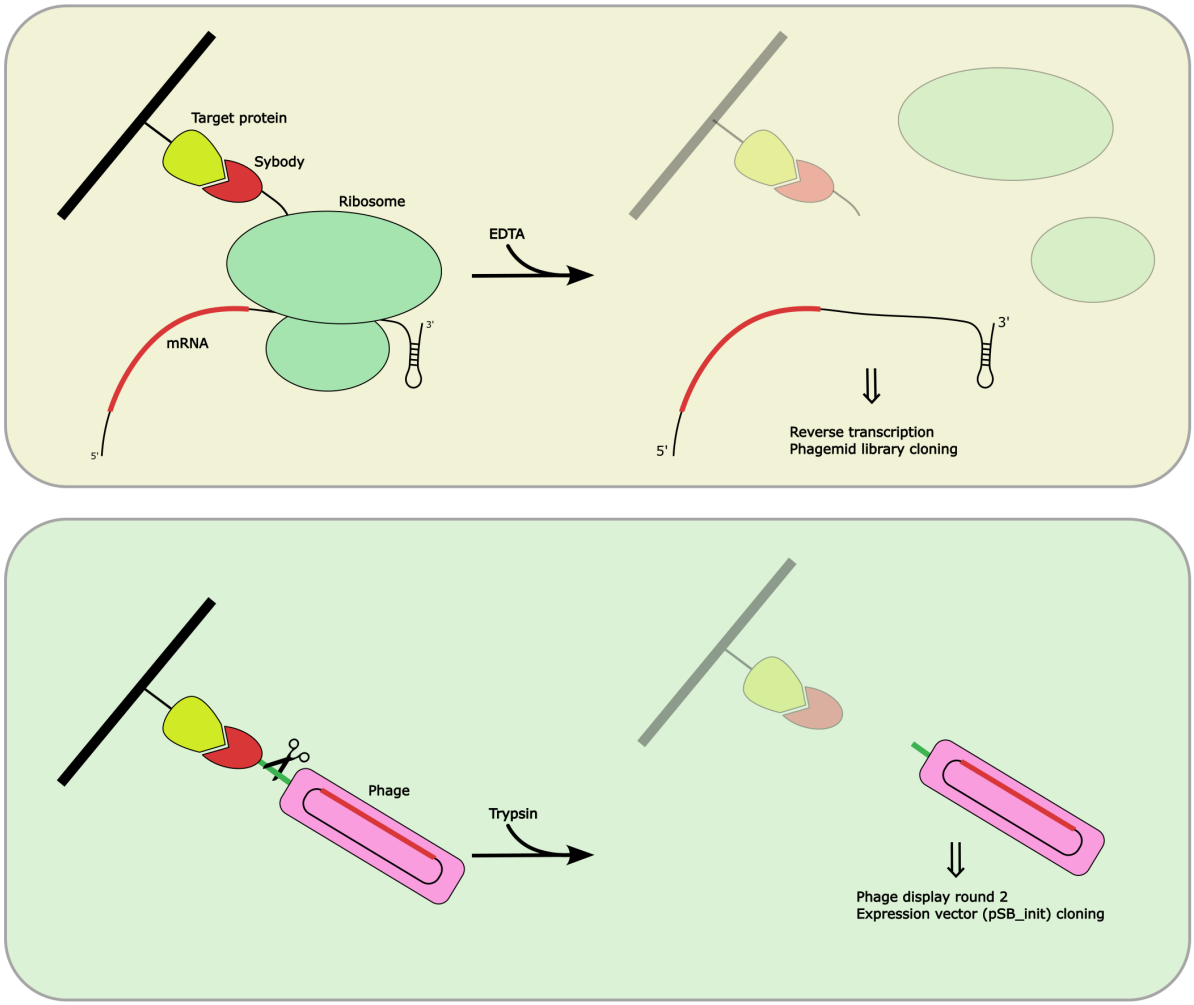

Figure 3.8: Sybody selection pipeline. Schematic outlining the principle behind the sybody selection pipeline, starting with the first round of ribosome display (*top*), followed by two rounds of phage display (*bottom*).

3.3.2. Ribosome display

In ribosome display, selection is performed via "solution panning". In this technique, each mRNA library is separately mixed with ribosome complexes and the biotinylated target protein of interest to allow target-sybody complex formation. The solution is then incubated with streptavidin beads to immobilise the target protein, washed to remove non-specifically bound ribosome complexes, and the mRNA eluted by dissociation of ribosomes with EDTA. The eluted mRNA is converted to a cDNA library by the addition of reverse transcriptase, and then analysed by qPCR to assess the amount and the degree of degradation of the enriched mRNA. Enrichment is determined using primers that target the 5' region of the cDNA library to quantify the number of transcripts that were pulled down against the target protein. For the first round of selection, 10^6-10^7 different sequences are expected in the resulting cDNA library. The degree of mRNA degradation is determined using qPCR primers that target the 3' region of the cDNA library. The ratio of 3' reads to 5' reads then gives a degree of mRNA degradation. As mRNA degradation occurs from the 5' end, a ratio of 5':3' of ~1 indicates there is no significant degradation of mRNA. The results of the qPCR from the ribosome display round of *Pa*MprF selection is shown below in **Table 3.1:**

Table 3.1: qPCR results of ribosome display. qPCR quantified amounts of mRNA enriched from the first round of sybody selection against *Pa*MprF.

Library	5' total RNA sequences	3' total RNA sequences	5':3' RNA ratio
Concave	3.25×10^6	1.66×10^6	1.95
Loop	3.24×10^6	1.33×10^6	2.43
Convex	4.16×10^6	2.62×10^6	1.58

The total RNA recovered from the first round of selection against *Pa*MprF was ~10^6 sequences, with no significant degradation of transcripts. This indicates the first round of selection was successful. The cDNA library was then cloned into a phagemid library for the second round of selection.

3.3.3. Phage display

For the first round of phage display, the immobilisation surface is changed to neutravidin-coated 96-well plates. In addition, a negative control biotinylated protein (AcrB in this instance) is used to assess the level of non-specific binding within the pool of selected sybodies. Using a membrane protein as the negative control accounts for non-specific binding to the detergent micelle present around the target protein. A phage library is produced from transformation of phagemids into SS320 *E. coli*, resulting in the sybodies selected from ribosome display being presented at the surface of phages on a PIII coat protein. A trypsin-sensitive sequence is present between two domains of the PIII coat protein, so that the presented sybody can be cleaved from the phage body. Selection then occurs in a similar manner to ribosome display via solution panning, with the biotinylated protein being incubated with the phage library solution before being applied to the neutravidin-coated plate for immobilisation. Plates are washed to remove non-specific binders and then eluted by addition of trypsin which cleaves the linker between the immobilised sybody and the phage. The plasmids in each phage encoding the sequences of the enriched sybodies can then be analysed by qPCR.

In this round of qPCR, the DNA enriched from binding to the target protein and to the negative control protein are both analysed. The ratio of target DNA to negative control DNA gives an enrichment factor which quantifies the specificity of binders to the target protein. For the first round of phage display, it is common for the enrichment factors for difficult membrane protein targets to be <1. However, for selections to be successful these values must be at least >2 following the second round of phage display. For *Pa*MprF, the enrichment factors for the three sybody libraries after the first round were 1.2, 1.4, and 0.7 for concave, loop, and convex libraries, respectively (**Table 3.2**).

The eluted phages from the first selection are then used to re-infect SS320 *E. coli* to produce a new phage library for the second round of phage display. In this final round of selection, the immobilisation surface is once again changed to streptavidin beads. Again, the negative control biotinylated protein AcrB is used for the calculation of enrichment factors following selection, and the biotinylated protein and phage library solution are incubated together before being immobilised onto the streptavidin beads and washed to remove non-specific binders. However, in this final round of selection, an additional washing step is performed using an excess of *unbiotinylated* target protein (5 μM unbiotinylated compared to 50 nM biotinylated). The purpose of this washing step is to select for sybody binders that have slow off-rates of binding, as these binders will be less likely to dissociate from the immobilised biotinylated target to bind to the unbiotinylated target protein present in the wash buffer. As such, this step leads to the enrichment of sybody binders that have higher affinities for the target protein.

Following this off-rate selection, the phages are eluted as before and analysed by qPCR. The qPCR results from the *Pa*MprF sybody selections along with enrichment factors demonstrating successful selection following the second round of phage display are shown in **Table 3.2:**

Table 3.2: qPCR results of phage display. qPCR quantified amounts of DNA enriched from the first and second rounds of phage display for *Pa*MprF sybody selections.

Library	**Phage display round 1**			**Phage display round 2**		
	***Pa*MprF enriched DNA copy number**	**AcrB enriched DNA copy number**	**Enrichment factor**	***Pa*MprF enriched DNA copy number**	**AcrB enriched DNA copy number**	**Enrichment factor**
Concave	6.22×10^2	5.09×10^2	1.2	3.53×10^5	9.52×10^3	37.0
Loop	1.18×10^3	8.35×10^2	1.4	2.15×10^6	2.01×10^5	10.7
Convex	1.08×10^3	1.46×10^3	0.7	2.85×10^4	2.34×10^3	12.1

After the second round of phage display, enrichment factors were 37.0, 10.7 and 12.1 for the concave, loop and convex libraries, respectively, demonstrating a successful enrichment compared to the negative control. The sybody sequences present in the enriched phagemid library were subcloned into an expression vector and transformed into MC1061 *E. coli*. 95

colonies from each sybody library were selected for expression of sybodies in the periplasm of 1 mL *E. coli* cultures. Periplasmic fractions of these cultures were then used for an Enzyme Linked Immunosorbent Assay (ELISA) to identify specific binders for the target protein.

3.3.4. Assessment of sybody binders by ELISA

To confirm that the selected sybodies bind specifically and with high affinity to *Pa*MprF, an ELISA assay is carried out using the periplasmic extract of the selected clones. A schematic of the assay is shown in **Figure 3.9:**

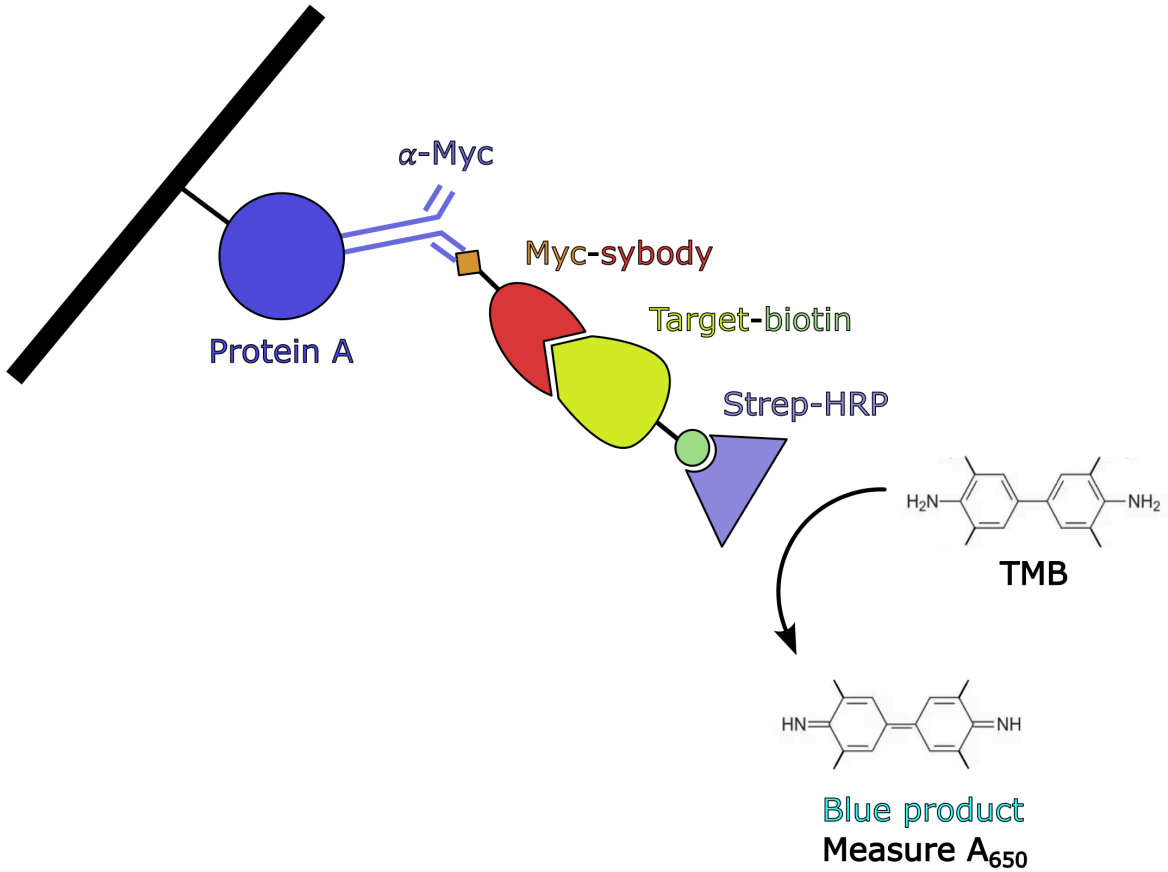

Figure 3.9: ELISA sybody screening schematic.

This ELISA takes place in 96-well immunoplates coated with protein A, which binds to the F_C region of a monoclonal anti-c-Myc antibody. Each periplasmic extract, representing a single Myc-tagged sybody, is added to two wells of the plate so that the Myc-antibody binds to the

Myc tag. Then, biotinylated target protein is added to one well, and biotinylated AcrB as a negative control to the other. After washing, a streptavidin-conjugated Horse Radish Peroxidase (HRP) is added to bind to the biotin tag on the membrane protein, and the amount of bound HRP determined by a chromogenic reaction with 3,3′,5,5′-Tetramethylbenzidine (TMB) which produces a blue compound that absorbs at 650 nm. Therefore, in this assay an ELISA signal is obtained for each expressed sybody that demonstrates its ability to bind to both the target protein and AcrB. The signals for each sybody are then compared to identify target protein specific sybody binders that would be suitable to be taken forward to small-scale purification and characterisation.

Only sybodies that display an increased ELISA signal for binding the target protein above the background level of AcrB (at least 1.5x) are classified as hits. In addition, it is important to select sybodies that exhibit a range of ELISA signals, and not simply select those that give the greatest absorbance at 650 nm. This is because different signals may indicate different binding modes of the sybodies, and therefore increase the diversity of the binders chosen for purification, and also because variations in signal may be due to different expression levels of the sybodies. Bar charts showing the ELISA signals of *Pa*MprF sybodies selected for purification are given in **Figure 3.10:**

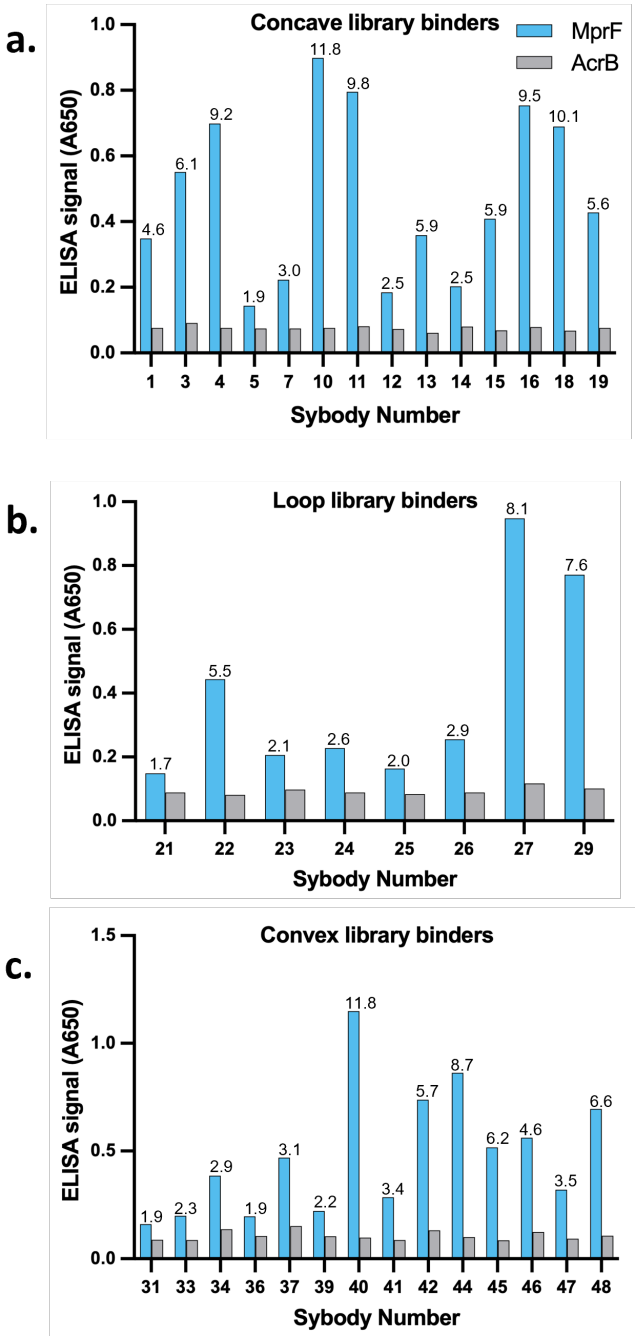

Figure 3.10: ELISA results for *Pa*MprF sybodies. Bar charts showing the ELISA signal against *Pa*MprF (blue bars) and against AcrB (grey bars) for sybodies from each library (**a.** Concave, **b.** Loop, **c.** Convex) that were selected for small-scale purification. Ratios of *Pa*MprF:AcrB ELISA signal are given above each bar.

Each of the selected hits was sequenced to identify any duplicate sybodies. The unique sybodies (32 in total; 14 from the concave library, 8 from the loop library, and 10 from the convex library) were then expressed in MC1061 for small-scale purification.

3.3.5. Purification of selected sybodies

Selected sybodies were expressed in 50 mL *E. coli* cultures for medium-scale purification via IMAC. Eluates from IMAC containing the sybodies were analysed by SEC on a Sepax SRT-10C SEC100 column to assess if each sybody binder is suitable for large-scale expression. Sybodies with extensive column interactions give broad peaks that elute >13 mL; these are unsuitable to use with other SEC columns so are discarded. Sybodies that elute at <11 mL oligomerise and are also discarded. Example chromatograms from the *Pa*MprF sybody binders are shown in **Figure 3.11** below:

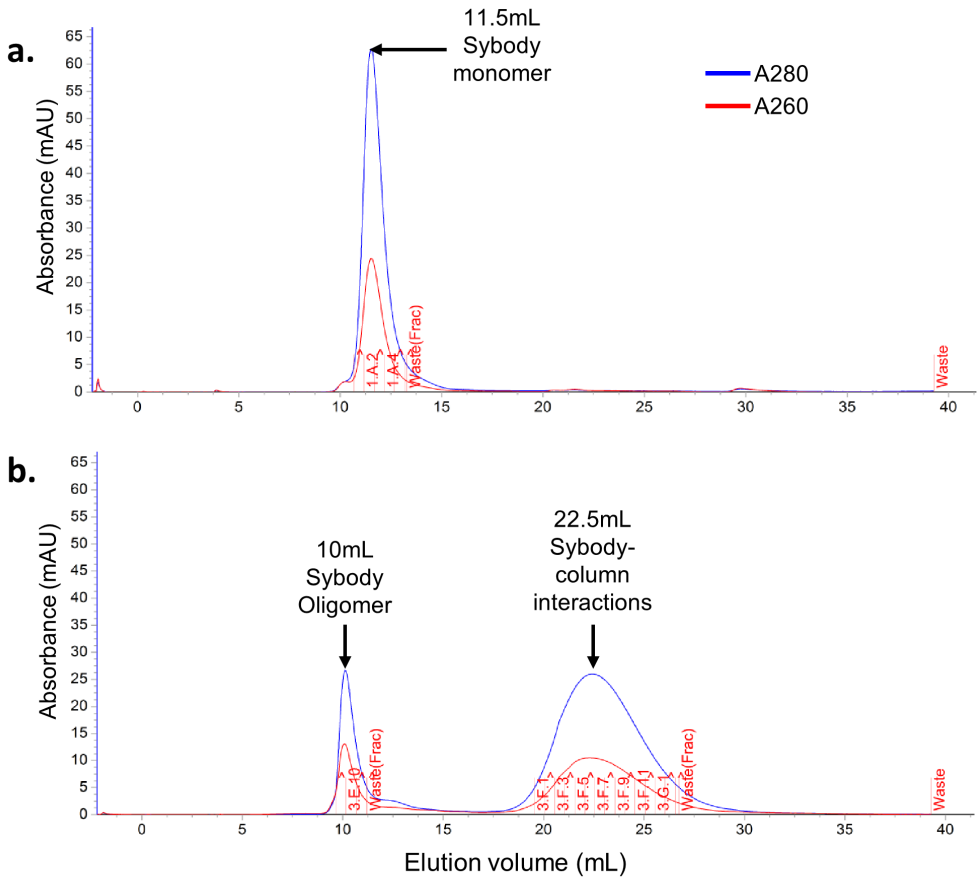

Figure 3.11: Example sybody SEC chromatograms. SEC traces of sybody binders that were **a.** taken forward and **b.** discarded following small-scale purification.

The sybody in **Figure 3.11a** runs as a narrow peak with elution volume ~11.5 mL, and was taken forward. The sybody in **Figure 3.11b** elutes from the column at ~22.5 mL in a broad peak, indicating extensive column interactions and was discarded.

Following small-scale purification, only one sybody was discarded, leaving 31 unique *Pa*MprF binders (14 from the concave library, 8 from the loop library, and 9 from the convex library) that were suitable to take forward for binding site characterisation. The full alignment of all sybody sequences, as well as a phylogenetic tree indicating the clustering of similar sybody sequences is given in **Appendix 4.**

3.3.6. Sybody selection yielded two unique TM binders

Following purification, the selected sybodies were analysed to identify possible *Pa*MprF TM region binders for cryo-EM studies. To assess binding mode, a pulldown assay was performed using the purified TM construct *Pa*MprF^{545}, where His-tagged sybodies were immobilised on nickel affinity resin and incubated with untagged *Pa*MprF^{545}. Results of this pulldown assay are shown in **Figure 3.12a.** Intensities of each band were analysed in ImageJ and are plotted in **Figure 3.12b.**

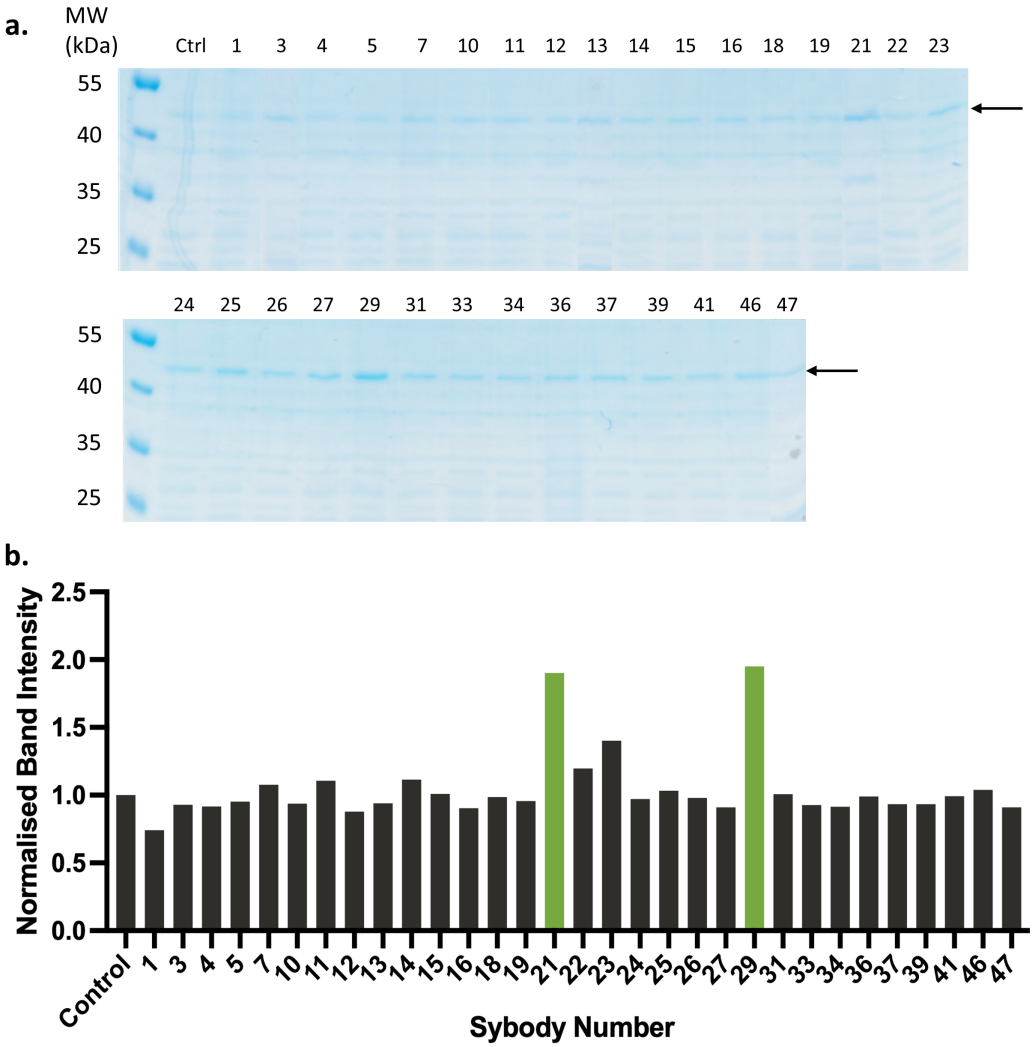

Figure 3.12: Sybody pulldown results. a. SDS-PAGE gels (12%, Coomassie stain) for sybody pulldown experiments. A control lane (Ctrl) was run where no sybody binder was applied to affinity resin before *Pa*MprF^{545} incubation. The band corresponding to *Pa*MprF^{545} is highlighted with a black arrow. **b.** Bar chart of *Pa*MprF^{545} band intensities from the pulldown assay, relative to the intensity in the control lane. Lanes at >1.5x control intensity are coloured green.

The pulldown experiment shows that even in the control lane, there is a small fraction of *Pa*MprF^{545} which binds non-specifically to affinity resin. Nevertheless, **Figure 3.12b** shows that there were two sybody samples that gave a nearly two-fold enrichment of *Pa*MprF^{545} binding compared to the control: sybodies 21 and 29. This suggests that these two binders recognise an epitope on the *Pa*MprF TM region.

Sybodies 21 and 29 are both from the loop library, which typically utilise a binding loop at CDR3 of the sybody scaffold (residues 112-120 in the full alignment). An alignment of CDR3 from all the selected loop library binders (sybody numbers 21-29) is shown in **Figure 3.13:**

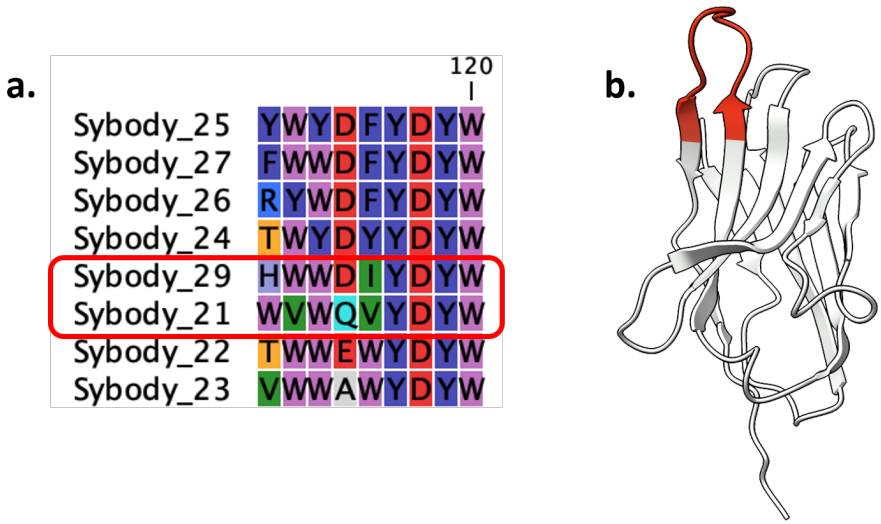

Figure 3.13: Alignment of CDR 3 regions for all *Pa*MprF Loop library binders. a. Alignment of loop library sybody binders, generated with CLC sequence viewer (QIAgen). Residues are coloured based on Rasmol colour scheme (polar = bright colours, non-polar = darker colours). The sequences of the TM-specific sybodies 21 and 29 are highlighted in red. **b.** General structure of the Loop library sybodies (PDB:3P0G; (Rasmussen *et al.* 2011)) with CDR 3 coloured red.

Inspection of this CDR alignment shows that of all the loop library binders, only 21 and 29 share both a pair of tryptophan residues at positions 112-114 and a hydrophobic amino acid at position 116 in the centre of CDR 3. The similarity between these sequences suggests that sybodies 21 and 29 may bind at the same or a similar epitope in *Pa*MprF, and the presence of a hydrophobic binding region supports the finding from the pulldown that these two sybodies likely bind to the TM region of *Pa*MprF. Accordingly, these binders were taken forward for structural studies in complex with *Pa*MprF.

3.4. Cryo-EM studies of *Pa*MprF-Sybody complexes

Structural characterisation of a *Pa*MprF-Sybody complex was focused on sybodies 21 and 29, and the better expressing of the two - Sybody29 - was selected and trialed in initial cryo-EM experiments to determine whether it could improve sample behaviour for high-resolution structural characterisation.

3.4.1. Optimisation of *Pa*MprF-Sybody29 complex grid preparation

For *Pa*MprF-Sybody29 complex cryo-EM grids, *Pa*MprF SapNPs were produced as described in **section 3.2.1.** The peak fraction corresponding to *Pa*MprF-SapNPs following SEC was concentrated to 0.77 mg/mL. This was then mixed with a 1.2-fold molar excess of purified Sybody29, incubated on ice for 15 minutes, spun at 100,000 g for 30 minutes to remove aggregate, and then used for grid preparation. Optimisation of grid preparation found that longer blot times of 6 seconds on 300 mesh holey carbon grids gave sufficiently thin ice for the collection of a small-scale dataset to further characterise the sample. An example of such a grid is shown in **Figure 3.14:**

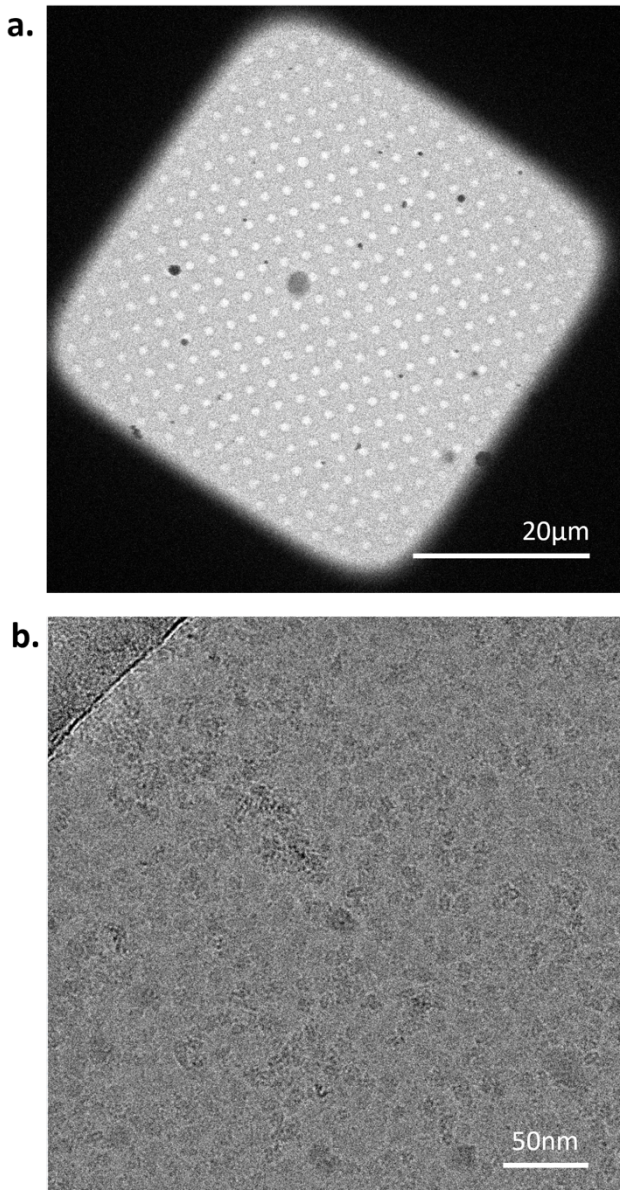

Figure 3.14: Screening images of *a.* example grid square and *b.* single hole of optimised *Pa*MprF-Sybody29 cryo-EM grid. Optimised *Pa*MprF-Sybody29 complex grid with 6 s blotting time and 0.77 mg/mL sample concentration.

3.4.2. Sybody29 binding significantly improves *Pa*MprF-SapNP sample for Cryo-EM

The small-scale dataset at 1.2 Å/pixel for the *Pa*MprF-SapNPs bound to Sybody29 were processed as outlined in **Methods (2.9.5.).** 2D classes from these data are shown in **Figure 3.15:**

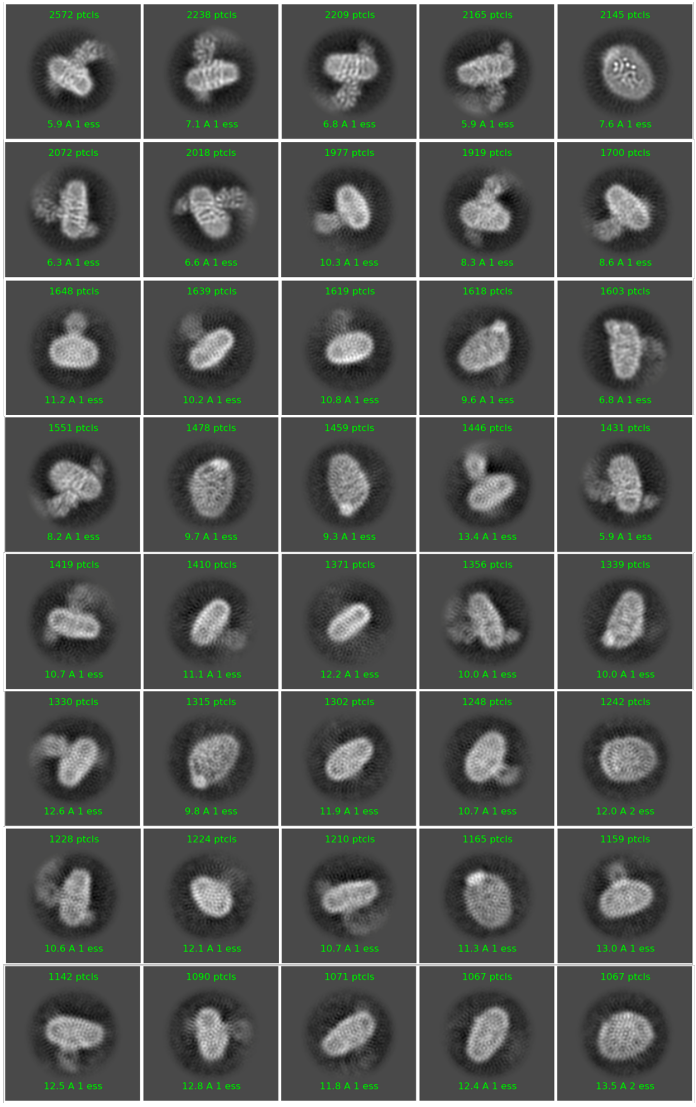

Figure 3.15: *Pa*MprF-Sybody29 2D classification. The best 40 2D classes of ~100k *Pa*MprF-Sybody29 complex particles (40 iterations, 240 Å box size, 130 Å circular mask diameter). Particles per set and class resolution are given for each class.

As can be seen from these classes, the addition of Sybody29 has resulted in a more varied set of side views of particles compared to the previous sample of *Pa*MprF alone, suggesting that the sybody is disrupting the previously observed preferential orientation. Indeed, the sybody can be seen in the above classes to be binding on the opposite face of the soluble domain of *Pa*MprF, which may be the reason for this disruption of orientational bias. In addition, the soluble domain can be clearly resolved in side view classes, which may be due to the presence of an additional recognisable feature from the sybody binding increasing the overall particle size and improving the alignment of particles.

Due to the encouraging 2D classes, an *ab initio* reconstruction was performed followed by non-uniform (NU) refinement with the best ~50,000 particles. The model from this refinement (at 6.1 Å resolution, calculated by gold-standard Fourier shell correlation (GSFSC) after auto-tightening) is shown in **Figure 3.16:**

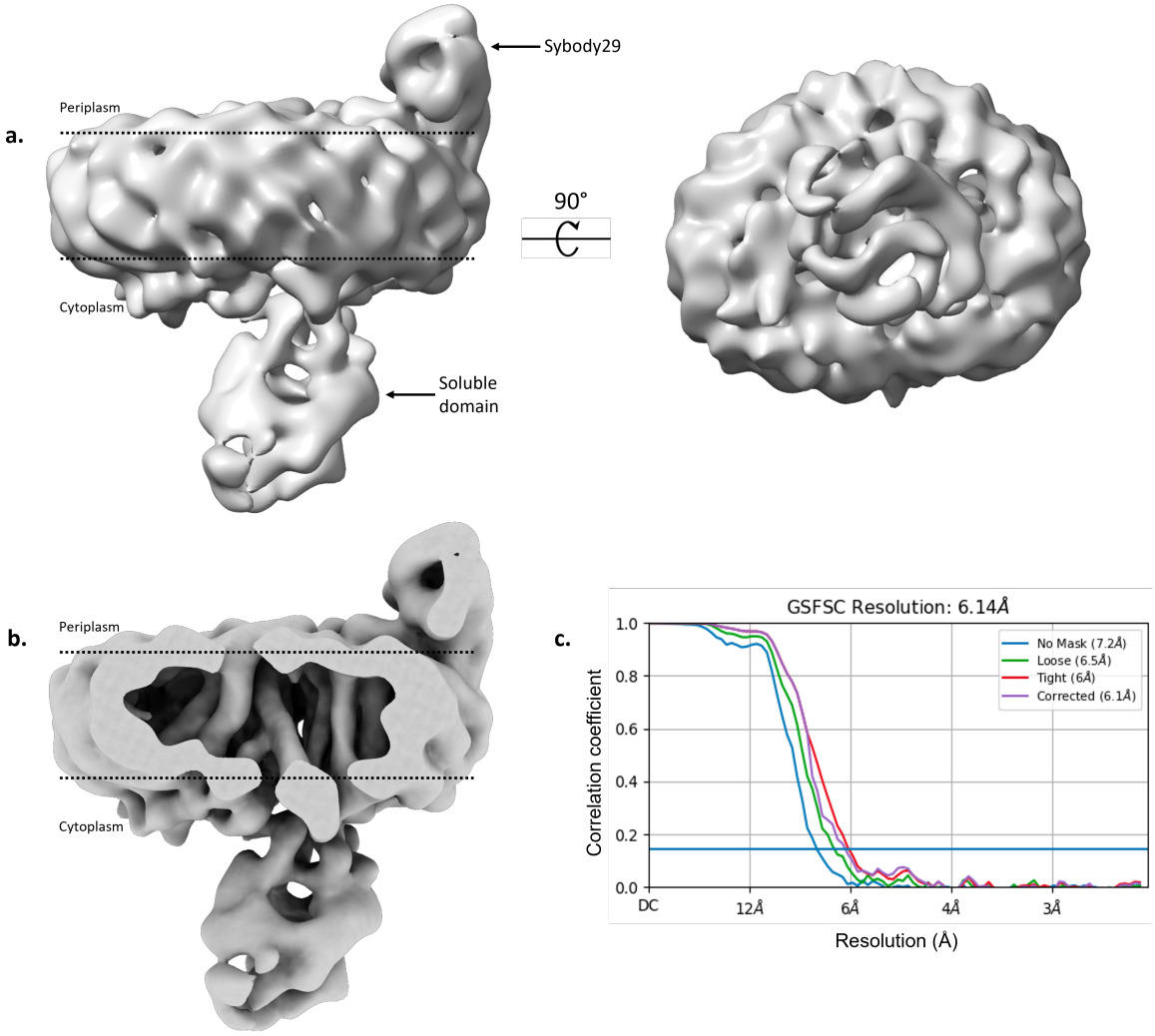

Figure 3.16: *Pa*MprF-Sybody29 model: a. NU-refinement model of *Pa*MprF-Sybody29 SapNPs showing side and top views. Membrane borders are marked with dotted lines. **b.** Side view of model clipping through the SapNP, showing well-resolved TM helices of *Pa*MprF. **c.** GSFSC plot for the model.

This model exhibits the same dimensions as that of the previous small-scale dataset of *Pa*MprF alone, except the sybody can be seen clearly binding on the periplasmic face of *Pa*MprF. In addition, a clipped view through the core of the particle shows the presence of well-defined TM α-helices (**Figure 3.16b**), showing that much higher resolution has been achieved in the

small-scale collection, and that the use of the sybody binder has ameliorated many of the problems with the previous sample that were hindering high-resolution characterisation.

In light of this, this sample was used to collect a high-resolution dataset for structural characterisation of the *Pa*MprF-Sybody29 SapNP complex.

3.4.3. High-resolution characterisation of *Pa*MprF-Sybody29 complex to 3.28 Å

A high-resolution dataset at 0.83 Å/pixel of *Pa*MprF-Sybody29 SapNPs was collected as outlined in **Methods (2.9.4.)**. The data were processed following the flowchart in **Figure 3.17.** Briefly, following removal of poor particles by initial 2D classification, heterogeneous refinement using three starting models led to around 30 % of particles being sorted into the third, poorly defined class. The particles comprising this class were discarded. The two remaining classes resembling the previously obtained low resolution *Pa*MprF-Sybody29 SapNP complex were then taken forward for a round of 3D classification. One class from this classification gave a map with a significantly better defined sybody, so this particle set (comprising 111k particles) was taken forwards to a further round of non-uniform refinement. Post-processing of this output using a map sharpening *B*-factor of -85 Å gave the map that was used to build a model of *Pa*MprF-Sybody29 SapNP.

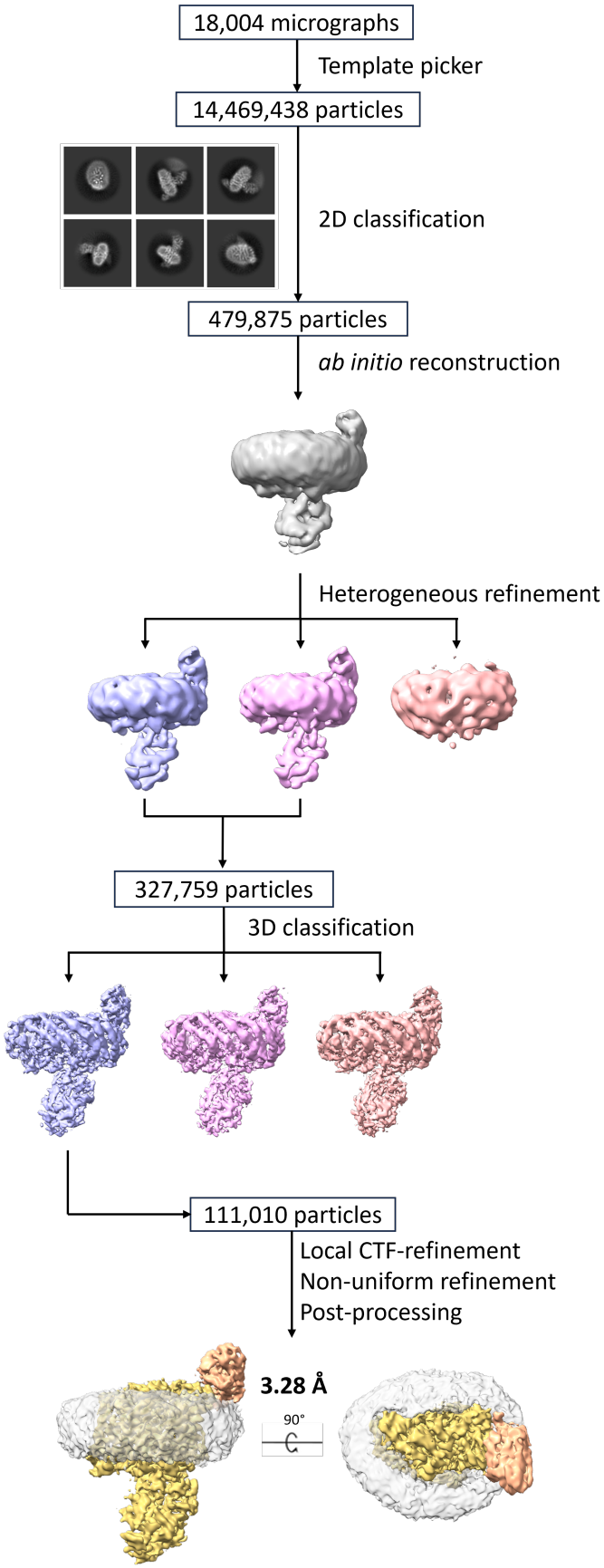

Figure 3.17: *Pa*MprF-Sybody29 complex processing flowchart. Flowchart outlining the steps involved in processing the high-resolution cryo-EM dataset to the final cryo-EM map at 3.28 Å GSFSC (*Pa*MprF = yellow, Sybody29 = orange, SapNP = transparent)

The final cryo-EM map, coloured according to local resolution, is shown in **Figure 3.18,** along with the FSC curves for the final non-uniform refinement that produced the map:

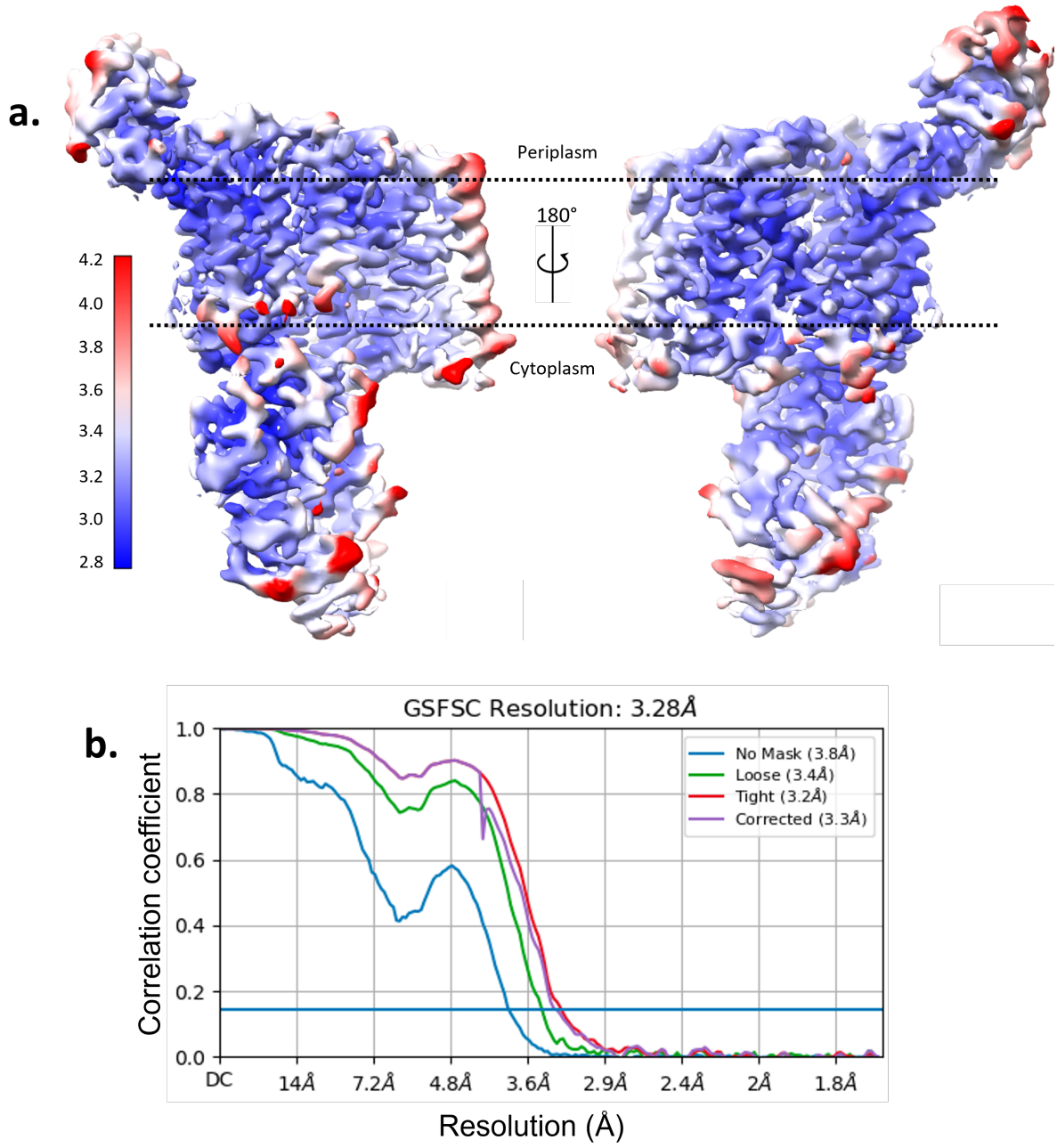

Figure 3.18: *Pa*MprF-Sybody complex resolution information. a. The final cryo-EM map of *Pa*MprF-Sybody29 coloured according to local resolution in Å. For clarity, the SapNP surrounding *Pa*MprF has been removed. **b.** Gold-standard FSC curves from the final non-uniform refinement job in CryoSPARC using different masks. At FSC = 0.143, the resolution was determined to be 3.28 Å.

3.5. Structural analysis of *Pa*MprF

The obtained high-resolution cryo-EM map allowed for a model of the *Pa*MprF-Sybody29 complex to be built. The statistics from model-building, as well as the details of cryo-EM collection and processing are given in **Table 3.3** below:

Table 3.3: *Pa*MprF-Sybody29 Cryo-EM data collection, reconstruction and model building statistics.

Data collection:	
Magnification	105,000
Voltage (kV)	300
Defocus range (μm)	-0.75 to -2.25
Pixel size (Å)	0.83
Electron dose ($e^-/Å^2$)	42.4
Dose rate ($e^-/Å^2/s$)	7.85
Reconstruction:	
Number of particles	111,010
Symmetry	C1
Resolution at FSC=0.143 (Å)	3.28
Map sharpening *B*-factor (Å)	-85
Model composition:	
Non-hydrogen atoms	6198
Protein residues	807
Rms deviations:	
Bonds (Å)	0.010
Angles (°)	0.670
Molprobity validation:	
Clashscore, all atoms	7.68
Molprobity score	1.26
Poor rotamers (%)	0.14
Ramachandran Plot (% favoured)	95.32
Ramachandran Plot (% allowed)	4.68
Ramachandran Plot (% outliers)	0.00

The remainder of this Chapter is dedicated to discussing this model and its implications on *Pa*MprF activity.

3.5.1. *Pa*MprF architecture

The model of *Pa*MprF-Sybody29, along with a topology diagram, is shown in **Figure 3.19:**

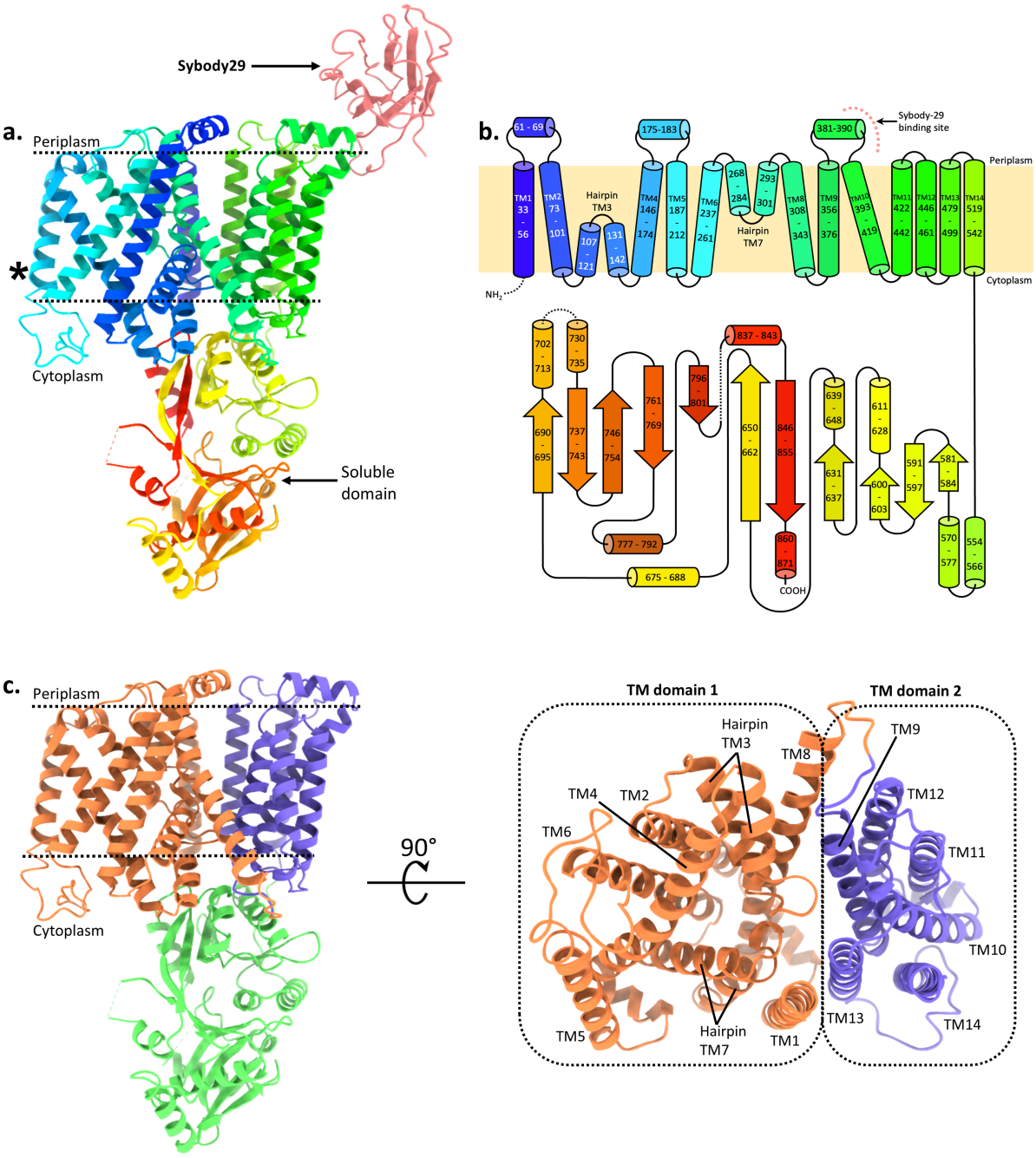

Figure 3.19: *Pa*MprF-Sybody29 complex model. a. Side view of the complex, *Pa*MprF coloured from N- to C-terminus as a rainbow, Sybody29 coloured pink. TM5 is marked with an asterisk. **b.** Topology diagram of *Pa*MprF, with residue numbers on secondary structure elements. Black dotted lines indicate unresolved features in model. **c.** Side (*left*) and top view (*right*-viewing from cytoplasmic face clipped through the soluble domain) of *Pa*MprF (sybody removed for clarity). TM domain 1 = orange, TM domain 2 = purple, soluble domain = green.

The structure of *Pa*MprF is similar to *Rt*MprF, exhibiting the same overall topology at the transmembrane (TM) region as outlined in the **Introduction (1.3.3.)**. The TM region can be separated into two distinct domains (**Figure 3.19c**), with TM domain 1 (TMs 1-8) comprising

the previously characterised "flippase" domain of the protein (Ernst *et al.* 2015), and TM domain 2 (TMs 9-14) the bundle connected to the soluble synthase domain, previously suspected to anchor the synthase domain in proximity to the membrane. Two small regions of the *Pa*MprF structure were not modelled due to their absence in the EM map, both occurring in the soluble domain (loops 715-719, and 806-834), suggesting that these regions were too flexible to be resolved. Each TM helix fitted to the corresponding density in the final cryo-EM map is shown in **Appendix 5.**

The soluble domain of *Pa*MprF reported here is very similar to the previously published crystal structure of the *Pa*MprF soluble domain alone (PDB:4v35; (Hebecker *et al.* 2015)), with an RMSD of 0.627 Å when aligned. This indicates that the *Pa*MprF cryo-EM model soluble domain is not in a conformationally distinct state compared to this crystal structure, with the only significant difference between these structures being the unresolved loop at residues 806-834 in the cryo-EM structure.

From inspection of the local resolution plot (**Figure 3.18a**), the majority of the TM region of *Pa*MprF is well resolved to <3.2 Å. The poorest resolved map section (to ~4 Å) in this region occurs at TM helix 5 (marked with an asterisk in **Figure 3.19a**). Interestingly, in *Rt*MprF this helix makes up part of the dimer interface. As *Pa*MprF is purified as a monomer, the absence of the dimer contact could result in an increased flexibility in TM5, resulting in the poor local resolution observed.

The two hairpin helices (TMs 3 and 7) comprising the suspected lipid binding and transport motif previously discussed in the **Introduction (1.3.3.)** are present and oriented similarly when compared to *Rt*MprF. These hairpin helices and the conserved salt bridge at this location are discussed further in **Section 3.5.5.**

The interaction between *Pa*MprF and Sybody29 occurs at the periplasmic end of TM helix 10 and at an amphipathic helix between TM helices 9 and 10 (**Figure 3.20**).

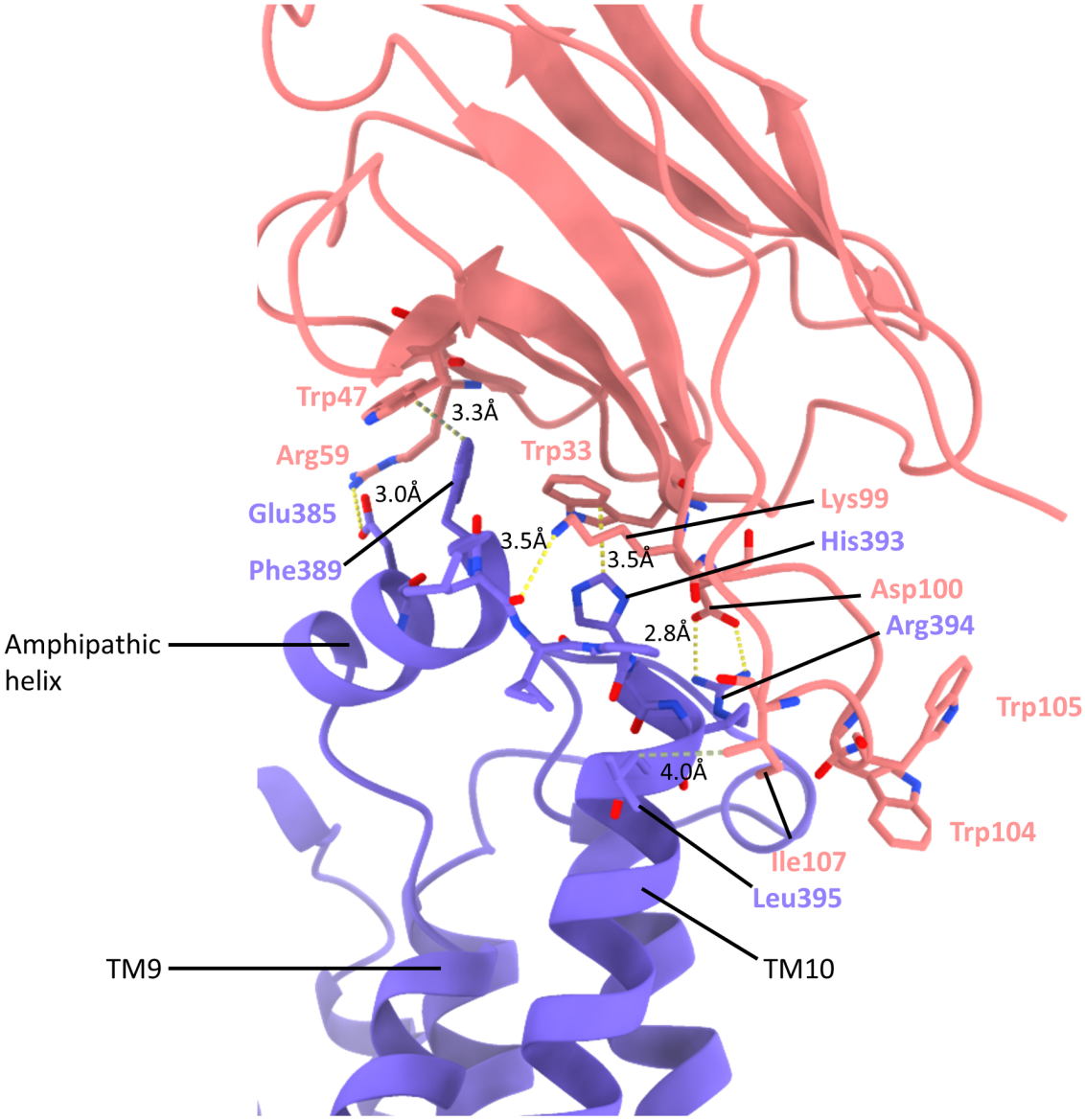

Figure 3.20: *Pa*MprF-Sybody interaction surface. View of interaction surface between *Pa*MprF TM domain 2 (purple) and Sybody29 (pink). Polar interactions are marked with yellow dashed lines, hydrophobic interactions marked with grey dashed lines.

The buried surface area at this interaction face is 614 Å^2, similar to other reported values for sybody-protein complexes (Ahmad *et al.* 2021). A combination of hydrogen bonding and π-stacking/cation-π interactions form the majority of the interface, with one main hydrophobic contact between the hydrophobic residue previously identified in the Sybody29 CDR3 loop

(Ile107, see **Figure 3.13**) and Leu395 on *Pa*MprF TM10. Interestingly, the two tryptophan residues in the sybody CDR3 loop (Trp104 and Trp105) are not directly involved in the binding interface, and instead may stabilise the interaction by positioning at the membrane-solvent interface in a similar manner to tryptophan residues that are often found capping TM helices of membrane proteins (Schiffer *et al.* 1992).

Overall, the *Pa*MprF conformation is very similar to the previously determined low resolution map of *Pa*MprF alone (**Figure 3.21**), indicating that the binding of Sybody29 has not introduced any major conformational changes.

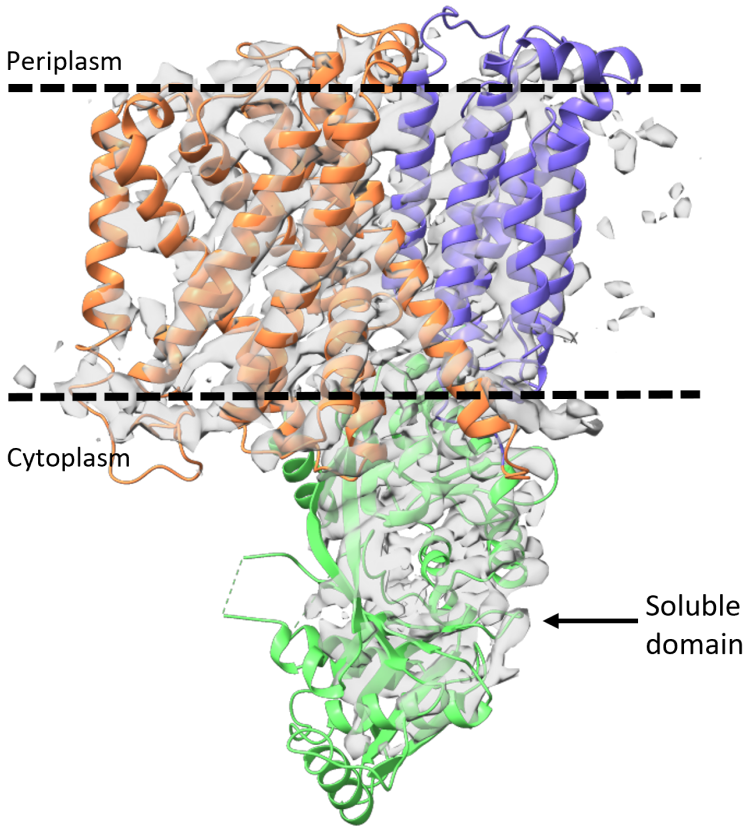

Figure 3.21: *Pa*MprF model aligned to low resolution map in the absence of Sybody29. *Pa*MprF (TM domain 1 = orange, TM domain 2 = purple, soluble domain = green) model fitted into previously obtained low resolution map of uncomplexed *Pa*MprF (**Section 3.2.3.**). The map-model correlation coefficient (CC) for this fit is 0.597**.**

Taken together, alignment of *Pa*MprF and *Rt*MprF structures indicates that global structural topology is unchanged, highlighting the conservation of key structural elements despite the low sequence identity between the two homologues. However, comparison between the two

MprF homologues also highlights that the protein can be divided into three domains that appear to be shifted as rigid bodies relative to each other: (i) the soluble domain, (ii) TM domain 1 comprising TM helices 1-8 and (iii) a TM domain 2 comprising TM helices 9-14. The significant positional shifts of domains between *Rt*MprF and *Pa*MprF are discussed in detail in **sections 3.5.3. and 3.5.4.**

3.5.2. Cryo-EM density indicates *Pa*MprF is bound to multiple lipid molecules

In the final cryo-EM map of *Pa*MprF, there were several features that could not be accounted for by protein and likely represent lipid bound to *Pa*MprF. These lipid binding sites are shown in **Figure 3.22:**

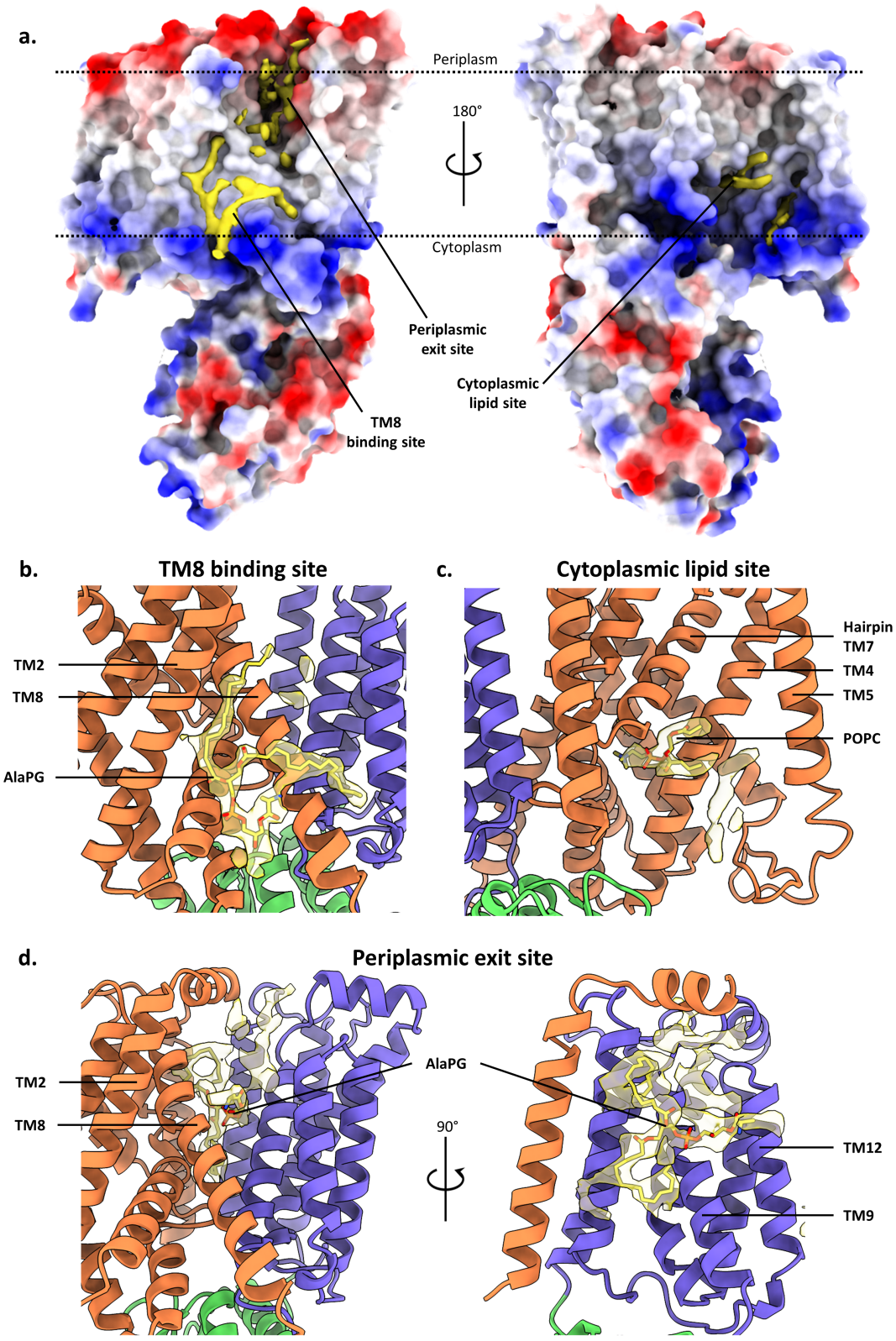

Figure 3.22: *Pa*MprF Lipid binding sites. a. The *Pa*MprF structure (TM domain 1 = orange, TM domain 2 = purple, soluble domain = green) is shown aligned to all the lipid features (yellow) present in the final cryo-EM map. **b.** View of lipid binding site at TM8, with an AlaPG molecule (yellow sticks) fitted into the map. **c.** View of cytoplasmic lipid binding site with a POPC molecule (yellow sticks, with hydrophobic tails removed) fitted into the map. **d.** View of lipid signal present between TM domains with a molecule of AlaPG (yellow sticks) fitted into the map.

A lot of lipid signal is present at both the outside face of *Pa*MprF and the groove running between the two TM domains. **Figure 3.22b** shows there is a lipid molecule bound at the cytoplasmic leaflet by TM8, and is discussed further in **section 3.5.4.**

The cytoplasmic pocket of *Rt*MprF that was occupied by a LysPG molecule also appears to be occupied in *Pa*MprF (**Figure 3.22c**). The characteristic branching core of a phospholipid can be resolved, with the hydrophobic lipid tails presumably being too flexible to be resolved here. Interestingly, there is no lipid headgroup density seen deep in the cytoplasmic pocket as in *Rt*MprF. As such, a POPC headgroup (rather than AlaPG) has been modelled into this map in **Figure 3.22c.** There is also lipid signal nearer to TM5. In *Rt*MprF, this site is occupied by the tail of one PG molecule that contributes to the dimer interface, so this may be what is observed in *Pa*MprF, with the rest of the lipid being too flexible to be resolved in the absence of it contributing to a stable dimer interface.

Figure 3.22d highlights the significant amount of signal observed at the TM domain interface, at a similar site to the bound lipid at the periplasmic exit in *Rt*MprF. An AlaPG molecule has been fitted into this map in **Figure 3.22d,** but the low resolution of this map region makes it difficult to identify a continuous section into which to fit a lipid molecule. Indeed, any orientation of a single AlaPG molecule in this site leaves excess map features unoccupied, suggesting there may be the capacity in this more open state of *Pa*MprF for multiple lipids to occupy this cavity at the same time.

3.5.3. The Soluble Domain of *Pa*MprF is significantly displaced compared to *Rt*MprF

When superposed individually, the soluble domains of both *Rt* and *Pa*MprF align well (**Figure 3.23**) with an RMSD of 0.953 Å. The most notable difference between the soluble domains of both structures is that in *Rt*MprF, a loop between two α-helices extends towards the TM region and makes β-strand interactions with residues in the loop between TM helices 5 and 6 (L5-6, **Figure 3.23, right**) of TM domain 1. This loop in *Pa*MprF (residues 806-834) is not resolved in the final cryo-EM map, suggesting flexibility in this region of the protein.

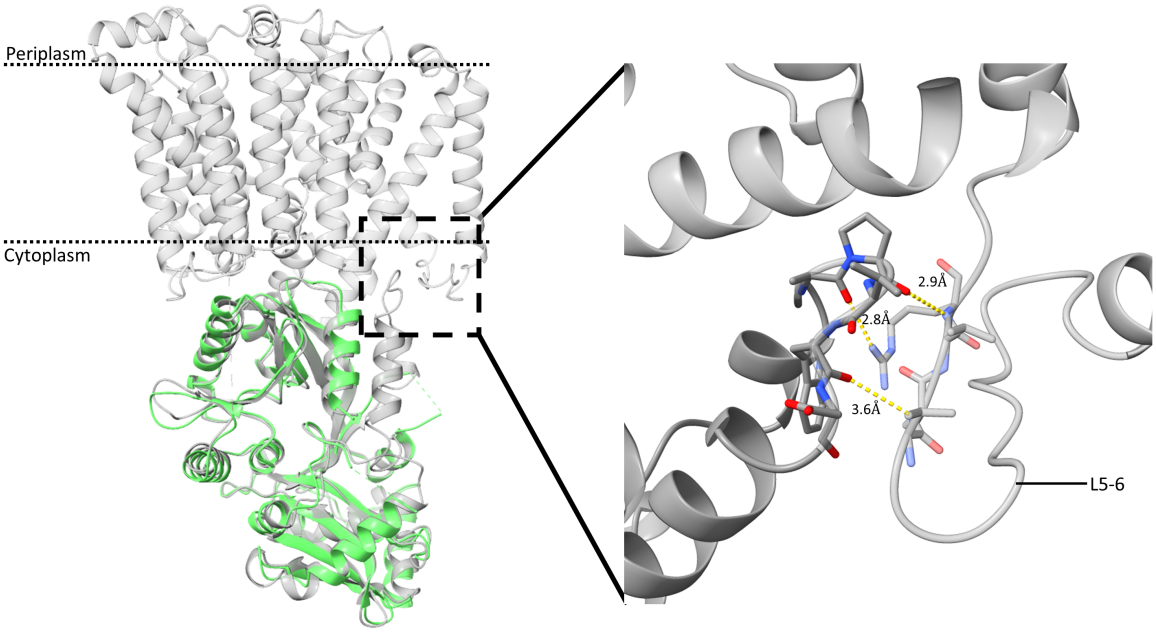

Figure 3.23: Alignment of MprF soluble domains. *Left*: The soluble domain of *Rt*MprF (green) is aligned to the soluble domain of *Pa*MprF (grey) – RMSD 0.953 Å. The TM region of *Pa*MprF has been removed for clarity. ***Right*:** The interaction between the *Rt*MprF soluble domain loop and the loop between TMs 5 and 6 (L5-6).

Whilst the soluble domains of the two homologues are structurally very similar, aligning the *Pa* and *Rt*MprF structures at TM domain 2 shows that there is a pronounced rigid body rotation and translation of the soluble domain of PaMprF towards a position more perpendicular to the membrane (**Figure 3.24**).

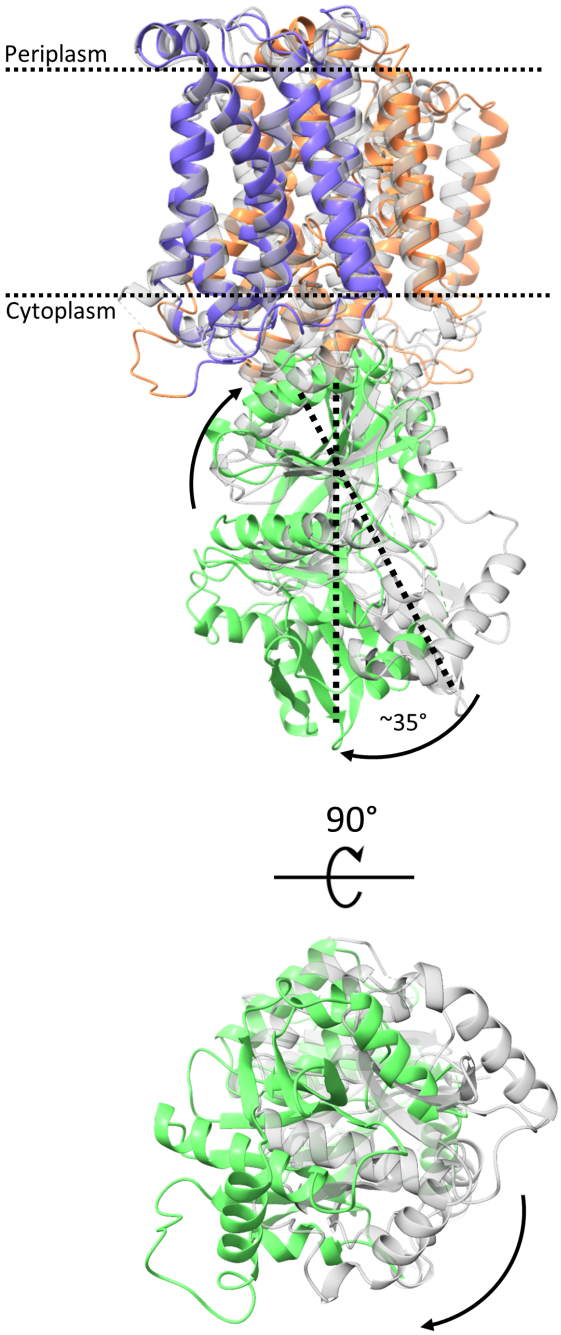

Figure 3.24: Rigid body movement of the *Pa*MprF soluble domain. Structures of *Rt*MprF (grey) and *Pa*MprF (TM domain 1 = orange, TM domain 2 = purple, soluble domain = green) are aligned by TM domain 2. ***Top*:** side view of MprF along the short axis of TM domain 2, showing the rigid body rotation of the soluble domain relative to the TM region that occurs between *Rt* and *Pa*MprF. ***Bottom***: top view from cytoplasmic side with the TM region clipped for clarity.

As shown in **Figure 3.24,** the soluble domain in *Pa*MprF is rotated away from TM domain 1. TM domain 1 contains the loop L5-6 which forms contacts with the soluble domain of *Rt*MprF. This may explain why the soluble domain loop 806-834 is not resolved in the *Pa*MprF

structure, as the interaction of this loop with L5-6 of TM domain 1 would be broken to facilitate the rigid body movement of the soluble domain away from the plane of the membrane, increasing flexibility at loop 806-834. Therefore, this interaction in *Rt*MprF may act as "latch" to hold the soluble domain in place closer to the plane of the membrane.

The observed positional shift of the soluble domain relative to the membrane likely reflects an inherent flexibility of the soluble domain, which could be required in order to access both its substrates: PG from the membrane as well as charged-tRNA from the cytosol as a source of amino acids for aminoacylation (see **section 3.6.2.**). Similar to *Rt*MprF, there is no resolvable ligand signal at the soluble domain for either PG or aminoacyl-tRNA. As such, further structural characterisation of *Pa*MprF bound to substrate analogues is required before substrate handoff to the soluble domain can be fully elucidated.

3.5.4. The TM domains of *Pa*MprF separate to open a deep cleft

In addition to rigid body movements in the soluble domain, alignment of the two structures to either of the two TM domains reveals that there is a significant displacement of the TM domains from each other (**Figure 3.25**).

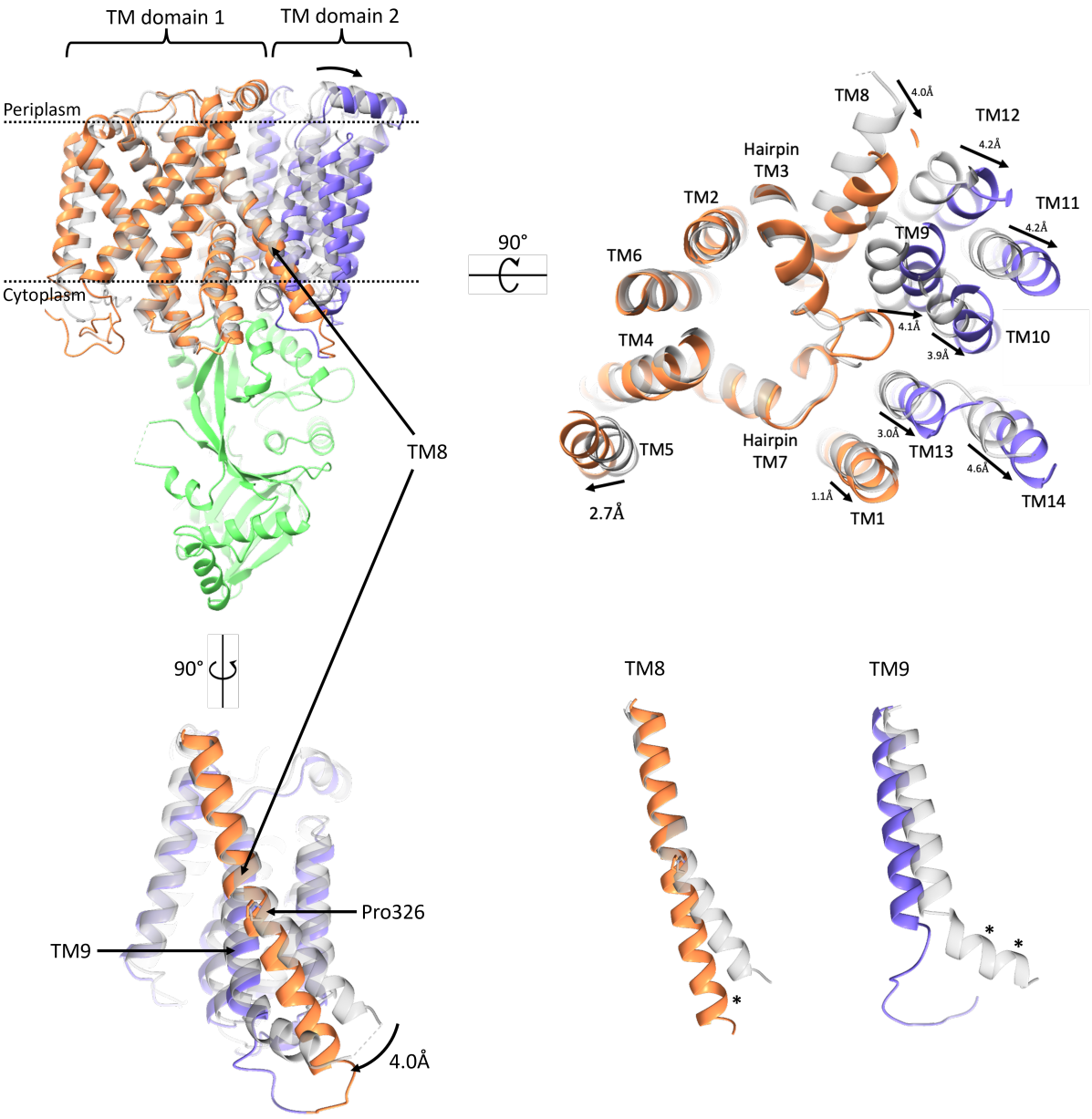

Figure 3.25: Displacement of TM domains. Alignment of *Rt*MprF (grey, soluble domain removed for clarity) to *Pa*MprF (TM domain 1 = orange, TM domain 2 = purple, soluble domain = green) aligned at TM domain 1. ***Top left***: side view of structures. ***Top right*****:** top view of structures from the cytoplasmic side of the protein (soluble domain removed for clarity). ***Bottom left***: view of TM8 clipped through TM domain 1. The proline hinge point of TM8 (Pro326 in *Pa*MprF) is shown. ***Bottom right***: side views of both TM8 and TM9, with * marking sections of α-helix that alternate between the two structures.

TM domain 2 (TMs 9-14) is significantly shifted away from TM domain 1 (TMs 1-8) in *Pa*MprF, by ~3 Å or more for all helices. The motion appears to originate from TM8 (**Figure 3.25, bottom left**), the C-terminal helix of TM domain 1, which has a hinging point at a proline residue (Pro326 in *Pa*MprF) halfway down the helix at the centre of the membrane. This

proline residue is highly conserved across MprF homologues, and previous work by Ernst *et al.* (2015) of the corresponding residue in *Sa*MprF found that mutation of this proline to alanine mildly reduced MprF flippase activity.

The two conformations of TM8 seen in *Rt* and *Pa*MprF may be stabilised by alternate formation of α-helix interactions (**Figure 3.25, bottom right**); in *Rt*MprF, the cytoplasmic end of TM9 contains a stretch of α-helical secondary structure which is disordered in *Pa*MprF, whereas the cytoplasmic end of TM8 in *Pa*MprF contains additional α-helical secondary structure absent in *Rt*MprF TM8. Such "helix-swapping" would presumably provide the energy minima to facilitate MprF adopting these distinct conformations. In addition, the *Pa*MprF TM8 is in proximity to the bound lipid molecule highlighted previously in **Figure 3.22b,** which is absent in the *Rt*MprF structure**.** Therefore, this bound lipid may help to stabilise this conformation of *Pa*MprF in addition to the helix-swapping that is observed at this hinging helix.

The effect of this TM domain separation can be seen by looking at the electrostatic surface of the two structures in **Figure 3.26:**

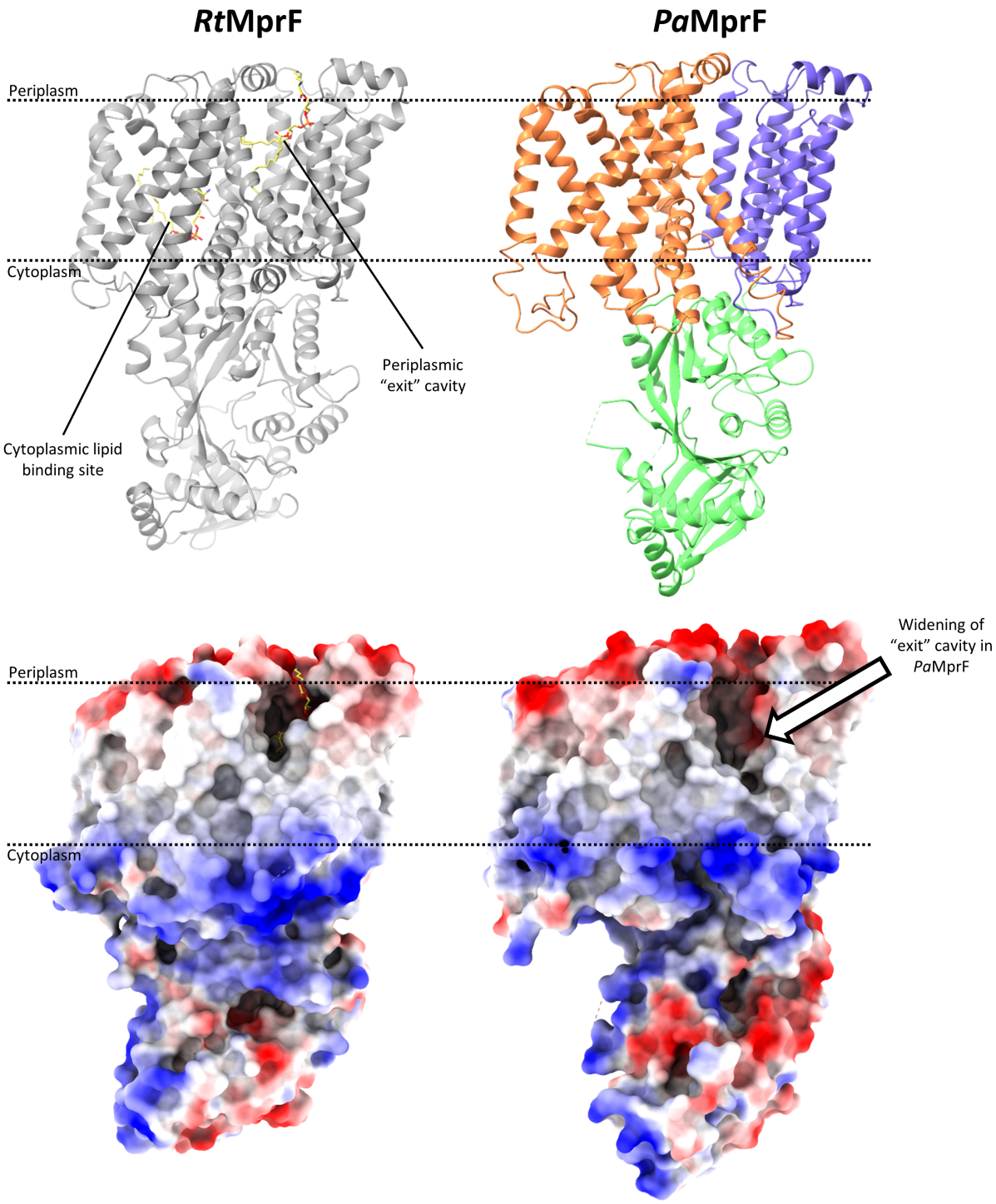

Figure 3.26: Electrostatic surface comparison of *Rt* and *Pa*MprF. Comparison of *Rt*MprF (left panels) and *Pa*MprF (right panels). ***Top*:** cartoon depiction of *Rt* (grey) and *Pa*MprF (TM domain 1 = orange, TM domain 2 = purple, soluble domain = green) side views at the periplasmic "exit site". The bound LysPG lipids (yellow sticks) from the *Rt*MprF model are shown for clarity. ***Bottom*:** electrostatic surfaces (blue: positive, white: neutral, red: negative) of the models at the same viewing angle as the top panels.

Due to the shift in TM domain 2 relative to TM domain 1, the periplasmic "exit" site for lipid in *Pa*MprF is much wider, as can be seen from the electrostatic surface. This domain separation results in the lipid accessible cleft extending down further into the membrane, creating a near complete groove from one side of the membrane to the other.

3.5.5. Structural analysis reveals a possible alternate lipid translocation pathway

As discussed in the **Introduction (1.3.3.),** Song *et al.* (2021) hypothesised from the *Rt*MprF structure that a conserved salt bridge (E295-R319 in *Pa*MprF) within TM domain 1, in the vicinity of the tips of the two hairpin helices, could act as a gate that separates in the "open" state of MprF to facilitate lipid translocation. Given the significant positional shifts in domains between *Rt*MprF and *Pa*MprF, these residues were inspected for any conformational changes. However, this salt bridge is "closed" in both MprF structures as shown in **Figure 3.27:**

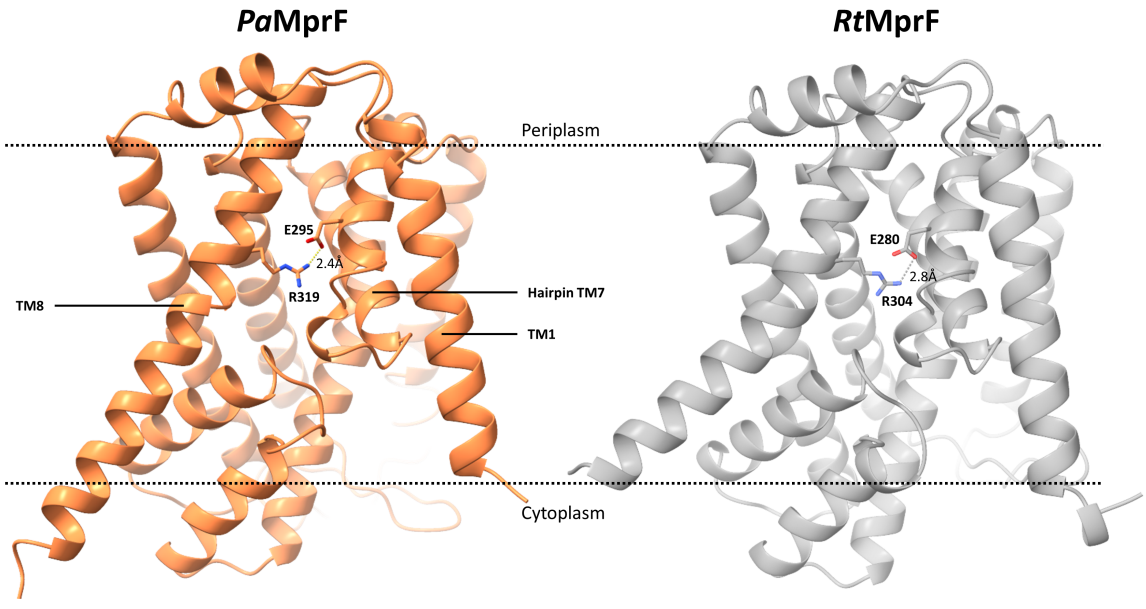

Figure 3.27: MprF conserved salt-bridge interaction. View of *Pa* (orange) and *Rt*MprF (grey) TM domain 1 through the short axis of the protein (clipped through TM domain 2), highlighting the conserved salt bridge interaction between glutamate (hairpin helix TM7) and arginine (TM8) residues.

This indicates that the TM domain 1 of *Pa*MprF is in a similar state as found in *Rt*MprF, with the main conformational shift between the two structures occurring instead between rigid bodies of TM domains 1 and 2.

Given the abundance of lipid signal present at the widened interface between the separated TM domains 1 and 2 in *Pa*MprF, an analysis of the solvent accessible surface of the interior of *Pa*MprF was carried out in HOLLOW, a program that places dummy atoms within the interior space of a protein to visualise binding pockets or solvent channels (Ho and Gruswitz 2008). The output of this analysis is shown in **Figure 3.28:**

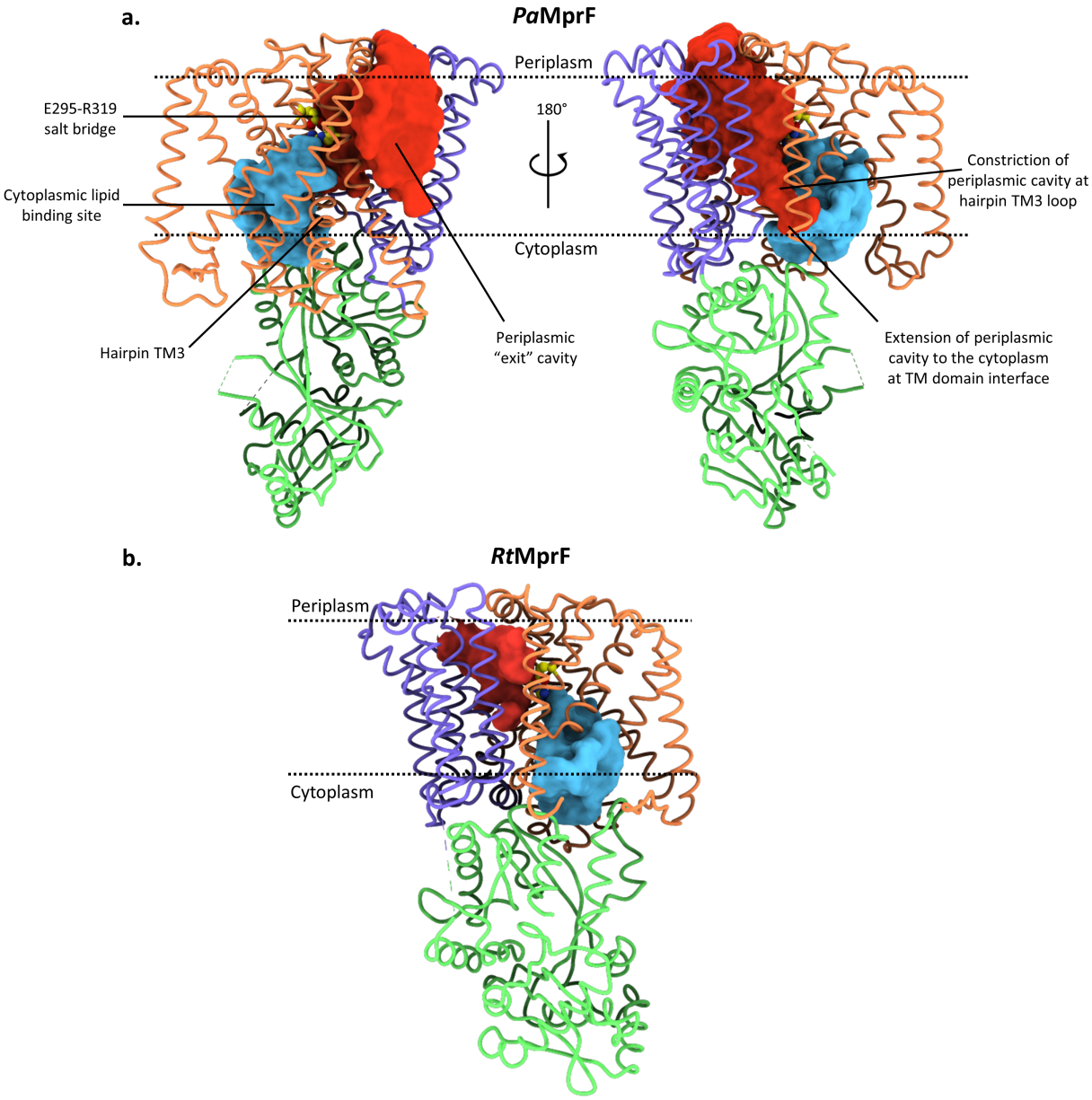

Figure 3.28: *Pa*MprF interior solvent accessible surface. a. *Pa*MprF (TM domain 1 = orange, TM domain 2 = purple, soluble domain = green) ribbon model overlaid with solvent accessible interior surfaces generated by HOLLOW. The E295-R319 salt bridge residues are highlighted as yellow spheres. A solvent accessible pocket at the cytoplasmic lipid binding site is shown in blue, and a solvent accessible channel at the TM domain interface is shown in red. **b.** One chain of *Rt*MprF (PDB:7DUW) coloured as in **a.,** with the electrostatic surface of lipid binding sites coloured to match the HOLLOW analysis in **a.**, demonstrating the periplasmic cavity (red) only extending from the periplasm to the tip of hairpin TM3.

As can be seen in **Figure 3.28a,** the previously identified cytoplasmic lipid binding pocket from *Rt*MprF is present in *Pa*MprF (blue surface) but also does not extend past the E295-R319 salt bridge (yellow spheres). However, there is now a very wide solvent accessible channel (red surface) running down the interface between TM domains 1 and 2, towards the side of the

cytoplasmic lipid binding pocket, and in fact reaching all the way through the protein. This suggests that there may be an alternate pathway of lipid permeation through *Pa*MprF to the path through the opened salt bridge originally suggested by Song *et al.* (2021). The width of this channel on the cytoplasmic side of *Pa*MprF appears in this structure too narrow to accommodate a full lipid molecule. This suggests that there could be further structural rearrangement at this region to produce a more open pathway for lipid transport. The constriction point on this side of the protein occurs by the loop at the end of hairpin TM3. The local resolution of the EM map at this loop is lower than the surrounding structure, suggesting a degree of flexibility at this region and supporting the idea that further conformational change at this site is required for a fully "open" state of *Pa*MprF.

3.6. Chapter Discussion

3.6.1. Sybody29 significantly improved sample behaviour of *Pa*MprF

The strategy described in this Chapter to generate sybody binders to the *Pa*MprF TM region resulted in the successful determination of a high-resolution structure of monomeric *Pa*MprF by cryo-EM. This synthetic nanobody library approach to generate binders was chosen instead of the more widely utilised method of camelid immunisation (Arbabi Ghahroudi *et al.* 1997) because for immunisation, the target protein must remain folded for a prolonged period at the body temperature of the camelid that has been immunised (~37°C for hours to days). All the selection steps using the synthetic library were carried out at 4°C, and so better suited to *Pa*MprF, a membrane protein with low stability.

The Seeger group sybody selection platform was also chosen over other nanobody selection platforms that use yeast (McMahon *et al.* 2018) or phage (Moutel *et al.* 2016) display, as the initial libraries for these platforms are generated through transformation into cells, and so the size of the library is limited by transformation efficiency (e.g. yeast library size is $\sim 10^8$, phage library size is $\sim 10^{10}$). Limitations on library size reduce the diversity of unique binding modes that can be represented, and so reduce the likelihood that unique binders can be raised for a target. The sybody selection platform, however, uses ribosome display as a first round of selection. This selection round is not limited by cell competency, which enables a much larger library (1.6×10^{12} molecules of mRNA, $\sim 10^{12}$ unique sybody sequences) to be used. Another limitation of synthetic libraries is that selection bias can occur, where sybodies which bind non-specifically to the target are enriched. This is accounted for in the sybody selection platform, as different selection techniques are used, and the medium used to immobilise the target protein is changed with each round to limit the non-specific binding of particular sybodies to certain surfaces. Taken together, the result is a diverse library of unique sybody

sequences that can be used to robustly select highly specific binders with a variety of binding modes for a particular target protein, and which resulted in the successful generation of sybody binders targeting the TM region of *Pa*MprF.

The success of this approach was due to the significant improvement of *Pa*MprF-SapNP sample behaviour in vitreous ice when in complex with the Sybody29 binder; 2D classification of *Pa*MprF-SapNPs previously highlighted issues with preferential orientation, with side views of the protein being very limited and thus hindering high-resolution reconstruction. Addition of a sybody binder saw the appearance of many more side views in 2D classification. This may be because of the location of the sybody binding site on the periplasmic face of *Pa*MprF: the preferred orientation observed previously could have been due to the periplasmic face of the TM domain adhering to the air-water interface, something which could be disrupted by the presence of Sybody29. In addition, Sybody29 increased the size of the *Pa*MprF monomer and provided a recognisable feature on the periplasmic face of the protein to aid in particle alignment during reconstruction.

3.6.2. *Pa*MprF exhibits major structural changes compared to *Rt*MprF

Despite low sequence homology, the global structural elements of *Pa*MprF are similar to that of the previously published *Rt*MprF, with core structural features within domains broadly maintained. However, there are significant rigid-body shifts in the relative positions of domains that raise interesting questions about the mechanisms of lipid modification and transport.

The soluble domain of *Pa*MprF undergoes a rigid-body translation and rotation away from the plane of the membrane compared to *Rt*MprF. Previous cryo-EM work from Song *et al.* (2021)

on the *Rt*MprF dimer identified a number of alternate conformations during 3D classification. These conformations were sorted into minor classes that were not pursued to high-resolution, but clearly demonstrated the soluble domain occupying a number of orientations at different angles to the plane of the membrane. The cryo-EM processing of the *Pa*MprF dataset in this Chapter, however, did not yield any minor classes that displayed this level of soluble domain flexibility. The occurrence of alternate soluble domain configurations is unsurprising given the requirement for this domain to bind to both PG from the membrane and aminoacyl-tRNA^{Ala} from the cytosol, however it is still unclear precisely how both substrates are acquired, as neither high-resolution structure displays bound substrate nor indicates an orientation of the soluble domain with an obvious access to bulk membrane lipids. Hebecker *et al.* (2015) previously suggested a substrate tunnel for PG to access the active site of the soluble domain for aminoacylation (**Figure 3.29a**). This tunnel, however, is situated on the face of the soluble domain that is furthest from the plane of the membrane. It is possible that the conformation of the *Pa*MprF soluble domain represents an intermediate position and that further rigid body rotation positions this proposed substrate tunnel closer to the membrane. Alternatively, PG could access the soluble domain active site on the face of the soluble domain closest to the membrane in the *Rt*MprF structure, and the *Pa*MprF conformation could represent the structural rearrangement after lipid binding, with the soluble domain poised to access cytoplasmic aminoacyl-tRNA^{Ala}. Indeed, comparison of the electrostatic surfaces of full-length *Pa*MprF with the previously published *Pa*MprF soluble domain crystal structure reveals an opening of the substrate groove at the same face as the predicted tRNA binding site (**Figure 3.29b**).

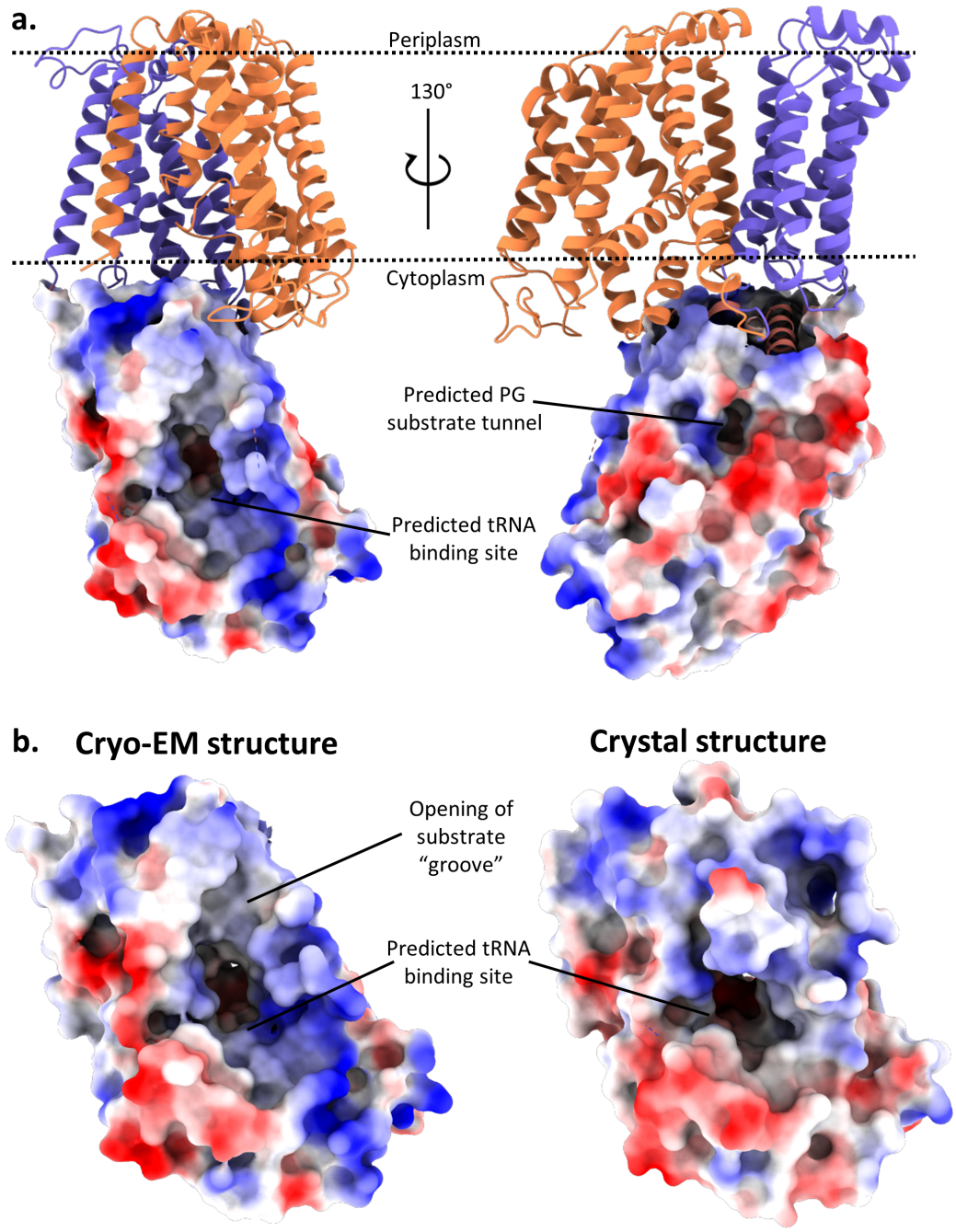

Figure 3.29: *Pa*MprF soluble domain substrate binding sites. a. View of full-length *Pa*MprF showing the electrostatic surface of the soluble domain (cartoon of TM domain 1 in orange and TM domain 2 in purple shown for clarity). The predicted tRNA binding site is highlighted, as well as the PG substrate tunnel predicted by Hebecker *et al.* (2015) on the opposite face of the domain. **b.** Comparison of electrostatic surfaces of the *Pa*MprF soluble domain from the full-length cryo-EM structure, and the previously published soluble domain crystal structure by Hebecker *et al.* (2015), viewed from the predicted tRNA binding site.

The highlighted substrate groove in **Figure 3.29b** is closed off in the previously published *Pa*MprF soluble domain crystal structure by the loop containing residues 806-834. This loop (discussed in **section 3.5.3.**) is not resolved in the *Pa*MprF cryo-EM structure, suggesting

flexibility at this region. The absence of this loop expands the substrate groove near the predicted tRNA binding site, raising the possibility that this is the PG binding site, and that rearrangement of this flexible loop is required for PG binding. Such a site would be consistent with the structurally similar FemX enzyme (Fonvielle *et al.* 2013) discussed in the **Introduction (1.3.2.),** which also binds its substrate on the same face of the protein as the tRNA used for aminoacylation. However, further structural studies utilising aminoacyl-lipid analogues and tRNA acceptor stem substrates are required to fully elucidate the mechanism of substrate binding at the soluble domain.

Within the TM region of *Pa*MprF, there is a significant expansion of the two TM domains which separate with near rigid-body movement as far as ~4.5 Å in places. The reason for this observed structural difference between *Rt*MprF and *Pa*MprF is unclear. One possibility is the different lipid composition used for nanodisc reconstitution of the homologues; it has been demonstrated that bulk lipid can significantly affect transport properties of other solute and lipid transporters (Parker and Newstead 2017, Bushell *et al.* 2019), and so the different lipid compositions could alternately stabilise the more closed or open states demonstrated by the two structures. Additionally, the published *Rt*MprF structure was obtained following reconstitution into membrane scaffold protein (MSP) nanodiscs, which form nanodiscs of fixed sizes based on the length of the MSP construct used (Denisov *et al.* 2004). In contrast, the SapNP reconstitution used in this Chapter involves the polymerisation of SapA to accommodate membrane proteins of varying size. As such, the scaffold protein in the resulting SapNPs can more tightly adhere to the target protein producing more compact nanodiscs (Flayhan *et al.* 2018). Indeed, the choice of scaffold protein has been recently shown to influence the structures of reconstituted membrane proteins (Dalal *et al.* 2024). The sybody binder could also potentially be stabilising *Pa*MprF in a more open conformation; there appears to be increased soluble domain flexibility in the 2D classes for *Pa*MprF alone (**Figure 3.5**) compared to the *Pa*MprF-sybody complex (**Figure 3.15**), suggesting that Sybody29

binding somehow contributes to the stabilisation of the soluble domain in a single conformation. If Sybody29 is locking *Pa*MprF in a more open conformation, the loss of the interaction between the TM domain loop L5-6 and the soluble domain (see **Section 3.5.3**) could prevent the soluble domain from sampling conformations closer to the membrane plane, reducing its flexibility as assessed by 2D classification. However, the Sybody29 binding site is far from the hinging point between the two TM domains, and there does not appear to be any significant structural rearrangement at this binding site in *Pa*MprF, As will be discussed in **Chapter 5,** Sybody29 does not significantly affect *Pa*MprF lipid transport activity, further supporting that structural differences are not due to Sybody29 binding**.** The other possible explanation for the difference between the structures is that of oligomeric state, as *Rt*MprF is dimeric and *Pa*MprF monomeric. Structural changes as a result of oligomerisation would be an appealing explanation, as this would imply a regulatory mechanism of reducing MprF activity *in vivo* at high MprF concentrations. This would then provide an additional level of control over aminoacylated PG levels *in vivo*, which have been shown to be detrimental to CAMP resistance of *P. aeruginosa* cells at high concentrations (Arendt *et al.* 2013). The effect of MprF oligomerisation state on activity is therefore something that requires further study before it can be attributed to the structural changes observed in this Chapter.

3.6.3. *Pa*MprF structural data suggests possible alternate lipid transport routes

The separation of TM domains observed in *Pa*MprF compared to *Rt*MprF greatly expands the size of the periplasmic exit cavity, producing a lipid-exposed groove that spans nearly the full width of the membrane. In addition, the domain separation produces a channel through the core of the protein, extending from the cytoplasm to the periplasm at the TM domain interface (**Figure 3.30**). Interestingly, this channel is different from the previously proposed route of lipid transport (A in **Figure 3.30**), suggesting an alternate route that is used to translocate AlaPG to the periplasmic leaflet (B in **Figure 3.30**).

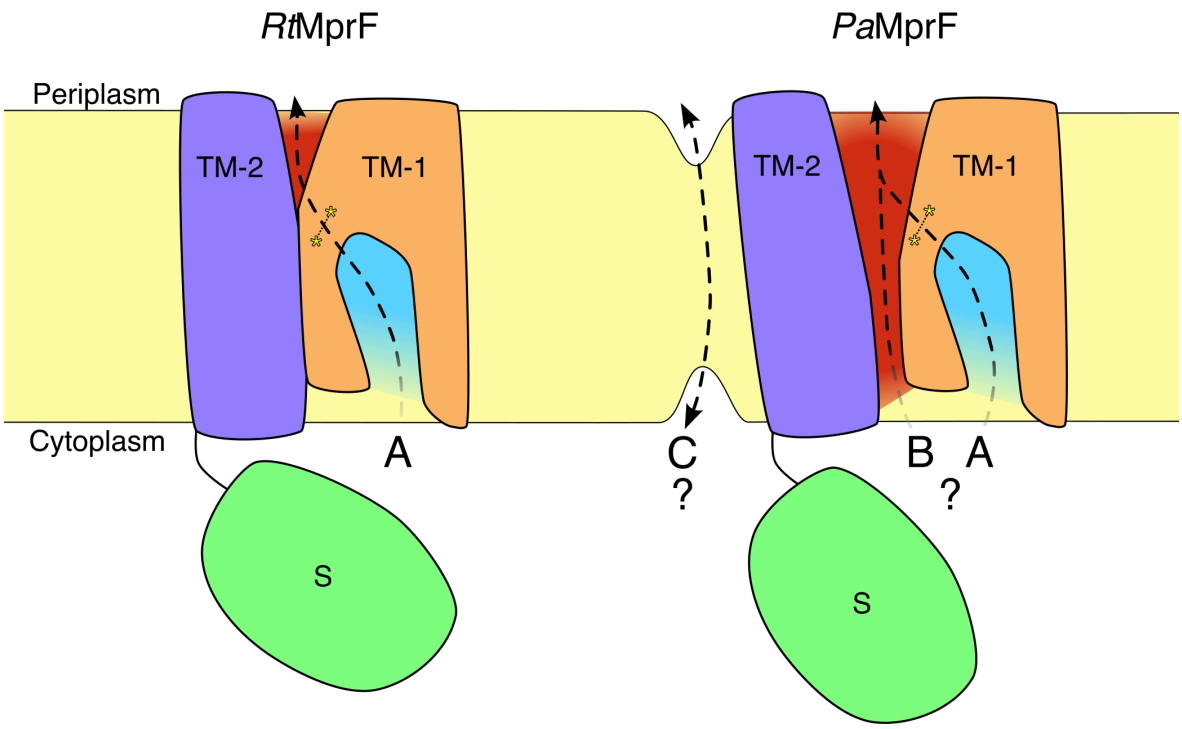

Figure 3.30: Possible MprF-mediated lipid transport pathways. Schematic of *Rt*MprF (*left*) and *Pa*MprF (*right*) structures, coloured as in **Figure 3.28.** The conserved salt bridge residues are shown as yellow asterisks. The lipid transport route proposed by Song *et al.* (2021) is labelled A, the route between the TM domains suggested by the *Pa*MprF structure is labelled B, and a credit-card/out-of-the-groove route is labelled C.

A lipid transport mechanism at the TM domain interface would be consistent with previous *in vivo* studies of MprF activity. Ernst *et al.* (2015) assessed the ability of TM constructs of *Sa*MprF to confer daptomycin resistance to cells when the soluble domain of *Sa*MprF was also expressed *in trans.* They found that daptomycin resistance was comparable to WT when only residues 1-393 of the TM domain were expressed. In *Pa*MprF, this construct corresponds to TM domain 1 and the first 2 TM helices of TM domain 2. Furthermore, truncation to residues 1-320 reduced daptomycin minimum inhibitory concentration by 50%; such a truncation removes the TM domain 2 helices, suggesting that helices from TM domain 2 are required for maximal lipid transport activity of MprF. As TM 9 makes up part of the solvent accessible channel at the TM domain interface, this is evidence of its involvement in defining the lipid transport pathway. Further truncation to residues 1-274 gave daptomycin resistance comparable to cells not expressing MprF; this truncation removes TM helix 8, which forms a significant component of the TM domain interface from the side of TM domain 1. This indicates

that TMs 1-7 do not exhibit lipid transport activity alone, and since the cytoplasmic lipid binding site is formed by these helices, this suggests that lipid from the cytoplasm accesses a different pathway to that proposed by Song *et al*. (2021).

Another alternate lipid transport pathway more consistent with the credit-card model discussed in the **Introduction (1.1.)** could be the sizeable groove at the periplasmic exit in *Pa*MprF (C in **Figure 3.30**). Such lipid transport grooves are commonly seen in scramblase structures, with hydrophilic lipid headgroups able to access the groove while their hydrophobic tails remain in the membrane. The groove at the periplasmic exit of *Pa*MprF contains a patch of negatively charged and polar residues in TM domain 2, but this hydrophilic surface does not extend through to the cytoplasm, suggesting such a groove would not function as described for other scramblases. On the other hand, further conformational change may be required to fully open this groove to the cytoplasm to allow lipid headgroups access.

Due to the possible alternate lipid transport pathways suggested by the *Pa*MprF structural data, the question of by what route AlaPG is translocated from the cytoplasmic leaflet to the periplasmic leaflet of the inner bacterial membrane is further explored by functional assessment of *Pa*MprF-mediated AlaPG transport in **Chapter 5.**

Chapter 4: *In vitro* assessment of *Pa*MprF function and interactions

4.1. Introduction

There are many questions surrounding the lipid translocase activity of *Pa*MprF that have not been addressed in the literature. To date, no previous studies have used an *in vitro* lipid transport assay to assess *Pa*MprF function. Lipid translocation assays are inherently sophisticated, hence establishing such an assay is a substantial investment of time and resources. Importantly, it would need to first be demonstrated that purified *Pa*MprF is catalytically active via an assessment of synthase activity *in vitro*. This Chapter is an account of the work establishing *in vitro* assays for both synthase and lipid translocase activities of *Pa*MprF. For the assessment of *Pa*MprF synthase activity, all the components involved in the aminoacylation of PG must be provided. As *Pa*MprF uses a charged-tRNA^{Ala} as a substrate, the *P. aeruginosa* tRNA^{Ala} and tRNA^{Ala}-synthetase (AlaRS) were both purified. The roles of these components in aminoacyl-PG production are summarised in **Figure 4.1**.

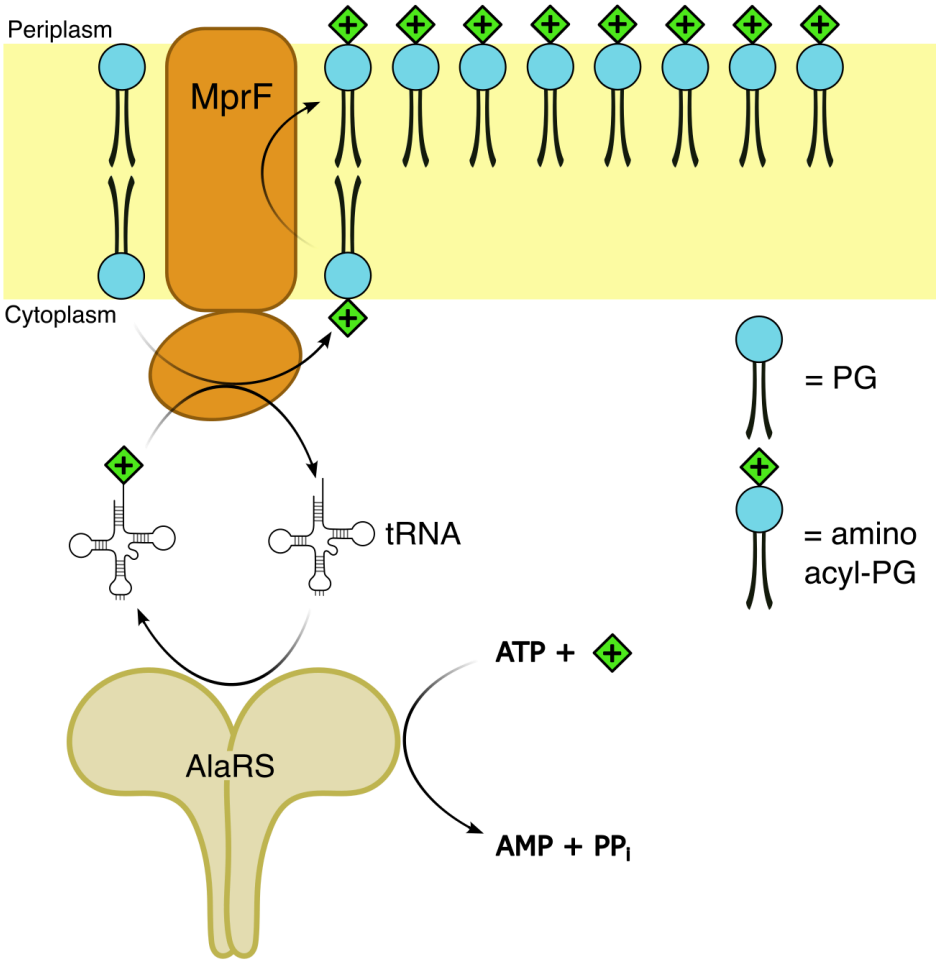

Figure 4.1: Key components involved in aminoacyl-PG production.

Another area of interest is the ability of *Pa*MprF to access cytoplasmic tRNA, as discussed in the **Introduction (1.3.2.).** One possibility is that *Pa*MprF and AlaRS interact in order for AlaRS to handoff charged-$tRNA^{Ala}$ directly at the bacterial membrane, however there is no previous biochemical evidence of such an interaction. Since AlaRS was produced for use in functional assays, this work allowed the investigation of a possible *Pa*MprF-AlaRS complex which is also explored in this Chapter.

4.2. *Pa*MprF and AlaRS form a complex *in vitro*

4.2.1. Purification of AlaRS

The sequence of AlaRS was recombinantly expressed in *E. coli* as outlined in **Methods (2.4.11.)**. The results of a purification of 2 L of cell culture are shown below in **Figure 4.2:**

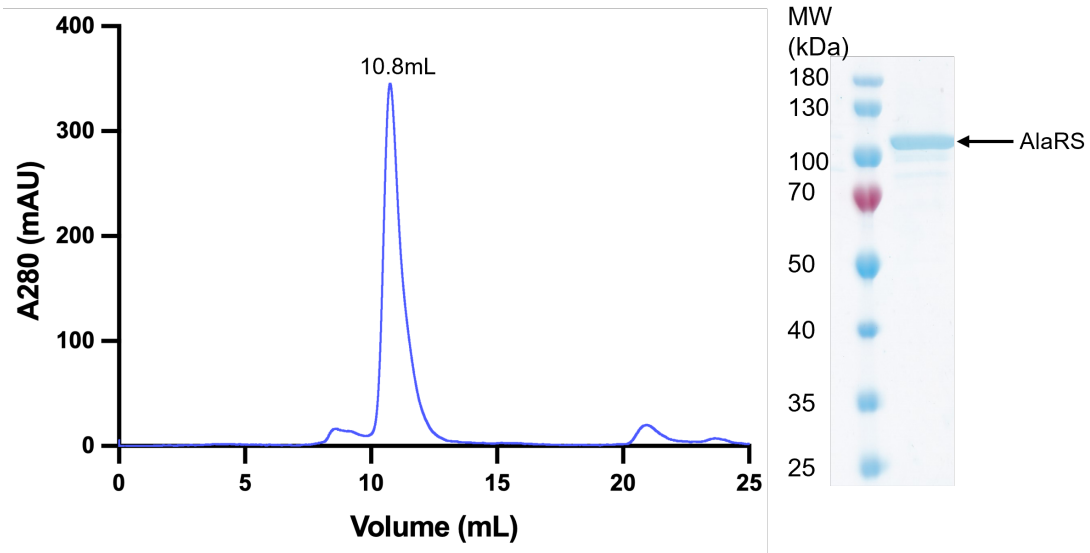

Figure 4.2: AlaRS purification. *Left:* SEC chromatogram of AlaRS purification. *Right:* SDS-PAGE gel (12 %, Coomassie stained) of peak fraction of AlaRS

AlaRS elutes from the SEC column at elution volume 10.8 mL in a single homogeneous peak, and was isolated at >95 % purity as analysed by SDS-PAGE. The SEC elution volume corresponds to an apparent molecular weight of ~400 kDa. The AlaRS monomer has a molecular weight of 95 kDa, suggesting that AlaRS is purifying as a tetramer. This is consistent with the existing literature, where there is evidence of the *E. coli* AlaRS purifying as a tetramer (Putney *et al.* 1981).

The purified AlaRS was used to assess suspected complex formation with *Pa*MprF.

4.2.2. *Pa*MprF is enriched on affinity resin bound to AlaRS

Initial work investigating the putative AlaRS-*Pa*MprF interaction was carried out via pulldown assay, where His-tagged AlaRS was immobilised on Nickel affinity resin and then exposed to untagged *Pa*MprF. After washing to remove non-specifically bound *Pa*MprF, the remaining bound protein was eluted and analysed via SDS-PAGE. Results of the AlaRS-MprF pulldown are shown in **Figure 4.3:**

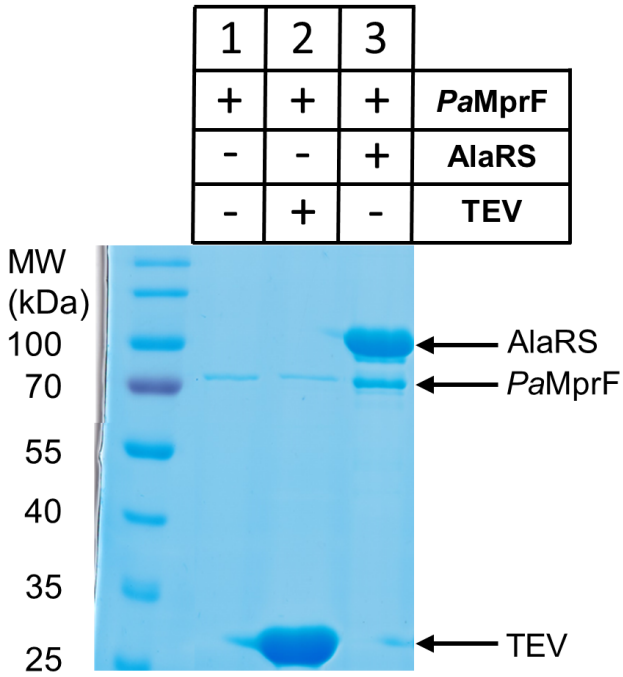

Figure 4.3: AlaRS-MprF pull-down assay. SDS-PAGE (10 %, Coomassie stain) gel of pull-down assay of resin incubated without His-tagged protein (lane 1), or with His-tagged TEV (lane 2)/His-tagged AlaRS (lane 3) prior to incubation with untagged *Pa*MprF.

This pulldown shows that a small amount of *Pa*MprF binds non-specifically to the affinity resin in the absence of AlaRS (lane 1). Addition of His-tagged TEV before *Pa*MprF (lane 2) gives a *Pa*MprF band of similar intensity to lane 1, indicating that *Pa*MprF does not bind non-specifically to immobilised protein. Addition of AlaRS before *Pa*MprF (lane 3) results in increased MprF binding, suggesting that AlaRS and MprF interact. Following this promising result, SEC experiments were performed to investigate the possible *Pa*MprF-AlaRS complex.

4.2.3. *Pa*MprF and AlaRS co-elute on SEC

*Pa*MprF and AlaRS were mixed at a 1:1 molar ratio before being assessed by SEC. The results of these SEC experiments are shown in **Figure 4.4:**

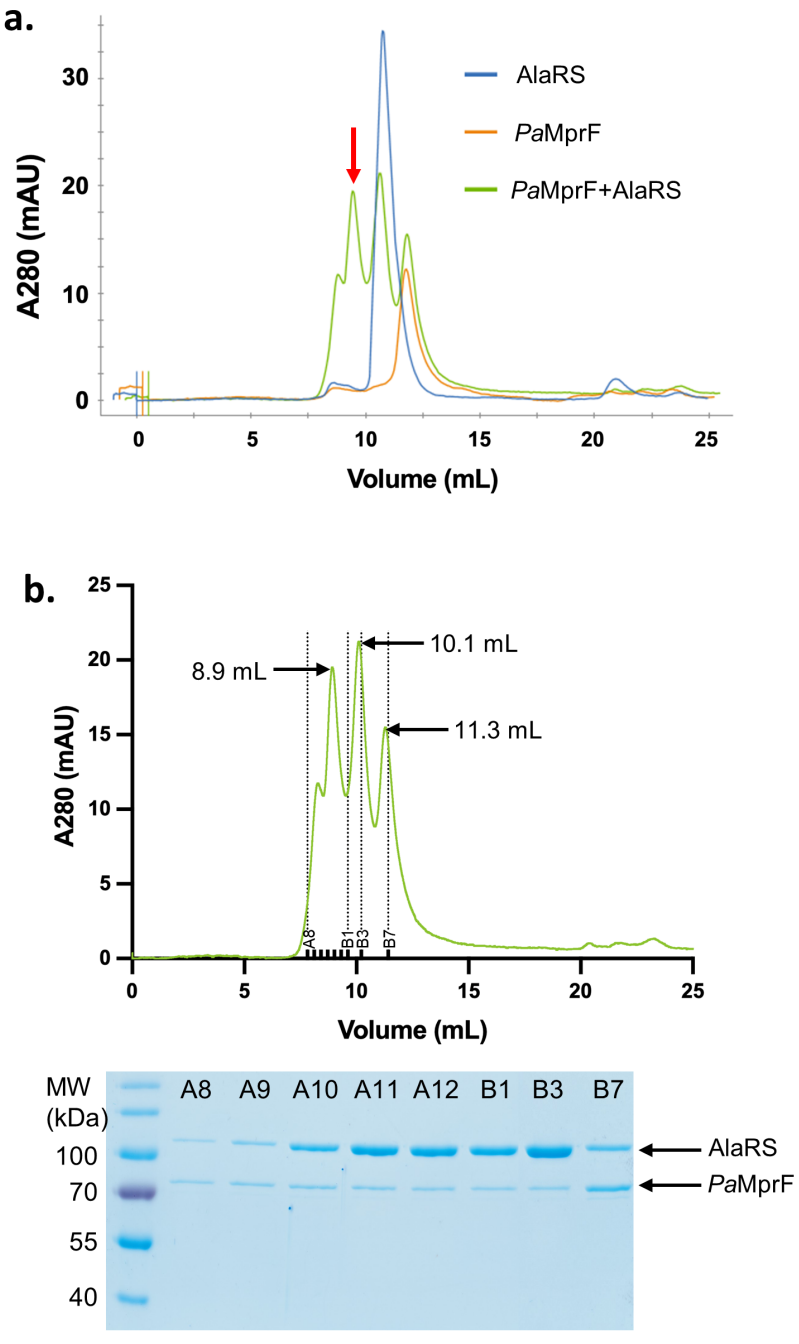

Figure 4.4: MprF-AlaRS SEC chromatograms. a. Overlay of SEC traces of AlaRS (blue), *Pa*MprF (orange) and both together (green). The peak at 8.9 mL that only appears on combination of *Pa*MprF and AlaRS is highlighted with a red arrow. **b.** SEC trace of *Pa*MprF-AlaRS with a 10 %, Coomassie stained SDS-PAGE gel of fractions. A8-A10 = void volume, A11-A12 = 8.9 mL peak, B3 = 10.1 mL peak, B7 = 11.3 mL peak.

Control experiments of AlaRS (blue) and *Pa*MprF (orange) alone in panel **a.** of **Figure 4.4** show single species with elution volumes of 10.1 mL and 11.3 mL respectively. However, a 1:1 molar ratio mixture of *Pa*MprF:AlaRS (green) shows the appearance of a third peak with a lower elution volume of 8.9 mL, indicating the existence of a higher molecular weight species. Panel **b.** shows that *Pa*MprF and AlaRS are present in this 8.9 mL peak. Column calibrations give the apparent MW of the 10.1 mL peak as ~400 kDa, suggesting AlaRS alone runs as a tetramer. The *Pa*MprF monomer runs at an apparent MW of ~230 kDa at 11.3 mL elution volume, and the 8.9 mL peak has an apparent MW of ~640 kDa. This suggests that the higher MW species at 8.9 mL corresponds to a 4:1 AlaRS:MprF complex.

Interestingly, the incubation of an equimolar quantity of both proteins does not lead to the complete shift of the *Pa*MprF peak to a lower elution volume, indicating that not all *Pa*MprF is bound to AlaRS. This could indicate that the interaction between these two species has a modest K_D, and so a higher concentration of AlaRS would be required for all *Pa*MprF molecules to form complexes. Similarly, it could be the case that interaction between the two proteins is transient in nature, resulting in fast-binding kinetics that would give rise to the presence of both individual species and the complex species at any given time as seen in this co-elution SEC profile.

4.2.4. *Pa*MprF does not co-elute with a catalytic fragment of AlaRS, AlaRS^{440}

This potential interaction was investigated further by assessing whether *Pa*MprF could bind to a truncated form of AlaRS, to provide insight on where the interaction surface between these two proteins may be. The AlaRS full sequence comprises three distinct domains (Swairjo *et al.* 2004): an N-terminal catalytic domain, responsible for aminoacylation of tRNA (residues 1-440); an editing domain, for proofreading and removing incorrectly aminoacylated $tRNA^{Ala}$

(residues 441-698); and a C-terminal oligomerisation domain (residues 699-874), as shown in **Figure 4.5**:

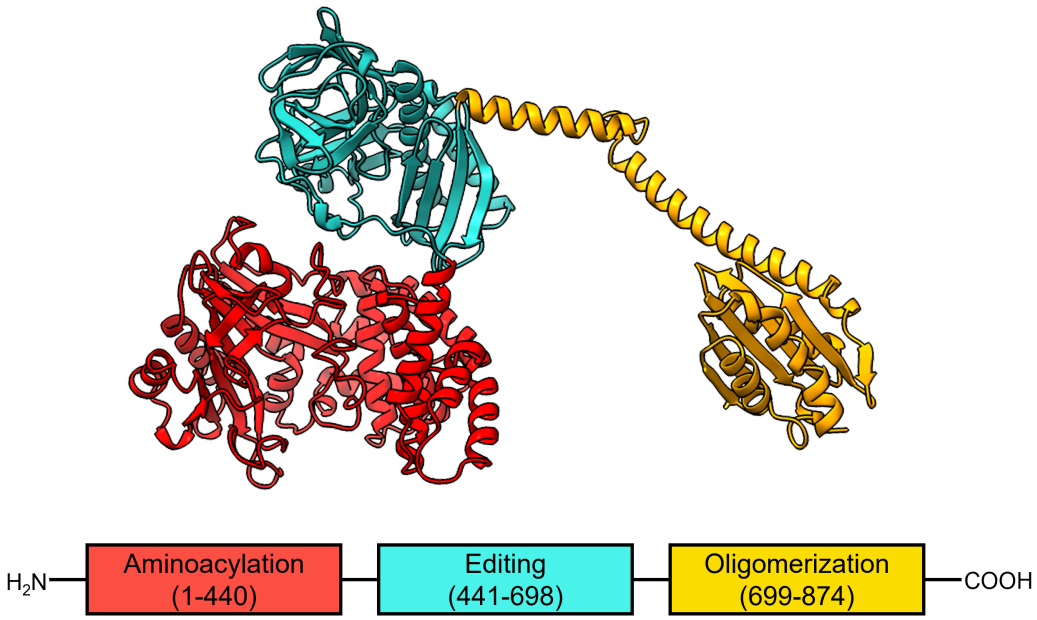

Figure 4.5: AlaRS domain organisation. Predicted AlphaFold structure of the *P. aeruginosa* AlaRS (UniProt accession: Q9I553), coloured by domain (aminoacylation = red, editing = blue, oligomerisation = yellow). Residue boundaries for domains are shown schematically below.

As such, a truncated construct of the aminoacylation domain of AlaRS, construct AlaRS^{440}, was cloned, expressed and purified as outlined in **Methods (2.4.12.)** to determine whether *Pa*MprF interacted with AlaRS at this catalytic domain. The SEC co-elution experiment above was repeated with the purified construct and the results of this co-elution are shown in **Figure 4.6:**

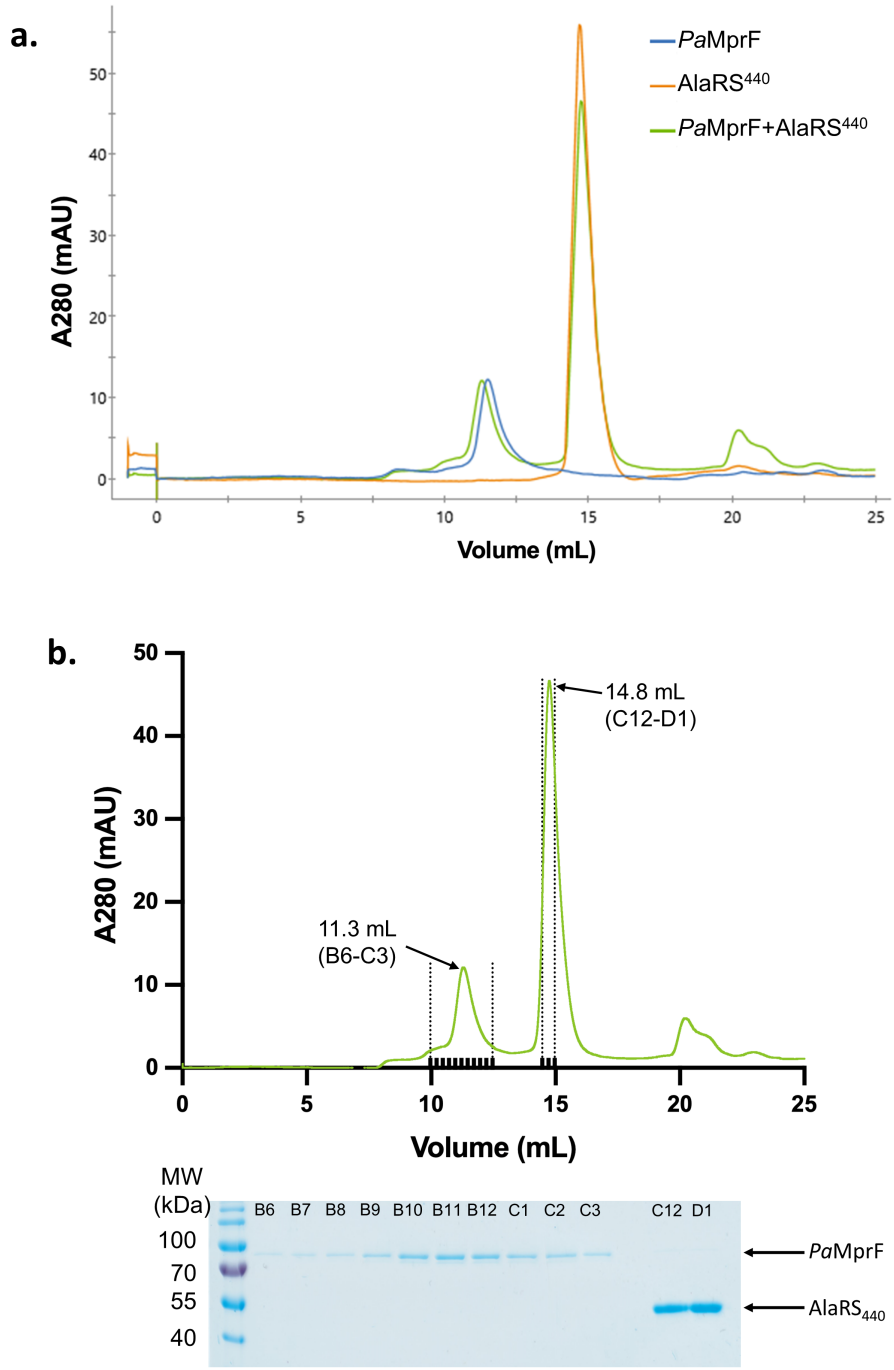

Figure 4.6: MprF-AlaRS^{440} SEC chromatograms. a. Overlay of SEC traces of *Pa*MprF (blue), AlaRS^{440} (orange) and both together (green). **b.** SEC trace of *Pa*MprF-AlaRS with a 10 %, Coomassie stained SDS-PAGE gel of fractions. B9-C2 = 11.3 mL peak, C12-D1 = 14.8 mL peak.

The overlaid SEC chromatograms in **Figure 4.6a** show that addition of AlaRS^{440} to *Pa*MprF does not lead to a significant reduction in the elution volume of *Pa*MprF, nor the appearance of a third peak at a lower elution volume as was seen with *Pa*MprF and full-length AlaRS. Indeed, the SDS-PAGE gel in **Figure 4.6b** highlights the absence of any AlaRS^{440} in the 11.3 mL

*Pa*MprF peak. This indicated that AlaRS^{440} does not co-elute with *Pa*MprF on SEC and therefore suggests that *Pa*MprF binds to AlaRS not at the catalytic domain, but at its editing or oligomerisation domains.

The interaction between *Pa*MprF and full-length AlaRS was then further characterised by SPR to estimate the affinity constant (K_D) for their interaction.

4.2.5. SPR suggests a 7 μM K_D for the *Pa*MprF-AlaRS interaction

SPR experiments were conducted using an NTA sensor chip, immobilising His-tagged AlaRS to the surface of this chip to act as ligand and then flowing increasing concentrations of *Pa*MprF over the surface of this chip as an analyte. The sensorgram from this SPR experiment and the saturation curve derived from this sensorgram are shown in **Figure 4.7.**

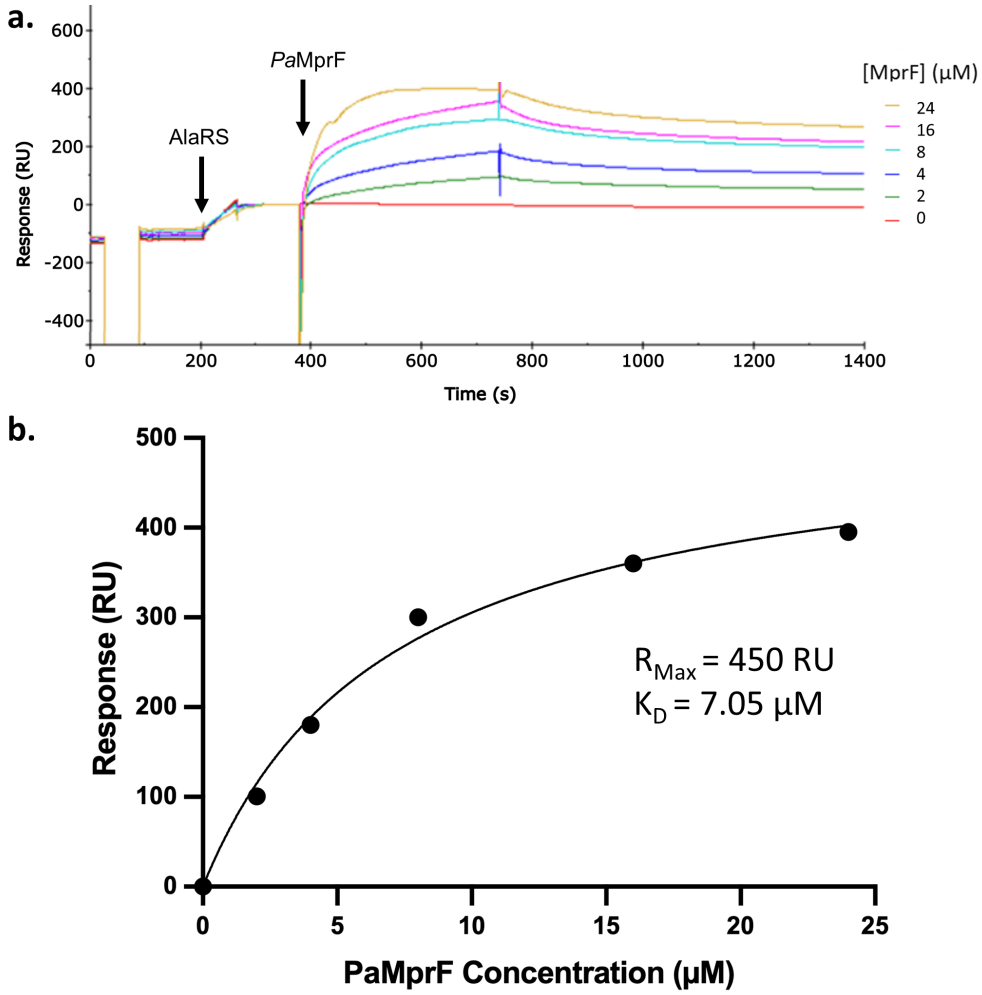

Figure 4.7: *Pa*MprF-AlaRS SPR. a. Adjusted sensorgram of *Pa*MprF-AlaRS SPR experiments. The NTA sensor chip was regenerated at t = 20 s, then loaded with His-tagged AlaRS at t = 200 s. Association phase of *Pa*MprF injection started at t = 380 s, and then dissociation phase washing at t = 740 s. **b.** Saturation curve obtained from RU values at the end of the association phase for each *Pa*MprF concentration. Points are fitted to a Langmuir isotherm (R^2 = 0.993) giving an estimated K_D of ~7 µM.

The SPR data in **Figure 4.7a** above show that *Pa*MprF binds to immobilised AlaRS in a concentration dependent manner, saturating at high [*Pa*MprF] as shown by the saturation curve in **Figure 4.7b.** Fitting to this saturation curve gives an estimate for the K_D of the interaction of ~7 µM. Together with the previous experiments, this provides clear biochemical evidence that *Pa*MprF and AlaRS interact with moderate affinity, to form a complex in solution.

4.3. Purified *Pa*MprF can modify NBD-PG *in vitro*

4.3.1. $tRNA^{Ala}$ synthesis and purification by modified IVT

The assessment of *Pa*MprF aminoacylation activity requires charged-$tRNA^{Ala}$ as a substrate for the addition of L-alanine to a PG headgroup. A mixed isolate of *E. coli* tRNAs is available commercially, but production of a specific alanine-cognate tRNA requires the use of *in vitro* transcription (IVT). Charging of tRNA with its cognate amino acid requires the presence of a CCA-3' sequence, the universally conserved site of aminoacylation. In standard run-off IVT, a T7 RNA polymerase is used to synthesise an RNA sequence by transcription of a synthetic gene. However, run-off transcription often results in the 3' extension of RNA transcripts (Krupp 1988, Triana-Alonso *et al.* 1995). As such, this technique applied to a tRNA sequence could result in tRNA products with 3' extensions that would render them unable to be aminoacylated. Therefore, the *P. aeruginosa* $tRNA^{Ala}$ sequence was produced by IVT using a modified synthetic gene sequence shown below in **Figure 4.8**:

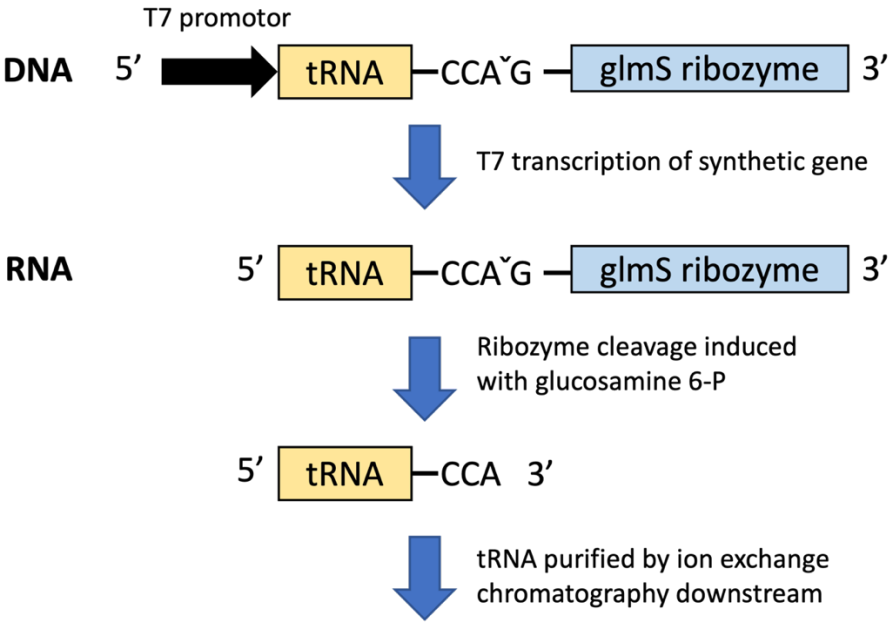

Figure 4.8: tRNA *in vitro* transcription protocol. tRNA of interest is fused to the glmS ribozyme in a synthetic gene. The gene is transcribed and then the ribozyme cleaves itself at the CCAˇG site upon induction with glucosamine-6-P, leaving the required CCA-3' acceptor stem crucial for tRNA function.

The *P. aeruginosa* $tRNA^{Ala}$ gene sequence (strain PAO1, locus tag: PA4280.3) was fused to a glmS ribozyme sequence. The glmS ribozyme was first discovered in *B. subtilis* upstream of the *glmS* gene which encodes an enzyme that produces glucosamine-6-phosphate (GlcN6P) and functions as the first step in the synthesis of sugar components for cell-wall synthesis (Winkler *et al.* 2004). The glmS ribozyme sequence is activated in the presence of GlcN6P, resulting in it catalysing self-cleavage of the ribozyme sequence from mRNA at a 5'-AˇG cleavage site. Such specific metabolite induced activation of mRNA cleavage has since been utilised in IVT of RNA constructs to produce uniform 3' transcript ends by fusing the gene of interest to the glmS ribozyme gene sequence at the 5'-AˇG cleavage site (Batey and Kieft 2007, Reinhard *et al.* 2017). In this modified IVT protocol, the synthetic gene is produced by standard run-off IVT with T7 RNA polymerase. Then glmS ribozyme auto-cleavage is activated by incubation with GlcN6P to produce a separated tRNA sequence with a uniform CCA-3'. The tRNA and glmS RNA sequences are then separated by ion exchange chromatography (IEX) (Anderson *et al.* 1996, Shields *et al.* 1999). The result of the IEX purification of *P. aeruginosa* $tRNA^{Ala}$ is shown in **Figure 4.9:**

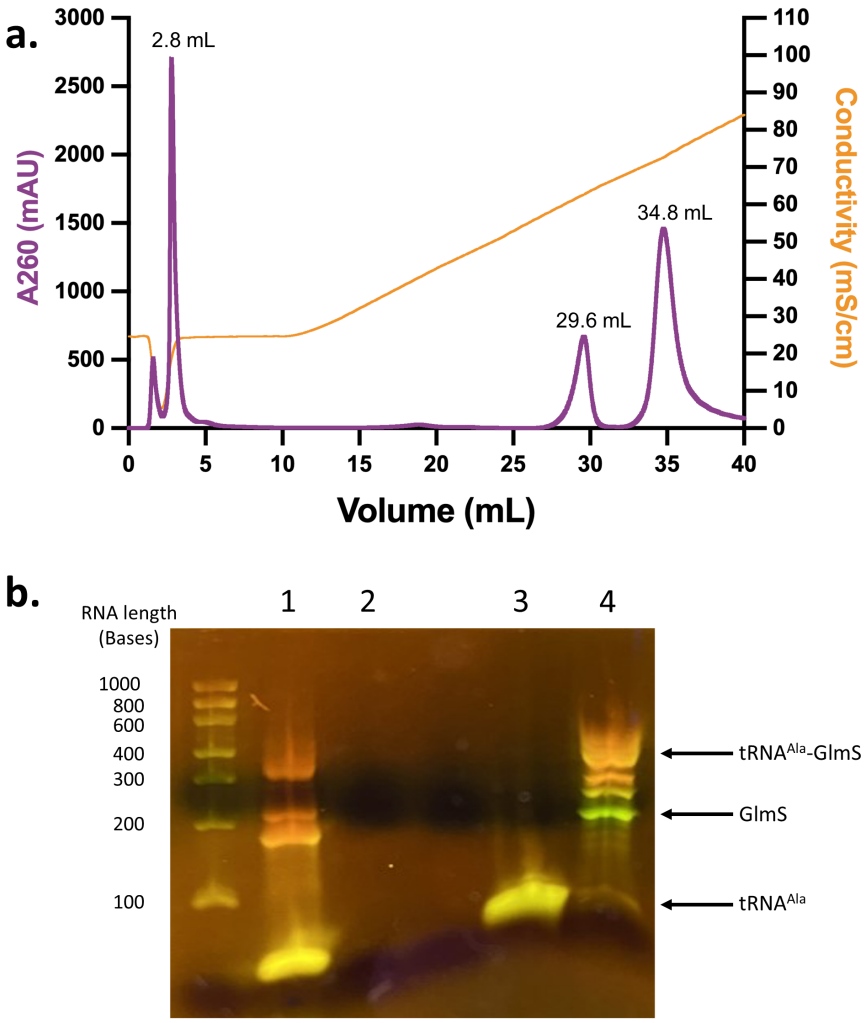

Figure 4.9: *P. aeruginosa* tRNA^{Ala} purification. a. IEX chromatogram showing elution of RNA from an anion exchange column with increasing salt concentration. **b.** Denaturing 4 % agarose gel of: *1)* IVT mixture before IEX separation, *2)* IEX peak at 2.8 mL, *3)* IEX peak at 29.6 mL, *4)* IEX peak at 34.8 mL. The altered migration of bands in lanes 3 and 4 compared to lane 1 is a result of the difference in salt concentration between the samples, as can be seen from the non-uniform running front at the bottom of the gel.

The IEX chromatogram in **Figure 4.9a** shows that two peaks eluted from the anion exchange column as the salt concentration of the elution buffer is increased, one at 29.6 mL and one at 34.8 mL. The agarose gel in **Figure 4.9b** shows that the peak at 29.6 mL corresponds to tRNA^{Ala} (expected length = 75 bases), and that the tRNA is successfully separated from the Glms ribozyme (expected length = 200 bases) and uncleaved tRNA^{Ala}-GlmS (expected length = 275 bases) which elute together in the broader peak at 34.8 mL. The peak fractions corresponding to tRNA^{Ala} were pooled and concentrated to 50 µM for use in the *Pa*MprF synthase assay described in the next section.

4.3.2. Purified *Pa*MprF is catalytically active

To assess the ability of *Pa*MprF to aminoacylate lipid substrate, a modified activity assay to that used by Hebecker *et al.* (2011) was employed. In this assay, the purified *P. aeruginosa* AlaRS was mixed with *in vitro* transcribed and purified $tRNA^{Ala}$ in the presence of L-alanine, ATP, and an ATP-regenerating system of creatine phosphate and creatine phosphokinase to produce charged-$tRNA^{Ala}$. *Pa*MprF is then added to this mixture, along with a molar mixture of 100:1 POPG:NBD-PG. NBD-PG (16:0, 6:0) is a PG lipid with a nitrobenzoxadiole (NBD) fluorophore replacing one of the hydrophobic lipid tails. The reaction is incubated overnight at 4°C and then the lipids from the sample are extracted (described in **Methods – 2.3.1.**) and separated by 1D thin-layer chromatography (TLC). This separates the PG from alanylated PG, and the resulting TLC plate can be imaged with blue light to identify NBD-lipid spots. The results of this experiment are shown in **Figure 4.10:**

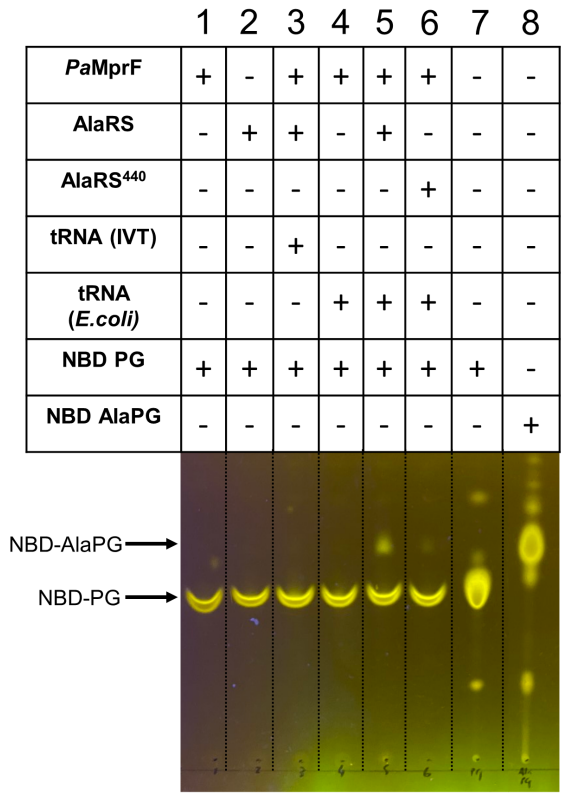

Figure 4.10: *Pa*MprF aminoacylation TLC assay. TLC results of aminoacylation assay (imaged with blue-light). Two control lanes for NBD-PG (7) and NBD-AlaPG (8) demonstrate expected mobilities of these species.

The results of this assay demonstrate that NBD-AlaPG can be produced *in vitro*, but only in lanes 5 and 6 when *Pa*MprF is mixed with AlaRS or AlaRS^{440} and a commercially available *E. coli* tRNA mixture, and the presence of these components in isolation (lanes 1, 2, and 4) is not sufficient for lipid aminoacylation. This demonstrates that purified *Pa*MprF is catalytically active. Since the successful aminoacylation of NBD labelled lipids requires a functional interaction between these lipids and *Pa*MprF, this result also confirms the suitability of NBD-labelled lipids for the planned lipid transport assay. Although a modified NBD-AlaPG spot is also produced in lane 6 when AlaRS^{440} is used for tRNA charging, the size of this spot is significantly smaller when compared to the spot in lane 5 where full-length AlaRS is added. This is despite both AlaRS constructs being used at the same concentration in this assay. This suggests that aminoacylation of PG by *Pa*MprF is more efficient when full-length AlaRS is present, providing further evidence that *Pa*MprF and AlaRS form a complex to facilitate efficient substrate handoff of charged-tRNA^{Ala} and further supporting the observation that AlaRS^{440} does not interact with *Pa*MprF.

Interestingly, use of IVT transcribed tRNA with the other components (lane 3), does not result in the production of a visible AlaRS spot. Instead, tRNA extracted from *E. coli* is required for *Pa*MprF to successfully aminoacylate PG.

4.4. Establishment of a liposome-based lipid transport assay

4.4.1. *Pa*MprF can be successfully reconstituted into liposomes

Initial liposome reconstitution attempts used the lipid composition that had previously been optimised for *Pa*MprF reconstitution into SapNPs (7:3 POPC:POPG). Liposomes were made as outlined in **Methods (2.6.1.).** In brief, chloroform-solubilised lipid stocks were dried

overnight, rehydrated in buffer, and extruded to form liposomes. Liposomes were then destabilised by titration with DDM, before being incubated with *Pa*MprF. Detergent was removed through several additions of adsorbent beads. Proteoliposomes were then pelleted by ultracentrifugation and resuspended for analysis via SDS-PAGE to confirm insertion of *Pa*MprF. The results of this reconstitution are shown below in **Figure 4.11:**

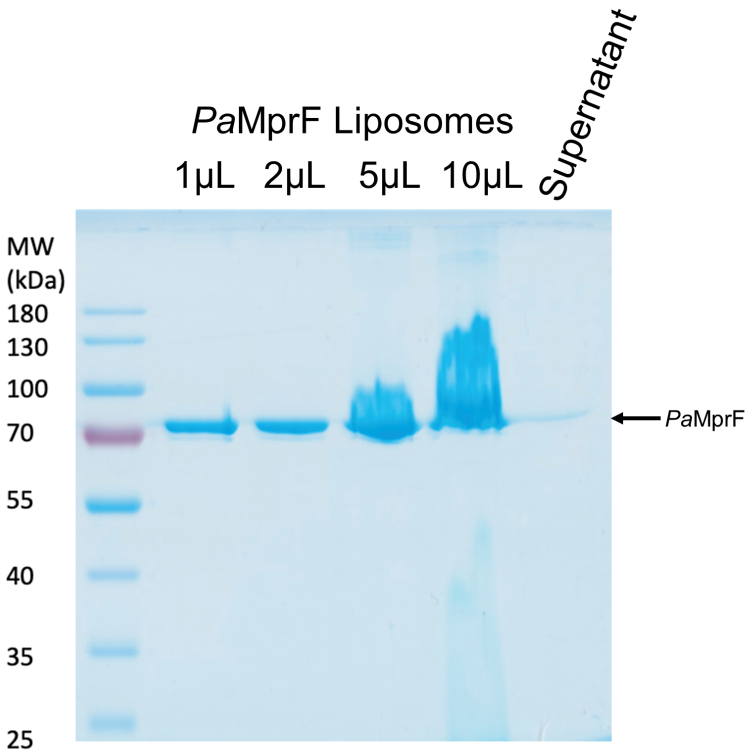

Figure 4.11: *Pa*MprF liposome SDS-PAGE. SDS-PAGE gel (12 %, Coomassie stained) of *Pa*MprF liposomes (1, 2, 5, 10 µL of the same sample loaded to estimate concentration) and the supernatant of the reconstitution mixture following ultracentrifugation.

The majority of *Pa*MprF (~50 %) was recovered in the liposome pellet following ultracentrifugation, with some *Pa*MprF remaining in solution as shown by the weak *Pa*MprF band in the "supernatant" lane of **Figure 4.11.** The smearing of the *Pa*MprF bands at larger sample volumes of liposomes is indicative of the presence of high lipid concentration. This result indicates that *Pa*MprF can be successfully reconstituted into liposomes using a 7:3 POPC:POPG ratio, and hence can be used for establishing a liposome-based lipid transport assay.

4.4.2. Initial trials suggest *Pa*MprF can translocate NBD-AlaPG *in vitro*

Following demonstration that *Pa*MprF can be successfully reconstituted into liposomes composed of the lipid mixture optimised for SapNP trials, initial experiments assessing the ability of *Pa*MprF to transport lipid in these liposomes were conducted. For this, a reduced *Pa*MprF concentration was used (1:100 *Pa*MprF:lipid (w/w)) and the lipid mixture used for liposome reconstitution was doped with 0.4 mol% tail-labelled NBD-AlaPG for use as a reporter lipid. Liposomes were produced as described previously. Control (empty) liposomes were treated as described in **Methods (2.6.1.),** but no *Pa*MprF was added before detergent removal.

In this assay, reconstituted liposomes are continuously monitored in a fluorimeter recording the fluorescence of the NBD-lipid (excitation = 460 nm, emission = 520 nm). The NBD fluorophore can be attached to an acyl tail of a lipid species (**Figure 4.12b**) or to the headgroup. Dithionite, a membrane impermeable compound which bleaches NBD fluorescence, is then added to the sample (**Figure 4.12a**). In empty liposomes, only NBD-lipid in the outer leaflet is bleached, leading to a decrease in fluorescence to ~50 % of its starting value. In liposomes containing an active lipid transporter, the inner leaflet lipids are exposed over time, resulting in the measured fluorescence decreasing below 50 % (**Figure 4.12c**). Over time, the fluorescence would plateau at a final value which represents the proportion of liposomes that contain at least one copy of active lipid transporter. As is widely observed in the literature for use of this assay, fluorescence time-courses never reach a final plateau of 0 % the starting value since there is always a population of liposomes that will be refractory to protein insertion (~15-25 %) (Falzone and Accardi 2020), giving a base-line background fluorescence.

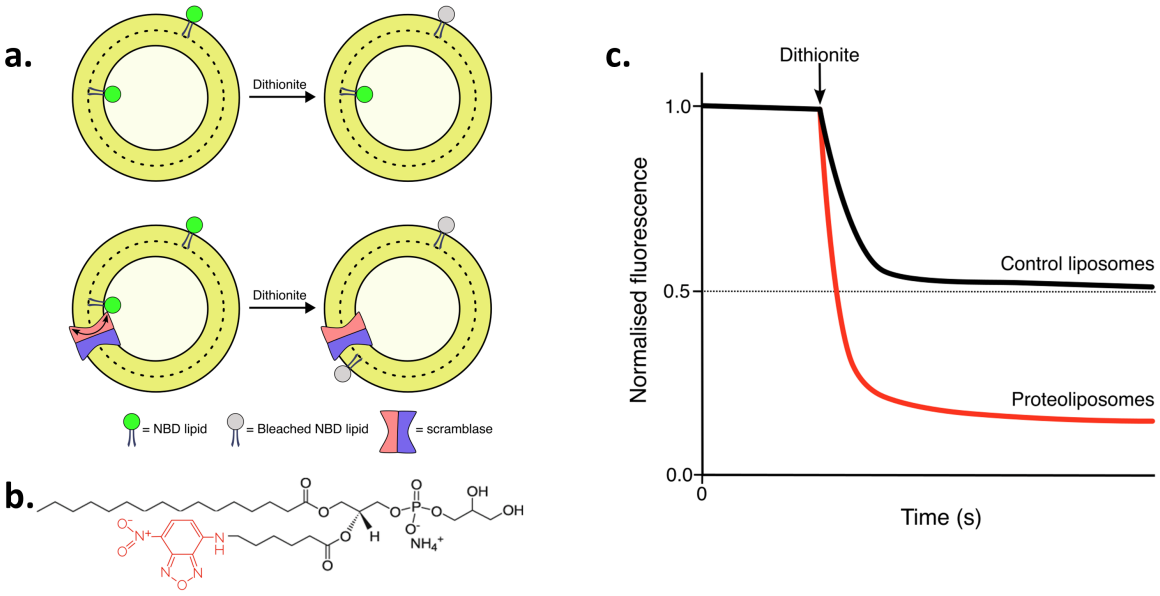

Figure 4.12: *in vitro* Lipid transport assay schematic. a. Schematic of the liposome-based lipid transport assay used in this Chapter. **b.** The skeletal formula of an acyl tail-labelled NBD lipid (NBD-PG) is shown with the NBD fluorophore coloured red. **c.** Idealized fluorescence time-courses for control liposomes (black) and proteoliposomes (red) containing an active lipid transporter.

The results of the first test of this assay in *Pa*MprF liposomes are shown in **Figure 4.13.** For all curves shown in this Chapter, three separate reconstitutions were performed, and fluorescence values measured before dithionite addition were set to a normalized value of 1. Fluorescence time-courses shown are the averages of these three replicates. Fluorescence measurements were performed at 25°C. After two minutes of equilibration at this temperature, dithionite was added to liposomes, and fluorescence continuously monitored for 10 minutes. Triton X-100 was then added to solubilise liposomes and expose any remaining protected lipid to dithionite for the 0 % baseline measurement.

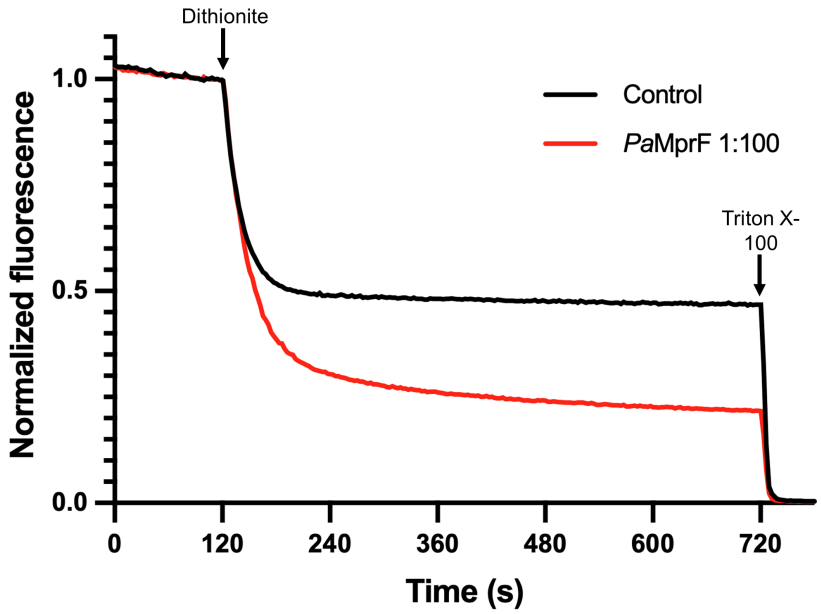

Figure 4.13: *Pa*MprF lipid transport assay. Time-course measuring NBD-AlaPG fluorescence in empty (black) and *Pa*MprF reconstituted (red) liposomes.

As seen in **Figure 4.13,** the empty liposomes decrease to 50 % of starting fluorescence on dithionite addition, as expected. There is a minor yet steady linear decay after reaching this value (rate constant ~1x10^{-5} s^{-1}) until Triton X-100 is added. This linear decrease following plateau is well-described in the literature, reported to represent both the very slow leak of dithionite into liposomes and the photobleaching of the NBD fluorophore (Malvezzi *et al.* 2018). In addition, the spontaneous flip-flop of NBD-labelled phospholipids could also be contributing to this slow linear decrease.

For *Pa*MprF liposomes, the fluorescence decrease on dithionite addition is significantly greater than for the empty liposomes. This decrease occurs in two phases, a marked rapid decrease followed by a slower non-linear decrease that eventually starts to plateau at ~20 % of the starting fluorescence. This two-phase decay of fluorescence in proteoliposomes is widely characterised in the literature exploring scramblase-type lipid transporters (Brunner and Schenck 2019, Falzone and Accardi 2020). This suggests that *Pa*MprF is exposing lipid from the inner to the outer leaflet over time, and is hence functioning as a lipid transporter of NBD-AlaPG.

This initial result was further corroborated by producing a concentration series of liposomes containing different *Pa*MprF:lipid ratios on reconstitution. The results of the liposome transport assay of this concentration series are shown in **Figure 4.14:**

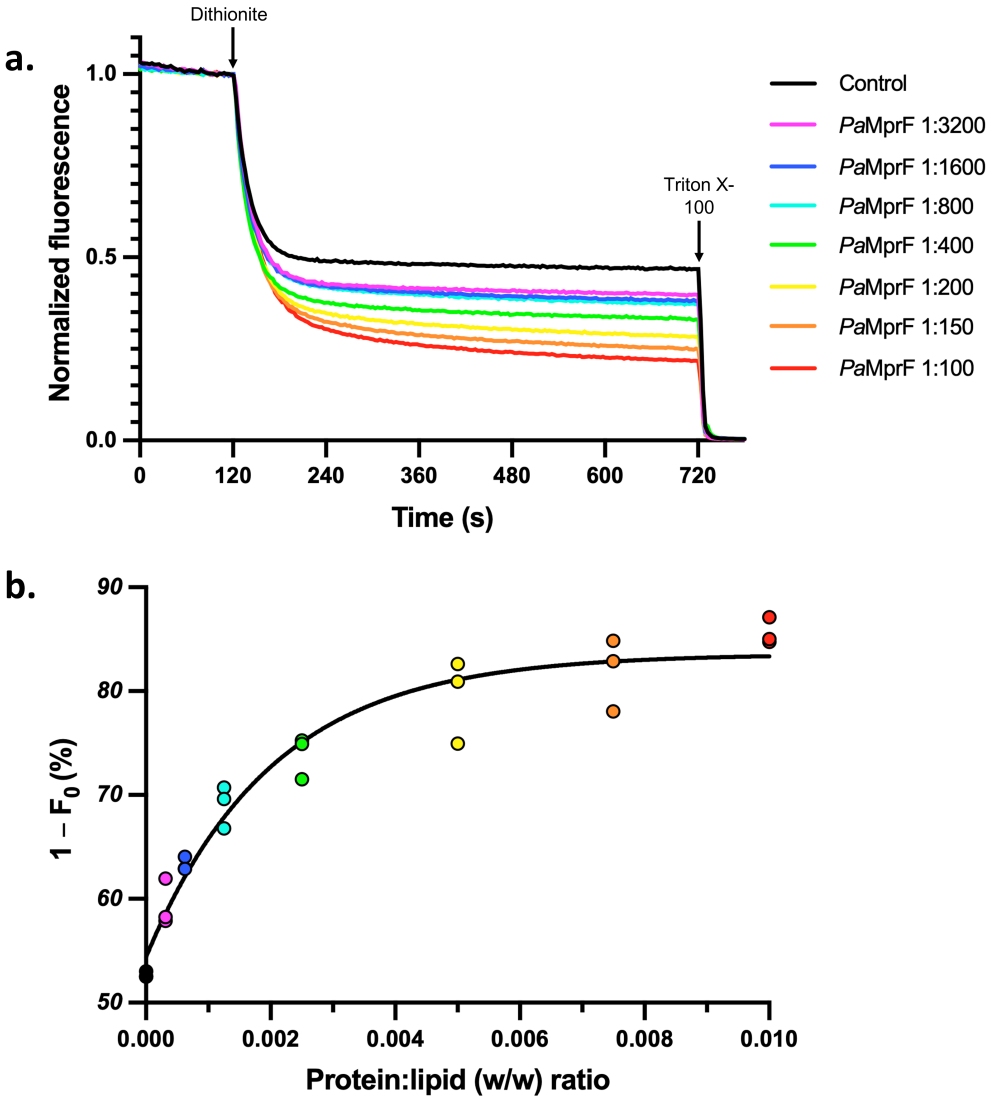

Figure 4.14: *Pa*MprF:lipid concentration series. **a.** Lipid transport assay fluorescence time courses for liposomes with different *Pa*MprF:lipid (w/w) ratios. **b.** A plot of the 1-F_0 vs. *Pa*MprF:lipid (w/w) ratio for each replicate. A mono-exponential fit for the data is shown (R^2 = 0.953), saturating at 1-F_0 = 83.6 %.

In **Figure 4.14a,** the magnitude of the fluorescence decrease observed on dithionite addition is correlated to the concentration of *Pa*MprF: as *Pa*MprF concentration relative to lipid is increased during liposome reconstitution, the observed fluorescence decrease is increased. By

taking the final plateau values (F_0) of each replicate at each concentration, subtracting them from 1 (1-F_0) and plotting these against the *Pa*MprF:lipid ratio, the curve shown in **Figure 4.14b** is produced. This curve highlights that the magnitude of the observed fluorescence decrease begins to saturate as *Pa*MprF concentration increases. Such behavior is also reported in the literature (Menon *et al.* 2011), and is consistent with lipid transport being dependent on protein concentration; as transporter concentration is increased, more liposomes in the reconstitution will contain at least one copy of transporter. However, since a population of liposomes are refractory to protein insertion, there will be a transporter concentration at which all available liposomes will contain at least one transporter. Beyond this concentration, the final fluorescence plateau value recorded will be unchanged, and instead only the rate at which the plateau is achieved will be increased. Therefore, the presence of this saturation curve with a *Pa*MprF concentration series is consistent with the hypothesis that the lipid transport being measured is dependent on *Pa*MprF.

Nevertheless, there are alternative explanations for the observation that reconstitution of liposomes with *Pa*MprF results in a fluorescence decrease compared to empty liposomes:

1. *Pa*MprF is transporting dithionite into liposomes, rather than exposing lipid to the surface of liposomes.
2. *Pa*MprF is exposing inner leaflet lipid to the surface of liposomes, but this is a non-specific effect from the presence of protein secondary structure.
3. *Pa*MprF is not transporting lipid, but lipid is instead preferentially oriented upon reconstitution, possibly induced by a preferential orientation of *Pa*MprF.

In order to rule out each of these possibilities, extensive control experiments were carried out, which are described in the following sections.

4.4.3. Fluorescence decrease is not a result of dithionite transport into liposomes

The first possible alternate explanation for fluorescence decrease is that *Pa*MprF is facilitating dithionite leaking into liposomes to bleach inner leaflet NBD-lipid. This would be consistent with the observed concentration series, as such an effect would also be dependent on *Pa*MprF concentration. Therefore, this possibility was explored by assessing the permeability of control and *Pa*MprF reconstituted liposomes to dithionite using NBD labelled glucose (NBDG). NBDG is a soluble fluorophore, and so when added to a liposome reconstitution mixture before detergent removal with Biobeads, a population of NBDG will be contained within liposomes following detergent removal. Once external NBDG is removed, the permeability of liposomes to dithionite can be assessed by the same method as the lipid transport assay: fluorescence of the NBD label inside the liposome lumen is monitored over time before and after dithionite addition. The results of this NBDG permeability assay for control liposomes and a series of liposomes at three *Pa*MprF:lipid (w/w) concentrations are shown in **Figure 4.15:**

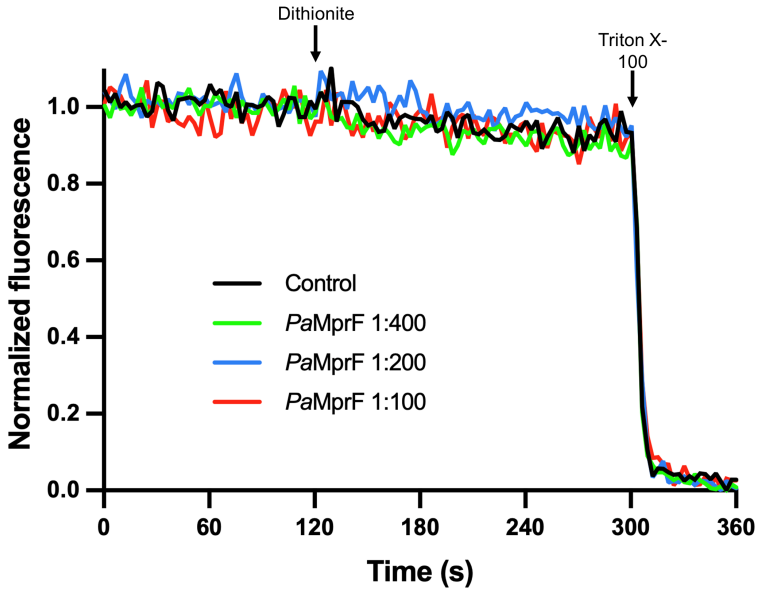

Figure 4.15: NBDG permeability assay. Single replicates of normalized fluorescence time-courses for empty (black) and *Pa*MprF reconstituted (green, blue, red) liposomes at different *Pa*MprF:lipid (w/w) ratios.

This permeability assay is noisier than previous lipid transport assays, as a large proportion of NBDG adsorbs to the surface of Biobeads during the detergent removal stage of liposome formation leading to much lower final NBD fluorescence signal after reconstitution compared to experiments using an NBD fluorophore attached to a lipid. Nevertheless, this assay demonstrates that *Pa*MprF reconstituted POPC:POPG 7:3 liposomes are not significantly more permeable to dithionite than control liposomes containing no *Pa*MprF. Addition of Triton X-100 at the end of the time course confirms that all measured liposomes contained a population of NBDG, and the gradient of fluorescence decrease after dithionite addition but before detergent solubilisation shows that all measured liposome samples behave similarly. Proteoliposomes are therefore no more permeable to dithionite than control liposomes, which demonstrates that *Pa*MprF is not acting as a dithionite channel nor nonspecifically facilitating dithionite leakage into liposomes.

This can also be demonstrated by using an alternate fluorescence bleaching compound to dithionite. One such agent is fatty-acid free Bovine Serum Albumin (BSA) which can be used in a back-extraction assay (Maeda *et al.* 2020, Li *et al.* 2021). In this variant of the transport assay, fatty-acid free BSA at 2 mg/mL is added to liposomes instead of dithionite. BSA extracts lipids from the outer leaflet of liposomes, and as a large soluble protein (~67 kDa MW) is unable to access inner leaflet lipid. BSA binding quenches the fluorescence of outer leaflet NBD by ~50 %, and so BSA addition should drop total fluorescence to ~75 % in empty liposomes. In liposomes reconstituted with active lipid transporters, the fluorescence drop should be larger. The results of the BSA back-extracted experiment are shown in **Figure 4.16:**

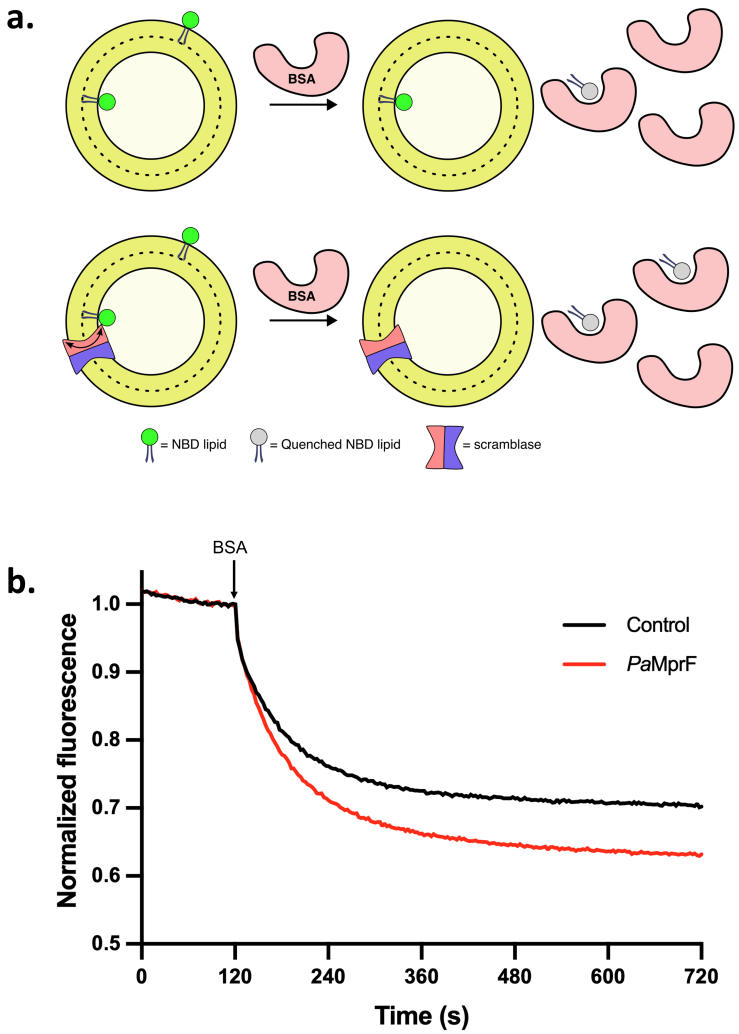

Figure 4.16: BSA back-extraction assay. a. Schematic of rationale behind the BSA back-extraction assay. **b.** Normalized fluorescence time-courses for empty (black) and 1:200 (w/w) *Pa*MprF:lipid reconstituted (red) liposomes (averages of three independent reconstitutions).

A similar result is observed with this assay as with the dithionite assay: fluorescence decrease on addition of BSA is greater for *Pa*MprF liposomes than control liposomes. This further demonstrates that the observed difference is not a result of dithionite leakage, but a difference in the distribution of lipid between control and proteoliposomes. Interestingly, a similar gradual linear decrease in fluorescence is observed in control liposomes, regardless of whether the BSA or dithionite assay is used. This observation strengthens the hypothesis that both NBD photobleaching and spontaneous NBD-lipid flip-flip contribute to the observed fluorescence decrease in control liposomes, rather than attributing the effect solely to dithionite leakage into the liposomes.

4.4.4. Fluorescence decrease is specific to *Pa*MprF

The second possible explanation for the observed fluorescence decrease is that *Pa*MprF is non-specifically facilitating the flip-flop of lipids between leaflets of the membrane due to the presence of protein secondary structure. Indeed, some simple antimicrobial peptides with α-helical structures have been shown to accelerate lipid flip-flop *in vitro* (Nguyen *et al.* 2019). Therefore, this was explored further by repeating the lipid transport assay but with the additional control of liposomes reconstituted with a different membrane protein. *Ilyobacter tartaricus* ATP-synthase c-ring subunit was used for these control experiments. This protein was chosen as a negative control as it is a stable membrane protein that can easily be reconstituted into liposomes, and is a similar size to *Pa*MprF (~100 kDa) so there would be a roughly comparable lipid-exposed surface area for each unit of protein. The same concentration of c-ring and *Pa*MprF (1:100 (w/w) protein:lipid) was used for liposome reconstitution. The results of the liposome transport assay using this control protein are shown in **Figure 4.17:**

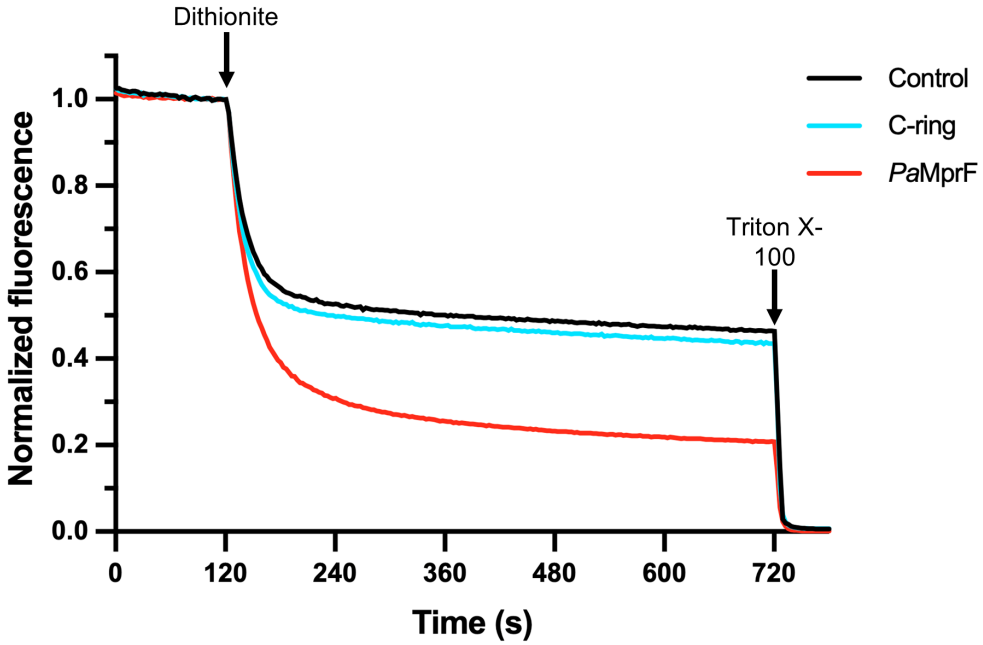

Figure 4.17: Control protein lipid transport assay. Normalized fluorescence time-courses for empty (black), c-ring reconstituted (blue) and *Pa*MprF reconstituted (red) liposomes. Curves are averages of three independent reconstitutions.

Liposomes reconstituted with c-ring give a similar fluorescence decrease on dithionite addition to empty liposomes, with no significant difference in final plateau values and linear rates of decrease over time. However, *Pa*MprF liposomes reconstituted from the same bulk lipid give a significantly lower final fluorescence plateau after dithionite addition, with a clear two-phase non-linear decrease before the plateau is reached, as observed previously. This demonstrates that the c-ring is not able to transport lipid, and that the fluorescence decrease observed is specific to proteoliposomes containing *Pa*MprF.

4.4.5. Fluorescence decrease is not a result of lipid asymmetry on reconstitution

The final possible explanation for the observed fluorescence decrease, other than lipid translocation by *Pa*MprF, is that the reporter NBD-lipid in proteoliposomes is preferentially oriented compared to control liposomes. As seen in electrostatic surface figures of *Pa*MprF in **Chapter 3,** *Pa*MprF has a generally negatively charged periplasmic face, and a generally positively charged cytoplasmic face. Therefore, if there were preferential orientation of *Pa*MprF into liposomes, as has been observed for reconstitution of other membrane proteins in the literature (Young *et al.* 1997), this alternate distribution of charge across the membrane could influence the populations of NBD-labelled reporter lipid in each leaflet upon formation of the liposomes, resulting in lipid asymmetry that could give a fluorescence decrease on addition of dithionite that is lower than control liposomes containing no *Pa*MprF. This scenario, however, is unlikely for *Pa*MprF, as the proteoliposome fluorescence time-courses decrease in two phases on dithionite addition, unlike the single-phase decrease for control liposomes. Lipid asymmetry, if present, would result in similar one-phase curves, as the rate of fluorescence decrease would be proportional to just the rate constant for dithionite bleaching, rather than a combination of dithionite bleaching and lipid transport rate constants. Nevertheless, for completeness this alternative explanation for the observed result was explored. First the orientation of *Pa*MprF in liposomes was assessed.

For orientational assessment of *Pa*MprF, the method developed by Deutschmann *et al.* (Deutschmann *et al.* 2022) was used. In brief, *Pa*MprF was labelled at solvent accessible lysine residues (all of which reside in the soluble domain and so on the same side of the membrane) with a fluorophore derivative of Cy5. This fluorophore is bleached in the presence of the reducing agent tris(2-carboxyethyl)phosphine (TCEP), which is membrane impermeable. Liposomes were produced containing the Cy5-labelled *Pa*MprF (1:100 (w/w) *Pa*MprF:lipid, the same ratio as for transport experiments) and then the fluorescence of Cy5 (excitation = 639 nm, emission = 670 nm) monitored over time. TCEP was added to bleach fluorescence of soluble domain-exposed *Pa*MprF, and then liposomes solubilised with Triton X-100 to bleach fluorescence of soluble-domain protected *Pa*MprF. Therefore, the ratio of fluorescence decrease after TCEP to that after Triton gives an approximation of the ratio between inwardly:outwardly oriented *Pa*MprF. The results of this orientation assay are shown in **Figure 4.18:**

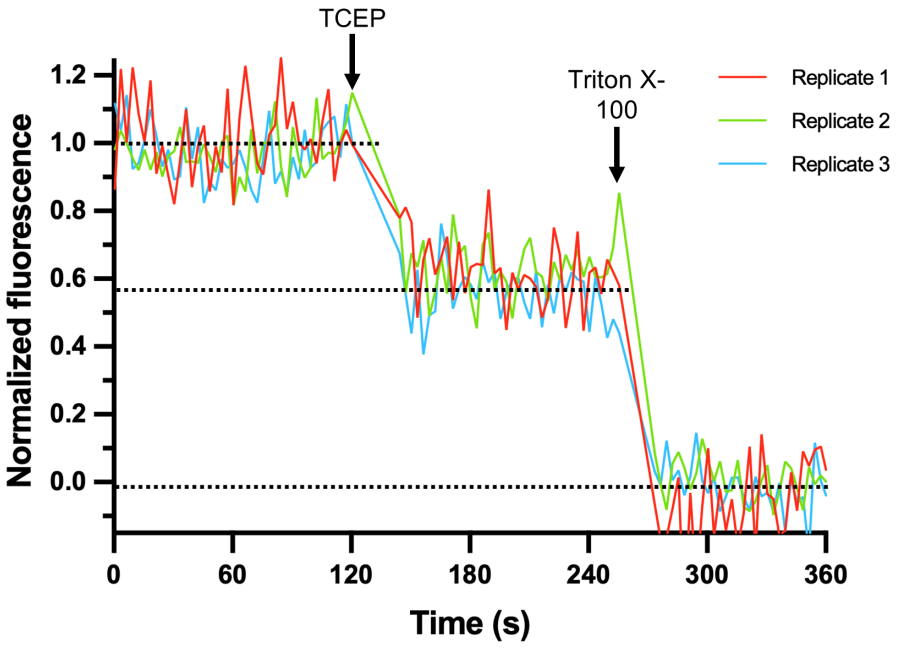

Figure 4.18: *Pa*MprF orientation assay. Normalized fluorescence time-courses of three independent reconstitutions of *Pa*MprF-Cy5. Dotted lines are shown giving estimates of the normalized fluorescence plateaus.

Similar to the NBDG permeability assay, the noise in this experiment is significant as the concentration of *Pa*MprF used for liposome reconstitution, and thus the fluorophore concentration, is very low. In spite of this, the time-courses for each reconstitution replicate show that TCEP and Triton X-100 addition give a similar fluorescence decrease (~40 % decrease on TCEP addition, and ~60 % on Triton X-100 addition). This highlights that *Pa*MprF is not significantly preferentially oriented in liposomes, and that independent reconstitutions of *Pa*MprF give a consistently similar ratio. Therefore, lipid asymmetry in proteoliposomes is not a result of preferential orientation of *Pa*MprF.

The fact that the observed fluorescence decrease in liposome transport assays is a result of *Pa*MprF exposing inner leaflet lipid rather than lipid asymmetry on reconstitution can also be demonstrated by the inactivation of *Pa*MprF in liposomes following reconstitution (**Figure 4.19**).

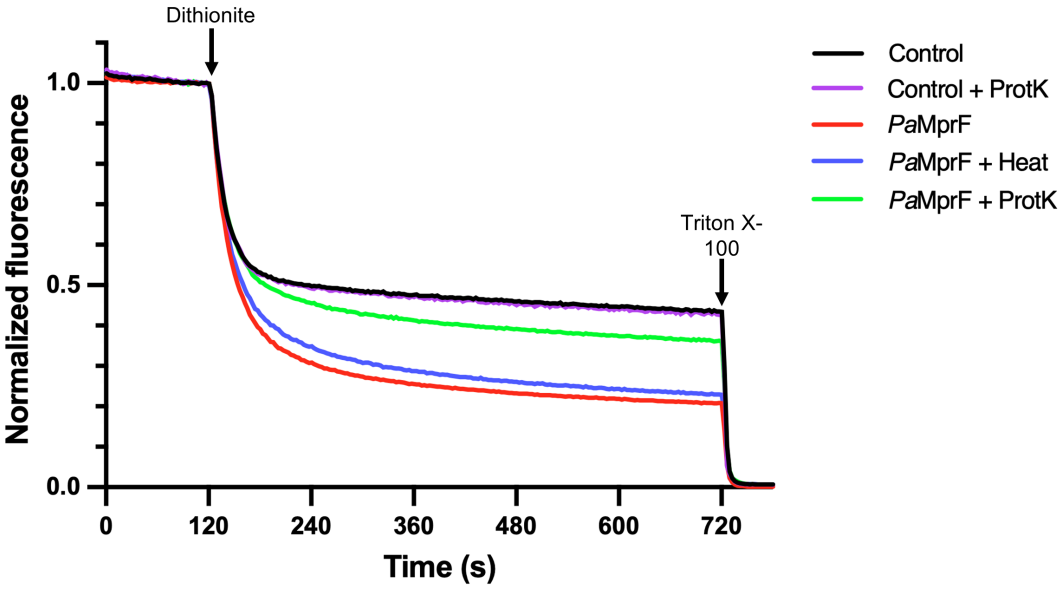

Figure 4.19: Liposome transport assay of inactivated *Pa*MprF. Normalized fluorescence time-courses for *Pa*MprF liposomes that are differently treated after reconstitution and before measurement. Untreated (red), mildly heat treated (blue), and proteinase K treated (green). Empty control liposomes were also measured (black) and proteinase K treated (purple).

In **Figure 4.19,** one batch of proteoliposomes was made and then split into three identical samples that were differently treated before fluorescence measurement. One was kept

untreated on ice, one was heat treated at 37°C for 30 minutes, and one was heat treated 37°C for 30 minutes with the addition of 0.17 mg/mL proteinase K (ProtK). Mild heat treatment of liposomes results in a slower rate of initial fluorescence decrease, suggesting that the heat treatment denatures a population of the *Pa*MprF present in liposomes and thus reduces the number of functional lipid transporters, reducing the rate of total lipid transport. This effect is increased dramatically by treatment with ProtK, which sees the initial rate of decrease and the final plateau value of fluorescence being altered to levels more similar to the control liposomes. Proteinase treatment would not affect the lipid distribution across liposomes leaflets directly, as shown by the same proteinase treatment not affecting the fluorescence decrease of control liposomes. Therefore, the reduction in fluorescence decrease after proteinase treatment must be due to degradation of *Pa*MprF in liposomes. This implies that fluorescence decrease is dependent on *Pa*MprF integrity and reflects the transport of lipid between liposome leaflets.

4.5. Chapter Discussion

4.5.1. *Pa*MprF and AlaRS form a complex

The route by which *Pa*MprF accesses aminoacylated $tRNA^{Ala}$ from the cytosol is currently unclear. Once charged by its cognate tRNA synthetase, aminoacyl-tRNAs are typically bound to EF-Tu, a transcription factor which transports the tRNA to the ribosome for protein synthesis (Louie *et al.* 1984). EF-Tu is expressed at high levels in the cell (Neidhardt *et al.* 1977), and has a high affinity for charged-tRNAs (Louie *et al.* 1984). Once bound by EF-Tu, aminoacylated-$tRNA^{Ala}$ would therefore be inaccessible to *Pa*MprF, raising the possibility of a mechanism in the cell to deliver the charged-tRNA to the membrane before it can be sequestered by EF-Tu. Indeed, some homologues of MprF provide further evidence of the existence of such mechanisms; in *Mycobacterium,* the *lysX* gene encodes an MprF-like protein fused to a lysyl-

tRNA synthetase (Maloney *et al.* 2009), suggesting that the issue of accessing aminoacyl-tRNA can be addressed by having the relevant tRNA synthetase in proximity to MprF.

Using interaction studies, I have demonstrated that *Pa*MprF and AlaRS form a complex in solution, with an estimated K_D of interaction of ~7 μM. This highlights a possible route through which *Pa*MprF receives charged-$tRNA^{Ala}$ substrate from the cytosol for PG aminoacylation, and binding of AlaRS to *Pa*MprF could be seen as an analogous mechanism to that of the *Mycobacterium* protein LysX for providing proximity of substrate. Identification of this complex biochemically also opens up the possibility of the structural characterisation of the *Pa*MprF-AlaRS complex, as such a complex would be of a suitable size for cryo-EM studies. Currently, the exact nature of tRNA binding to the soluble domain of *Pa*MprF is unknown, so further study of this complex in the future could provide key insight into the aminoacylation of lipid by the synthase domain of MprF.

4.5.2. Purified *Pa*MprF is catalytically active, but requires tRNA derived from *E. coli*

The synthase assay established in this Chapter demonstrates that recombinantly expressed and purified *Pa*MprF is catalytically active, and furthermore can bind to and modify NBD-labelled PG. Both of these factors together highlight the suitability of using purified *Pa*MprF in a liposome transport assay that uses similar NBD-labelled reporter lipids.

In addition, this assay showed that aminoacylation of NBD-PG does not occur with tRNA produced by IVT, and instead tRNA extracted from *E. coli* is required to give the resulting NBD-AlaPG spot observed by TLC. Whilst IVT transcribed tRNA would have the same RNA sequence as cell extracted tRNA, it would be lacking the extensive post-transcriptional modifications that occur within the cell (McCloskey and Nishimura 1977). This could then suggest that binding to *Pa*MprF or AlaRS for aminoacylation is dependent on the presence of certain post-

transcriptional modifications not present in IVT tRNA. A similar result was observed by Hebecker *et al.* (2011), whose aminoacylation assay based on radioactivity noted much lower levels of AlaPG produced by MprF when IVT tRNA was used in place of a commercial tRNA mix extracted from *E. coli.* However, in their study IVT tRNA was produced by run-off transcription of a tRNA gene alone, and so lower aminoacylation could have been explained by a large proportion of IVT tRNA having additional bases at the 3' end preventing them from being charged. In my experiments, this is accounted for in the production of IVT tRNA using a glmS ribozyme. The results in this Chapter now suggest that a requirement for the post-transcriptional modification of tRNA can consistently explain the similar result in both studies.

4.5.3. *Pa*MprF can transport NBD-labelled lipid *in vitro*

The key achievement of the work described in this Chapter is the establishment of the NBD-lipid-based liposome transport assay to probe lipid transport mediated by *Pa*MprF. The results detailed here from initial experiments with this assay highlight that *Pa*MprF proteoliposomes exhibit a significantly increased rate of NBD-AlaPG lipid transport compared to empty liposomes and liposomes reconstituted with c-ring control protein. Furthermore, this lipid transport is dependent on *Pa*MprF concentration, and was shown to be a protein specific effect, due to the reduction in transport observed after proteinase K treatment. The extensive controls outlined in this Chapter also allow the conclusion that the observed fluorescence decrease is not a result of transport of dithionite into liposomes, nor an asymmetrical distribution of lipid during reconstitution. Taken together, these data demonstrate that *Pa*MprF specifically translocates NBD-AlaPG between the inner and outer leaflets of liposomes.

Following establishment of this assay and the robust demonstration of *Pa*MprF-mediated lipid transport being measured, the next Chapter describes how this assay was used to probe the key functional unknowns surrounding *Pa*MprF: the energy source for lipid transport, the lipid substrate specificity, and the nature of the transport pathway through the protein.

Chapter 5: Characterising the mechanism of lipid translocation by *Pa*MprF

5.1. Introduction

Having established a lipid transport assay to assess *Pa*MprF activity *in vitro* (**Chapter 4**), this Chapter focuses on characterising the mechanism of *Pa*MprF-mediated transport using this assay. To date, no such *in vitro* characterisation of an MprF homologue has been performed, so the energy source for lipid transport and the specificity of lipid transport are currently unknown. In addition, the structural characterisation of *Pa*MprF in **Chapter 3** has raised the possibility of an alternate lipid transport route to that proposed earlier from a study of *Rt*MprF (Song *et al.* 2021). As such, the details of the lipid transport pathway through MprF require further elucidation by functional assessment of key residues along the proposed routes of transport.

This Chapter seeks to shed light on these mechanistic unknowns by focusing on (i) the energetics of lipid transport, (ii) assessing *Pa*MprF selectivity using a range of different NBD labelled lipid substrates, and (iii) probing the lipid transport pathway through site directed mutagenesis of key *Pa*MprF residues and subsequent assessment of mutant lipid transport activity.

In order to address all of these functional questions, a quantification of lipid transport from fluorescence time-course experimental data is required. For this, experimental data is fitted to a lipid transport model previously derived by Malvezzi *et al.* (2018). The rationale behind this model and demonstration of the resulting fit to experimental data is discussed below.

5.2. Energetics of *Pa*MprF-mediated lipid transport

5.2.1. Characterisation of *Pa*MprF by fitting to three-state model

The rates of lipid transport between liposome leaflets by *Pa*MprF can be estimated by fitting the experimental data from the liposome transport assay to a three-state model previously derived by Malvezzi *et al.* (2018). The full derivation of this model can be found in **Methods (2.6.3.).** Conceptually, for every liposome containing an active lipid translocase, the time-course of the fluorescence decrease is described as:

$$L_i \underset{\beta}{\overset{\alpha}{\rightleftharpoons}} L_o \xrightarrow{\gamma} L_*$$

Where L_i is the population of NBD fluorescent lipid in the inner leaflet of the liposome, L_o is the population in the outer leaflet, and L_* is the population of NBD lipid bleached by dithionite. Interconversion between L_i and L_o is mediated by *Pa*MprF, with α and β representing the forwards and reverse rate constants for translocation ("scrambling", Scr). γ is the rate constant for bleaching of L_o to L_* and is irreversible. The total fluorescence of a population of liposomes at any given time, $F_{tot}(t)$, is given as:

$$F_{tot}(t) = f_0 F_{PF}(t) + (1 - f_0) F_{Scr}(t)$$

Where $F_{PF}(t)$ is the fluorescence of protein-free liposomes, $F_{Scr}(t)$ is the fluorescence of liposomes containing at least one active scramblase molecule, and f_0 is the fraction of liposomes that are protein-free. $F_{PF}(t)$ can be written in terms of γ as:

$$F_{PF}(t) = L_i^{PF} + (1 - L_i^{PF})e^{-\gamma t}$$

Where L_i^{PF} is the fraction of NBD lipid in the inner leaflet of protein-free liposomes. Similarly, $F_{Scr}(t)$ can be written in terms of α, β and γ as:

$$F_{tot}(t) = f_0(L_i^{PF} + (1 - L_i^{PF})e^{-\gamma t}) + \frac{(1 - f_0)\big(\alpha(\lambda_2 + \gamma)(\lambda_1 + \alpha + \beta)e^{\lambda_1 t} + \lambda_1\beta(\lambda_2 + \alpha + \beta + \gamma)e^{\lambda_2 t}\big)}{D(\alpha + \beta)}$$

Where:

$$\lambda_1 = \frac{(\alpha+\beta+\gamma) - \sqrt{(\alpha+\beta+\gamma)^2 - 4\alpha\gamma}}{2} \quad , \quad \lambda_2 = \frac{(\alpha+\beta+\gamma) + \sqrt{(\alpha+\beta+\gamma)^2 - 4\alpha\gamma}}{2}$$

And:

$$D = (\lambda_1 + \alpha)(\lambda_2 + \beta + \gamma) - \alpha\beta$$

The values for γ and L_i^{PF} can be determined from fitting the experimentally determined fluorescence time-course for protein-free liposomes to the expression for $F_{PF}(t)$. An additional linear decay (rate constant = m) can be added to this expression to estimate the rate constant for photobleaching of NBD/permeation of dithionite into liposomes:

$$F_{PF}(t) = L_i^{PF} + \big(1 - L_i^{PF}\big)e^{-\gamma t} - mt$$

Fitting this expression to the control curve obtained from empty liposomes gives the plot shown in **Figure 5.1.**

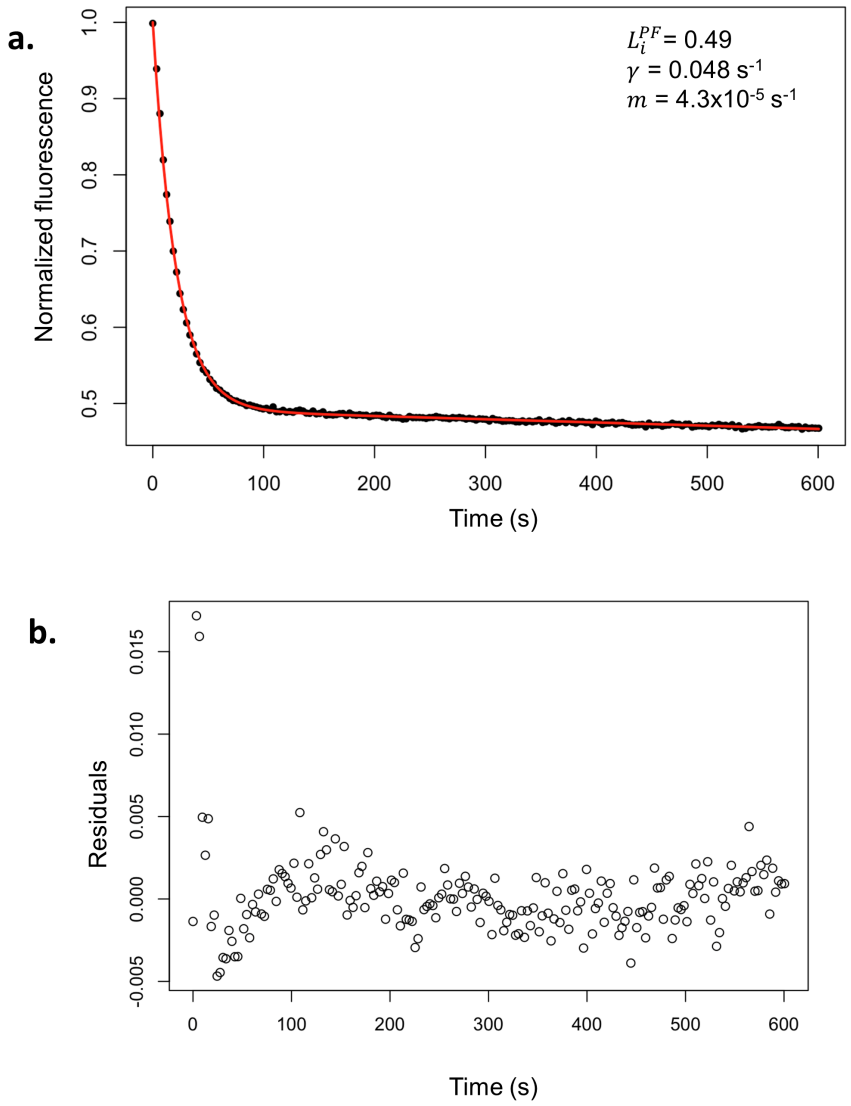

Figure 5.1: Fitting control liposomes. a. Experimental data (black points) of control liposome fluorescence time-course overlaid with a curve fitted from the three-state model (red line). Estimated values of L_i^{PF}, γ and m from this fit are shown. **b.** Residual plot of experimental data to the fitted model.

The values for γ and L_i^{PF} from this control example are 0.048 s^{-1} and 0.49 respectively, consistent with values reported in the literature and expected for this experiment. The linear rate of decay has a rate constant of 4.3x10^{-5} s^{-1}, again similar to values reported in the literature (Lee *et al.* 2018, Malvezzi *et al.* 2018). This value is small enough that it can be ignored in the following determination of rate constants, since rate constants for dithionite bleaching and, as will be demonstrated, lipid transport are several orders of magnitude larger. The residual plot in **Figure 5.1b** demonstrates the quality of the fit to the experimental data, as residual values are very small and are randomly distributed around the line $y = 0$.

These pre-determined values of γ and L_i^{PF} can then be fixed for a given batch of liposomes, so that the only values being solved for are f_0, α and β. Fitting using this formula was carried out on experimental data from independent reconstitutions of *Pa*MprF at 1:200 *Pa*MprF:lipid (w/w) using NBD-AlaPG as a reporter lipid to better characterise the transport of its substrate. The fit and residual plot of this fit are shown in **Figure 5.2,** along with a plot of the resulting rate constants derived from this dataset.

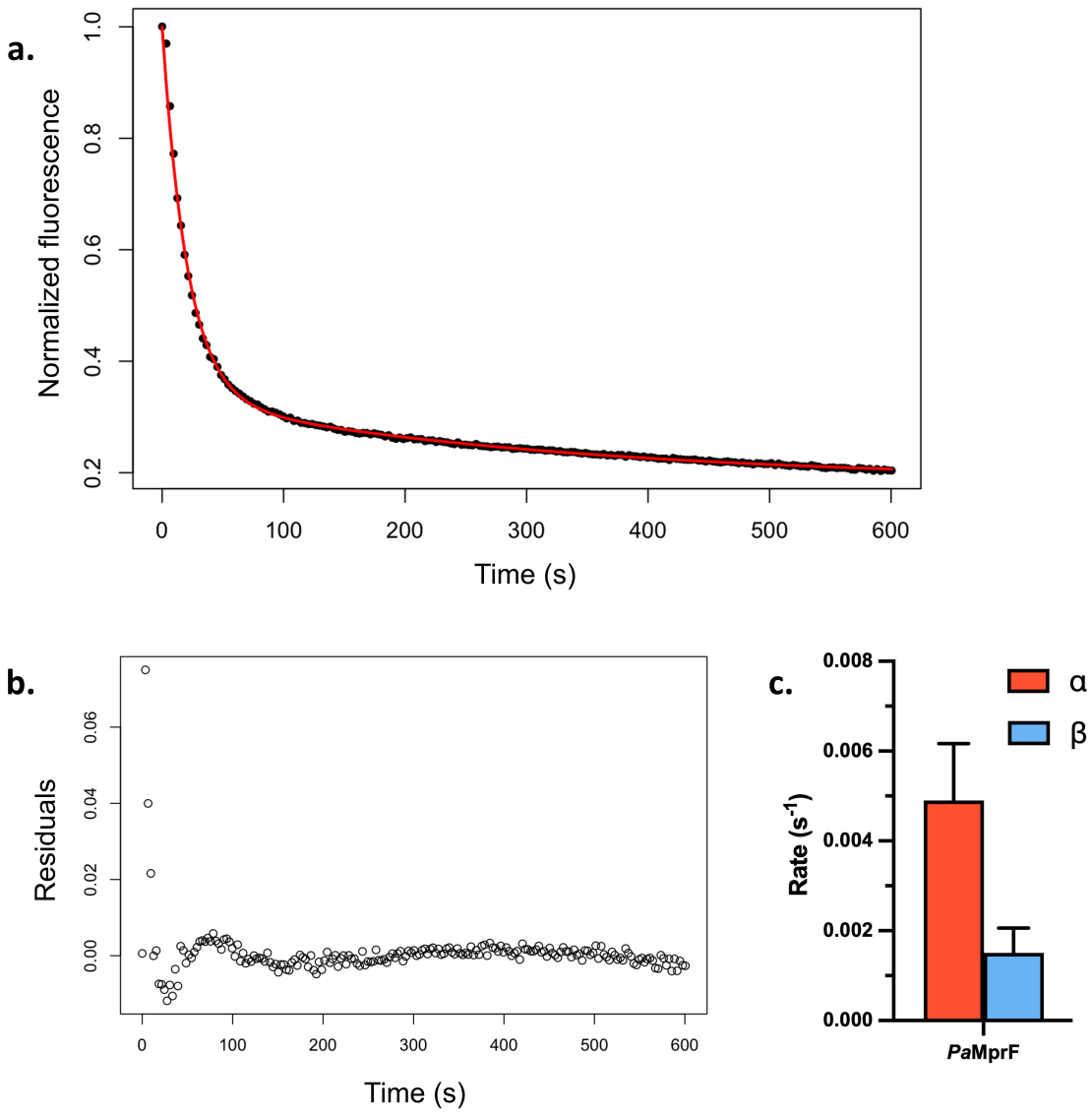

Figure 5.2: Determination of lipid transport rate constants. a. Experimental data (black points) of *Pa*MprF liposome fluorescence time-course overlaid with curve fitted from three-state model (red line). **b.** Residual plot of experimental data to the fitted model. **c.** Bar chart showing the mean α (red) and β (blue) rate constants for lipid transport from fitting (error bars = standard deviation, n = 8).

Figure 5.2 again shows the quality of fit of the three-state model to an example replicate of *Pa*MprF liposome experimental data, with a residual plot again demonstrating the random distribution of residuals around y = 0. The mean rate constants for forwards and reverse lipid transport were calculated as α = 0.0049 s^{-1} and β = 0.0015 s^{-1}, two orders of magnitude greater than the linear decay observed in control liposomes.

Similarly prepared liposomes have been shown to have a distribution of diameters between 100-400 nm, with an average diameter of 150 nm (Malvezzi *et al.* 2018). Assuming this average diameter, the number of lipids per liposome would be ~200,000 (Mimms *et al.* 1981). Therefore, a reconstitution with a 1:200 (w/w) *Pa*MprF:lipid ratio corresponds to an average of ~7 molecules of *Pa*MprF per liposome. From SDS-PAGE analysis of liposomes, ~50 % of *Pa*MprF is successfully reconstituted, so this corresponds to roughly 3-4 *Pa*MprF monomers embedded into each liposome. Assuming *Pa*MprF is facilitating transport of all lipid species in the liposome, the rate of lipid transport would correspond to:

$$Lipid\ Transport\ Rate = \frac{(Total\ lipids\ per\ liposome) \times (Macroscopic\ Rate\ Constant)}{Number\ of\ \mathrm{Pa}MprF\ molecules\ per\ liposome}$$

Hence, ~300 lipids would be transported per second per *Pa*MprF monomer, similar to values reported for scramblases in the literature (Bushell *et al.* 2019). It is important to note that the values of α and β reported here are macroscopic rate constants, and as such are affected by many microscopic factors (e.g. number of *Pa*MprF molecules per individual liposome, the specific activity of each molecule) (Lee *et al.* 2018). For this reason, the values of α and β can vary across reconstitution experiments due to variation in the preparation of liposomes.

The observed difference between α and β is ~3-fold. Previous studies have also observed differences between the determined values of α and β, with it commonly being the case that $\alpha > \beta$ (Lee *et al.* 2018, Malvezzi *et al.* 2018, Bushell *et al.* 2019). This difference has been suggested to be a result of some scramblases being preferentially oriented in liposomes and favouring lipid transport in one direction (Malvezzi *et al.* 2018). The orientation assay carried out in **Chapter 4** demonstrated that approximately 60 % of the *Pa*MprF population is oriented with the soluble domain contained within the liposome lumen following reconstitution. As $\alpha > \beta$ for *Pa*MprF liposomes, this suggests that *Pa*MprF slightly favours the transport of AlaPG from the cytoplasmic leaflet to the periplasmic leaflet of the bacterial inner membrane. Alternatively, other *Pa*MprF-independent factors may result in this disparity. For example, liposome surface tension may mildly favour the transfer of lipid from the inner to the outer leaflet. Similarly, dithionite chemically bleaches NBD to the non-fluorescent aminobenzoxadiazole, and an influence of this chemical modification on transport kinetics cannot be ruled out.

5.2.2. *Pa*MprF lipid transport rates are unaffected by Sybody29

As described in Results **Chapter 3**, there are significant structural differences between *Pa*MprF and *Rt*MprF. Whilst it is appealing to consider that these represent different activity states of the protein, the possibility must be considered that the structural changes may be a consequence of Sybody29 binding to *Pa*MprF. Therefore, the effect of Sybody29 binding was investigated using the liposome transport assay, by determining the rate constants with the three-state model outlined above. For *Pa*MprF-sybody liposomes, *Pa*MprF was incubated with a 5-fold molar excess of Sybody29 on ice for 30 minutes before addition to destabilised liposomes. Lipid transport with NBD-AlaPG was assessed as above, and fluorescence time-courses fitted to obtain values for α and β. These values are shown in comparison to *Pa*MprF liposomes alone in **Figure 5.3:**

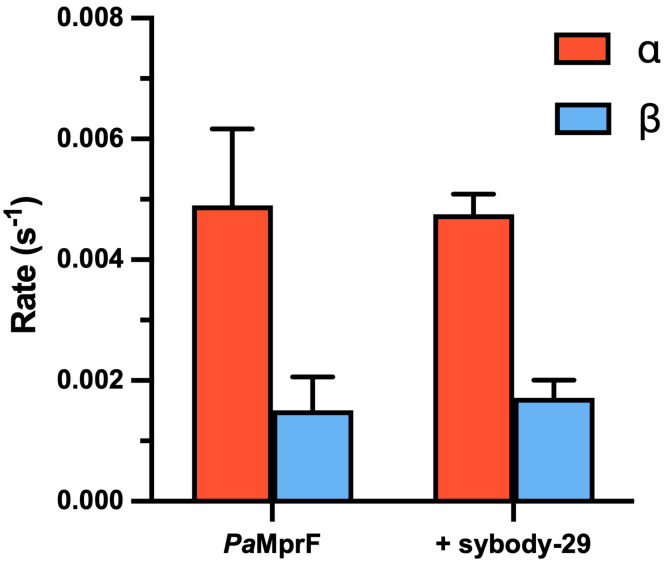

Figure 5.3: Effect of Sybody29 on *Pa*MprF-mediated lipid transport. Bar charts of α and β rate constants for *Pa*MprF (n = 8) and *Pa*MprF-Sybody29 (n = 3) proteoliposomes (error bars = standard deviation).

The determined values of *Pa*Mpr-Sybody29 liposome rate constants are not significantly different to those obtained from *Pa*MprF liposomes, indicating that Sybody29 does not have an effect on the rate of lipid transport mediated by *Pa*MprF in liposomes.

Based on this result, it is unlikely that the binding of Sybody29 induces a strong structural alteration in *Pa*MprF, in line with the similarity of *Pa*MprF cryo-EM maps determined with and without bound Sybody29 discussed in **Chapter 3.**

5.2.3. *Pa*MprF lipid transport rates are unaffected by common activators

The energetics of MprF-mediated lipid transport have been a matter of speculation since the discovery of the protein. Whilst the work described above and in **Chapter 4** has demonstrated that *Pa*MprF can transport NBD-labelled lipid in proteoliposomes under "standard" buffer conditions (100mM HEPES pH 7.6, 100mM KCl), it could be the case that *Pa*MprF transport rates are stimulated by the presence of an activating compound or ion gradient. TMEM16

family lipid scramblases have been shown to exhibit a 4-fold increase in transport rates in the presence of 0.5 mM Ca^{2+} (Bushell *et al.* 2019), and the bacterial LtaA lipid transporter is similarly stimulated by the establishment of a proton gradient across liposomes (Zhang *et al.* 2020). MprF-mediated lipid transport has previously been suggested to be driven by the proton-motive force (Song *et al.* 2021). Therefore, the effect of liposome pH gradients on lipid transport rates, as well as the effect of other possible activators and energy sources, was investigated by their addition to liposome samples before dithionite addition in fluorescence time-course measurements. The effect of an induced concentration gradient of AlaPG between liposome leaflets on lipid transport rates was also of interest, and so the lipid hydrolase PA0919 (discussed in the **Introduction – 1.3.4.**) was purified for this purpose. However, the purified PA0919 could not hydrolyse NBD-labelled AlaPG and so this effect could not be investigated (see **Appendix 6** for details). The effects of Ca^{2+} (1 mM), ATP (1 mM), pH gradients (low external pH = 7.2, high external pH = 8.0, in both cases a ΔpH of 0.4 units between inside and outside), and a high external Na^{+} gradient (100 mM NaCl replacing KCl in the liposome buffer to ensure internal and external solutions were isotonic) were tested by triplicate measurement of independent *Pa*MprF liposome reconstitutions. In addition, the previously demonstrated effects of mild heat treatment and proteinase K treatment of proteoliposomes (**section 4.4.5**) were measured in triplicate to quantify their effects on lipid transport rates. The resulting mean α and β values derived from these experiments are shown in **Figure 5.4,** alongside the values for *Pa*MprF in the absence of any activating conditions (Control).

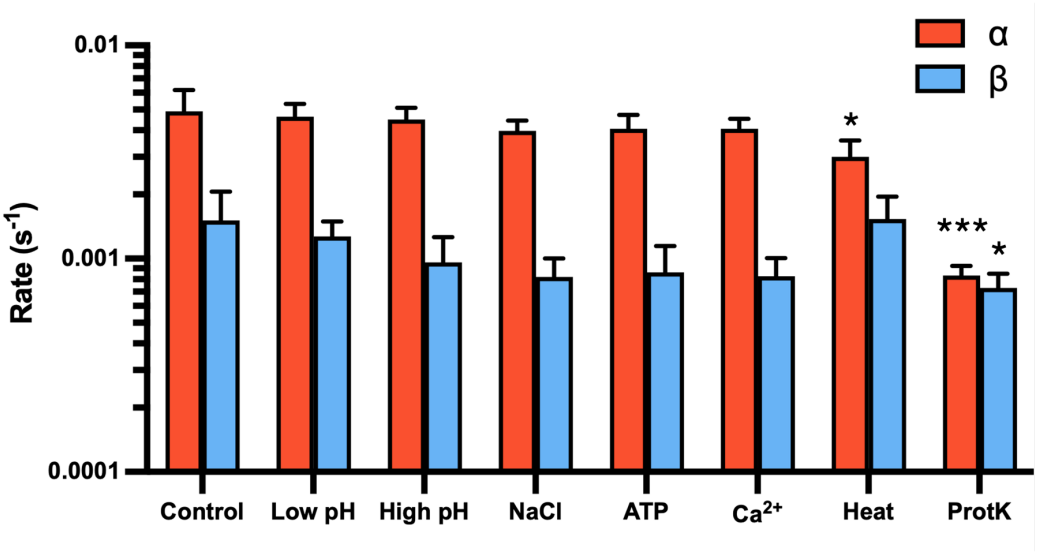

Figure 5.4: Effect of common activators on lipid transport rates. Bar chart plotting α (red) and β (blue) rate constants of *Pa*MprF-mediated lipid transport in the absence (Control) and presence of common activators, as well as following heat and proteinase K (ProtK) treatment. WT values are previously reported (n = 8), all other values are n = 3 (error bars = standard deviation). Asterisks mark values of α and β statistically significant from Control values determined by unpaired *t*-tests (* = $P \leq 0.05$, ** = $P \leq 0.01$, *** = $P \leq 0.001$).

Figure 5.4 demonstrates that none of the conditions tested resulted in an increase in the values of α and β. This suggests that *Pa*MprF is indeed acting as a passive rather than an active transporter - a scramblase - since the presence of common energy sources does not result in an increase in the rate of lipid transport.

Indeed, the only conditions that give a significant difference in rate constants compared to untreated *Pa*MprF liposomes are heat-treated and proteinase K treated samples, both of which give a decrease in rate constants. The decrease is modest for heat-treated samples, with α decreasing from 0.0049 s^{-1} to 0.0030 s^{-1}. However, proteinase treatment results in a 6-fold decrease in the rate of forwards lipid transport, decreasing to 0.0008 s^{-1}, and the rate of reverse transport also decreasing from 0.0015 s^{-1} to 0.0007 s^{-1}. This quantifies the effect seen previously, confirming that heat and proteinase treatment act to significantly reduce the rates of lipid transport mediated by *Pa*MprF, as expected.

5.2.4. *Pa*MprF lipid transport does not require the PMF

Whilst the rate analysis above suggests that the presence of a pH gradient does not significantly increase the rate of lipid transport, the permeability of empty and *Pa*MprF reconstituted liposomes was tested using the pH sensitive dye 8-hydroxypyrene-1,3,6-trisulfonic acid (HPTS) to confirm that proteoliposomes are able to maintain a pH gradient like the one that was used above for analysis of lipid transport rates. If proteoliposomes can maintain a pH gradient, this would then suggest that the lack of difference in lipid transport rates is due to *Pa*MprF transporting lipid independently of the PMF.

HPTS is a fluorescent compound (emission maximum = 510 nm) with a pKa of ~7, and the conjugate acid-base pair at this pKa have two different excitation maxima. The deprotonated form has an excitation maximum at 455 nm, and the protonated form at 405 nm, with an isosbestic point for the dye at 419 nm excitation wavelength. Therefore, HPTS can be used to monitor the pH of a solution through the change in its excitation maximum. A calibration curve characterising HPTS behaviour is shown in **Figure 5.5:**

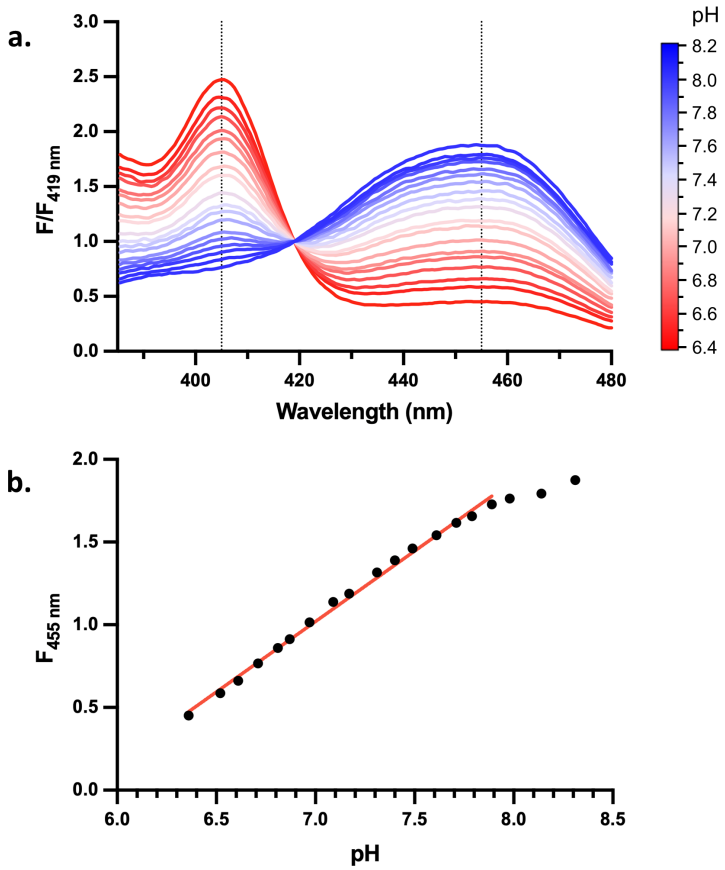

Figure 5.5: HPTS calibration curve. a. Excitation spectra (emission fixed at 510 nm) of HPTS in different pH solutions (pH 6.4-8.2, coloured red-blue). Spectra are normalized to the isosbestic point of HPTS at 419 nm. The pH sensitive excitation peaks at 405 nm and 455 nm are marked with dotted lines. **b.** Calibration curve showing the linear relationship between the normalized $F_{455\ nm}$ excitation peak and pH. A linear fit between pH 6.4–7.8 is shown in red (R^2 = 0.997).

Figure 5.5a shows the change in the magnitude of excitation peaks 405 nm and 455 nm as pH is varied. **Figure 5.5b** focuses on just the normalized 455 nm peak and shows its linear relationship with the changing pH, demonstrating that HPTS can be used as a pH sensor over the linear range of 6.4 – 7.8 pH units.

HPTS was reconstituted into empty and *Pa*MprF loaded liposomes at pH 7.6 in the same manner as previously described for the soluble dye NBDG in **Chapter 4**. External HPTS was removed, as for NBDG previously, such that the only fluorescence signal measured corresponded to HPTS contained within liposomes. Liposomes were then diluted in buffer at pH 7.2 or pH 8.0 (corresponding to the pH values used in the previous section to assess pH

effect on lipid transport rates) to give a ΔpH of 0.4 units, and the fluorescence of HPTS was monitored over time at excitation = 455 nm, emission = 510 nm. After 3 minutes, Triton X-100 was added to solubilise liposomes and expose HPTS to the bulk buffer (**Figure 5.6**).

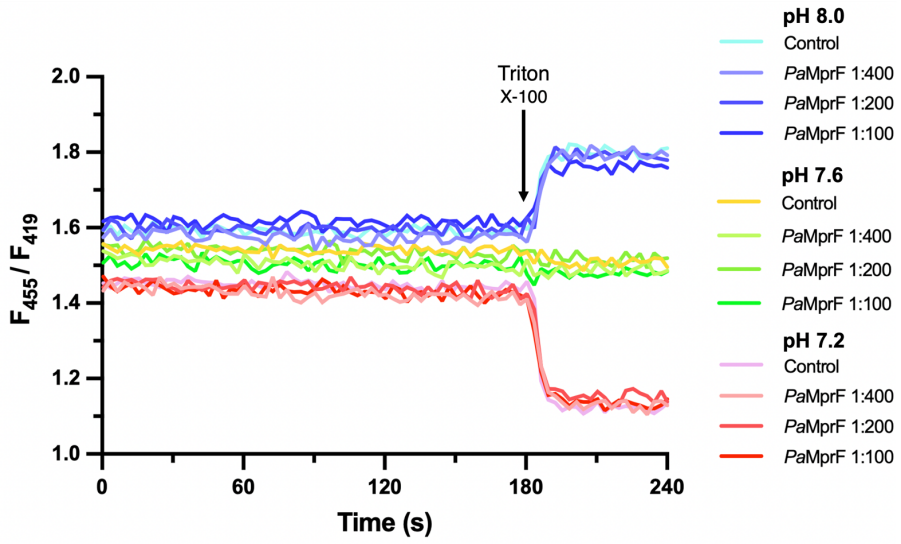

Figure 5.6: HPTS proton permeability assay. Fluorescence time-courses (excitation = 455 nm, normalized to 419 nm) of HPTS within empty (control) and *Pa*MprF reconstituted (at several *Pa*MprF:lipid (w/w) ratios) liposomes. Liposomes were diluted in pH 7.2 (red traces), pH7.6 (green traces), or pH 8.0 (blue traces) buffer. Liposomes were solubilised with Triton X-100 at 180 s.

Figure 5.6 demonstrates that proteoliposomes containing increasing amounts of *Pa*MprF are no more permeable to protons than control liposomes, as for both low and high pH reconstitution, there is no concomitant increase/decrease in the fluorescence of HPTS over the initial time-course. The maintenance of a pH gradient across the liposome membrane can be demonstrated by the addition of Triton X-100, as solubilisation of liposomes then results in an increase/decrease in the fluorescence of HPTS, representing the dye then being exposed to the different pH of the buffer outside the liposomes. Furthermore, the control traces of liposomes diluted in pH 7.6 buffer demonstrate that the change in fluorescence of HPTS is not an artefact of Triton X-100 addition. Therefore, proteoliposomes are able to withstand the pH gradient of 0.4 units used in the previous assessment of energy sources, further supporting the conclusion that *Pa*MprF-mediated lipid transport is not reliant on the PMF.

5.3. Specificity of *Pa*MprF-mediated lipid transport

5.3.1. *Pa*MprF exhibits broad substrate specificity

The functional data presented in this Chapter suggest that *Pa*MprF is passively transporting lipid *in vitro,* and is therefore functioning as a bidirectional scramblase. One hallmark feature of scramblases is their promiscuity, being able to transport a range of lipid substrates. As such, the substrate specificity of *Pa*MprF was tested *in vitro* using a variety of commercially available NBD-labelled lipids. The first lipids tested were tail-linked NBD-PG and NBD-PC, to reflect the bulk lipid composition used for liposome reconstitution. In addition, since it has been demonstrated in the literature that expressing the soluble domain of a lysinylating MprF homologue *in trans* with the TM domain of an alanylating homologue provides cells with maximal resistance to CAMPs *in vivo* (Slavetinsky *et al.* 2012), it is understood that the TM region of MprF likely displays a degree of relaxed specificity to differently aminoacylated PG substrates. As such, both NBD-AlaPG and NBD-LysPG were tested in this experiment. The *Pa*MprF:lipid (w/w) ratio was increased for these liposomes to 1:100, to yield larger rate constants for lipid transport such that differences in rates could be more easily quantified. An example of a normalized fluorescence time-course for each of these lipid species is shown in **Figure 5.7:**

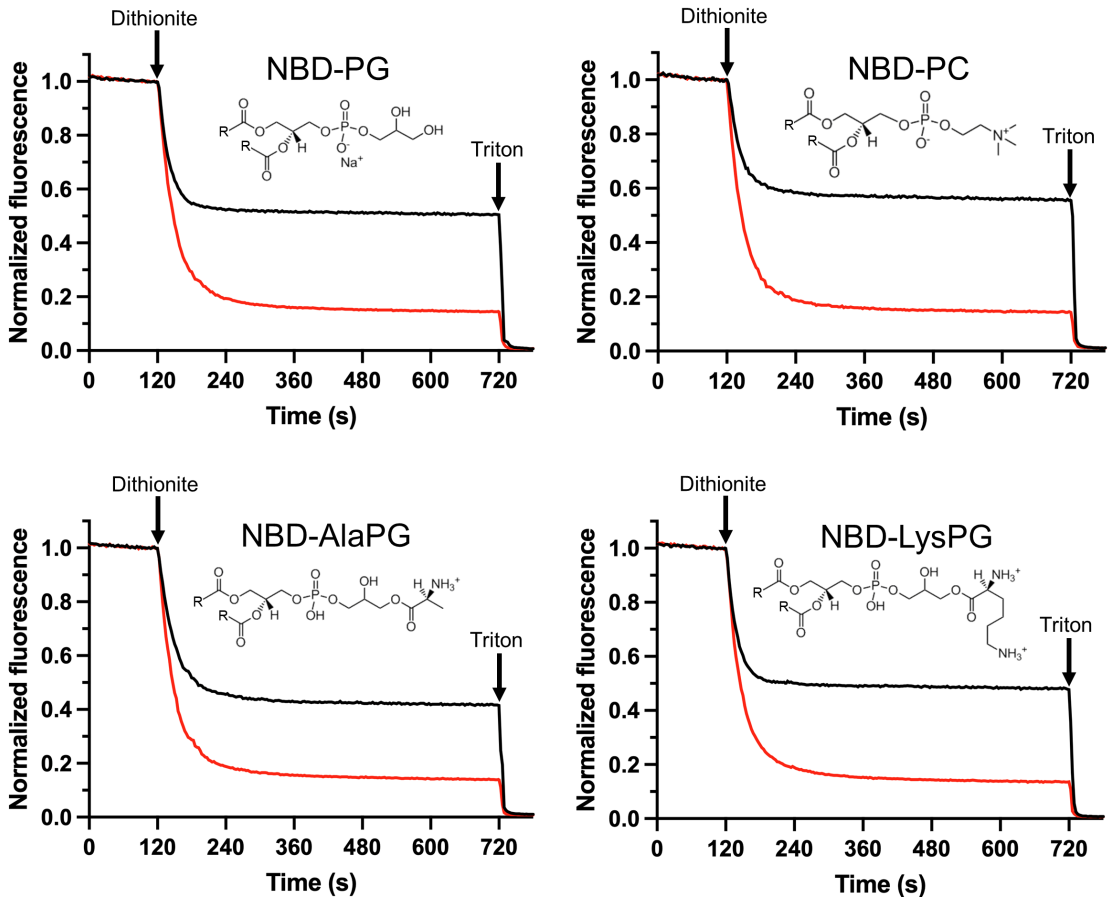

Figure 5.7: *Pa*MprF-mediated transport of different NBD-lipid species. Normalized fluorescence time-courses of different NBD-lipids in empty (black) and *Pa*MprF reconstituted (red) liposomes. Skeletal formulae of the headgroups of the NBD-lipids are shown.

Figure 5.7 shows that for the four lipid species tested, there is a similar decrease in fluorescence on dithionite addition, suggesting that *Pa*MprF is able to transport all of these NBD-labelled lipids and thus exhibits broad substrate specificity. As expected, NBD-LysPG is transported, providing *in vitro* evidence that *Pa*MprF TM has broad aminoacylated-lipid specificity, as demonstrated *in vivo* (Slavetinsky *et al.* 2012). In addition, NBD-PG and NBD-PC are also transported, highlighting that this relaxed specificity extends to non-aminoacylated lipids. This high level of promiscuity provides further evidence that *Pa*MprF is functioning as a scramblase *in vitro.*

To further analyse the *Pa*MprF-mediated transport of the different substrates, the time-courses for each lipid were fitted to the three-state model for lipid transport to obtain values

for the forwards and reverse rate constants of lipid transport. As can be observed from **Figure 5.7,** the plateau value for each control set of liposomes varies depending on the NBD-lipid being used. This is due to different lipid species partitioning slightly differently between liposome leaflets, with the rate constant for dithionite bleaching also varying depending on lipid identity (Falzone and Accardi 2020). As such, triplicate controls of empty liposomes from independent reconstitutions containing each lipid species were fitted to obtain values of γ and L_i^{PF} for each NBD-labelled lipid. These values were then used for each set of proteoliposomes containing the corresponding lipid, to ensure differences in γ and L_i^{PF} as a result of reporter lipid identity were accounted for. Three independent *Pa*MprF liposome reconstitutions were carried out for each NBD lipid species. Each replicate was fitted to the lipid transport model and the mean values of α and β from fitting for each lipid species are reported below in **Figure 5.8:**

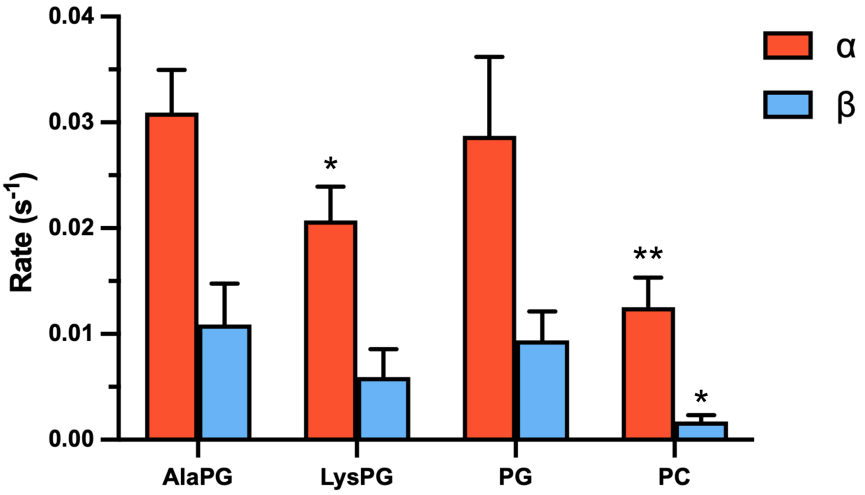

Figure 5.8: Lipid transport rate constants for different NBD-labelled lipids. Bar chart showing the fitted values of α (red) and β (blue) for transport of different lipid species by *Pa*MprF. n = 3, error bars represent standard deviation. Asterisks mark values of α and β statistically significant from AlaPG values determined by unpaired *t*-tests (* = $P \leq 0.05$, ** = $P \leq 0.01$).

Based on this rate analysis, *Pa*MprF has a slight substrate preference for NBD-AlaPG, with α = 0.031 s^{-1} and β = 0.011 s^{-1}. NBD-LysPG is transported at a slightly lower rate of α = 0.021 s^{-1}. NBD-PC is transported almost 3-fold slower in the inside-to-outside direction (α = 0.013 s^{-1})

than AlaPG, and 6-fold slower in the outside-to-inside direction (β = 0.0017 s^{-1}) than NBD-AlaPG. As NBD-PC is a non-native lipid to *P. aeruginosa,* it is perhaps unsurprising that *Pa*MprF transports this NBD-lipid at a slower rate than aminoacylated PG lipids. Interestingly, NBD-PG transport rates are not significantly different to NBD-AlaPG. This may be due to PG having a smaller headgroup than the alanylated derivative, and so being able to access the same lipid transport pathway that aminoacylated lipids utilise.

To further probe the range of substrates transported by *Pa*MprF, NBD-PE was also tested in the liposome transport assay. For this lipid and all previously tested lipids, the NBD fluorophore had been attached onto one of the fatty acid tails of the lipid. Therefore, a PE lipid was also tested in which the NBD fluorophore had been introduced at the headgroup, *N*-NBD-PE. The results of the liposome transport assay using these two PE lipid reporters are shown in **Figure 5.9:**

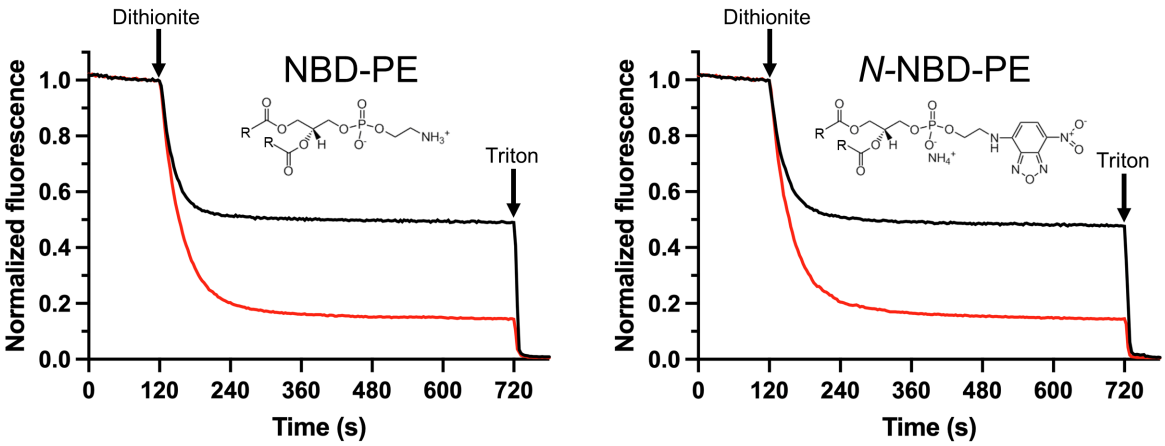

Figure 5.9: *Pa*MprF transport of NBD-PE and *N*-NBD-PE. Normalized fluorescence time-courses of different NBD-lipids in empty (black) and *Pa*MprF reconstituted (red) liposomes. Skeletal formulae of the headgroups of the NBD-lipids are shown.

As with the previous lipid species tested, *Pa*MprF is able to transport NBD-PE as well as *N*-NBD-PE. This rather unexpected result further highlights the broad range of lipid headgroups that can be transported by *Pa*MprF, including large lipid headgroups that do not occur in bacteria. The *N*-NBD-PE headgroup also has a different charge distribution compared to the

aminoacylated lipids that are the physiological substrate of *Pa*MprF, showing the range of charges that can be present on a lipid headgroup and still be transported. This result is further support for the hallmark characteristic of promiscuity identified in other scramblases which are capable of transporting a range of different sized and charged lipid headgroups (Menon *et al.* 2011, Malvezzi *et al.* 2018, Alvadia *et al.* 2019, Bushell *et al.* 2019).

5.3.2. *Pa*MprF can transport the "giant" lipid NBD-PEG2000PE

The experiments described above have confirmed that *Pa*MprF is able to transport a wide variety of commercially available NBD-labelled lipids, with different degrees of charge distributions across the headgroups of these species. Such remarkable promiscuity raises the question of whether there is a limit on the size of lipid headgroup that can be transported by *Pa*MprF. This question has been previously addressed in the literature for other highly promiscuous scramblases through the use of lipid reporters with "giant" PEGylated headgroups (Malvezzi *et al.* 2018). In these experiments, a distearoyl-sn-glycero-3-phosphoethanolamine (DSPE) lipid with a PEG2000 headgroup (DSPE-PEG2000-amine) is covalently linked to NBD (**Figure 5.10a**) and purified as outlined in **Methods (2.3.3.),** producing an NBD reporter lipid with a molecular weight of ~3 kDa, approximately 4-fold larger than the NBD-lipids used for the previously described transport assays. Results of the liposome transport assay using this lipid in *Pa*MprF reconstituted liposomes are shown in **Figure 5.10:**

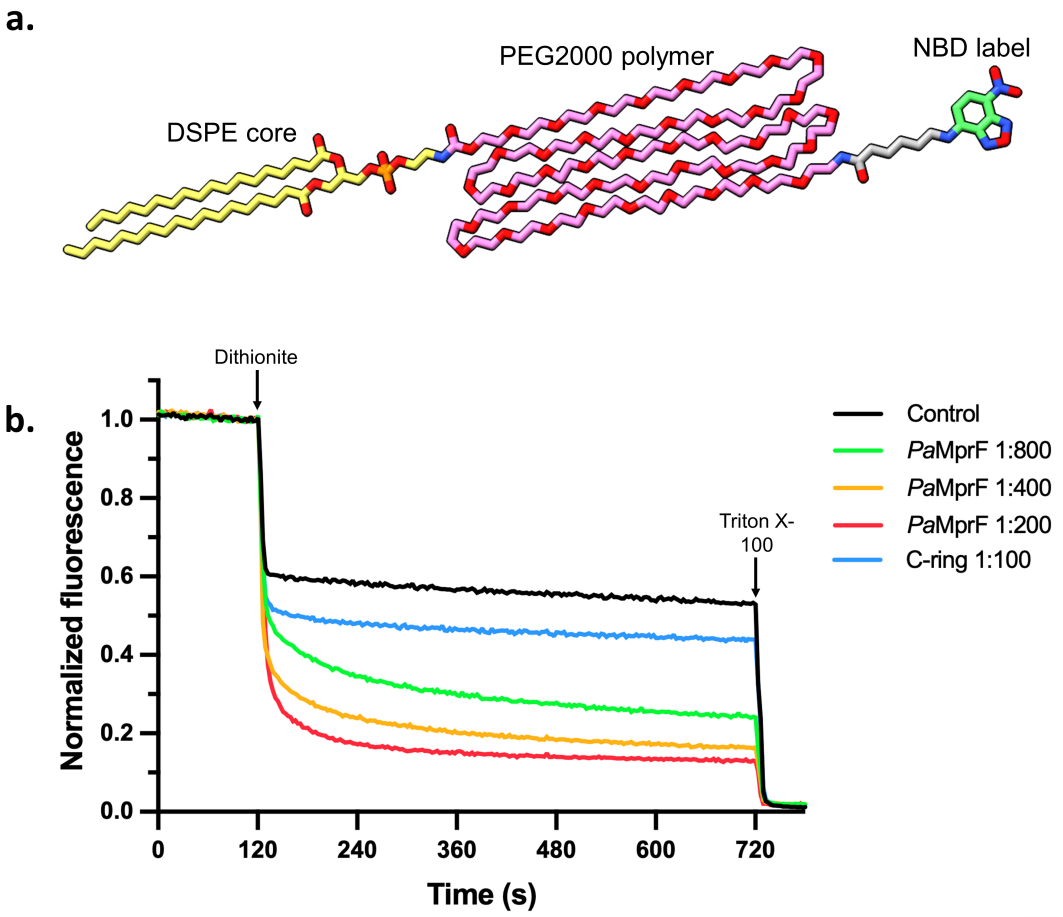

Figure 5.10: DSPE-PEG2000-NBD transport assay. a. Model of the DSPE-PEG2000-NBD reporter lipid (DSPE core = yellow, PEG2000 polymer = pink, NBD = green). Previous studies have shown that the PEG2000 polymer adopts a globular conformation with a radius of ~25 Å (Malvezzi *et al.* 2018). **b.** Normalized fluorescence time-courses assessing DSPE-PEG2000-NBD transport in the established liposome transport assay for control liposomes (black), C-ring reconstituted liposomes (blue), and *Pa*MprF reconstituted liposomes at different *Pa*MprF:lipid (w/w) ratios (red, orange, green).

Similar to NBDG, DSPE-PEG2000-NBD adsorbs more strongly to Biobeads than smaller NBD-lipids, resulting in less NBD lipid being incorporated into final liposomes and so fluorescence time-courses with more noise. Nevertheless, the control traces for empty and c-ring containing liposomes here indicated that dithionite bleaching of outer leaflet NBD labels (the steep initial descent of the curves and a near-right-angled transition to the plateau phase) occurs much more rapidly than for the previously used NBD-lipids. This is consistent with the literature (Malvezzi *et al.* 2018) and is due to increased collision of the NBD label with dithionite due to the NBD label being covalently linked to a long and flexible headgroup that extends away from the surface of liposomes. In contrast, proximity to the membrane has been shown to slow the

dithionite bleaching rate (Menon *et al.* 2011, Malvezzi *et al.* 2013, Malvezzi *et al.* 2018). However, this rapid dithionite bleaching in control liposomes is in stark contrast to the *Pa*MprF reconstituted liposomes which demonstrate a much slower rate of fluorescence decrease before reaching a plateau that is significantly lower than in the control traces. Indeed, the rate at which a plateau is reached and the magnitude of the fluorescence decrease both increase with increasing *Pa*MprF concentration, as demonstrated with NBD-AlaPG in the previous Chapter. This indicates that *Pa*MprF is indeed capable of transporting the large-headgroup of the DSPE-PEG2000-NBD lipid. This remarkable ability is something which has been observed in the literature for other characterised scramblases; both opsin and afTMEM16 are capable of scrambling DSPE-PEG2000-NBD (Malvezzi *et al.* 2018). This finding had led to the hypothesis that such promiscuous scramblases are capable of transporting these "giant" lipids via a non-specific "out-of-the-groove" mechanism, in which local deformation of the bilayer around a transport site within a protein could reduce the hydrophobic thickness of the bilayer in this region to facilitate a non-specific movement of lipids between membrane leaflets. This phenomenon has been shown to occur outside the core transport pathway of these scramblases by assessing whether increasing the concentration of unlabelled DSPE-PEG2000 affects the transport rate of labelled DSPE-PEG2000-NBD (Malvezzi *et al.* 2018). The hypothesis is, if transport occurs through the scramblase protein even in the case of DSPE-PEG2000, then a higher concentration of unlabeled DSPE-PEG2000 would slow the passage of DSPE-PEG2000-NBD through the protein by competition, whereas "out-of-the-groove" transport would be unaffected or even accelerated. This hypothesis was tested for *Pa*MprF at four 'competitive' unlabelled DSPE-PEG2000 concentrations and the curves fitted to the three-state model defined previously to assess rate constants for lipid transport (**Figure 5.11**).

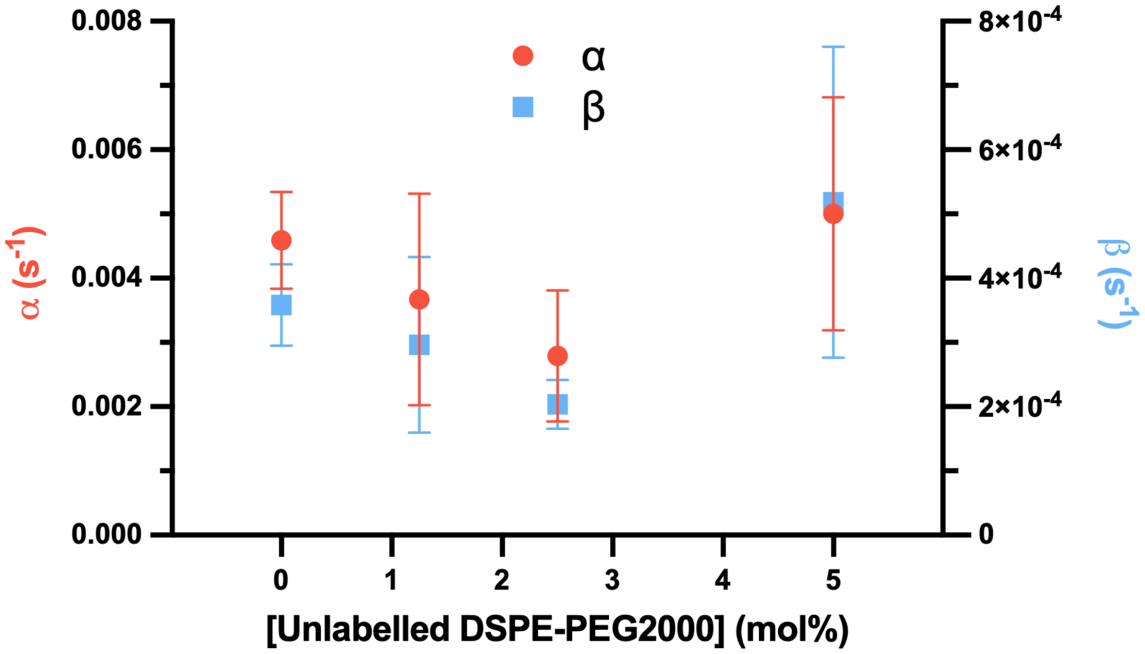

Figure 5.11: Effect of unlabelled DSPE-PEG2000 on lipid transport rates. Plots of the rate constants α (red) and β (blue) in liposomes containing different concentrations of unlabelled DSPE-PEG2000 (n = 3, error bars = standard deviation).

There is no significant difference between forwards and reverse rate constants of DSPE-PEG2000-NBD transport in liposomes containing different concentrations of unlabelled DSPE-PEG2000, suggesting that, similar to afTMEM16, *Pa*MprF is transporting DSPE-PEG2000-NBD via an out-of-the-groove mechanism.

5.4. Investigating *Pa*MprF-mediated lipid transport via mutagenesis

5.4.1. *Pa*MprF is resistant to mutations at the cytoplasmic lipid binding site

Whilst this Chapter has so far explored the energy source and substrate specificity of *Pa*MprF-mediated lipid transport, the molecular details of the lipid transport pathway remain unknown. As such, the remainder of this Chapter focuses on probing the lipid transport

pathway of *Pa*MprF through the study of *Pa*MprF mutants in the established liposome transport assay, in an attempt to identify mutants with a decreased rate of lipid transport.

A lipid transport route has been previously proposed, based on the observed lipid binding cavities in *Rt*MprF. Previous work by Ernst *et al.* (2015) had already identified a number of conserved residues across MprF homologues that when mutated to alanine in *S.aureus* MprF resulted in an increased sensitivity of cells to daptomycin, despite the levels of LysPG in membranes being unaffected. This suggested that these residues identified were involved in lipid transport, rather than lipid aminoacylation. Two of these residues correspond to the conserved salt bridge between the lipid binding sites later identified by Song *et al.* (2021): residues E295 and R319 in *Pa*MprF. Song *et al.* mutated the corresponding residues in *Rt*MprF, as well as two highly conserved tyrosine residues at the cytoplasmic binding pocket (Y318 and Y322 in *Pa*MprF) and assessed the effect on LysPG content in cells. Surprisingly, both the salt-bridge and tyrosine mutants tested by Song *et al.* saw an *increase* in cellular LysPG content compared to WT MprF. This increase was greatest for the residues at the conserved salt bridge, especially for the charge reversal mutation E295K, where LysPG content was 30 times greater. There was also an increase in surface-exposed LysPG content, despite the E295K charge reversal mutation expressing at much lower levels than the WT. This led to the suggestion that such mutations are stimulating the activity of the transport domain of MprF. The location of these mutations in the *Pa*MprF structure are highlighted in **Figure 5.12:**

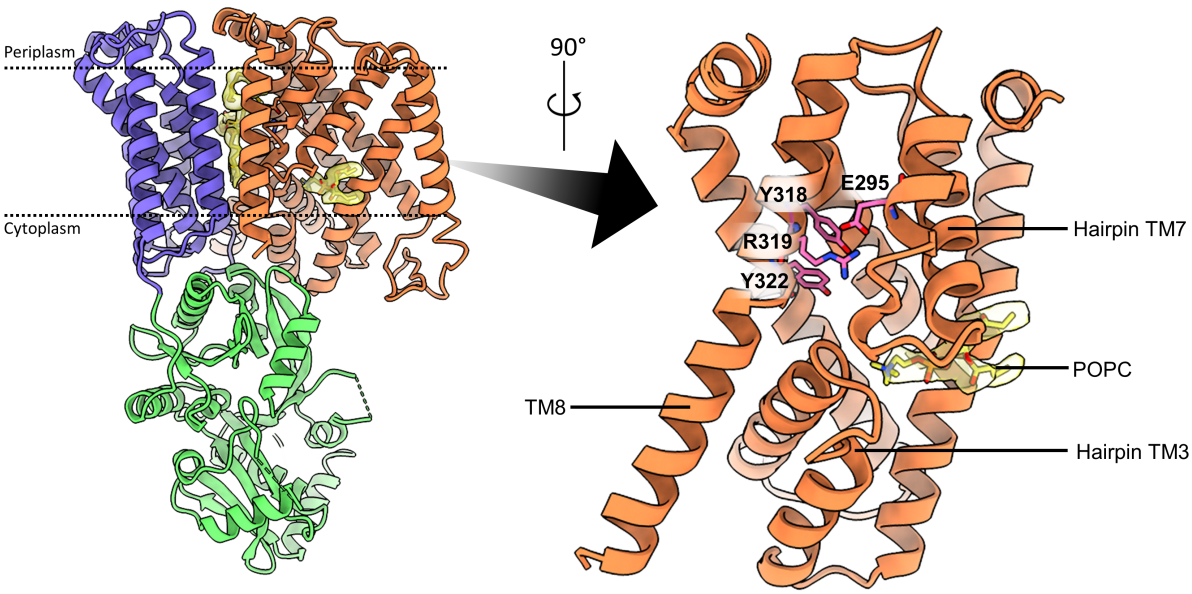

Figure 5.12: Conserved residues at cytoplasmic lipid pocket. *Left: Pa*MprF model (TM domain 1 = orange, TM domain 2 = purple, soluble domain = green) with cytoplasmic/periplasmic pocket lipid maps and bound lipids shown in yellow. *Right:* enlarged side view along short axis of *Pa*MprF (clipping through TM domain 2) highlighting the conserved residues at the cytoplasmic lipid binding pocket in pink.

Based on these prior results, I generated mutations at the corresponding sites in *Pa*MprF, (E295Q, E295R, R319A, R319E, Y318A, Y322A) and purified these *Pa*MprF mutants for reconstitution in liposomes to test their lipid transport ability *in vitro* compared to WT *Pa*MprF. A representative purification of one of these mutants is shown below in **Figure 5.13:**

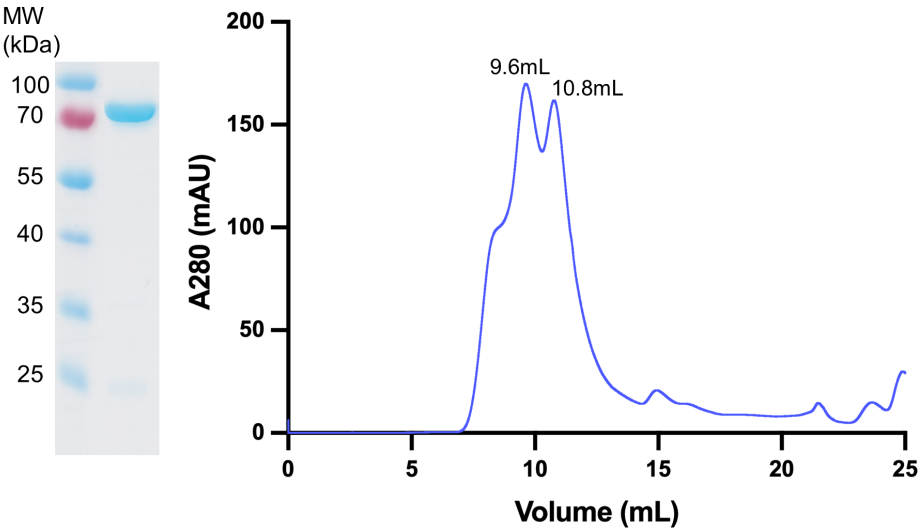

Figure 5.13: *Pa*MprF R319E purification. SEC chromatogram of R319E *Pa*MprF purification (right), along with SDS-PAGE gel (12 %, Coomassie stain) of the peak fraction at 11 mL (left).

*Pa*MprF mutants all behaved similarly to the WT on SEC (SEC traces for all mutants in this Chapter are given in **Appendix 7**), giving a void volume peak at ~8.5 mL, a higher order *Pa*MprF oligomer at 9.6 mL, and the typical *Pa*MprF monomer peak at 11 mL, indicating that mutants were stably expressed and isolated at high purity. The peak corresponding to the *Pa*MprF monomer for each mutant was pooled and concentrated for use in lipid transport assays. Initial liposome reconstitutions focused on the conserved salt bridge mutants E295Q/R and R319A/E. Three independent reconstitutions of each mutant were carried out alongside three reconstitutions with WT *Pa*MprF as a control, using the same bulk lipid as used previously, and NBD-AlaPG as a reporter lipid. The same ratio of *Pa*MprF:lipid was used for all mutants so that changes in rates of lipid transport could be directly compared within a reconstitution experiment. Fluorescence decay results are most comparable within a same-batch reconstitution experiment due to variation during liposome reconstitution (Arndt *et al.* 2022), so for all mutant experiments in this Chapter, liposome reconstitutions were always performed with WT *Pa*MprF samples as a control for direct comparison within a group of liposomes. An example of individual fluorescence time-courses of the mutants compared to WT is shown in **Figure 5.14:**

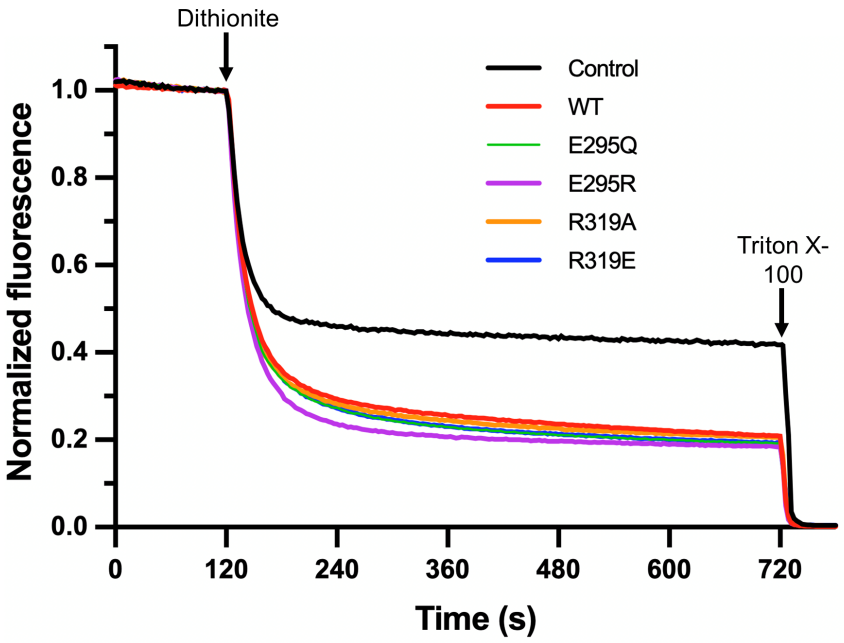

Figure 5.14: *In vitro* lipid transport by *Pa*MprF mutants. Normalized fluorescence time-courses of empty (black), *Pa*MprF WT (red), E295Q (green), E295R (purple), R319A (orange), and R319E liposomes (blue). Traces are averages of three independent replicates.

Figure 5.14 demonstrates that all mutants tested are capable of transporting NBD-AlaPG *in vitro*, as there is a decrease in fluorescence for all mutants significantly below the plateau for empty liposomes. Furthermore, E295Q, R319A and R319E all appear to behave similarly to WT, as the initial rate of fluorescence decrease and final plateau value are similar. However, E295R appears to transport lipid at a faster rate than WT, as the initial rate of decrease is faster for E295R time-courses, reaching a stable plateau much sooner than other mutants. This observation can be quantified by fitting these traces to the lipid transport model to obtain estimates of the rate constants for forwards and reverse lipid transport (**Figure 5.15**).

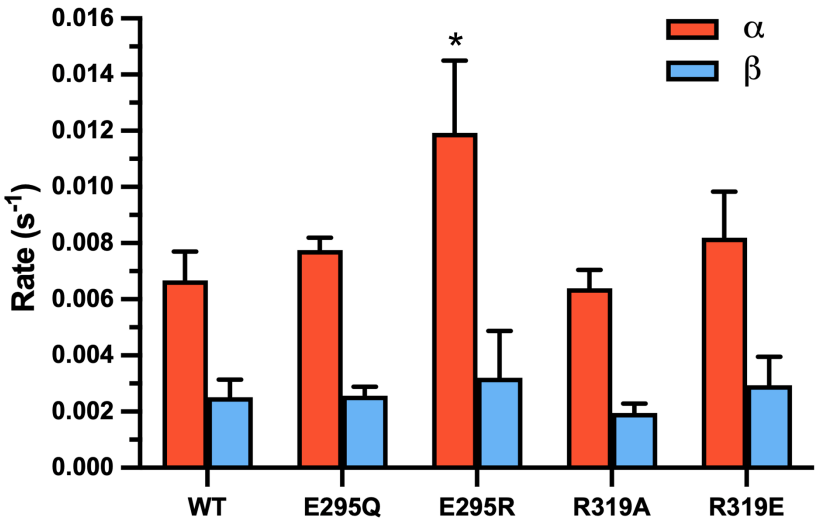

Figure 5.15: Lipid transport rates for *Pa*MprF salt bridge mutants. n = 3, error bars represent standard deviation. Asterisks mark values of α and β statistically significant from WT values determined by unpaired *t*-tests (* = $P \leq 0.05$).

Rate analysis shows that there is no significant difference in lipid transport rates between WT and E295Q, R319A and R319E mutants. However, the rate of forwards lipid transport is almost 2-fold higher for E295R compared to WT, 0.0119 s^{-1} compared to 0.0067 s^{-1}. This suggests that E295R is a transport stimulating mutation of *Pa*MprF, consistent with the *in vivo* functional data of Song *et al.* (2021).

These liposome reconstitutions were repeated for the conserved tyrosine residue mutants Y318A and Y322A. Examples of the raw data and the estimates of α and β compared to WT are shown below in **Figure 5.16:**

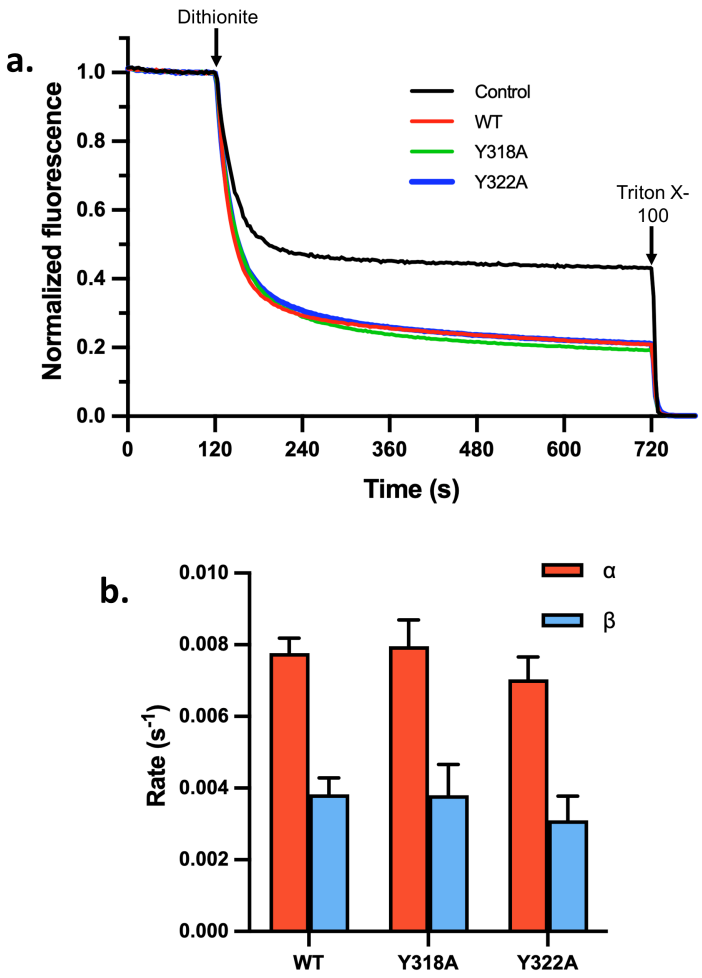

Figure 5.16: *Pa*MprF Y318A and Y322A lipid transport. a. Normalized fluorescence time-courses of empty (black), *Pa*MprF WT (red), Y318A (green) and Y322A (blue) liposomes. **b.** Bar chart showing the mean α and β rate constants for lipid transport from fitting (error bars = standard deviation, n = 3).

Figure 5.16a shows that Y318A and Y322A fluorescence time-courses are very similar to WT, and analysis of lipid transport rate constants in **Figure 5.16b** shows that mutation of these conserved residues to alanine does not significantly alter the rates of lipid transport compared to WT.

To further investigate the residues at this cytoplasmic lipid binding pocket, a similar approach was adopted to that of Lee *et al.* (2018), whereby tryptophan residues were introduced to the binding pocket, replacing smaller hydrophobic lining residues. Such an increase in side chain volume is expected to sterically restrict access to the pocket, and so if lipid transport is occurring via this route, a reduction in the rates of lipid transport would be expected. For this

experiment, three residues near the top of the binding pocket and on the cytoplasmic side of the conserved salt bridge/tyrosine residues were selected (**Figure 5.17**).

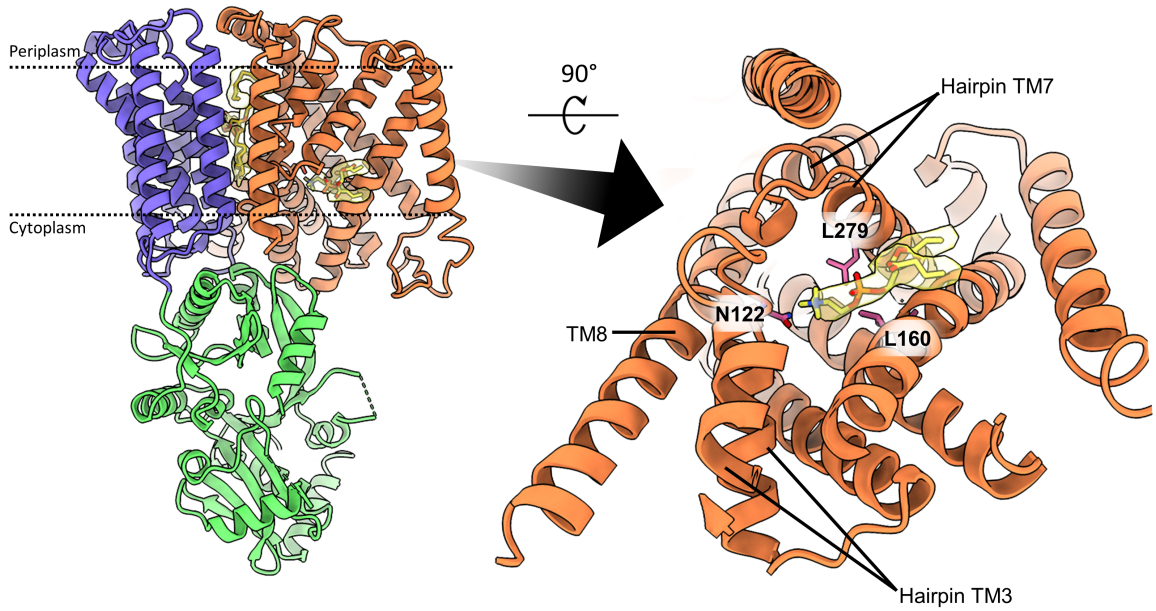

Figure 5.17: Cytoplasmic pocket residues selected for Trp mutation. *Left: Pa*MprF model (TM domain 1 = orange, TM domain 2 = purple, soluble domain = green) with cytoplasmic/periplasmic pocket lipid densities and bound lipids shown in yellow. *Right:* enlarged view of the cytoplasmic lipid binding site of *Pa*MprF from the cytoplasmic side, clipping through the soluble domain (TM domain 2 removed for clarity). The three residues at the entrance of this site selected for mutation to tryptophan are highlighted in pink.

All three of these residues were mutated to tryptophan to produce a triple mutant *Pa*MprF, N122W/L160W/L279W, with a maximally occluded cytoplasmic binding cavity. This mutant was then expressed and purified as for the other mutants described (**Figure 5.18**).

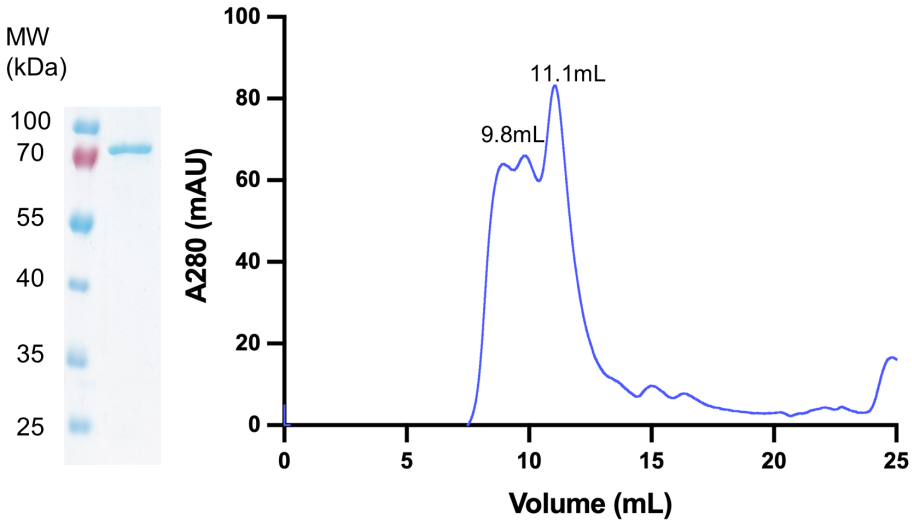

Figure 5.18: *Pa*MprF N122W/L160W/L279W purification. SEC chromatogram of *Pa*MprF N122W/L160W/L279W purification (right), along with SDS-PAGE gel (12 %, Coomassie stain) of the peak fraction at 11 mL (left).

Although expressing at a lower level than single site *Pa*MprF mutants, the N122W/L160W/L279W mutant produces a typical SEC chromatogram, suggesting stable expression, and is isolated at similar high purity to other mutants. The lipid transport capabilities of this mutant were then assessed as described above compared to WT *Pa*MprF (**Figure 5.19**).

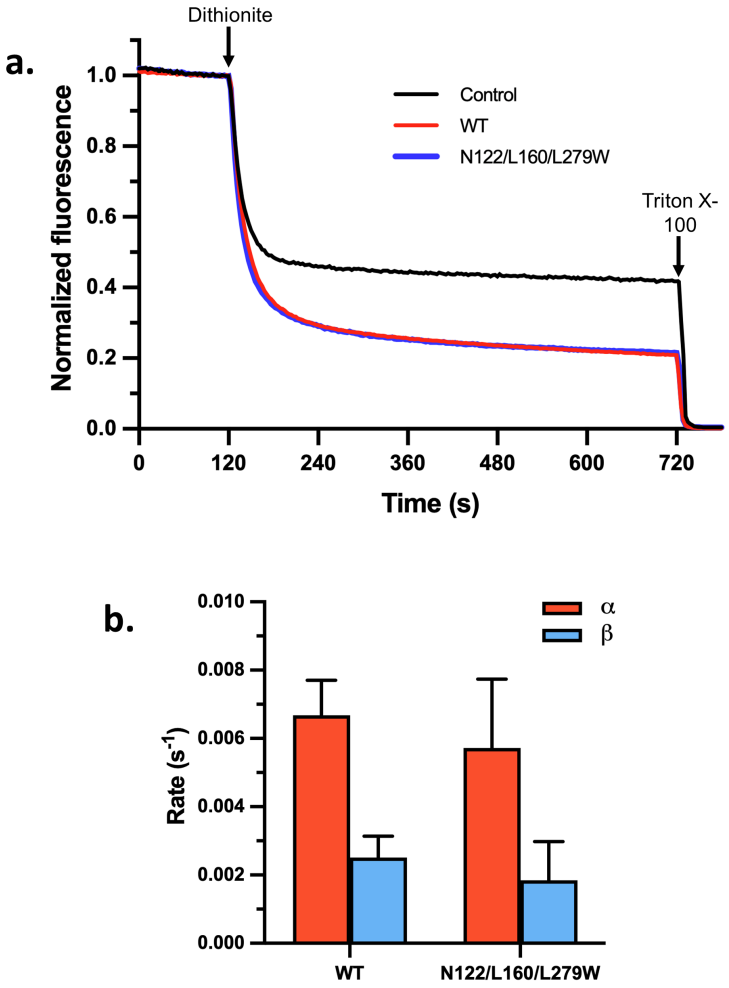

Figure 5.19: Effect of tryptophan mutation on *Pa*MprF lipid transport. a. Normalized fluorescence time-courses of empty (black), *Pa*MprF WT (red) and N122W/L160W/L279W *Pa*MprF (blue) liposomes. **b.** Bar chart showing the mean α and β rate constants for lipid transport from fitting (error bars = standard deviation, n = 3).

Fluorescence traces for the triple mutant show that this construct, surprisingly, is also able to transport NBD-AlaPG, and in a similar manner to WT. This is further confirmed by rate analysis, which indicates no significant difference in α and β compared to WT. This suggests that the addition of three tryptophan side chains around the cytoplasmic lipid binding site does not significantly obstruct lipid transport by *Pa*MprF.

5.4.2. *Pa*MprF is resistant to mutations at the TM domain interface

As no mutation at the cytoplasmic lipid binding site reduced *Pa*MprF lipid transport activity compared to WT, I investigated whether mutation of residues at the interface between TM domains 1 and 2 could have any such effect. If so, this would provide supporting evidence to the lipid transport pathway suggested by the new *Pa*MprF structural data presented in **Chapter 3**. Initial mutagenesis at the TM domain interface focused on introducing tryptophan residues at constriction points along the previously identified channel to attempt to occlude lipid transport. The residues selected for these initial experiments are highlighted in **Figure 5.20:**

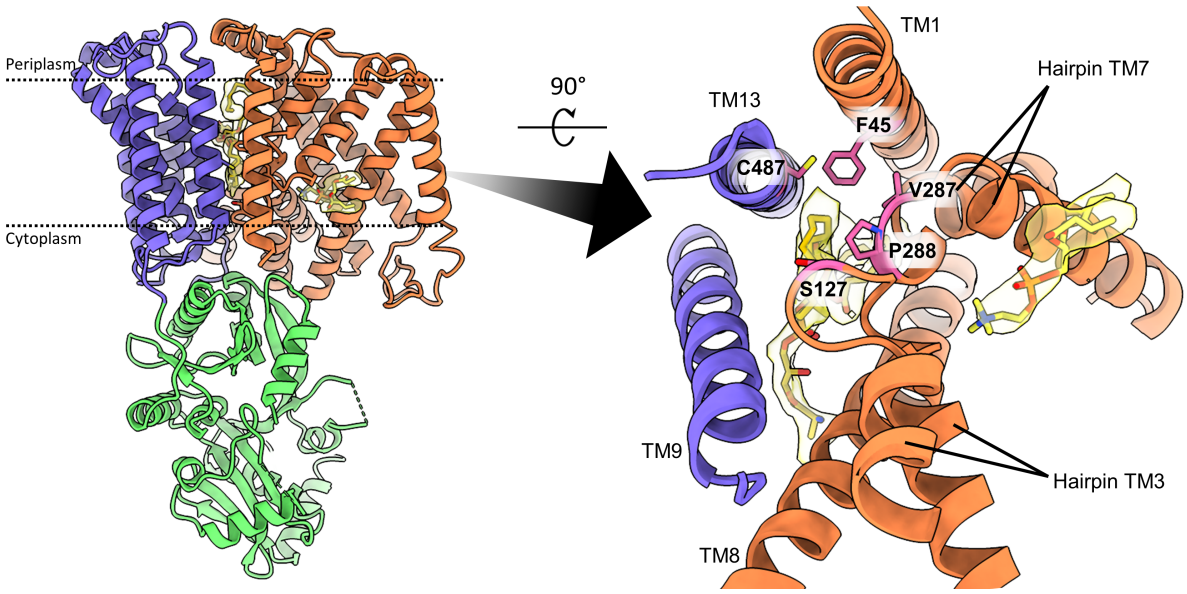

Figure 5.20: TM interface residues selected for Trp mutation. *Left: Pa*MprF model (TM domain 1 = orange, TM domain 2 = purple, soluble domain = green) with cytoplasmic/periplasmic pocket lipid densities and bound lipids shown in yellow. *Right:* enlarged view of the TM domain interface of *Pa*MprF from the cytoplasmic side, clipping through the soluble domain. The five residues chosen for mutagenesis are highlighted in pink. TM helices not involved in this interface are removed for clarity.

P288 has been previously highlighted as a residue of interest, as it is conserved across MprF homologues, and mutation by Ernst *et al.* (2015) of the corresponding residue in *S.aureus* to alanine resulted in reduced resistance of cells to daptomycin, suggesting its involvement in lipid transport as membrane LysPG content was unchanged. P288 and four other residues at

the TM domain interface (F45, S127, V287, C487) were mutated to tryptophan, and each single tryptophan mutant was expressed and purified as described previously. The mutants were then reconstituted in triplicate alongside WT *Pa*MprF in liposomes containing NBD-AlaPG to assess their lipid transport activity (**Figure 5.21**).

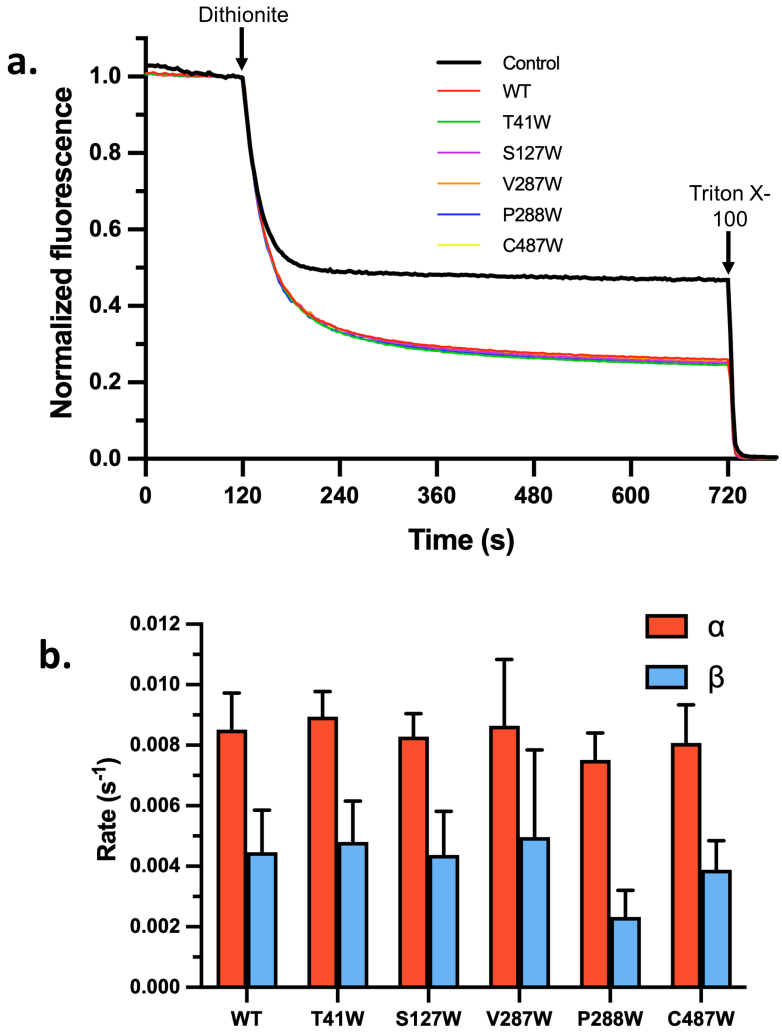

Figure 5.21: Effect of tryptophan mutations at the TM interface on *Pa*MprF lipid transport. a. Normalized fluorescence time-courses for empty (black), WT (red), T41W (green), S127W (purple), V287W (orange), P288W (blue), and C487W (yellow) *Pa*MprF liposomes. **b.** Bar charts showing mean α and β rate constants for lipid transport from fitting (error bars = standard deviation, n = 3).

Similar to previously tested *Pa*MprF mutants, all single tryptophan mutants displayed NBD-AlaPG transport activity, with **Figure 5.21a** showing overlapping fluorescence time-courses.

The analysis of rate constants in **Figure 5.21b** confirms that there is no significant reduction in the rates of lipid transport for any mutant compared to WT *Pa*MprF.

In light of this, more disruptive mutations were produced at the TM domain interface. Noting that introduction of a positively charged arginine residue at E295 saw a stimulation of lipid transport (Song *et al.* 2021), three further single arginine mutants were produced at the TM interface to probe whether introduction of positive charge at this hydrophobic location could be accommodated and if so, what effect it could have on lipid transport. The three sites chosen for this mutagenesis were F45, V287, and A491, as these residues occupy different positions at the constriction point along the length of the solvent accessible channel, as highlighted in **Figure 5.22:**

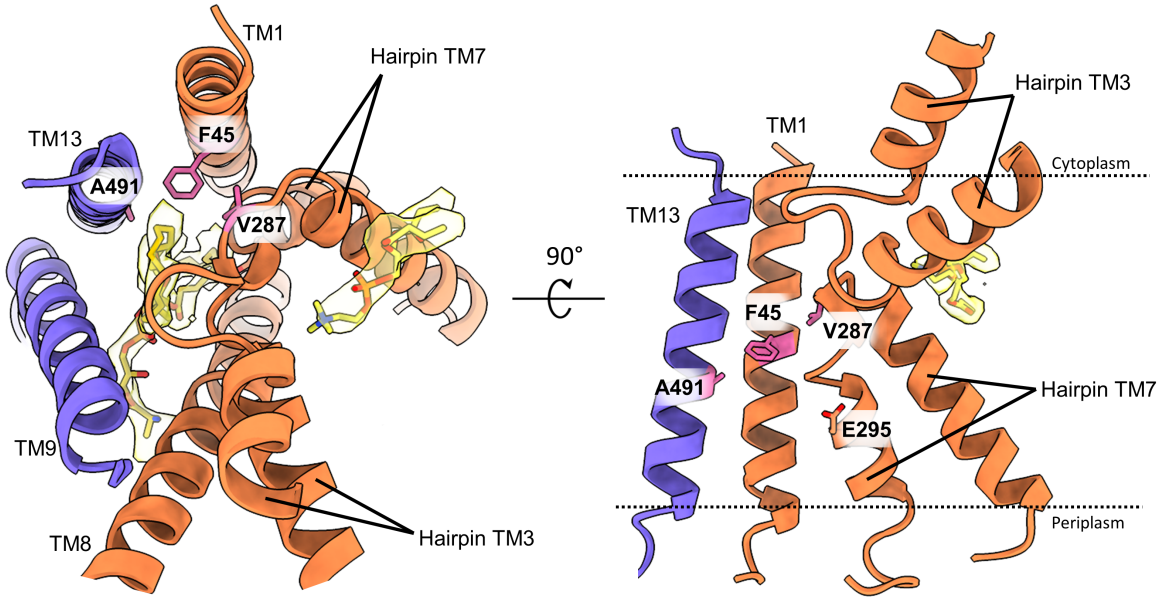

Figure 5.22: TM interface residues selected for Arg mutation. *Left:* View of the TM domain interface of *Pa*MprF from the cytoplasmic side, clipping through the soluble domain (as in **Figure 5.20**). The three residues chosen for mutagenesis to arginine are highlighted in pink. *Right:* View rotated 90°. Periplasmic lipid and TMs 8 and 9 removed for clarity. The position of the conserved residue E295 relative to these residues is shown.

All arginine mutants purified as expected, and were then tested for NBD-AlaPG transport activity as before (**Figure 5.23**).

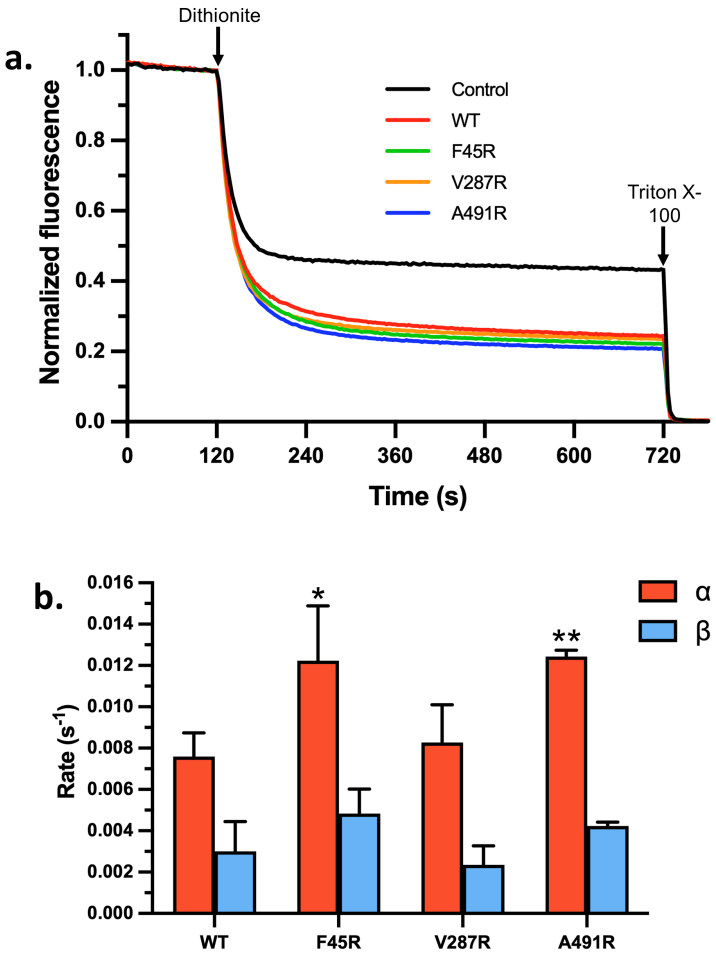

Figure 5.23: Effect of arginine mutations at the TM domain interface on *Pa*MprF transport activity. a. Normalized fluorescence time-courses for empty (black), WT (red), F45R (green), V287R (orange) and A491R (blue) *Pa*MprF liposomes. **b.** Bar charts showing mean α and β rate constants for lipid transport from fitting (error bars = standard deviation, n = 3). Asterisks mark values of α and β statistically significant from WT values determined by unpaired *t*-tests (* = $P \leq 0.05$, ** = $P \leq 0.01$).

Figure 5.23b shows that both F45R and A491R forwards rates of lipid transport are significantly greater than WT by almost two-fold, with α = 0.0122 s^{-1} for F45R and 0.0124 s^{-1} for A491, compared with α = 0.0076 s^{-1} for WT. Interestingly, there is no significant difference in rate constants between WT and V287R. F45R and A491R are closer to the periplasmic exit of *Pa*MprF, whereas V287R occupies a position closer to the cytoplasmic side of the membrane (as seen in **Figure 5.22**). Introduction of arginine residues at F45 and A491 gives a similar stimulating effect of *Pa*MprF-mediated lipid transport to that of E295R. Indeed, E295 is in close proximity to these two residues, suggesting that there is a general region of *Pa*MprF towards the periplasmic exit site, but not towards the cytoplasmic side, where introduction of a positive

charge stimulates the transport of NBD-AlaPG. The exact mechanism of this simulation is as yet unclear, and requires further investigation.

5.4.3. Targeted UV crosslinking of *Pa*MprF does not inhibit lipid transport

As none of the introduced mutations have resulted in a *Pa*MprF protein with significantly reduced lipid transport capabilities, I attempted to crosslink *Pa*MprF in such a way as to prevent lipid transport. Residue pairs within *Pa*MprF were chosen for the introduction of disulfide bonds, but such attempts did not produce any lipid transport-deficient *Pa*MprF mutants (see **Appendix 8** for details), likely reflecting that the residues chosen were too far apart to form a crosslink. As such, a targeted UV crosslinking method was then employed (Isom *et al.* 2020). In this method, the artificial amino acid p-benzoyl-l-phenylalanine (BPA) was incorporated at chosen sites within the coding sequence using the amber stop codon TAG, and a co-expressed tRNA/tRNA-synthetase pair that recognise TAG and insert BPA into the polypeptide chain during protein synthesis. BPA is a compound that radicalises on illumination with UV light at 365 nm, and then forms covalent cross-links to neighbouring alkyl carbon centres (**Figure 5.24**).

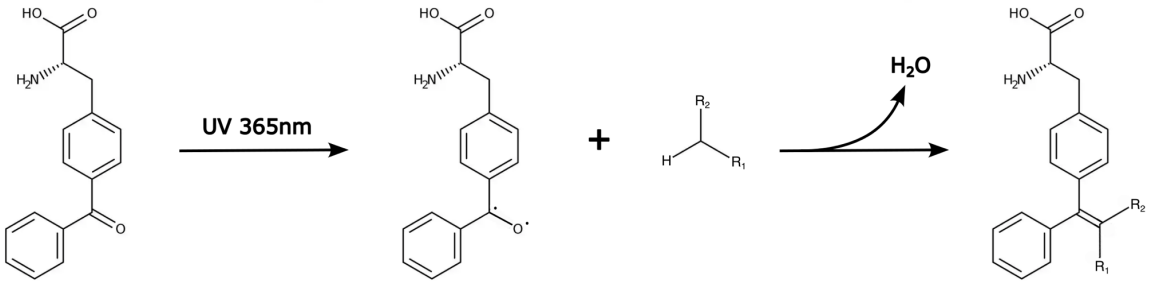

Figure 5.24: BPA cross-linking reaction mechanism.

A number of BPA substitutions were designed at either the cytoplasmic lipid binding site or the TM domain interface, with the aim of producing a mutant that could be crosslinked to lipid as it passes through the protein. The ability of these mutants to transport lipid would then be assessed by the established liposome transport assay to determine whether any BPA residues

introduced could block lipid transport through crosslinking to substrate lipid. Following BPA mutagenesis, the expression of these mutants was tested in *E.* coli BL21 as outlined in **Methods (2.4.8.)**. The sites chosen for BPA mutagenesis and the results of the test expression of these mutants are shown below in **Figure 5.25:**

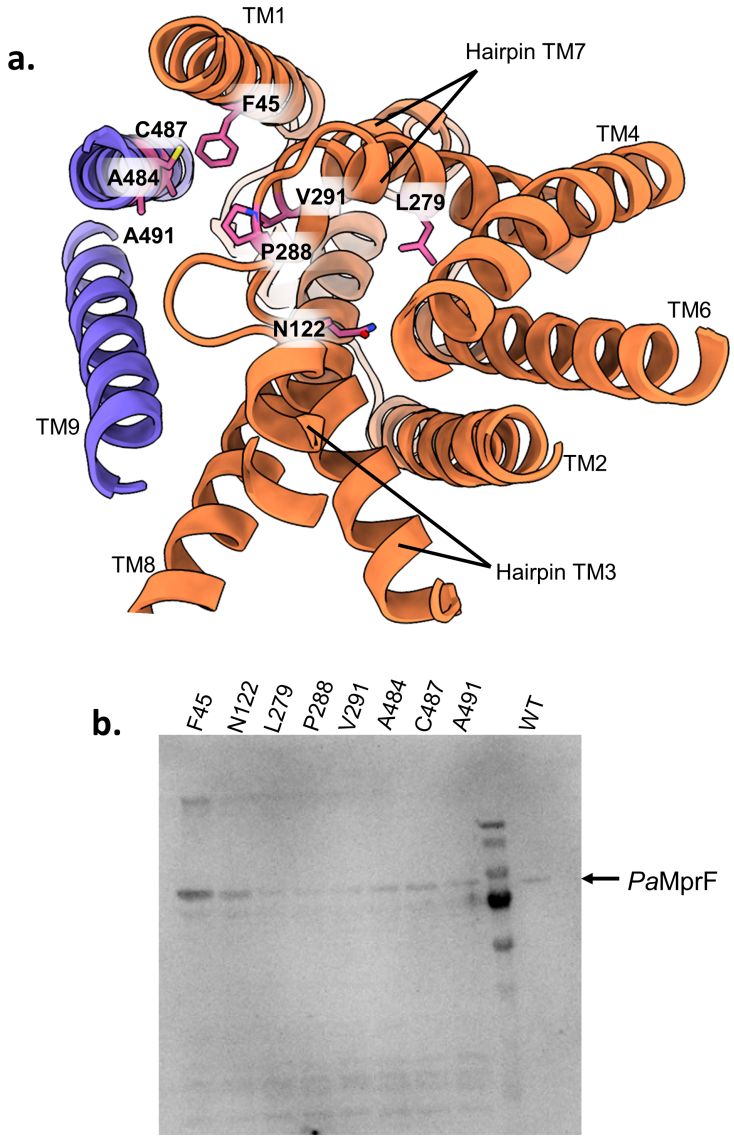

Figure 5.25: *Pa*MprF BPA mutagenesis. a. View of *Pa*MprF TM domain from the cytoplasmic side, clipping through the soluble domain (as in **Figure 5.20,** lipid densities removed for clarity). The eight residues in *Pa*MprF chosen for BPA mutagenesis are highlighted in pink. **b.** Western blot showing results of the *Pa*MprF BPA mutant test expressions and purifications. A positive control of His-tagged WT *Pa*MprF is loaded on the right-hand lane.

As shown in **Figure 5.25b,** only two *Pa*MprF BPA mutants could be expressed and purified with a reasonable yield: F45BPA and N122BPA. F45 is located at the TM domain interface, and N122 at the cytoplasmic lipid binding cavity. Of all the BPA constructs generated, these two

reside the furthest away from each possible lipid transport cavity. The poor expression of the other BPA constructs likely reflects the fact that the BPA moiety is larger than all naturally occurring amino acids, and so requires sufficient space within the protein to accommodate its introduction during protein folding. In light of their positive small-scale expression results, F45BPA and N122BPA were both expressed and purified large-scale as with the other *Pa*MprF mutants described in this Chapter. An example purification of N122BPA is shown in **Figure 5.26:**

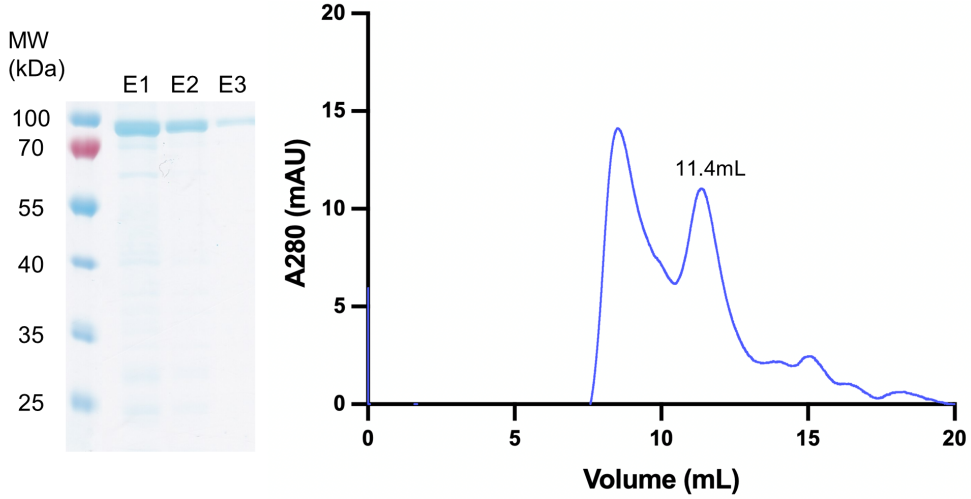

Figure 5.26: *Pa*MprF BPA mutant purification. Example purification of N122BPA. *Left:* SDS-PAGE gel (12 %, Coomassie stain) of elution fractions from affinity chromatography before SEC. *Right*: SEC chromatogram of N122BPA purification.

The yields from these purifications were significantly lower than other mutants, as expected from using a non-natural amino acid translation system. Despite this, both mutants behaved as expected for *Pa*MprF on size exclusion chromatography, predominantly eluting at ~11 mL (although with a much more significant aggregate peak at ~8.5 mL). The monomer peak fractions from SEC were pooled and concentrated for reconstitution into liposomes.

For liposome experiments, BPA mutants were reconstituted in triplicate (alongside empty liposomes and WT *Pa*MprF proteoliposome controls) with NBD-AlaPG as a reporter lipid, as for previous mutant experiments. The "pre-crosslinking" fluorescence time-courses of these samples were measured, and then remaining sample was illuminated on ice for 15 minutes

with UV light at 365 nm to promote BPA crosslinking. Fluorescence time-courses were then obtained following crosslinking. Time-courses were fitted to the lipid transport model to obtain rate constants for forwards and reverse lipid transport, which were then compared before and after UV illumination for each mutant. Examples of these time-courses, and the derived values for α and β are shown in **Figure 5.27:**

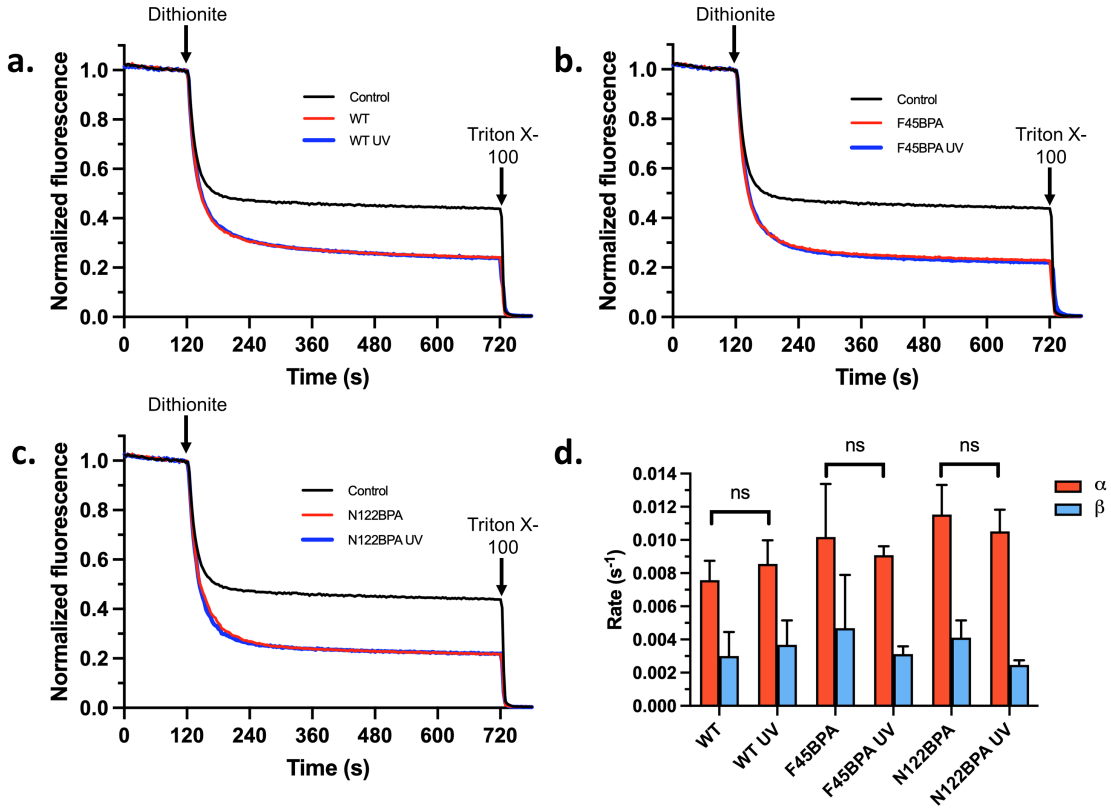

Figure 5.27: *Pa*MprF BPA mutant lipid transport. a, b, c. Fluorescence time-course measurements for WT, F45BPA and N122BPA mutant liposomes respectively, showing raw data of empty liposomes (black), liposomes before UV treatment (red) and liposomes after UV treatment (blue). **d.** Bar charts showing mean α and β rate constants for lipid transport from fitting (error bars = standard deviation, n = 3).

After UV treatment, there was no significant reduction in the fluorescence decay of liposomes for F45BPA and N122BPA mutant liposomes (**Figure 5.27b, c**). Analysis of triplicate lipid transport rate constants for each sample and WT liposomes confirms this (**Figure 5.27d**), with no observed significant decrease in α or β after UV treatment. This suggests that lipid transport is unlikely to occur in proximity to residues F45 or N122, as BPA-crosslinking of transported lipid to these residues would have been expected to reduce the fluorescence decay of liposome measurements, as shown previously for liposomes treated with heat or proteinase.

5.5. Chapter Discussion

5.5.1. *Pa*MprF behaves like a passive lipid scramblase

The experiments in this Chapter demonstrate that *Pa*MprF is able to transport lipid in the absence of an external energy source, and that the presence of common activators does not stimulate transport activity *in vitro,* suggesting that *Pa*MprF is passively scrambling lipid. It was previously suggested by Song *et al.* (2021) that lipid transport in *Rt*MprF could be energised by the PMF, through protonation and separation of the conserved Glu-Arg salt bridge between the two lipid binding pockets. However, this suggestion was based exclusively on structural analysis without any experimental evidence. The *in vitro* assessment of *Pa*MprF lipid transport in this Chapter demonstrates that *Pa*MprF lipid transport is not stimulated by a proton gradient across liposome membranes established by higher/lower external pH. Importantly, this independence from any external energy source or activator means that *Pa*MprF facilitates *bidirectional* lipid scrambling, with forward and backward scrambling rates within the same order of magnitude.

5.5.2. *Pa*MprF is highly promiscuous

I have shown that *Pa*MprF is capable of transporting a wide range of NBD-labelled reporter lipids. Both alanylated and lysinylated NBD-PG can be transported, supporting existing evidence that any selectivity of substrate is determined at the aminoacylation step by the soluble domain of MprF, and that the TM region exhibits a much more relaxed degree of substrate specificity (Slavetinsky *et al.* 2012, Song *et al.* 2021). Surprisingly, this relaxed specificity extends far beyond differently modified PG lipids, as I have shown that *Pa*MprF is capable of transporting NBD lipids with the naturally occurring PE and PC headgroups, as well as non-native lipid headgroups with different charge distributions (*N*-NBD-PE) and "giant" sizes (PEG2000-PE). This remarkable promiscuity is further evidence of *Pa*MprF functioning

as a lipid scramblase, as this is a hallmark characteristic of other previously identified scramblase proteins. For example, the human scramblase TMEM16F has been shown to be capable of transporting NBD-PE, NBD-PC and *N*-NBD-PE (Alvadia *et al.* 2019), and the fungal *af*TMEM and the GPCR opsin have both been shown to be capable of transporting *N*-NBD-PE and PEG2000NBD-PE (Malvezzi *et al.* 2018). Taken together, the experimental evidence presented in this Chapter presents a compelling case for the characterisation of *Pa*MprF as a highly promiscuous phospholipid scramblase.

5.5.3. No *Pa*MprF mutation reduced lipid transport

Despite extensive mutagenic and crosslinking attempts, no disruption of potential lipid transport pathways resulted in a reduced lipid transport rate by *Pa*MprF *in vitro*. Previous studies have introduced tryptophan residues along the transport grooves of scramblases, resulting in reductions in lipid transport when key gating residues were mutated (Lee *et al.* 2018). A similar strategy was employed in this Chapter with *Pa*MprF; the introduction of three tryptophan residues at the cytoplasmic lipid binding site still produced a mutant capable of transporting NBD-AlaPG with no significant reduction in rate compared to WT. Such tryptophan residues would produce a significant steric obstruction to lipid if transport occurred through this pathway. Given this, it seems likely that in the N122W/L160W/L279W *Pa*MprF mutant the lipid transport pathway occurs separately from the characterised cytoplasmic lipid binding site. However, introduction of single tryptophan residues at the TM domain interface, the other candidate site for lipid transport, also gave mutants that transported at the same rate as WT. One possible explanation for this is that the single tryptophan mutants were not sufficient to sterically obstruct transport, and that accommodation of the mutations could be achieved through an increased separation of the two TM domains. In addition, the use of tryptophan mutagenesis in the literature has been in hydrophilic transport grooves that are only accessed by lipid headgroups. In *Pa*MprF, it has been suggested that the full lipid molecule moves through the protein due to the hydrophobic

nature of the TM domain interface. As such, introduction of tryptophan at a hydrophilic groove could have more of an obstructive effect, whereas its introduction at a mostly hydrophobic pathway could be a less significant disruption provided its size can be accommodated.

Another explanation for all tryptophan mutants being as active as WT *Pa*MprF is that lipid transport is occurring by an "out-of-the-groove mechanism", where local deformation of the bilayer by *Pa*MprF causes more spontaneous lipid transport at the protein surface. This is thought to be a mechanism involved in the fungal *af*TMEM16 scramblase activity (Malvezzi *et al.* 2018), as obstruction of the substrate groove within the protein by tryptophan mutagenesis hinders lipid transport of small substrates like NBD-PE, but not of larger substrates like PEG2000-NBD-PE. This suggested that *af*TMEM16 has two possible lipid transport pathways, one through the protein, and one "out-of-the-groove" at the protein surface. Such alternate transport pathways could also be present in *Pa*MprF, but more mutagenesis studies are required to investigate this further.

It could also be the case that transport is occurring by one or both of the identified internal pathways but that the tryptophan residues introduced are not large enough to obstruct transport, or that the protein undergoes further significant conformational change to fully open a pathway for lipid translocation. This is supported by the fact that MprF homologues are found in archaea, which have isoprenyl membrane lipids that are larger than eubacterial phospholipids. Furthermore, an MprF homologue has been identified in *Listeria* which lysinylates, and then presumably transports, cardiolipin (Thedieck *et al.* 2006), a lipid which is twice as big as PG. If such MprF homologues are responsible for the modification and transport of these larger lipid species, it is conceivable that an obstruction of transport pathways would require significantly larger compounds than tryptophan side chains in order to limit transport of PG through the *Pa*MprF TM fold. As such, future work should focus on assessing whether *Pa*MprF can transport large NBD-labelled lipids like cardiolipin.

5.5.4. *Pa*MprF lipid transport is stimulated by the introduction of positive charge

Interestingly, several *Pa*MprF mutants were found to stimulate the transport of the NBD-AlaPG reporter lipid in liposome experiments. One of these mutants, E295R, is in line with the finding by Song *et al.* (2021) whereby introduction of a positive charge at this conserved salt bridge residue in *Rt*MprF increased the amount of LysPG synthesised by cells 30-fold compared to WT, despite the mutant expressing at a lower level than WT *Rt*MprF. Two other mutations in *Pa*MprF were found to give similar stimulating effects: F45R and A491R. Both residues are found at the TM domain interface away from the cytoplasmic lipid binding site. All three of these residues are found at a similar height in the bilayer and around the periplasmic exit in *Pa*MprF, suggesting that any introduction of positive charge at this region stimulates the transport of NBD-AlaPG. This is further supported by the V287R mutant; this mutant gave no significant transport rate increase compared to WT *Pa*MprF, and V287 is situated closer to the cytoplasm, away from the periplasmic exit.

The mechanism by which positively charged residues in this region stimulate NBD-AlaPG transport is unclear, and future experiments should further explore the possible stimulating effects of these mutations and whether the effects extend to differently charged/sized reporter lipids.

Chapter 6: Discussion

6.1. Collective evidence suggests that *Pa*MprF acts as a lipid scramblase

The work described in this thesis provides important structural and functional insight into MprF activity. I have demonstrated via *in vitro* assessment of NBD-lipid fluorescence in liposomes that *Pa*MprF is able to transport lipid between liposome leaflets. Whilst it was speculated in the literature that *Pa*MprF lipid transport would be energised (Ernst *et al.* 2009), most likely by the PMF (Song *et al.* 2021), my initial liposome experiments in **Chapter 4** showed that *Pa*MprF can rapidly transport lipid in the absence of a primary energy source. The rate analysis in **Chapter 5** confirmed that transport is unaffected by the presence of common activators. This would suggest that *Pa*MprF is instead acting as a passive phospholipid scramblase, driving lipid distribution towards an equilibrium between both membrane leaflets. Such a classification would be consistent with earlier work in *S. aureus* wild-type cells, which found that LysPG is evenly distributed between the inner and outer leaflets of the membrane (Ernst *et al.* 2009).

In addition, I have established in **Chapter 5** that *Pa*MprF is able to transport a wide range of different NBD-lipid species with both native and non-native headgroups. This finding is consistent with earlier work that demonstrated relaxed specificity at the transport domain of MprF for different aminoacyl-PG species (Slavetinsky *et al.* 2012). Such substrate promiscuity is widely observed in characterised eukaryotic scramblases (Malvezzi *et al.* 2018, Bushell *et al.* 2019), and thus provides further support for the classification of *Pa*MprF as a scramblase.

Although *Pa*MprF can transport a range of lipid substrates, rate analysis in **Chapter 5** suggests that both NBD-AlaPG and NBD-PG transport is favoured *in vitro*. Since unmodified PG

comprises ~25 % of the *P. aeruginosa* membrane (Ghorbal *et al.* 2013) and AlaPG only ~6 % (Klein *et al.* 2009), this observation raises questions as to how AlaPG transport is favoured *in vivo.* One possibility could be that by fusing the aminoacylating soluble domain to the TM transport domain, MprF is able to increase the concentration of AlaPG in the local environment around the transport domain, thus increasing the likelihood of transport of AlaPG over unmodified PG. Such a selectivity-by-proximity mechanism is bolstered by previous work that has characterised MprF dimers (Song *et al.* 2021) and tetramers (Ernst *et al.* 2015), as such oligomers would concentrate aminoacylation domains of MprF in one location in the membrane, leading to much higher local concentrations of AlaPG in proximity to the MprF TM domains.

These findings would make *Pa*MprF the first dedicated phospholipid scramblase in bacteria to be characterised. Such non-specific scrambling activity of *Pa*MprF would be consistent with wider analyses of the MprF family of proteins; it has recently been shown that the MprF lipid transport domain is widespread in bacteria and archaea, often fused to different lipid modifying soluble enzymes such as O-antigen ligases (**Figure 6.1b**) and glycosyltransferases (**Figure 6.1c**) (Hauser *et al.* 2022). This suggests that the MprF transport domain can transport differently modified lipid species depending on the identity of the fused enzyme. In conjunction with the described selectivity-by-proximity mechanism, the attachment of the relevant lipid-modifying enzyme to MprF would then increase the transport of that modified species over bulk lipid. MprF transport domains have also been identified that are not fused to a soluble enzyme. For example, YbhN in *E. coli* is found in proximity to cardiolipin synthesis genes in the *E. coli* genome and interacts with proteins involved in PG and cardiolipin synthesis (**Figure 6.1d**) (Hauser *et al.* 2022), suggesting a role in membrane homeostasis and transport of unmodified bulk lipid species.

In addition to direct MprF homologues, the eukaryotic DedA family members VMP1 and TMEM41B have recently been demonstrated to be phospholipid scramblases (Li *et al.* 2021). There are no experimentally determined structures of any DedA family members, but *in silico* structural predictions of this family suggest the presence of the characteristic double inverted hairpin helix motif found in MprF. The recent characterisation of scramblase activity of DedA family members provides further evidence to support the classification of *Pa*MprF as a phospholipid scramblase, since these families are predicted to share this key structural feature. This is even further supported by the identification of fusions of DedA domains to MprF soluble domains in some bacterial species (**Figure 6.1e**) (Roney and Rudner 2023), again suggesting that DedA and MprF lipid transport domains are somewhat interchangeable and involved in the transport of phospholipid species in a broader biological context.

Recent phylogenetic classification of DedA proteins in bacteria divided them into three sub-families (Todor *et al.* 2023) based on predicted structures and conserved residues at the predicted re-entrant helices. The largest sub-family is COG0586, which share conserved acidic residues in the loop of their 1st re-entrant helix. These residues are essential for protein activity (Kumar and Doerrler 2014, Roney and Rudner 2023). Transporters with similar architecture which couple substrate transport to positively charged ion co-transport have similarly placed acidic residues, leading to the suggestion that these residues would be protonated during a lipid transport cycle and so would couple lipid transport to the PMF (Scarsbrook *et al.* 2021). Of note, the eukaryotic DedA scramblases VMP1 and TMEM41B are most closely related to the COG0398 DedA sub-family. Members of this sub-family lack the acidic residues at re-entrant hairpin loops predicted to couple lipid transport to the PMF in the COG0586 DedA subgroup, consistent with functional characterisations demonstrating that VMP1 and TMEM41B do not require an energy source for lipid transport. Inspection of the loops in the re-entrant helices of MprF homologues shows that there is no wide conservation of acidic residues, suggesting

that, if the mechanism of lipid transport is shared between DedA and MprF proteins, MprF would also not be energised by the PMF, as I have demonstrated experimentally.

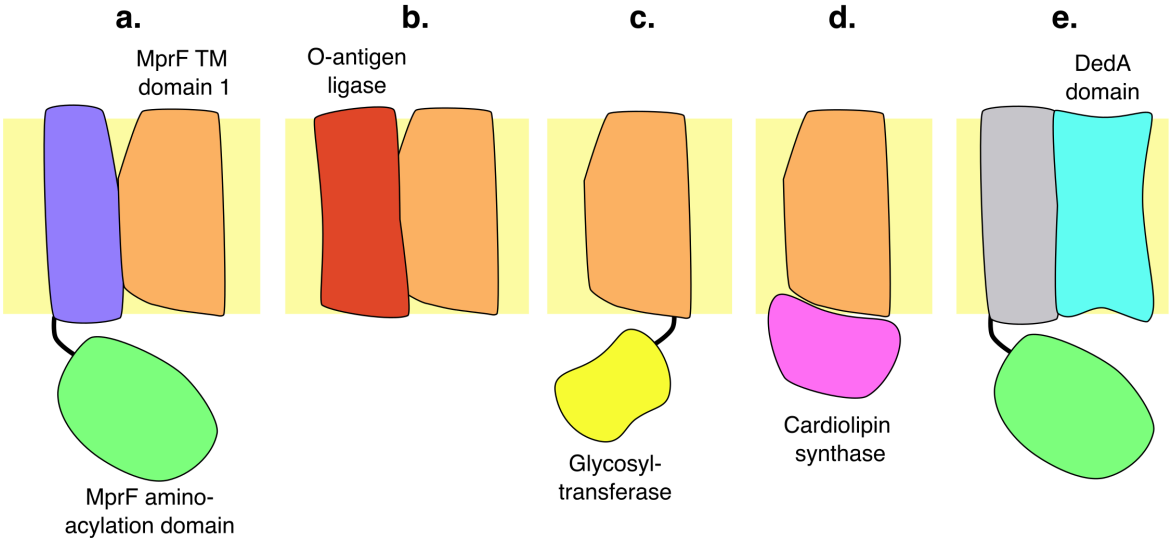

Figure 6.1: MprF domain gene-fusions and interactions occurring in bacteria and archaea. Examples of MprF gene fusions/interactions. **a.** MprF, with transport domain (TM domain 1) coloured orange, and aminoacylation domain green. **b.** Fusion of MprF transport domain to an O-antigen ligase domain coloured red (example UniProt accession: A0A7Y7WPY0). **c.** Fusion of MprF transport domain to glycosyl-transferase coloured yellow (example UniProt accession: A0A4D6GR23). **d.** MprF transport domain (YbhN) binding to a cardiolipin synthase coloured pink (ClsB). **e.** Fusion of MprF aminoacylation domain to DedA domain coloured cyan (example UniProt accession: A0A495IKP1).

6.2. Novel insight into the putative lipid transport pathway

By employing sybody binders to improve cryo-EM sample behaviour, I have elucidated the first high-resolution structure of a full-length MprF homologue from a pathogenic bacterium, *P. aeruginosa.* Comparison of this structure to the previously published MprF structure from *R. tropici* (Song *et al.* 2021) in **Chapter 3** highlights the structural conservation of individual domains despite the low sequence homology between proteins. However, the structure of *Pa*MprF reveals significant displacement of the TM domains relative to *Rt*MprF, resulting in the widening of a groove in contact with bulk lipid that nearly extends the full width of the membrane, together with the opening of a channel through the core of the protein at the TM domain interface that connects the cytoplasm with the periplasm. Previous work on *Rt*MprF

led to the proposal of a lipid transport pathway in which the entire lipid molecule moves through the core of MprF, with a conserved salt bridge (E295-R319 in *Pa*MprF) acting as a gate between the cytoplasm and periplasm (**Figure 6.2,** pathway A) (Song *et al.* 2021). However, the channel present at the TM domain interface in *Pa*MprF suggests instead that, if lipid is transported through the core of *Pa*MprF, it could access this channel with the salt bridge remaining unaffected (**Figure 6.2,** pathway B).

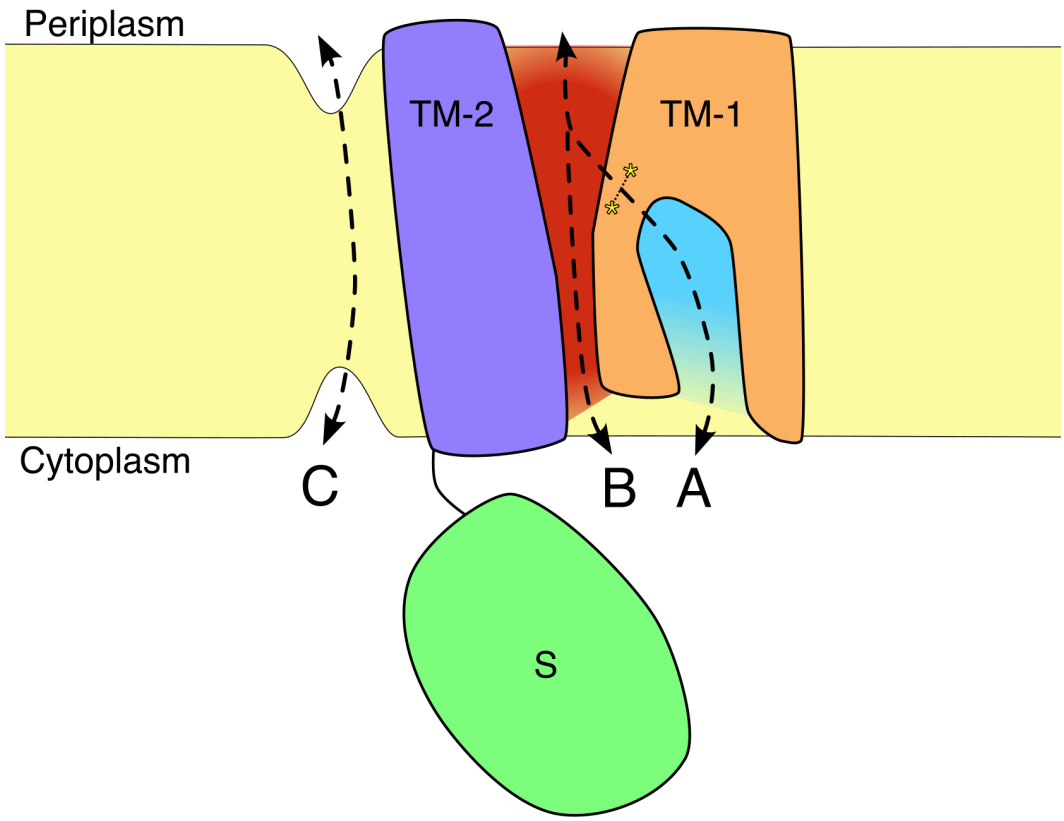

Figure 6.2: Possible *Pa*MprF lipid transport pathways. Schematic of *Pa*MprF (TM domain 1 = orange, TM domain 2 = purple, soluble domain = green, cytoplasmic cavity = blue, TM interface channel = red, E295-R319 salt bridge = yellow asterisks). The lipid pathways investigated in this thesis are labelled (A = transport via disruption of E295-R319 salt bridge, B = transport through TM interface channel, C = transport through membrane-exposed groove via credit-card mechanism or through membrane deformation via out-of-the-groove mechanism).

I explored these two alternative putative lipid pathways via mutagenesis in **Chapter 5** and surprisingly, introduction of large tryptophan residues at both the cytoplasmic lipid binding site and the TM domain interface did not significantly impair lipid transport. Indeed, even attempts to crosslink transported lipid to the artificial amino acid BPA at either site did not

reduce *Pa*MprF-mediated lipid transport. These findings suggest that it is unlikely the full AlaPG lipid molecule is transported by either route through the core of the protein. Both *Rt*MprF and *Pa*MprF cryo-EM structures resolve a lipid bound in the cytoplasmic cavity of TM domain 1, and yet I have shown that introduction of three tryptophan residues simultaneously at this cavity does not affect *Pa*MprF-mediated lipid transport. As such, it is unclear what the function of such a lipid binding site is. Given the soluble domain of *Rt*MprF approaches the membrane at this lipid binding site, it could be that this cavity is involved in the transfer of PG between the membrane and the soluble domain before/after aminoacylation. Such a function would explain the fact that a lysine-modified PG headgroup is clearly resolved in the *Rt*MprF structure (Song *et al.* 2021), whereas no such alanine-modified headgroup is resolved in the presented *Pa*MprF structure (**Figure 6.3**), which features a more distally oriented soluble domain. This hypothesis should be tested by assessing the ability of *Pa*MprF mutants at this site to aminoacylate lipid compared to WT. Specifically, the *Pa*MprF triple mutant N122W/L160W/L279W, which presumably occludes this lipid binding site, should be tested for PG aminoacylation activity in comparison to WT *Pa*MprF; a reduction in aminoacylation activity of this tryptophan mutant would then imply that this site is involved in substrate hand-off to the soluble domain. For such quantitative assessment of activity, the TLC aminoacylation assay used in **Chapter 4** could be modified to use radiolabelled lipid for a more sensitive comparison between *Pa*MprF constructs (Hebecker *et al.* 2011).

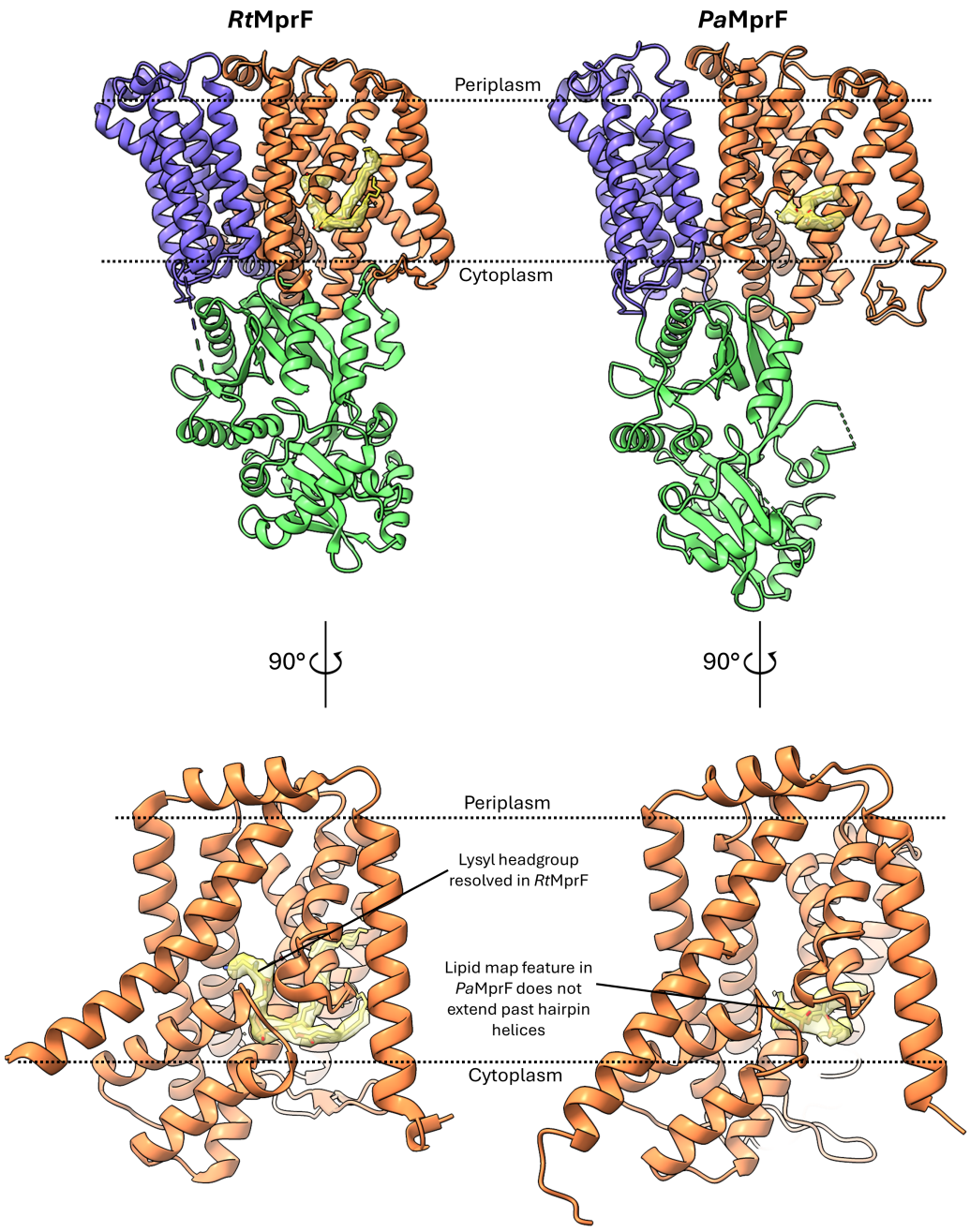

Figure 6.3: MprF cytoplasmic lipid binding site comparison. Structures of *Rt*MprF (PDB:7DUW; (Song *et al.* 2021), left panels) and *Pa*MprF (right panels) are shown (TM domain 1 = orange, TM domain 2 = purple, soluble domain = green) overlaid with the cryo-EM map feature corresponding to bound lipid at the cytoplasmic cavity of each protein (opaque yellow surface). LysPG is fitted to the *Rt*MprF density, and a truncated POPC molecule is fitted to the *Pa*MprF density (both yellow sticks). Bottom panels show a rotated view clipping through TM domain 2, highlighting the difference in resolved lipid headgroup between both structures.

The *Pa*MprF cryo-EM structure presented here also revealed a widening of a lipid-exposed groove at the previously proposed periplasmic lipid exit site. Lipid-exposed grooves are commonly observed in TMEM16 family scramblases (Brunner *et al.* 2014, Bushell *et al.* 2019),

raising the possibility of a credit-card transport mechanism for *Pa*MprF. However, further structural rearrangement would be required to produce a groove that extends the full width of the membrane, as would be required for such a mechanism. As discussed in **Chapter 3**, the use of SapA as a scaffold protein for *Pa*MprF structural studies may have influenced the conformation *Pa*MprF adopts when reconstituted, with the tight nanodisc potentially restricting the further expansion of TM domains. Alternatively, as suggested for some TMEM16 scramblases (Malvezzi *et al.* 2018, Falzone *et al.* 2022), *Pa*MprF may transport lipid via an out-of-the-groove mechanism through deformation of the bilayer in proximity to this groove (**Figure 6.2,** pathway C). Such a mechanism would be consistent with the observation in **Chapter 5** of this thesis that *Pa*MprF is able to transport lipids with "giant" headgroups such as DSPE-PEG2000-NBD. It would also be consistent with the observation that the *Pa*MprF-Sybody29 cryo-EM processing yielded no minor classes of alternate *Pa*MprF conformations, implying a degree of structural rigidity, and yet Sybody29 binding does not impact lipid transport rates *in vitro;* if lipid transport does not require a catalytic cycle of conformation changes within *Pa*MprF and is instead occurring via membrane deformation from a more "open" MprF structure, then Sybody29 binding potentially promoting this structure would not reduce lipid transport rates *in vitro,* as I have demonstrated experimentally. No membrane deformation of the SapNP at this groove was observed in *Pa*MprF cryo-EM maps, but this may be due to the tighter nature of SapA nanodiscs compared to other scaffolds. As such, future work should attempt to structurally characterise *Pa*MprF reconstituted into MSP nanodiscs of a fixed larger size to determine whether membrane deformation can be observed when nanodisc size is increased. Such experiments would also shed light on the impact of scaffold protein choice on the conformation that *Pa*MprF adopts when reconstituted. Future efforts should be focused on assessing the ability of *Pa*MprF to deform the membrane as described for other scramblases (Feng *et al.* 2019, Falzone *et al.* 2022); this could be achieved via coarse-grain MD simulations. Such simulations could also highlight any regions at the surface of *Pa*MprF with increased association with AlaPG molecules, which could direct future mutagenic

work if such regions are involved in facilitating lipid transport. This *in silico* work has recently been initiated in collaboration with Prof. Phillip Stansfeld at the University of Warwick. Alternatively, the presence of *Pa*MprF-mediated membrane deformation and its influence on lipid transport could be investigated structurally and functional via *in vitro* methods. Structurally, *Pa*MprF-reconstituted liposomes could be investigated via cryo-electron tomography to directly visualise the extent of liposome deformation around embedded *Pa*MprF particles, an approach recently applied to Piezo ion channels (Haselwandter *et al.* 2022). Functionally, *Pa*MprF could be reconstituted into liposomes containing bulk lipid with different acyl tail lengths and thus different membrane thicknesses. The *Pa*MprF-mediated lipid transport rates could then be quantified by the NBD transport assay utilised in this thesis to assess whether thinner membranes stimulate lipid transport, as has been characterised for other lipid scramblases expected to function via an "out-of-the-groove" mechanism (Bushell *et al.* 2019, Falzone *et al.* 2022).

The three potential lipid transport pathways investigated in this thesis are summarised in **Table 6.1** below:

Table 6.1: Summary of evidence presented in this thesis for and against each proposed *Pa*MprF lipid transport mechanism.

Transport pathway	Supporting evidence	Contradicting evidence
Salt-bridge separation (A)	• Bound lipid at cytoplasmic cavity resolved in both *Pa*MprF and *Rt*MprF structures. • Salt-bridge residues highly conserved.	• Mutation of salt bridge residues to alanine does not affect transport rates *in vitro*. • Obstruction of cytoplasmic cavity with tryptophan residues does not reduce lipid transport rates *in vitro*. • Lipid transport in liposomes is not influenced by pH gradients.
TM domain interface (B)	• *Pa*MprF structure reveals a complete channel between cytoplasm and periplasm at TM domain interface.	• Obstruction of interface with tryptophan residues does not reduce lipid transport rates *in vitro*. • Cross-linking attempts with targeted disulfide bonds and BPA artificial amino acid do not reduce lipid transport rates *in vitro*.
Credit-card/out-of-the-groove (C)	• *Pa*MprF is able to transport a range of substrates *in vitro,* including "giant" substrates with headgroups larger than the cytoplasmic cavity/TM domain interface. • *Pa*MprF structure reveals widening of lipid-exposed groove at periplasmic lipid exit site.	• Lipid-exposed groove does not extend the full width of membrane in *Pa*MprF structure. • No deformation of SapNP around this groove in cryo-EM map.

Previous *in vivo* experiments had identified mutations in *Rt*MprF that were suggested to increase the rate of lipid transport, with the most drastic stimulating mutation being alteration of the conserved salt bridge glutamate (E295 in *Pa*MprF) to a positively charged residue (Song *et al.* 2021). In **Chapter 5** of this thesis, I produced a similar mutation in *Pa*MprF - E295R - and demonstrated that lipid transport in this mutant *in vitro* is significantly enhanced compared to WT *Pa*MprF, consistent with the previous *in vivo* data. Furthermore, similar arginine mutations of residues in proximity to E295R (F45R and A491R) also enhanced lipid transport, suggesting that the previously observed increase in lipid transport *in vivo* is not a result of disruption of the conserved salt bridge, but rather the introduction of a positive charge at a particular

location at the TM domain interface of *Pa*MprF. Interestingly, several of the MRSA gain-of-function MprF mutations discussed in the **Introduction (1.3.6.)** introduce positively charged residues at the TM region (Bayer *et al.* 2015). One such mutation, M347R, corresponds to V369 in *Pa*MprF, which is also located in proximity to F45 and A491 (**Figure 6.4**). M347R increases surface positive charge of MRSA strains (Bayer *et al.* 2015), further supporting the suggestion that positively charged residues at this location stimulate MprF-mediated aminoacyl-PG transport.

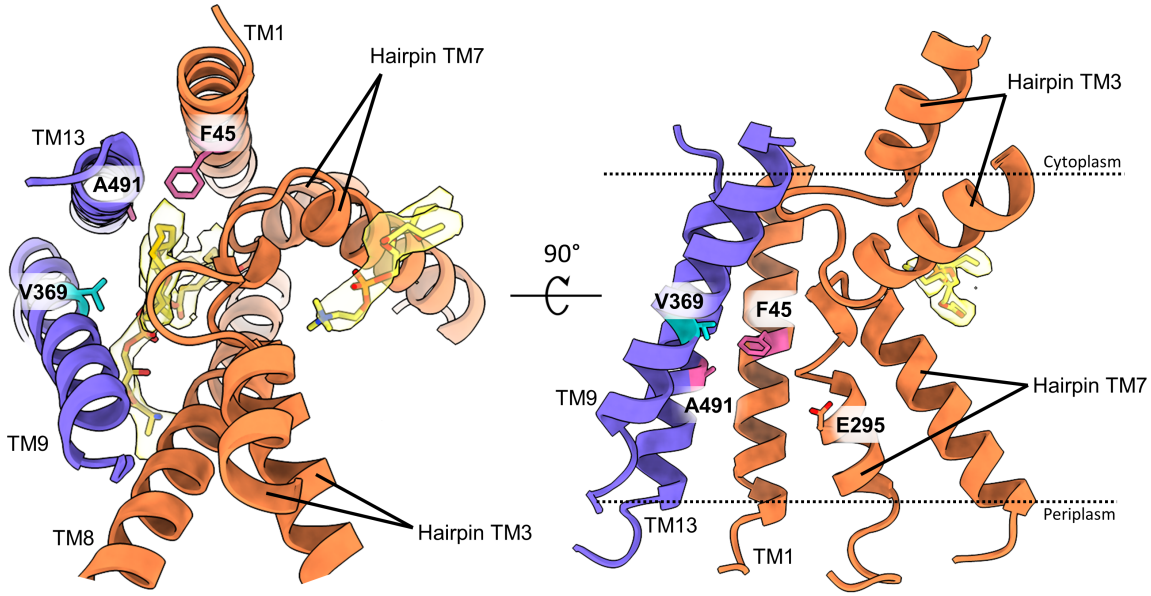

Figure 6.4: Residues that stimulate MprF transport when mutated to arginine. View of the *Pa*MprF TM domain interface (as in **Figure 5.22**). F45 and A491 are coloured pink, V369 (M347 in *Sa*MprF) is coloured cyan.

These residues all reside at the TM domain interface, and so the introduction of a large, charged arginine residue could increase the separation between TM domains. If lipid transport is occurring via the groove at the TM domain interface, increased domain separation could further widen the groove at this location, increasing lipid transport. These arginine mutants should therefore also be investigated by MD simulations; atomistic simulations could identify whether these mutations induce significant domain separation, and coarse grain simulations could then assess whether there is a subsequent increase in membrane thinning at this groove, whilst additionally probing the accessibility of the TM domain interface to AlaPG in comparison to WT.

6.3. Considerations on the oligomeric state of *Pa*MprF

Interestingly, the work in **Chapter 3** has demonstrated that *Pa*MprF is purified predominantly as a monomer, although previous work in the Bublitz group has confirmed that *Pa*MprF is also able to form higher order oligomers (Lundie-Brown 2018) and so it is possible that *Pa*MprF oligomerises when reconstituted into liposomes. One potential explanation for the significant structural differences observed between *Pa*MprF and *Rt*MprF is that of different oligomerisation state. Whether the more "open" *Pa*MprF structure is more conducive to lipid transport, and thus whether such oligomerisation regulates lipid transport remains unclear. As such, future mutagenesis work should be targeted at the dimerisation interface identified in the *Rt*MprF cryo-EM structure (Song *et al.* 2021) to identify *Pa*MprF mutants that do not form higher order oligomers. Such mutants should then be tested in the established lipid transport assay in comparison to WT *Pa*MprF to assess whether rates of lipid transport are significantly impaired/enhanced. Rates of transport for *Rt*MprF should also be assessed and compared to *Pa*MprF, to identify any differences that may arise from oligomerisation state.

6.4. Substrate binding at the soluble domain

Although not within the scope of this thesis, one further question raised by the *Pa*MprF cryo-EM structure in **Chapter 3** is that of how substrate binds at the soluble domain. The absence of a clearly resolved soluble domain loop (residues 806-834) results in the appearance of a hydrophobic groove, which is absent in the previous *Pa*MprF soluble domain crystal structure (Hebecker *et al.* 2015). This suggests that structural rearrangement of this flexible loop could open a PG binding site on the same face of the soluble domain as the predicted tRNA binding site. Such a PG binding site is at odds with the substrate pathway suggested from previous crystallographic studies of the *Pa*MprF soluble domain (Hebecker *et al.* 2015), but more consistent with the substrate binding mode of similar enzymes (Fonvielle *et al.* 2013) and in

support of the soluble domain conformations that were observed as minor classes in the processing of previous *Rt*MprF cryo-EM data (Song *et al.* 2021). As such, future work should focus on structural characterisation of *Pa*MprF using aminoacyl-lipid analogues or tRNA acceptor stem substrates. Indeed, such work could be complemented by exploring the nature of the interaction between *Pa*MprF and AlaRS identified in **Chapter 4**. The formation of such a complex provides an explanation for the mechanism by which aminoacyl-tRNA "escapes" the dedicated protein synthesis pathway for use at the bacterial membrane, and structural characterisation of this complex would provide further insight into the nature of the *Pa*MprF tRNA binding site. Binding studies in this thesis suggest the affinity for this interaction is modest, so future work should aim to stabilise the *Pa*MprF-AlaRS complex, for example through crosslinking (Kastner *et al.* 2008), to prevent dissociation during grid preparation for cryo-EM. Alternatively, this interaction could be investigated structurally with the expression and purification of the soluble domain of *Pa*MprF alone; removal of the *Pa*MprF TM domain may increase the stability and yield of the soluble domain, and so could provide a faster route to characterisation of the interface between the *Pa*MprF soluble domain and AlaRS.

An additional unknown is whether the *Pa*MprF-AlaRS interaction acts to increase local concentration of charged-tRNA to favour PG aminoacylation indirectly, or if charged-tRNA is handed-off directly from AlaRS to the *Pa*MprF soluble domain. This could be investigated following identification of the *Pa*MprF-AlaRS interface; key residues involved in the interaction could be mutated with the aim of disrupting complex formation. This disruption could be confirmed by repetition of the pull-down and SEC co-elution assays outlined in **Chapter 4** of this thesis. Constructs that do not form a complex could then be combined into a fusion protein, similar to the previously discussed LysX (Maloney *et al.* 2009). This fusion of mutant *Pa*MprF and AlaRS could then be tested for PG aminoacylation activity; reduction in aminoacylation of PG compared to WT *Pa*MprF/AlaRS would then imply that proximity of AlaRS to *Pa*MprF is not

sufficient for PG aminoacylation, and that a specific *Pa*MprF-AlaRS interaction is required for charged-tRNA to be directly handed-off from AlaRS to *Pa*MprF.

6.5. MprF's potential as an antimicrobial target

Much interest in MprF has stemmed from its potential as a target against antimicrobial-resistant bacteria. Inhibition of MprF activity could sensitise such bacteria to existing positively charged antibiotics, whilst also improving the efficacy of CAMPs produced by the human immune system during infections. In addition, targeting of the gain-of-function MprF mutants present in daptomycin-resistant MRSA (Ernst *et al.* 2018) could provide a valuable treatment for such severe antimicrobial-resistant clinical infections. Although compounds could be developed to inhibit the synthase activity of MprF, such compounds would likely target the tRNA binding site of the soluble domain and could therefore induce off-target effects by inhibiting protein synthesis in human cells (Ho *et al.* 2018). Instead, inhibition of MprF lipid transport activity may be a more valuable target for the development of novel antimicrobials, since the absence of MprF transport domain homologues in eukaryotes suggests such an approach would be unlikely to induce off-target effects. Furthermore, the TM domain of MprF is exposed at the cell surface in Gram-positive bacteria, and so would be more accessible to antimicrobials than the soluble domain within the cytoplasm. Indeed, recent work has shown that antibodies targeting extracellular loops of the *Sa*MprF TM domain sensitise MRSA strains to CAMPs, suggesting antibody binding inhibits *Sa*MprF-mediated transport of LysPG (Slavetinsky *et al.* 2022) and highlighting the potential of targeting the MprF TM domain therapeutically.

Since I have demonstrated that lipid transport by *Pa*MprF can be measured *in vitro* in liposomes, the work in this thesis has the potential to be translated into a 96-well plate-based high-throughput assay which could be used to screen libraries of small molecules to identify

compounds capable of inhibiting the lipid transport activity of *Pa*MprF. If aminoacylated-PG is transported through the core of *Pa*MprF via the cytoplasmic cavity (pathway A, **Figure 6.2**) or the TM domain interface (pathway B), both sites have the potential to be blocked by small-molecule binding given the limited accessibility of both pathways indicated by the available structural data. However, if lipid transport is occurring via a credit-card or out-of-the-groove mechanism (pathway C) in the vicinity of the wide lipid-exposed groove observed in the *Pa*MprF cryo-EM structure, such a wide groove is less likely to be "druggable" through small-molecule binding. Indeed, the high degree of promiscuity that *Pa*MprF displays *in vitro* further suggests that targeting lipid transport activity might prove difficult. As such, other bacterial lipid transporters involved in antimicrobial resistance may be more suitable for the development of novel antimicrobials. For example, LtaA, the Gram-positive flippase that transports the lipid onto which LTAs are attached at the bacterial surface, has recently been demonstrated to function via a trap-and-flip mechanism (Lambert *et al.* 2022). Lipid export by LtaA is reliant upon transitioning between distinct inward-open and outward-open conformations, making this mechanism more suitable for antimicrobial targeting, as compounds could be developed which access LtaA from the cell surface and bind at the outward-open substrate cavity to lock the transporter in this state.

6.6. Concluding remarks

The cumulative evidence I have presented here challenges several of the previously assumed characteristics of MprF-mediated lipid transport in bacteria. I have demonstrated that *Pa*MprF is capable of bidirectional lipid translocation *in vitro* in the absence of any external energy source. Combined with experiments that show the wide variety of lipid substrates that *Pa*MprF can transport, I conclude that *Pa*MprF is a highly promiscuous phospholipid scramblase, the first to be characterised in bacteria. MprF possesses a unique architecture compared to other characterised lipid transporters, comprising inverted hairpin helix repeats. *In silico* predictions of DedA protein structures suggest the presence of a similar architecture, and as eukaryotic members of the DedA family have recently also been shown to function as scramblases *in vitro* (Li *et al.* 2021), the work in this thesis implies the wider existence of a novel class of scramblases. The *Pa*MprF cryo-EM structure presented in this work offers several explanations as to how lipid is transported by MprF family proteins, and whilst I have presented data that favours a credit-card/out-of-the-groove transport mechanism, the exact nature of *Pa*MprF-mediated lipid transport remains uncertain. Future work should focus further on assessing which of the possible transport pathways highlighted in this thesis is the route by which this remarkable enzyme so efficiently catalyses such an energetically challenging process.

References

Abeyrathne, P. D., C. Daniels, K. K. Poon, M. J. Matewish and J. S. Lam (2005). "Functional characterization of WaaL, a ligase associated with linking O-antigen polysaccharide to the core of *Pseudomonas aeruginosa* lipopolysaccharide." Journal of Bacteriology **187**(9): 3002-3012.

Afonine, P. V., B. K. Poon, R. J. Read, O. V. Sobolev, T. C. Terwilliger, A. Urzhumtsev and P. D. Adams (2018). "Real-space refinement in PHENIX for cryo-EM and crystallography." Acta Crystallographica Section D **74**(Pt 6): 531-544.

Ahmad, J., J. Jiang, L. F. Boyd, A. Zeher, R. Huang, D. Xia, K. Natarajan and D. H. Margulies (2021). "Structures of synthetic nanobody–SARS-CoV-2 receptor-binding domain complexes reveal distinct sites of interaction." Journal of Biological Chemistry **297**(4): 101202.

Alvadia, C., N. K. Lim, V. Clerico Mosina, G. T. Oostergetel, R. Dutzler and C. Paulino (2019). "Cryo-EM structures and functional characterization of the murine lipid scramblase TMEM16F." eLife **8**: e44365.

Anderson, A., S. A. Scaringe, B. E. Earp and C. A. Frederick (1996). "HPLC purification of RNA for crystallography and NMR." RNA **2**(2): 110-117.

Arbabi Ghahroudi, M., A. Desmyter, L. Wyns, R. Hamers and S. Muyldermans (1997). "Selection and identification of single domain antibody fragments from camel heavy-chain antibodies." FEBS Letters **414**(3): 521-526.

Arendt, W., M. K. Groenewold, S. Hebecker, J. S. Dickschat and J. Moser (2013). "Identification and characterization of a periplasmic aminoacyl-phosphatidylglycerol hydrolase responsible for *Pseudomonas aeruginosa* lipid homeostasis." Journal of Biological Chemistry **288**(34): 24717-24730.

Arndt, M., C. Alvadia, M. S. Straub, V. Clerico Mosina, C. Paulino and R. Dutzler (2022). "Structural basis for the activation of the lipid scramblase TMEM16F." Nature Communications **13**(1): 6692.

Baldridge, R. D. and T. R. Graham (2012). "Identification of residues defining phospholipid flippase substrate specificity of type IV P-type ATPases." Proceedings of the National Academy of Sciences of the United States of America **109**(6): E290-298.

Batey, R. T. and J. S. Kieft (2007). "Improved native affinity purification of RNA." RNA **13**(8): 1384-1389.

Bayer, A. S., N. N. Mishra, L. Chen, B. N. Kreiswirth, A. Rubio and S. J. Yang (2015). "Frequency and distribution of single-nucleotide polymorphisms within mprF in Methicillin-Resistant *Staphylococcus aureus* clinical isolates and their role in cross-resistance to daptomycin and host defense antimicrobial peptides." Antimicrobial Agents and Chemotherapy **59**(8): 4930-4937.

Benjin, X. and L. Ling (2020). "Developments, applications, and prospects of cryo-electron microscopy." Protein Science **29**(4): 872-882.

Bisicchia, P., D. Noone, E. Lioliou, A. Howell, S. Quigley, T. Jensen, H. Jarmer and K. M. Devine (2007). "The essential YycFG two-component system controls cell wall metabolism in *Bacillus subtilis*." Molecular Microbiology **65**(1): 180-200.

Bligh, E. G. and W. J. Dyer (1959). "A rapid method of total lipid extraction and purification." Canadian Journal of Biochemistry and Physiology **37**(8): 911-917.

Bogdanov, M., K. Pyrshev, S. Yesylevskyy, S. Ryabichko, V. Boiko, P. Ivanchenko, R. Kiyamova, Z. Guan, C. Ramseyer and W. Dowhan (2020). "Phospholipid distribution in the cytoplasmic membrane of Gram-negative bacteria is highly asymmetric, dynamic, and cell shape-dependent." Science Advances **6**(23): eaaz6333.

Bretscher, M. S. (1973). "Membrane structure: some general principles." Science **181**(4100): 622-629.

Brown, S., J. P. Santa Maria, Jr. and S. Walker (2013). "Wall teichoic acids of gram-positive bacteria." Annual Review of Microbiology **67**: 313-336.

Brunner, J. D., N. K. Lim, S. Schenck, A. Duerst and R. Dutzler (2014). "X-ray structure of a calcium-activated TMEM16 lipid scramblase." Nature **516**(7530): 207-212.

Brunner, J. D. and S. Schenck (2019). Preparation of proteoliposomes with purified TMEM16 protein for accurate measures of lipid scramblase activity. Intracellular Lipid Transport: Methods and Protocols. **14:** 181-199.

Bublitz, M., J. P. Morth and P. Nissen (2011). "P-type ATPases at a glance." Journal of Cell Science **124**(15): 2515-2519.

Bushell, S. R., A. C. Pike, M. E. Falzone, N. J. Rorsman, C. M. Ta, R. A. Corey, T. D. Newport, J. C. Christianson, L. F. Scofano and C. A. Shintre (2019). "The structural basis of lipid scrambling and inactivation in the endoplasmic reticulum scramblase TMEM16K." Nature Communications **10**(1): 3956.

Chauhan, N., L. Farine, K. Pandey, A. K. Menon and P. Bütikofer (2016). "Lipid topogenesis - 35 years on." Biochimica et Biophysica Acta **1861**(8 Pt B): 757-766.

Chee Wezen, X., A. Chandran, R. S. Eapen, E. Waters, L. Bricio-Moreno, T. Tosi, S. Dolan, C. Millership, A. Kadioglu, A. Gründling, L. S. Itzhaki, M. Welch and T. Rahman (2022). "Structure-based discovery of lipoteichoic acid synthase inhibitors." Journal of Chemical Information and Modeling **62**(10): 2586-2599.

Chen, F.-J., T.-L. Lauderdale, C.-H. Lee, Y.-C. Hsu, I.-W. Huang, P.-C. Hsu and C.-S. Yang (2018). "Effect of a point mutation in mprF on susceptibility to daptomycin, vancomycin, and oxacillin in an MRSA clinical strain." Frontiers in Microbiology **9**: 1086.

Cheng, Y. (2018). "Membrane protein structural biology in the era of single particle cryo-EM." Current Opinion in Structural Biology **52**: 58-63.

Cheng, Y., N. Grigorieff, P. A. Penczek and T. Walz (2015). "A primer to single-particle cryo-electron microscopy." Cell **161**(3): 438-449.

Chin, J. W., A. B. Martin, D. S. King, L. Wang and P. G. Schultz (2002). "Addition of a photocrosslinking amino acid to the genetic code of *Escherichia coli*." Proceedings of the National Academy of Sciences of the United States of America **99**(17): 11020-11024.

Cho, J., C. Manna Adhar, S. Snelling Helah and L. Cheung Ambrose (2023). "GraS signaling in *Staphylococcus aureus* is regulated by a single D35 residue in the extracellular loop." Microbiology Spectrum **11**(5): e01982-01923.

Chua, G.-L., B. C. Tan, R. Y. J. Loke, M. He, C.-F. Chin, B. H. Wong, A. C. Y. Kuk, M. Ding, M. R. Wenk, L. Guan, F. Torta and D. L. Silver (2023). "Mfsd2a utilizes a flippase mechanism to mediate omega-3 fatty acid lysolipid transport." Proceedings of the National Academy of Sciences of the United States of America **120**(10): e2215290120.

Coakley, R. D., B. R. Grubb, A. M. Paradiso, J. T. Gatzy, L. G. Johnson, S. M. Kreda, W. K. O'Neal and R. C. Boucher (2003). "Abnormal surface liquid pH regulation by cultured cystic fibrosis bronchial epithelium." Proceedings of the National Academy of Sciences of the United States of America **100**(26): 16083-16088.

Coleman, J. A., M. C. Kwok and R. S. Molday (2009). "Localization, purification, and functional reconstitution of the P4-ATPase Atp8a2, a phosphatidylserine flippase in photoreceptor disc membranes." Journal of Biological Chemistry **284**(47): 32670-32679.

Coleman, J. A., F. Quazi and R. S. Molday (2013). "Mammalian P4-ATPases and ABC transporters and their role in phospholipid transport." Biochimica et Biophysica Acta **1831**(3): 555-574.

Dalal, V., M. J. Arcario, J. T. Petroff, B. K. Tan, N. M. Dietzen, M. J. Rau, J. A. J. Fitzpatrick, G. Brannigan and W. W. L. Cheng (2024). "Lipid nanodisc scaffold and size alter the structure of a pentameric ligand-gated ion channel." Nature Communications **15**(1): 25.

Dare, K., J. Shepherd, H. Roy, S. Seveau and M. Ibba (2014). "LysPGS formation in *Listeria monocytogenes* has broad roles in maintaining membrane integrity beyond antimicrobial peptide resistance." Virulence **5**(4): 534-546.

De Genst, E., K. Silence, K. Decanniere, K. Conrath, R. Loris, J. Kinne, S. Muyldermans and L. Wyns (2006). "Molecular basis for the preferential cleft recognition by dromedary heavy-chain antibodies." Proceedings of the National Academy of Sciences of the United States of America **103**(12): 4586-4591.

Delcour, A. H. (2009). "Outer membrane permeability and antibiotic resistance." Biochimica et Biophysica Acta **1794**(5): 808-816.

Denapaite, D., R. Brückner, R. Hakenbeck and W. Vollmer (2012). "Biosynthesis of teichoic acids in *Streptococcus pneumoniae* and closely related species: lessons from genomes." Microbial Drug Resistance **18**(3): 344-358.

Denisov, I. G., Y. V. Grinkova, A. A. Lazarides and S. G. Sligar (2004). "Directed self-assembly of monodisperse phospholipid bilayer nanodiscs with controlled size." Journal of the American Chemical Society **126**(11): 3477-3487.

Dennison, S. R., L. H. Morton, F. Harris and D. A. Phoenix (2016). "Low pH enhances the action of maximin H5 against *Staphylococcus aureus* and helps mediate lysylated phosphatidylglycerol-induced resistance." Biochemistry **55**(27): 3735-3751.

Deutschmann, S., L. Rimle and C. von Ballmoos (2022). "Rapid estimation of membrane protein orientation in liposomes." ChemBioChem **23**(2): e202100543.

Dutzler, R., E. B. Campbell, M. Cadene, B. T. Chait and R. MacKinnon (2002). "X-ray structure of a ClC chloride channel at 3.0 A reveals the molecular basis of anion selectivity." Nature **415**(6869): 287-294.

Dyda, F., D. C. Klein and A. B. Hickman (2000). "GCN5-related N-acetyltransferases: a structural overview." Annual Review of Biophysics **29**: 81-103.

Eckford, P. D. and F. J. Sharom (2005). "The reconstituted P-glycoprotein multidrug transporter is a flippase for glucosylceramide and other simple glycosphingolipids." Biochemical Journal **389**(Pt 2): 517-526.

El Ghachi, M., A. Bouhss, D. Blanot and D. Mengin-Lecreulx (2004). "The bacA gene of *Escherichia coli* encodes an undecaprenyl pyrophosphate phosphatase activity." Journal of Biological Chemistry **279**(29): 30106-30113.

El Ghachi, M., N. Howe, C.-Y. Huang, V. Olieric, R. Warshamanage, T. Touzé, D. Weichert, P. J. Stansfeld, M. Wang, F. Kerff and M. Caffrey (2018). "Crystal structure of undecaprenyl-pyrophosphate phosphatase and its role in peptidoglycan biosynthesis." Nature Communications **9**(1): 1078.

Emsley, P. and K. Cowtan (2004). "Coot: model-building tools for molecular graphics." Acta Crystallographica Section D **60**(Pt 12 Pt 1): 2126-2132.

Ernst, C. M., S. Kuhn, C. J. Slavetinsky, B. Krismer, S. Heilbronner, C. Gekeler, D. Kraus, S. Wagner and A. Peschel (2015). "The lipid-modifying multiple peptide resistance factor is an oligomer consisting of distinct interacting synthase and flippase subunits." mBio **6**(1): e0234014.

Ernst, C. M., C. J. Slavetinsky, S. Kuhn, J. N. Hauser, M. Nega, N. N. Mishra, C. Gekeler, A. S. Bayer and A. Peschel (2018). "Gain-of-function mutations in the phospholipid flippase MprF confer specific daptomycin resistance." mBio **9**(6): e0165918.

Ernst, C. M., P. Staubitz, N. N. Mishra, S.-J. Yang, G. Hornig, H. Kalbacher, A. S. Bayer, D. Kraus and A. Peschel (2009). "The bacterial defensin resistance protein MprF consists of separable domains for lipid lysinylation and antimicrobial peptide repulsion." PLoS Pathogens **5**(11): e1000660.

Fadok, V. A., D. R. Voelker, P. A. Campbell, J. J. Cohen, D. L. Bratton and P. M. Henson (1992). "Exposure of phosphatidylserine on the surface of apoptotic lymphocytes triggers specific recognition and removal by macrophages." Journal of Immunology **148**(7): 2207-2216.

Falord, M., G. Karimova, A. Hiron and T. Msadek (2012). "GraXSR proteins interact with the VraFG ABC transporter to form a five-component system required for cationic antimicrobial peptide sensing and resistance in *Staphylococcus aureus*." Antimicrobial Agents and Chemotherapy **56**(2): 1047-1058.

Falzone, M. E. and A. Accardi (2020). Reconstitution of proteoliposomes for phospholipid scrambling and nonselective channel assays. Expression, Purification, and Structural Biology of Membrane Proteins. **15:** 207-225.

Falzone, M. E., Z. Feng, O. E. Alvarenga, Y. Pan, B. Lee, X. Cheng, E. Fortea, S. Scheuring and A. Accardi (2022). "TMEM16 scramblases thin the membrane to enable lipid scrambling." Nature Communications **13**(1): 2604.

Falzone, M. E., J. Rheinberger, B. C. Lee, T. Peyear, L. Sasset, A. M. Raczkowski, E. T. Eng, A. Di Lorenzo, O. S. Andersen, C. M. Nimigean and A. Accardi (2019). "Structural basis of Ca(2+)-dependent activation and lipid transport by a TMEM16 scramblase." eLife **8**: e43229.

Feldman, M. F., C. L. Marolda, M. A. Monteiro, M. B. Perry, A. J. Parodi and M. A. Valvano (1999). "The activity of a putative polyisoprenol-linked sugar translocase (Wzx) involved in *Escherichia coli* O antigen assembly is independent of the chemical structure of the O repeat." Journal of Biological Chemistry **274**(49): 35129-35138.

Feng, S., S. Dang, T. W. Han, W. Ye, P. Jin, T. Cheng, J. Li, Y. N. Jan, L. Y. Jan and Y. Cheng (2019). "Cryo-EM studies of TMEM16F calcium-activated ion channel suggest features important for lipid scrambling." Cell Reports **28**(2): 567-579.

Flannagan, R. S., B. Heit and D. E. Heinrichs (2016). "Intracellular replication of *Staphylococcus aureus* in mature phagolysosomes in macrophages precedes host cell death, and bacterial escape and dissemination." Cellular Microbiology **18**(4): 514-535.

Flannagan, R. S., R. C. Kuiack, M. J. McGavin and D. E. Heinrichs (2018). "*Staphylococcus aureus* uses the GraXRS regulatory system to sense and adapt to the acidified phagolysosome in macrophages." mBio **9**(4): e0114318.

Flayhan, A., H. D. T. Mertens, Y. Ural-Blimke, M. Martinez Molledo, D. I. Svergun and C. Löw (2018). "Saposin lipid nanoparticles: a highly versatile and modular tool for membrane protein research." Structure **26**(2): 345-355.

Fonvielle, M., I. Li de La Sierra-Gallay, A. H. El-Sagheer, M. Lecerf, D. Patin, D. Mellal, C. Mayer, D. Blanot, N. Gale, T. Brown, H. van Tilbeurgh, M. Ethève-Quelquejeu and M. Arthur (2013). "The structure of FemX(Wv) in complex with a peptidyl-RNA conjugate: mechanism of aminoacyl transfer from Ala-tRNA(Ala) to peptidoglycan precursors." Angewandte Chemie **52**(28): 7278-7281.

Fowler, V. G., J. M. Miro, B. Hoen, C. H. Cabell, E. Abrutyn, E. Rubinstein, G. R. Corey, D. Spelman, S. F. Bradley and B. Barsic (2005). "*Staphylococcus aureus* endocarditis: a consequence of medical progress." Journal of the American Medical Association **293**(24): 3012-3021.

Frauenfeld, J., R. Löving, J.-P. Armache, A. F. P. Sonnen, F. Guettou, P. Moberg, L. Zhu, C. Jegerschöld, A. Flayhan, J. A. G. Briggs, H. Garoff, C. Löw, Y. Cheng and P. Nordlund (2016). "A saposin-lipoprotein nanoparticle system for membrane proteins." Nature Methods **13**(4): 345-351.

Friedman, L., J. D. Alder and J. A. Silverman (2006). "Genetic changes that correlate with reduced susceptibility to daptomycin in *Staphylococcus aureus*." Antimicrobial Agents and Chemotherapy **50**(6): 2137-2145.

Garde, S., P. K. Chodisetti and M. Reddy (2021). "Peptidoglycan: structure, synthesis, and regulation." EcoSal Plus **9**(2): ESP-0010-2020.

Geertsma, E. R. and R. Dutzler (2011). "A versatile and efficient high-throughput cloning tool for structural biology." Biochemistry **50**(15): 3272-3278.

Ghorbal, S. K., A. Chatti, M. M. Sethom, L. Maalej, M. Mihoub, S. Kefacha, M. Feki, A. Landoulsi and A. Hassen (2013). "Changes in membrane fatty acid composition of *Pseudomonas aeruginosa* in response to UV-C radiations." Current Microbiology **67**(1): 112-117.

Giannouli, S., A. Kyritsis, N. Malissovas, H. D. Becker and C. Stathopoulos (2009). "On the role of an unusual tRNAGly isoacceptor in *Staphylococcus aureus*." Biochimie **91**(3): 344-351.

Goren, M. A., T. Morizumi, I. Menon, J. S. Joseph, J. S. Dittman, V. Cherezov, R. C. Stevens, O. P. Ernst and A. K. Menon (2014). "Constitutive phospholipid scramblase activity of a G protein-coupled receptor." Nature Communications **5**(1): 5115.

Govan, J. R. and V. Deretic (1996). "Microbial pathogenesis in cystic fibrosis: mucoid *Pseudomonas aeruginosa* and Burkholderia cepacia." Microbiology Reviews **60**(3): 539-574.

Gründling, A. and O. Schneewind (2007). "Synthesis of glycerol phosphate lipoteichoic acid in *Staphylococcus aureus*." Proceedings of the National Academy of Sciences of the United States of America **104**(20): 8478-8483.

Guyet, A., A. Alofi and R. A. Daniel (2023). "Insights into the roles of lipoteichoic acids and MprF in *Bacillus subtilis*." mBio **14**(1): e0266722.

Hankins, M. (2019). "Towards the structural characterization of the *Pseudomonas aeruginosa* multiple peptide resistance factor, MprF". Master's Thesis, University of Oxford.

Hanson, B. R. and M. N. Neely (2012). "Coordinate regulation of Gram-positive cell surface components." Current Opinion in Microbiology **15**(2): 204-210.

Haselwandter, C. A., Y. R. Guo, Z. Fu and R. MacKinnon (2022). "Quantitative prediction and measurement of Piezo's membrane footprint." Proceedings of the National Academy of Sciences of the United States of America **119**(40): e2208027119.

Hauser, J. N., A. Kengmo Tchoupa, S. Zabel, K. Nieselt, C. M. Ernst, C. J. Slavetinsky and A. Peschel (2022). "PplT domain proteins–ubiquitous potential prokaryotic phospholipid translocases." BioRxiv **[Preprint]**.

Heaton, M. P. and F. C. Neuhaus (1992). "Biosynthesis of D-alanyl-lipoteichoic acid: cloning, nucleotide sequence, and expression of the *Lactobacillus casei* gene for the D-alanine-activating enzyme." Journal of Bacteriology **174**(14): 4707-4717.

Hebecker, S., W. Arendt, I. U. Heinemann, J. H. Tiefenau, M. Nimtz, M. Rohde, D. Söll and J. Moser (2011). "Alanyl ‐ phosphatidylglycerol synthase: mechanism of substrate recognition during tRNA ‐ dependent lipid modification in *Pseudomonas aeruginosa*." Molecular Microbiology **80**(4): 935-950.

Hebecker, S., J. Krausze, T. Hasenkampf, J. Schneider, M. Groenewold, J. Reichelt, D. Jahn, D. W. Heinz and J. Moser (2015). "Structures of two bacterial resistance factors mediating tRNA-dependent aminoacylation of phosphatidylglycerol with lysine or alanine." Proceedings of the National Academy of Sciences of the United States of America **112**(34): 10691-10696.

Helenius, J., D. T. Ng, C. L. Marolda, P. Walter, M. A. Valvano and M. Aebi (2002). "Translocation of lipid-linked oligosaccharides across the ER membrane requires Rft1 protein." Nature **415**(6870): 447-450.

Hiraizumi, M., K. Yamashita, T. Nishizawa and O. Nureki (2019). "Cryo-EM structures capture the transport cycle of the P4-ATPase flippase." Science **365**(6458): 1149-1155.

Ho, B. K. and F. Gruswitz (2008). "HOLLOW: generating accurate representations of channel and interior surfaces in molecular structures." BMC Structural Biology **8**(1): 49.

Ho, H., A. Miu, M. K. Alexander, N. K. Garcia, A. Oh, I. Zilberleyb, M. Reichelt, C. D. Austin, C. Tam, S. Shriver, H. Hu, S. S. Labadie, J. Liang, L. Wang, J. Wang, Y. Lu, H. E. Purkey, J. Quinn, Y. Franke, K. Clark, M. H. Beresini, M.-W. Tan, B. D. Sellers, T. Maurer, M. F. T. Koehler, A. T. Wecksler, J. R. Kiefer, V. Verma, Y. Xu, M. Nishiyama, J. Payandeh and C. M. Koth (2018). "Structural basis for dual-mode inhibition of the ABC transporter MsbA." Nature **557**(7704): 196-201.

Ho, J. M., E. Bakkalbasi, D. Söll and C. A. Miller (2018). "Drugging tRNA aminoacylation." RNA Biology **15**(4-5): 667-677.

Hou, Y. M. and P. Schimmel (1988). "A simple structural feature is a major determinant of the identity of a transfer RNA." Nature **333**(6169): 140-145.

Huang, Z., X. Chang, J. R. Riordan and Y. Huang (2004). "Fluorescent modified phosphatidylcholine floppase activity of reconstituted multidrug resistance-associated protein MRP1." Biochimica et Biophysica Acta **1660**(1): 155-163.

Islam, S. T. and J. S. Lam (2014). "Synthesis of bacterial polysaccharides via the Wzx/Wzy-dependent pathway." Canadian Journal of Microbiology **60**(11): 697-716.

Isom, G. L., N. Coudray, M. R. MacRae, C. T. McManus, D. C. Ekiert and G. Bhabha (2020). "LetB structure reveals a tunnel for lipid transport across the bacterial envelope." Cell **181**(3): 653-664.

Jenssen, H., P. Hamill and R. E. Hancock (2006). "Peptide antimicrobial agents." Clinical Microbiology Reviews **19**(3): 491-511.

Joyce, L. R., H. S. Manzer, J. da C. Mendonça, R. Villarreal, P. E. Nagao, K. S. Doran, K. L. Palmer and Z. Guan (2022). "Identification of a novel cationic glycolipid in *Streptococcus agalactiae* that contributes to brain entry and meningitis." PLoS Biology **20**(2): e3001555.

Julian, K., K. Kosowska-Shick, C. Whitener, M. Roos, H. Labischinski, A. Rubio, L. Parent, L. Ednie, L. Koeth, T. Bogdanovich and P. C. Appelbaum (2007). "Characterization of a daptomycin-nonsusceptible vancomycin-intermediate *Staphylococcus aureus* strain in a patient with endocarditis." Antimicrobial Agents and Chemotherapy **51**(9): 3445-3448.

Jumper, J., R. Evans, A. Pritzel, T. Green, M. Figurnov, O. Ronneberger, K. Tunyasuvunakool, R. Bates, A. Žídek, A. Potapenko, A. Bridgland, C. Meyer, S. A. A. Kohl, A. J. Ballard, A. Cowie, B. Romera-Paredes, S. Nikolov, R. Jain, J. Adler, T. Back, S. Petersen, D. Reiman, E. Clancy, M. Zielinski, M. Steinegger, M. Pacholska, T. Berghammer, S. Bodenstein, D. Silver, O. Vinyals, A. W. Senior, K. Kavukcuoglu, P. Kohli and D. Hassabis (2021). "Highly accurate protein structure prediction with AlphaFold." Nature **596**(7873): 583-589.

Jung, D., A. Rozek, M. Okon and R. E. Hancock (2004). "Structural transitions as determinants of the action of the calcium-dependent antibiotic daptomycin." Chemical Biology **11**(7): 949-957.

Kastner, B., N. Fischer, M. M. Golas, B. Sander, P. Dube, D. Boehringer, K. Hartmuth, J. Deckert, F. Hauer and E. Wolf (2008). "GraFix: sample preparation for single-particle electron cryomicroscopy." Nature Methods **5**(1): 53-55.

Kenward, M. A., M. R. Brown and J. J. Fryer (1979). "The influence of calcium or manganese on the resistance to EDTA, polymyxin B or cold shock, and the composition of *Pseudomonas aeruginosa* grown in glucose- or magnesium-depleted batch cultures." Journal of Applied Bacteriology **47**(3): 489-503.

Khelashvili, G., E. Kots, X. Cheng, M. V. Levine and H. Weinstein (2022). "The allosteric mechanism leading to an open-groove lipid conductive state of the TMEM16F scramblase." Communications Biology **5**(1): 990.

Kilelee, E., A. Pokorny, M. R. Yeaman and A. S. Bayer (2010). "Lysyl-phosphatidylglycerol attenuates membrane perturbation rather than surface association of the cationic antimicrobial peptide 6W-RP-1 in a model membrane system: implications for daptomycin resistance." Antimicrobial Agents and Chemotherapy **54**(10): 4476-4479.

Kingston, A. W., X. Liao and J. D. Helmann (2013). "Contributions of the σ(W) , σ(M) and σ(X) regulons to the lantibiotic resistome of *Bacillus subtilis*." Molecular Microbiology **90**(3): 502-518.

Kirchhofer, A., J. Helma, K. Schmidthals, C. Frauer, S. Cui, A. Karcher, M. Pellis, S. Muyldermans, C. S. Casas-Delucchi, M. C. Cardoso, H. Leonhardt, K. P. Hopfner and U. Rothbauer (2010). "Modulation of protein properties in living cells using nanobodies." Nature Structural & Molecular Biology **17**(1): 133-138.

Kiriukhin, M. Y., D. V. Debabov, D. L. Shinabarger and F. C. Neuhaus (2001). "Biosynthesis of the glycolipid anchor in lipoteichoic acid of *Staphylococcus aureus* RN4220: role of YpfP, the diglucosyldiacylglycerol synthase." Journal of Bacteriology **183**(11): 3506-3514.

Klein, S., C. Lorenzo, S. Hoffmann, J. M. Walther, S. Storbeck, T. Piekarski, B. J. Tindall, V. Wray, M. Nimtz and J. Moser (2009). "Adaptation of *Pseudomonas aeruginosa* to various

conditions includes tRNA‐dependent formation of alanyl‐phosphatidylglycerol." Molecular Microbiology **71**(3): 551-565.
Kornberg, R. D. and H. M. McConnell (1971). "Inside-outside transitions of phospholipids in vesicle membranes." Biochemistry **10**(7): 1111-1120.
Krupp, G. (1988). "RNA synthesis: strategies for the use of bacteriophage RNA polymerases." Gene **72**(1-2): 75-89.
Kubelt, J., A. K. Menon, P. Müller and A. Herrmann (2002). "Transbilayer movement of fluorescent phospholipid analogues in the cytoplasmic membrane of *Escherichia coli*." Biochemistry **41**(17): 5605-5612.
Kubica, M., K. Guzik, J. Koziel, M. Zarebski, W. Richter, B. Gajkowska, A. Golda, A. Maciag-Gudowska, K. Brix, L. Shaw, T. Foster and J. Potempa (2008). "A potential new pathway for *Staphylococcus aureus* dissemination: the silent survival of *S. aureus* phagocytosed by human monocyte-derived macrophages." PLoS One **3**(1): e1409.
Kuk, A. C., E. H. Mashalidis and S.-Y. Lee (2017). "Crystal structure of the MOP flippase MurJ in an inward-facing conformation." Nature Structural & Molecular Biology **24**(2): 171-176.
Kumar, S. and W. T. Doerrler (2014). "Members of the conserved DedA family are likely membrane transporters and are required for drug resistance in *Escherichia coli*." Antimicrobial Agents and Chemotherapy **58**(2): 923-930.
Lambert, E., A. R. Mehdipour, A. Schmidt, G. Hummer and C. Perez (2022). "Evidence for a trap-and-flip mechanism in a proton-dependent lipid transporter." Nature Communications **13**(1): 1022.
Lander, G. C. and R. M. Glaeser (2021). "Conquer by cryo-EM without physically dividing." Biochemical Society Transactions **49**(5): 2287-2298.
Lazarevic, V. and D. Karamata (1995). "The tagGH operon of *Bacillus subtilis* 168 encodes a two-component ABC transporter involved in the metabolism of two wall teichoic acids." Molecular Microbiology **16**(2): 345-355.
Lee, B.-C., G. Khelashvili, M. Falzone, A. K. Menon, H. Weinstein and A. Accardi (2018). "Gating mechanism of the extracellular entry to the lipid pathway in a TMEM16 scramblase." Nature Communications **9**(1): 3251.
Lennarz, W., J. Nesbitt 3rd and J. Reiss (1966). "The participation of sRNA in the enzymatic synthesis of OL-lysyl phosphatidylglycerol in *Staphylococcus aureus*." Proceedings of the National Academy of Sciences of the United States of America **55**(4): 934-941.
Lerouge, I. and J. Vanderleyden (2002). "O-antigen structural variation: mechanisms and possible roles in animal/plant–microbe interactions." FEMS Microbiology Reviews **26**(1): 17-47.
Li, M., D. J. Cha, Y. Lai, A. E. Villaruz, D. E. Sturdevant and M. Otto (2007). "The antimicrobial peptide‐sensing system aps of *Staphylococcus aureus*." Molecular Microbiology **66**(5): 1136-1147.
Li, M., Y. Lai, A. E. Villaruz, D. J. Cha, D. E. Sturdevant and M. Otto (2007). "Gram-positive three-component antimicrobial peptide-sensing system." Proceedings of the National Academy of Sciences of the United States of America **104**(22): 9469-9474.
Li, M. J., W. M. Atkins and W. D. McClary (2019). "Preparation of lipid nanodiscs with lipid mixtures." Current Protocols in Protein Science **98**(1): e100.
Li, Y. E., Y. Wang, X. Du, T. Zhang, H. Y. Mak, S. E. Hancock, H. McEwen, E. Pandzic, R. M. Whan and Y. C. Aw (2021). "TMEM41B and VMP1 are scramblases and regulate the distribution of cholesterol and phosphatidylserine." Journal of Cell Biology **220**(6): e202103105.
Loll, P. J. (2003). "Membrane protein structural biology: the high throughput challenge." Journal of Structural Biology **142**(1): 144-153.
López-Marqués, R. L., L. R. Poulsen, S. Hanisch, K. Meffert, M. J. Buch-Pedersen, M. K. Jakobsen, T. G. Pomorski and M. G. Palmgren (2010). "Intracellular targeting signals and lipid

specificity determinants of the ALA/ALIS P4-ATPase complex reside in the catalytic ALA α-subunit." Molecular Biology of the Cell **21**(5): 791-801.
Lorenz, N. (2016). "Cloning and recombinant expression of the bacterial resistance protein MprF for structural characterization". Diploma Thesis. Frankfurt, Goethe University.
Louie, A., N. Ribeiro, B. R. Reid and F. Jurnak (1984). "Relative affinities of all *Escherichia coli* aminoacyl-tRNAs for elongation factor Tu-GTP." Journal of Biological Chemistry **259**(8): 5010-5016.
Lukacs, G. L., O. D. Rotstein and S. Grinstein (1990). "Phagosomal acidification is mediated by a vacuolar-type H(+)-ATPase in murine macrophages." Journal of Biological Chemistry **265**(34): 21099-21107.
Lundie-Brown, J. (2018). "The multiple peptide resistance factor: towards a full-length structure and an understanding of its oligomeric complexes". Master's Thesis, University of Oxford.
Luo, Q., X. Yang, S. Yu, H. Shi, K. Wang, L. Xiao, G. Zhu, C. Sun, T. Li, D. Li, X. Zhang, M. Zhou and Y. Huang (2017). "Structural basis for lipopolysaccharide extraction by ABC transporter LptB(2)FG." Nature Structural & Molecular Biology **24**(5): 469-474.
Macfarlane, M. G. (1962). "Characterization of lipoamino-acids as O-amino-acid esters of phosphatidyl-glycerol." Nature **196**(4850): 136-138.
Maeda, S., H. Yamamoto, L. N. Kinch, C. M. Garza, S. Takahashi, C. Otomo, N. V. Grishin, S. Forli, N. Mizushima and T. Otomo (2020). "Structure, lipid scrambling activity and role in autophagosome formation of ATG9A." Nature Structural & Molecular Biology **27**(12): 1194-1201.
Maisey, H. C., K. S. Doran and V. Nizet (2008). "Recent advances in understanding the molecular basis of group B *Streptococcus* virulence." Expert Reviews in Molecular Medicine **10**: e27.
Maloney, E., D. Stankowska, J. Zhang, M. Fol, Q.-J. Cheng, S. Lun, W. R. Bishai, M. Rajagopalan, D. Chatterjee and M. V. Madiraju (2009). "The two-domain LysX protein of *Mycobacterium tuberculosis* is required for production of lysinylated phosphatidylglycerol and resistance to cationic antimicrobial peptides." PLoS Pathogens **5**(7): e1000534.
Malvezzi, M., K. K. Andra, K. Pandey, B.-C. Lee, M. E. Falzone, A. Brown, R. Iqbal, A. K. Menon and A. Accardi (2018). "Out-of-the-groove transport of lipids by TMEM16 and GPCR scramblases." Proceedings of the National Academy of Sciences of the United States of America **115**(30): E7033-E7042.
Malvezzi, M., M. Chalat, R. Janjusevic, A. Picollo, H. Terashima, A. K. Menon and A. Accardi (2013). "Ca2+-dependent phospholipid scrambling by a reconstituted TMEM16 ion channel." Nature Communications **4**(1): 2367.
Mandin, P., H. Fsihi, O. Dussurget, M. Vergassola, E. Milohanic, A. Toledo-Arana, I. Lasa, J. Johansson and P. Cossart (2005). "VirR, a response regulator critical for *Listeria monocytogenes* virulence." Molecular Microbiology **57**(5): 1367-1380.
Marek, M. and T. Günther-Pomorski (2016). Assay of flippase activity in proteoliposomes using fluorescent lipid derivatives. P-Type ATPases: Methods and Protocols. **18:** 181-191.
Marolda, C. L., B. Li, M. Lung, M. Yang, A. Hanuszkiewicz, A. R. Rosales and M. A. Valvano (2010). "Membrane topology and identification of critical amino acid residues in the Wzx O-antigen translocase from *Escherichia coli* O157:H4." Journal of Bacteriology **192**(23): 6160-6171.
Marques, M. A., M. D. Purdy and M. Yeager (2019). "CryoEM maps are full of potential." Current Opinion in Structural Biology **58**: 214-223.
Matano, L. M., H. G. Morris, A. R. Hesser, S. E. S. Martin, W. Lee, T. W. Owens, E. Laney, H. Nakaminami, D. Hooper, T. C. Meredith and S. Walker (2017). "Antibiotic that inhibits the ATPase activity of an ATP-binding cassette transporter by binding to a remote extracellular site." Journal of the American Chemical Society **139**(31): 10597-10600.
McCloskey, J. A. and S. Nishimura (1977). "Modified nucleosides in transfer RNA." Accounts of Chemical Research **10**(11): 403-410.

McMahon, C., A. S. Baier, R. Pascolutti, M. Wegrecki, S. Zheng, J. X. Ong, S. C. Erlandson, D. Hilger, S. G. F. Rasmussen, A. M. Ring, A. Manglik and A. C. Kruse (2018). "Yeast surface display platform for rapid discovery of conformationally selective nanobodies." Nature Structural & Molecular Biology **25**(3): 289-296.

Menon, I., T. Huber, S. Sanyal, S. Banerjee, P. Barré, S. Canis, J. D. Warren, J. Hwa, T. P. Sakmar and A. K. Menon (2011). "Opsin is a phospholipid flippase." Current Biology **21**(2): 149-153.

Mi, W., Y. Li, S. H. Yoon, R. K. Ernst, T. Walz and M. Liao (2017). "Structural basis of MsbA-mediated lipopolysaccharide transport." Nature **549**(7671): 233-237.

Mimms, L. T., G. Zampighi, Y. Nozaki, C. Tanford and J. A. Reynolds (1981). "Phospholipid vesicle formation and transmembrane protein incorporation using octyl glucoside." Biochemistry **20**(4): 833-840.

Misawa, Y., K. A. Kelley, X. Wang, L. Wang, W. B. Park, J. Birtel, D. Saslowsky and J. C. Lee (2015). "*Staphylococcus aureus* colonization of the mouse gastrointestinal tract is modulated by wall teichoic acid, capsule, and surface proteins." PLoS Pathogens **11**(7): e1005061.

Montigny, C., J. Lyons, P. Champeil, P. Nissen and G. Lenoir (2016). "On the molecular mechanism of flippase- and scramblase-mediated phospholipid transport." Biochimica et Biophysica Acta **1861**(8 Pt B): 767-783.

Moutel, S., N. Bery, V. Bernard, L. Keller, E. Lemesre, A. de Marco, L. Ligat, J. C. Rain, G. Favre, A. Olichon and F. Perez (2016). "NaLi-H1: A universal synthetic library of humanized nanobodies providing highly functional antibodies and intrabodies." eLife **5**.

Murray, C. J., K. S. Ikuta, F. Sharara, L. Swetschinski, G. R. Aguilar, A. Gray, C. Han, C. Bisignano, P. Rao and E. Wool (2022). "Global burden of bacterial antimicrobial resistance in 2019: a systematic analysis." The Lancet **399**(10325): 629-655.

Naganuma, M., S.-i. Sekine, Y. E. Chong, M. Guo, X.-L. Yang, H. Gamper, Y.-M. Hou, P. Schimmel and S. Yokoyama (2014). "The selective tRNA aminoacylation mechanism based on a single G•U pair." Nature **510**(7506): 507-511.

Neidhardt, F. C., P. L. Bloch, S. Pedersen and S. Reeh (1977). "Chemical measurement of steady-state levels of ten aminoacyl-transfer ribonucleic acid synthetases in *Escherichia coli*." Journal of Bacteriology **129**(1): 378-387.

Nesbitt, J. A., 3rd and W. J. Lennarz (1968). "Participation of aminoacyl transfer ribonucleic acid in aminoacyl phosphatidylglycerol synthesis. I. Specificity of lysyl phosphatidylglycerol synthetase." Journal of Biological Chemistry **243**(11): 3088-3095.

Neuhaus, F. C. and J. Baddiley (2003). "A continuum of anionic charge: structures and functions of D-alanyl-teichoic acids in Gram-positive bacteria." Microbiology and Molecular Biology Reviews **67**(4): 686-723.

Nguyen, M. H., M. DiPasquale, B. W. Rickeard, M. Doktorova, F. A. Heberle, H. L. Scott, F. N. Barrera, G. Taylor, C. P. Collier and C. B. Stanley (2019). "Peptide-induced lipid flip-flop in asymmetric liposomes measured by small angle neutron scattering." Langmuir **35**(36): 11735-11744.

Nosol, K., R. Bang-Sørensen, R. N. Irobalieva, S. K. Erramilli, B. Stieger, A. A. Kossiakoff and K. P. Locher (2021). "Structures of ABCB4 provide insight into phosphatidylcholine translocation." Proceedings of the National Academy of Sciences of the United States of America **118**(33).

Nothaft, H. and C. M. Szymanski (2010). "Protein glycosylation in bacteria: sweeter than ever." Nature Reviews Microbiology **8**(11): 765-778.

Pahil, K. S., M. S. A. Gilman, V. Baidin, T. Clairfeuille, P. Mattei, C. Bieniossek, F. Dey, D. Muri, R. Baettig, M. Lobritz, K. Bradley, A. C. Kruse and D. Kahne (2024). "A new antibiotic traps lipopolysaccharide in its intermembrane transporter." Nature **625**(7995): 572-577.

Palmgren, M. (2023). "P-type ATPases: Many more enigmas left to solve." Journal of Biological Chemistry **299**(11): 105352.

Park, J. G., S. Kim, E. Jang, S. H. Choi, H. Han, S. Ju, J. W. Kim, D. S. Min and M. S. Jin (2022). "The lysosomal transporter TAPL has a dual role as peptide translocator and phosphatidylserine floppase." Nature Communications **13**(1): 5851.

Parker, J. L. and S. Newstead (2017). "Structural basis of nucleotide sugar transport across the Golgi membrane." Nature **551**(7681): 521-524.

Percy, M. G. and A. Gründling (2014). "Lipoteichoic acid synthesis and function in Gram-positive bacteria." Annual Review of Microbiology **68**: 81-100.

Perez, C., S. Gerber, J. Boilevin, M. Bucher, T. Darbre, M. Aebi, J.-L. Reymond and K. P. Locher (2015). "Structure and mechanism of an active lipid-linked oligosaccharide flippase." Nature **524**(7566): 433-438.

Peschel, A., R. W. Jack, M. Otto, L. V. Collins, P. Staubitz, G. Nicholson, H. Kalbacher, W. F. Nieuwenhuizen, G. Jung and A. Tarkowski (2001). "*Staphylococcus aureus* resistance to human defensins and evasion of neutrophil killing via the novel virulence factor MprF is based on modification of membrane lipids with l-lysine." The Journal of Experimental Medicine **193**(9): 1067-1076.

Peschel, A., M. Otto, R. W. Jack, H. Kalbacher, G. Jung and F. Gotz (1999). "Inactivation of the dlt Operon in *Staphylococcus aureus* confers sensitivity to defensins, protegrins, and other antimicrobial peptides." Journal of Biological Chemistry **274**(13): 8405-8410.

Ploier, B. and A. K. Menon (2016). "A fluorescence-based assay of phospholipid scramblase activity." Journal of Visualized Experiments(115): e54635.

Pomorski, T., S. Hrafnsdóttir, P. F. Devaux and G. van Meer (2001). "Lipid distribution and transport across cellular membranes." Seminars in Cell and Developmental Biology **12**(2): 139-148.

Pomorski, T. and A. K. Menon (2006). "Lipid flippases and their biological functions." Cellular and Molecular Life Sciences **63**(24): 2908-2921.

Pomorski, T. G. and A. K. Menon (2016). "Lipid somersaults: Uncovering the mechanisms of protein-mediated lipid flipping." Progress in Lipid Research **64**: 69-84.

Punjani, A., J. L. Rubinstein, D. J. Fleet and M. A. Brubaker (2017). "cryoSPARC: algorithms for rapid unsupervised cryo-EM structure determination." Nature Methods **14**(3): 290-296.

Putney, S., R. Sauer and P. Schimmel (1981). "Purification and properties of alanine tRNA synthetase from *Escherichia coli* A tetramer of identical subunits." Journal of Biological Chemistry **256**(1): 198-204.

Quazi, F., S. Lenevich and R. S. Molday (2012). "ABCA4 is an N-retinylidene-phosphatidylethanolamine and phosphatidylethanolamine importer." Nature Communications **3**: 925.

Raetz, C. R. H., Z. Guan, B. O. Ingram, D. A. Six, F. Song, X. Wang and J. Zhao (2009). "Discovery of new biosynthetic pathways: the lipid A story." Journal of Lipid Research **50**: S103-S108.

Rasmussen, S. G., H. J. Choi, J. J. Fung, E. Pardon, P. Casarosa, P. S. Chae, B. T. Devree, D. M. Rosenbaum, F. S. Thian, T. S. Kobilka, A. Schnapp, I. Konetzki, R. K. Sunahara, S. H. Gellman, A. Pautsch, J. Steyaert, W. I. Weis and B. K. Kobilka (2011). "Structure of a nanobody-stabilized active state of the β(2) adrenoceptor." Nature **469**(7329): 175-180.

Reddy, V. S., M. A. Shlykov, R. Castillo, E. I. Sun and M. H. Saier, Jr. (2012). "The major facilitator superfamily (MFS) revisited." The FEBS Journal **279**(11): 2022-2035.

Reinhard, L., S. Sridhara and B. M. Hällberg (2017). "The MRPP1/MRPP2 complex is a tRNA-maturation platform in human mitochondria." Nucleic Acids Research **45**(21): 12469-12480.

Rick, P. D., K. Barr, K. Sankaran, J. Kajimura, J. S. Rush and C. J. Waechter (2003). "Evidence that the wzxE gene of *Escherichia coli* K-12 encodes a protein involved in the transbilayer movement of a trisaccharide-lipid intermediate in the assembly of enterobacterial common antigen." Journal of Biological Chemistry **278**(19): 16534-16542.

Rigaud, J.-L. and D. Lévy (2003). Reconstitution of membrane proteins into liposomes. Methods in Enzymology, Academic Press. **372:** 65-86.

Romsicki, Y. and F. J. Sharom (2001). "Phospholipid flippase activity of the reconstituted P-glycoprotein multidrug transporter." Biochemistry **40**(23): 6937-6947.

Roney, I. J. and D. Z. Rudner (2023). "The DedA superfamily member PetA is required for the transbilayer distribution of phosphatidylethanolamine in bacterial membranes." Proceedings of the National Academy of Sciences of the United States of America **120**(20): e2301979120.

Roney, I. J. and D. Z. Rudner (2023). "Two broadly conserved families of polyprenyl-phosphate transporters." Nature **613**(7945): 729-734.

Roy, H. and M. Ibba (2008). "RNA-dependent lipid remodeling by bacterial multiple peptide resistance factors." Proceedings of the National Academy of Sciences of the United States of America **105**(12): 4667-4672.

Roy, H. and M. Ibba (2009). "Broad range amino acid specificity of RNA-dependent lipid remodeling by multiple peptide resistance factors." Journal of Biological Chemistry **284**(43): 29677-29683.

Rubinchik, E., T. Schneider, M. Elliott, W. R. Scott, J. Pan, C. Anklin, H. Yang, D. Dugourd, A. Müller, K. Gries, S. K. Straus, H. G. Sahl and R. E. Hancock (2011). "Mechanism of action and limited cross-resistance of new lipopeptide MX-2401." Antimicrobial Agents and Chemotherapy **55**(6): 2743-2754.

Rubino, F. A., S. Kumar, N. Ruiz, S. Walker and D. E. Kahne (2018). "Membrane potential Is required for MurJ function." Journal of the American Chemical Society **140**(13): 4481-4484.

Saar-Dover, R., A. Bitler, R. Nezer, L. Shmuel-Galia, A. Firon, E. Shimoni, P. Trieu-Cuot and Y. Shai (2012). "D-alanylation of lipoteichoic acids confers resistance to cationic peptides in group B *streptococcus* by increasing the cell wall density." PLoS Pathogens **8**(9): e1002891.

Sahu, S. K., S. N. Gummadi, N. Manoj and G. K. Aradhyam (2007). "Phospholipid scramblases: an overview." Archives of Biochemistry and Biophysics **462**(1): 103-114.

Salah Ud-Din, A. I., A. Tikhomirova and A. Roujeinikova (2016). "Structure and functional diversity of GCN5-related N-acetyltransferases (GNAT)." International Journal of Molecular Sciences **17**(7).

Sauermann, R., M. Rothenburger, W. Graninger and C. Joukhadar (2008). "Daptomycin: a review 4 years after first approval." Pharmacology **81**(2): 79-91.

Scarsbrook, H. L., R. Urban, B. R. Streather, A. Moores and C. Mulligan (2021). "Topological analysis of a bacterial DedA protein associated with alkaline tolerance and antimicrobial resistance." Microbiology **167**(12).

Schiffer, M., C. H. Chang and F. J. Stevens (1992). "The functions of tryptophan residues in membrane proteins." Protein Engineering, Design and Selection **5**(3): 213-214.

Schnaith, A., H. Kashkar, S. A. Leggio, K. Addicks, M. Krönke and O. Krut (2007). "*Staphylococcus aureus* subvert autophagy for induction of caspase-independent host cell death." Journal of Biological Chemistry **282**(4): 2695-2706.

Shields, T. P., E. Mollova, L. Ste Marie, M. R. Hansen and A. Pardi (1999). "High-performance liquid chromatography purification of homogenous-length RNA produced by trans cleavage with a hammerhead ribozyme." RNA **5**(9): 1259-1267.

Simcock, P. W., M. Bublitz, F. Cipcigan, M. G. Ryadnov, J. Crain, P. J. Stansfeld and M. S. P. Sansom (2021). "Membrane binding of antimicrobial peptides is modulated by lipid charge modification." Journal of Chemical Theory and Computation **17**(2): 1218-1228.

Skrzypek, R., S. Iqbal and R. Callaghan (2018). "Methods of reconstitution to investigate membrane protein function." Methods **147**: 126-141.

Slavetinsky, C. J., J. N. Hauser, C. Gekeler, J. Slavetinsky, A. Geyer, A. Kraus, D. Heilingbrunner, S. Wagner, M. Tesar and B. Krismer (2022). "Sensitizing Staphylococcus aureus to antibacterial agents by decoding and blocking the lipid flippase MprF." eLife **11**: e66376.

Slavetinsky, C. J., A. Peschel and C. M. Ernst (2012). "Alanyl-phosphatidylglycerol and lysyl-phosphatidylglycerol are translocated by the same MprF flippases and have similar capacities to protect against the antibiotic daptomycin in *Staphylococcus aureus*." Antimicrobial Agents and Chemotherapy **56**(7): 3492-3497.

Smilova, M. (2017). "Towards a structural and functional characterisation of the bacterial multiple peptide resistance factor MprF". Master's Thesis, University of Oxford.

Smith, A. M., J. S. Harrison, C. D. Grube, A. E. Sheppe, N. Sahara, R. Ishii, O. Nureki and H. Roy (2015). "tRNA-dependent alanylation of diacylglycerol and phosphatidylglycerol in *Corynebacterium glutamicum*." Molecular Microbiology **98**(4): 681-693.

Smith, A. M., J. S. Harrison, K. M. Sprague and H. Roy (2013). "A conserved hydrolase responsible for the cleavage of aminoacylphosphatidylglycerol in the membrane of *Enterococcus faecium*." Journal of Biological Chemistry **288**(31): 22768-22776.

Sohlenkamp, C., K. A. Galindo-Lagunas, Z. Guan, P. Vinuesa, S. Robinson, J. Thomas-Oates, C. R. Raetz and O. Geiger (2007). "The lipid lysyl-phosphatidylglycerol is present in membranes of *Rhizobium tropici* CIAT899 and confers increased resistance to polymyxin B under acidic growth conditions." Molecular Plant-Microbe Interactions **20**(11): 1421-1430.

Song, D., H. Jiao and Z. Liu (2021). "Phospholipid translocation captured in a bifunctional membrane protein MprF." Nature Communications **12**(1): 2927.

Stansfeld, P. J., J. E. Goose, M. Caffrey, E. P. Carpenter, J. L. Parker, S. Newstead and M. S. Sansom (2015). "MemProtMD: automated insertion of membrane protein structures into explicit lipid membranes." Structure **23**(7): 1350-1361.

Straus, S. K. and R. E. Hancock (2006). "Mode of action of the new antibiotic for Gram-positive pathogens daptomycin: comparison with cationic antimicrobial peptides and lipopeptides." Biochimica et Biophysica Acta **1758**(9): 1215-1223.

Suzuki, J., D. P. Denning, E. Imanishi, H. R. Horvitz and S. Nagata (2013). "Xk-related protein 8 and CED-8 promote phosphatidylserine exposure in apoptotic cells." Science **341**(6144): 403-406.

Suzuki, J., T. Fujii, T. Imao, K. Ishihara, H. Kuba and S. Nagata (2013). "Calcium-dependent phospholipid scramblase activity of TMEM16 protein family members." Journal of Biological Chemistry **288**(19): 13305-13316.

Suzuki, J., M. Umeda, P. J. Sims and S. Nagata (2010). "Calcium-dependent phospholipid scrambling by TMEM16F." Nature **468**(7325): 834-838.

Swairjo, M. A., F. J. Otero, X.-L. Yang, M. A. Lovato, R. J. Skene, D. E. McRee, L. R. de Pouplana and P. Schimmel (2004). "Alanyl-tRNA synthetase crystal structure and design for acceptor-stem recognition." Molecular Cell **13**(6): 829-841.

Thedieck, K., T. Hain, W. Mohamed, B. J. Tindall, M. Nimtz, T. Chakraborty, J. Wehland and L. Jänsch (2006). "The MprF protein is required for lysinylation of phospholipids in listerial membranes and confers resistance to cationic antimicrobial peptides (CAMPs) on *Listeria monocytogenes*." Molecular Microbiology **62**(5): 1325-1339.

Thomas, C. and R. Tampé (2018). "Multifaceted structures and mechanisms of ABC transport systems in health and disease." Current Opinion in Structural Biology **51**: 116-128.

Timcenko, M., J. A. Lyons, D. Januliene, J. J. Ulstrup, T. Dieudonné, C. Montigny, M.-R. Ash, J. L. Karlsen, T. Boesen, W. Kühlbrandt, G. Lenoir, A. Moeller and P. Nissen (2019). "Structure and autoregulation of a P4-ATPase lipid flippase." Nature **571**(7765): 366-370.

Todor, H., N. Herrera and C. A. Gross (2023). "Three bacterial DedA subfamilies with distinct functions and phylogenetic distribution." mBio **14**(2): e0002823.

Traïkia, M., D. E. Warschawski, O. Lambert, J. L. Rigaud and P. F. Devaux (2002). "Asymmetrical membranes and surface tension." Biophysical Journal **83**(3): 1443-1454.

Triana-Alonso, F. J., M. Dabrowski, J. Wadzack and K. H. Nierhaus (1995). "Self-coded 3′ -extension of run-off transcripts produces aberrant products during in vitro transcription with T7 RNA polymerase." Journal of Biological Chemistry **270**(11): 6298-6307.

Ventola, C. L. (2015). "The antibiotic resistance crisis: part 1: causes and threats." Pharmacy and Therapeutics **40**(4): 277.

Vestergaard, A. L., J. A. Coleman, T. Lemmin, S. A. Mikkelsen, L. L. Molday, B. Vilsen, R. S. Molday, M. Dal Peraro and J. P. Andersen (2014). "Critical roles of isoleucine-364 and adjacent residues in a hydrophobic gate control of phospholipid transport by the mammalian P4-ATPase ATP8A2." Proceedings of the National Academy of Sciences of the United States of America **111**(14): E1334-1343.

Villanueva, M., B. García, J. Valle, B. Rapún, I. Ruiz de Los Mozos, C. Solano, M. Martí, J. R. Penadés, A. Toledo-Arana and I. Lasa (2018). "Sensory deprivation in *Staphylococcus aureus*." Nature Communications **9**(1): 523.

Vinuesa, P., F. Neumann-Silkow, C. Pacios-Bras, H. P. Spaink, E. Martínez-Romero and D. Werner (2003). "Genetic analysis of a pH-regulated operon from *Rhizobium tropici* CIAT899 involved in acid tolerance and nodulation competitiveness." Molecular Plant-Microbe Interactions **16**(2): 159-168.

Vishwakarma, R. A., S. Vehring, A. Mehta, A. Sinha, T. Pomorski, A. Herrmann and A. K. Menon (2005). "New fluorescent probes reveal that flippase-mediated flip-flop of phosphatidylinositol across the endoplasmic reticulum membrane does not depend on the stereochemistry of the lipid." Organic & Biomolecular Chemistry **3**(7): 1275-1283.

Wang, H., C. J. Gill, S. H. Lee, P. Mann, P. Zuck, T. C. Meredith, N. Murgolo, X. She, S. Kales, L. Liang, J. Liu, J. Wu, J. Santa Maria, J. Su, J. Pan, J. Hailey, D. McGuinness, C. M. Tan, A. Flattery, S. Walker, T. Black and T. Roemer (2013). "Discovery of wall teichoic acid inhibitors as potential anti-MRSA β-lactam combination agents." Chemical Biology **20**(2): 272-284.

Waterhouse, A., M. Bertoni, S. Bienert, G. Studer, G. Tauriello, R. Gumienny, F. T. Heer, T. A. P. de Beer, C. Rempfer, L. Bordoli, R. Lepore and T. Schwede (2018). "SWISS-MODEL: homology modelling of protein structures and complexes." Nucleic Acids Research **46**(W1): W296-w303.

Weidenmaier, C. and A. Peschel (2008). "Teichoic acids and related cell-wall glycopolymers in Gram-positive physiology and host interactions." Nature Reviews Microbiology **6**(4): 276-287.

Winkler, W. C., A. Nahvi, A. Roth, J. A. Collins and R. R. Breaker (2004). "Control of gene expression by a natural metabolite-responsive ribozyme." Nature **428**(6980): 281-286.

Wöhlert, D., M. J. Grötzinger, W. Kühlbrandt and Ö. Yildiz (2015). "Mechanism of Na(+)-dependent citrate transport from the structure of an asymmetrical CitS dimer." eLife **4**: e09375.

Workman, S. D. and N. C. Strynadka (2020). "A slippery scaffold: synthesis and recycling of the bacterial cell wall carrier lipid." Journal of Molecular Biology **432**(18): 4964-4982.

Workman, S. D., L. J. Worrall and N. C. J. Strynadka (2018). "Crystal structure of an intramembranal phosphatase central to bacterial cell-wall peptidoglycan biosynthesis and lipid recycling." Nature Communications **9**(1): 1159.

Wu, L., L. Liu, B. Xu, D. Huang and X.-W. Chen (2022). "In vitro and in vivo assay of the ER lipid scramblase TMEM41B." STAR protocols **3**(2): 101333.

Young, H. S., J.-L. Rigaud, J.-J. Lacapère, L. G. Reddy and D. L. Stokes (1997). "How to make tubular crystals by reconstitution of detergent-solubilized Ca2 (+)-ATPase." Biophysical Journal **72**(6): 2545-2558.

Zampaloni, C., P. Mattei, K. Bleicher, L. Winther, C. Thäte, C. Bucher, J.-M. Adam, A. Alanine, K. E. Amrein, V. Baidin, C. Bieniossek, C. Bissantz, F. Boess, C. Cantrill, T. Clairfeuille, F. Dey, P. Di Giorgio, P. du Castel, D. Dylus, P. Dzygiel, A. Felici, F. García-Alcalde, A. Haldimann, M. Leipner, S. Leyn, S. Louvel, P. Misson, A. Osterman, K. Pahil, S. Rigo, A. Schäublin, S. Scharf, P. Schmitz, T. Stoll, A. Trauner, S. Zoffmann, D. Kahne, J. A. T. Young, M. A. Lobritz and K. A. Bradley (2024). "A novel antibiotic class targeting the lipopolysaccharide transporter." Nature **625**(7995): 566-571.

Zhang, B., X. Liu, E. Lambert, G. Mas, S. Hiller, J. W. Veening and C. Perez (2020). "Structure of a proton-dependent lipid transporter involved in lipoteichoic acids biosynthesis." Nature Structural & Molecular Biology **27**(6): 561-569.

Zhang, G., V. Baidin, K. S. Pahil, E. Moison, D. Tomasek, N. S. Ramadoss, A. K. Chatterjee, C. W. McNamara, T. S. Young, P. G. Schultz, T. C. Meredith and D. Kahne (2018). "Cell-based screen for discovering lipopolysaccharide biogenesis inhibitors." Proceedings of the National Academy of Sciences of the United States of America **115**(26): 6834-6839.

Zheng, S., L. T. Sham, F. A. Rubino, K. P. Brock, W. P. Robins, J. J. Mekalanos, D. S. Marks, T. G. Bernhardt and A. C. Kruse (2018). "Structure and mutagenic analysis of the lipid II flippase MurJ from *Escherichia coli*." Proceedings of the National Academy of Sciences of the United States of America **115**(26): 6709-6714.

Zhou, X., T. T. Sebastian and T. R. Graham (2013). "Auto-inhibition of Drs2p, a yeast phospholipid flippase, by its carboxyl-terminal tail." Journal of Biological Chemistry **288**(44): 31807-31815.

Zhou, Z., K. A. White, A. Polissi, C. Georgopoulos and C. R. H. Raetz (1998). "Function of *Escherichia coli* MsbA, an essential ABC family transporter, in Lipid A and phospholipid biosynthesis." Journal of Biological Chemistry **273**(20): 12466-12475.

Zimmermann, I., P. Egloff, C. A. Hutter, F. M. Arnold, P. Stohler, N. Bocquet, M. N. Hug, S. Huber, M. Siegrist and L. Hetemann (2018). "Synthetic single domain antibodies for the conformational trapping of membrane proteins." eLife **7**: e34317.

Zimmermann, I., P. Egloff, C. A. Hutter, B. T. Kuhn, P. Bräuer, S. Newstead, R. J. Dawson, E. R. Geertsma and M. A. Seeger (2020). "Generation of synthetic nanobodies against delicate proteins." Nature Protocols **15**(5): 1707-1741.

Appendices

A1. MprF alignment

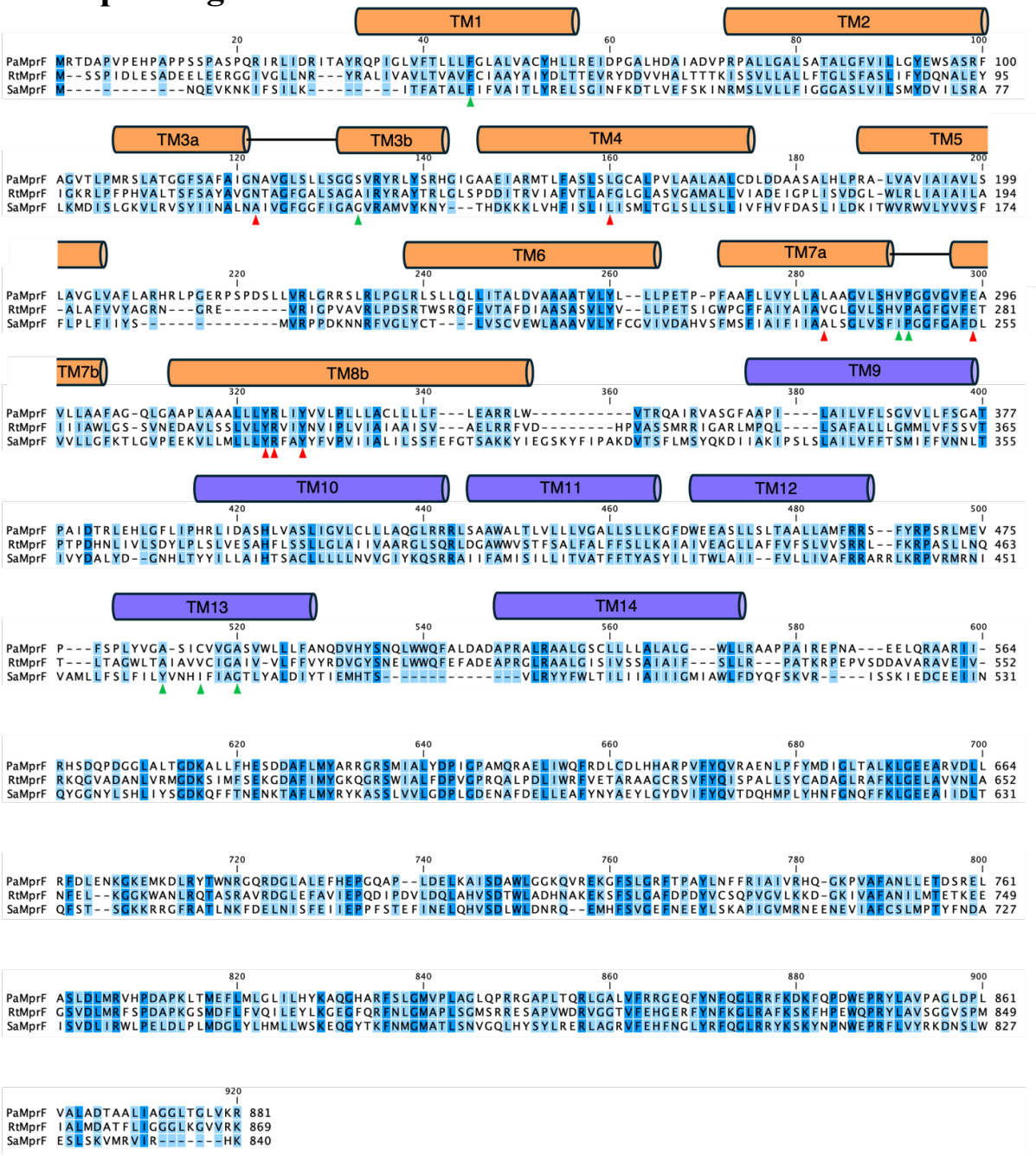

Figure A1.1: MprF alignment. Alignment of *P. aeruginosa* (*Pa*MprF), *R. tropici* (*Rt*MprF) and *S. aureus* (*Sa*MprF) MprF sequences, generated with CLC sequence viewer (QIAgen). Conserved residues are coloured based on conservation (white – blue = least – most conserved). TM helices for *Pa*MprF are depicted above the corresponding sequence (orange = TM domain 1, purple = TM domain 2). The residues mutated in *Pa*MprF in this thesis to investigate lipid transport are highlighted as triangles below sequences (red = cytoplasmic lipid binding pocket, green = TM domain interface).

A2. Polymerase Chain Reaction

For cloning full-length and truncated sequences of the wild-type constructs used in this thesis, Phusion High Fidelity DNA Polymerase (NEB) was used. PCR reaction mixes were assembled in 50 µL final volume as listed in **Table A2.1:**

Table A2.1: PCR reaction mix composition.

Component	Final concentration
5x Phusion HF buffer	1x
10 mM dNTPs	200 µM
10 µM Forward primer	0.5 µM
10 µM Reverse primer	0.5 µM
Template DNA	0.4 ng/µL
DMSO	3 % (v/v)
Phusion DNA Polymerase	0.02 units/µL

PCR thermo-cycling was performed in a Mastercycler® nexus X2 (Eppendorf) following the general scheme shown in **Table A2.2:**

Table A2.2: PCR thermo-cycling conditions

Step	Temperature (°C)	Time (s)	Cycles
Initial denaturation	98	30	1
Denaturation	98	10	30 (16 for mutagenesis)
Annealing	66-72 (Primer dependent)	30	
Elongation	72	15 per kb being replicated	
Final elongation	72	600	1

The primers used in this thesis were purchased from Eurofins Genomics, Ebersberg, and are listed in **Table A2.3** below:

Table A2.3: Primers used for cloning in this thesis

Primer Name	Primer sequence (5'-3')
*Pa*MprF_Fw_Seq	ATATATGCTCTTCTAGTCGCACCGACGCTCCCGTTCCAGAACAT
*Pa*MprF_Rv_Seq	TATATAGCTCTTCATGCGCGTTTCACCAATCCAGTCAGGCCGCC
*Pa*MprF^{545}_Rv	TATATAGCTCTTCATGCAGCCGCGCGCAGCAGCCAGCCAAGGG
*Pa*MprF_G37W_Fw	CGCCAGCCCATCTGGCTGGTCTTCACC
*Pa*MprF_G37W_Rv	GGTGAAGACCAGCCAGATGGGCTGGCGG
*Pa*MprF_T41C_Fw	CGGCCTGGTCTTCTGCTTGCTGCTGTTCGG
*Pa*MprF_T41C_Rv	CCGAACAGCAGCAAGCAGAAGACCAGGCCG
*Pa*MprF_T41W_Fw	CGGCCTGGTCTTCTGGTTGCTGCTGTTCGGC

*Pa*MprF_T41W_Rv	GCCGAACAGCAGCAACCAGAAGACCAGGCCG
*Pa*MprF_F45BPA_Fw	ACCTTGCTGCTGTAGGGCCTGGCGC
*Pa*MprF_F45BPA_Rv	AGCGCCAGGCCCTACAGCAGCAAGG
*Pa*MprF_F45W_Fw	CCTTGCTGCTGCGCGGCCTGGCGC
*Pa*MprF_F45W_Rv	GCGCCAGGCCGCGCAGCAGCAAGG
*Pa*MprF_N122BPA_Fw	CTTCGCCATCGGCTAGGCGGTAGGCC
*Pa*MprF_N122BPA_Rv	CAGGCCTACCGCCTAGCCGATGGCGAAGG
*Pa*MprF_N122W_Fw	GCCTTCGCCATCGGCTGGGCGGTAGGCCTGTCG
*Pa*MprF_N122W_Rv	CGACAGGCCTACCGCCCAGCCGATGGCGAAGGC
*Pa*MprF_V124C_Fw	CCATCGGCAATGCGTGCGGCCTGTCGCTGC
*Pa*MprF_V124C_Rv	GCGACAGGCCGCACGCATTGCCGATGGCG
*Pa*MprF_S127C_Fw	GCGGTAGGCCTGTGCCTGCTTTCCGGCG
*Pa*MprF_S127C_Rv	CGCCGGAAAGCAGGCACAGGCCTACCGC
*Pa*MprF_S127W_Fw	GCGGTAGGCCTGTGGCTGCTTTCC
*Pa*MprF_S127W_Rv	CGGAAAGCAGCCACAGGCCTACCGC
*Pa*MprF_L160W_Fw	GCCAGCCTTTCCTGGGGCTGCGCACTGC
*Pa*MprF_L160W_Rv	GCAGTGCGCAGCCCCAGGAAAGGCTGGC
*Pa*MprF_L279BPA_Fw	CCTGCTCGCCTAGGCCGCCGGCGTAC
*Pa*MprF_L279BPA_Rv	TACGCCGGCGGCCTAGGCGAGCAGG
*Pa*MprF_L279W_Fw	CTACCTGCTCGCCTGGGCCGCCGGCGTAC
*Pa*MprF_L279W_Rv	GTACGCCGGCGGCCCAGGCGAGCAGGTAG
*Pa*MprF_H286C_Fw	CGGCGTACTCAGCTGCGTACCGGGCGG
*Pa*MprF_H286C_Rv	TCCGCCCGGTACGCAGCTGAGTACGCCG
*Pa*MprF_V287R_Fw	GCGTACTCAGCCACCGCCCGGGCGGAGTCG
*Pa*MprF_V287R_Rv	CGACTCCGCCCGGGCGGTGGCTGAGTACG
*Pa*MprF_V287W_Fw	GCGTACTCAGCCACTGGCCGGGCGGAGTCG
*Pa*MprF_V287W_Rv	CGACTCCGCCCGGCCAGTGGCTGAGTACG
*Pa*MprF_P288BPA_Fw	CGTACTCAGCCACGTATAGGGCGGAGTCGG
*Pa*MprF_P288BPA_Rv	CCGACTCCGCCCTATACGTGGCTGAGTACG
*Pa*MprF_P288C_Fw	GCGTACTCAGCCACTGCCCGGGCGGAGTCG
*Pa*MprF_P288C_Rv	CGACTCCGCCCGGGCAGTGGCTGAGTACGC
*Pa*MprF_P288W_Fw	CGTACTCAGCCACGTATGGGGCGGAGTCG
*Pa*MprF_P288W_Rv	CGACTCCGCCCCATACGTGGCTGAGTACG
*Pa*MprF_G289C_Fw	GCCACGTACCGTGCGGAGTCGGG
*Pa*MprF_G289C_Rv	CCCGACTCCGCACGGTACGTGGC
*Pa*MprF_V291BPA_Fw	CGTACCGGGCGGATAGGGGGTGTTCGAGG
*Pa*MprF_V291BPA_Rv	GCAGCACCGCCTCCCACACCCCGACTCCGC
*Pa*MprF_E295A_Fw	CGGGGTGTTCGCGGCGGTGCTGC
*Pa*MprF_E295A_Rv	GCAGCACCGCCGCGAACACCCCG
*Pa*MprF_E295Q_Fw	GTCGGGGTGTTCCAGGCGGTGCTGC
*Pa*MprF_E295Q_Rv	GCAGCACCGCCTGGAACACCCCGAC
*Pa*MprF_E295R_Fw	GAGTCGGGGTGTTCCGCGCGGTGCTGCTGG
*Pa*MprF_E295R_Rv	CCAGCAGCACCGCGCGGAACACCCCGACTC
*Pa*MprF_Y318A_Fw	CGCGGCCCTGCTCTTGGCCCGCTTGATTTATGTGG
*Pa*MprF_Y318A_Rv	CACATAAATCAAGCGGGCCAAGAGCAGGGCCGCG
*Pa*MprF_Y318W_Fw	CGCGGCCCTGCTCTTGTGGCGCTTGATTTATGTGG
*Pa*MprF_Y318W_Rv	CCACATAAATCAAGCGCCACAAGAGCAGGGCCGCG
*Pa*MprF_R319A_Fw	CGGCCCTGCTCTTGTACGCCTTGATTTATGTGGTGC
*Pa*MprF_R319A_Rv	GCACCACATAAATCAAGGCGTACAAGAGCAGGGCC
*Pa*MprF_R319E_Fw	CGGCCCTGCTCTTGTACGAATTGATTTATGTGGTGC
*Pa*MprF_R319E_Rv	GCACCACATAAATCAATTCGTACAAGAGCAGGGCCGC
*Pa*MprF_Y322A_Fw	CTTGTACCGCTTGATTGCGGTGGTGCTGCCACTGC

*Pa*MprF_Y322A_Rv	GTGGCAGCACCACCGCAATCAAGCGGTACAAGAGC
*Pa*MprF_Y322W_Fw	CTTGTACCGCTTGATTTGGGTGGTGCTGCCACTGC
*Pa*MprF_Y322W_Rv	GTGGCAGCACCACCCAAATCAAGCGGTACAAGAGC
*Pa*MprF_V323C_Fw	GCTCTTGTACCGCTTGATTTATTGCGTGCTGCCACTGCTGC
*Pa*MprF_V323C_Rv	GCAGCAGTGGCAGCACGCAATAAATCAAGCGGTACAAGAGC
*Pa*MprF_I362C_Fw	GCACCGATCCTGGCGTGCCTGGTCTTCCTCTCC
*Pa*MprF_I362C_Rv	GAGAGGAAGACCAGGCACGCCAGGATCGGTGC
*Pa*MprF_F365BPA_Fw	GGCGATCCTGGTCTAGCTCTCCGGTGTCG
*Pa*MprF_F365BPA_Rv	ACGACACCGGAGAGCTAGACCAGGATCGCC
*Pa*MprF_V369BPA_Fw	GGTCTTCCTCTCCGGTTAGGTGCTGCTGTTTTCCGG
*Pa*MprF_V369BPA_Rv	CCGGAAAACAGCAGCACCTAACCGGAGAGGAAGACC
*Pa*MprF_L480C_Fw	GTACCCTTCTCGCCGTGCTACGTAGGCGCCAGC
*Pa*MprF_L480C_Rv	ATGCTGGCGCCTACGTAGCACGGCGAGAAGGG
*Pa*MprF_A484BPA_Fw	CCGCTTTACGTAGGCTAGAGCATCTGCGTGGTCG
*Pa*MprF_A484BPA_Rv	CGACCACGCAGATGCTCTAGCCTACGTAAAGCGG
*Pa*MprF_C487BPA_Fw	GGCGCCAGCATCTAGGTGGTCGGCGCC
*Pa*MprF_C487BPA_Rv	GGCGCCGACCACCTAGATGCTGGCGCC
*Pa*MprF_C487W_Fw	CCAGCATCTGGGTGGTCGGCGC
*Pa*MprF_C487W_Rv	GCGCCGACCACCCAGATGCTGGC
*Pa*MprF_A491BPA_Fw	CTGCGTGGTCGGCTAGTCGGTCTGGCTGC
*Pa*MprF_A491BPA_Rv	GCAGCCAGACCGACTAGCCGACCACGCAG
*Pa*MprF_A491R_Fw	GCGTGGTCGGCCGCTCGGTCTGGC
*Pa*MprF_A491R_Rv	CAGCCAGACCGAGCGGCCGACCACGC
*Pa*MprF_A491W_Fw	GCGTGGTCGGCTGGTCGGTCTGGCTGC
*Pa*MprF_A491W_Rv	GCAGCCAGACCGACCAGCCGACCACGC
AlaRS_Full_length_Fw	ATATATGCTCTTCTAGTAAAAGCGCTGAAATCCGTGAAGCCTTC
AlaRS_Full_length_Rv	TATATAGCTCTTCATGCAAGCCCTTGCTCGACGAAGCGCTGGG
AlaRS^{440}_Fw	ATATATGCTCTTCTAGTAAAAGCGCTGAAATCCGTGAAGCCTTC
AlaRS^{440}_Rv	TATATAGCTCTTCATGCAAAGGCACTGGAAGCGCGGGCG
tRNA^{Ala}_Fw	GATCCGCTCGCACCTAATACGACTCACTATA
tRNA^{Ala}_Rv	CCAGACCCTGATGGTGTCTGAAAAACGTAC
PA0919_Fw	ATATATGCTCTTCTAGTAAACTGGAAGCCCTGGACCTCGACGAC
PA0919_Rv	TATATAGCTCTTCATGCGGCATCGGGAGCGTTCTCGCGGTCG
qPCR_RD_5′_for	GGGAGACCACAACGGTTTCCC
qPCR_ RD_S_and_M_5′_rev	CACCGGGAAACCGCTTGCGGC
qPCR_ RD_L_5′_rev	GCCGCTAGCCGCACAGCTC
qPCR_ RD_tolA_3′_for	GCCGAATTCGGATCTGGTGGC
qPCR_ RD_tolA_3′_rev	CTGCTTCTTCCGCAGCTTTAGC
qPCR_PD_pDX_for	GACGTTCCGGACTACGGTTCC
qPCR_PD_pDX_rev	CACAGACAGCCCTCATAGTTAGC

A3. Sybody selection protocol

A3.1. Ribosome display

For each sybody library, an *in vitro* translation reaction mix was made up on ice using a PUREfrex® 2.1 kit (GeneFrontier) following manufacturer's instructions to 10 µL total volume. 0.7 µL of each sybody RNA library was added to one *in vitro* translation reaction mix and incubated at 37°C for 30 minutes to form ribosome complexes. While incubating, 12 µL Dynabeads MyOne Streptavidin T1 (Invitrogen) per library was washed with 500 µL Wash Buffer (50 mM Tris/acetate, 150 mM NaCl, 50 mM $MgAc_2$) supplemented with 0.5 % (w/v) BSA twice, before blocking in the same buffer for 20 minutes on ice. Reaction mixes were diluted to 100 µL in Wash Buffer supplemented with 0.5 % (w/v) BSA, 0.0261 % (w/v) DDM and 50 nM biotinylated *Pa*MprF and incubated on ice for 20 minutes to allow sybody-*Pa*MprF complex formation. Reaction mixes were then added to blocked Dynabeads and incubated for 5 minutes on ice, before washing Dynabeads three times with 500 µL Wash Buffer supplemented with 0.0261 % (w/v) DDM. 100 µL of Elution Buffer (50 mM Tris/acetate, 150 mM NaCl, 50 mM EDTA, 100 µg/mL yeast RNA) was added to Dynabeads and incubated for 10 minutes at RT. Supernatant containing eluted RNA was purified using an RNeasy micro kit (Qiagen) following manufacturer's instructions.

Purified RNA was reverse-transcribed to form a cDNA library for each enriched sybody library using an AffinityScript Reverse Transcriptase (Agilent) following manufacturer's instructions. cDNA for each library was purified using a Nucleospin Clean-up kit (Machery-Nagel). A sample of eluted cDNA was used for quantitative PCR (qPCR) analysis using primers listed in **Appendix 2**. The remaining cDNA was amplified by PCR using primers listed in **Appendix 2** and the non-proofreading polymerase GoTaq G2 (Promega) to prevent cDNA digestion. 1 µg of amplified cDNA for each sybody library was then digested with SapI (NEB) at 37°C for 1 hour. 10 µg of the phagemid vector pDX_init was also digested with SapI, and the digested vector mixed with digested cDNA at a 4:1 vector:insert (w/w) ratio. Inserts were ligated into the

phagemid by incubation with T4 DNA ligase (ThermoFisher), and incubated for 1.5 hours at 37°C. The full ligation mix of each sybody library was then electroporated into 50 µL electrocompetent SS320 *E. coli* and transferred to 25 mL SOC medium for outgrowth at 37°C for 30 minutes. The transformation efficiency was assessed by plating a serial dilution series of this culture on LB-agar plates supplemented with 120 µg/mL ampicillin. The remaining culture was diluted to 250 mL in 2YT medium (1.6 % (w/v) tryptone, 1 % (w/v) yeast extract, 8.5 mM NaCl) and grown at 37°C for phage production for the next rounds of selection.

A3.2. Phage generation

50 mL 2YT media for each sybody library, supplemented with 2 % (w/v) glucose, was inoculated with the overnight culture containing sybody sequences in pDX_init and grown to OD_{600} = 0.6. 10 mL of each culture was then added to 27 µL M13KO7 Helper Phage (NEB) at 10^{12} plaque forming units per mL. Cultures were incubated at 37°C for 30 minutes, then cells pelleted and resuspended in 50 mL 2YT supplemented with 200 µg/mL ampicillin and 25 µg/mL kanamycin for growth overnight shaking at 37°C to generate phages. The next day, cultures were centrifuged at 5,000 g for 30 minutes and 40 mL of the phage-containing supernatant collected. 10 mL phage precipitation solution was added (20 % (w/v) PEG6000, 2.5 M NaCl) and incubated on ice for 30 minutes. Phages were pelleted by centrifugation at 5,000 g for 30 minutes, and resuspended in 1 mL phosphate buffered saline (PBS). Cell debris was removed by centrifugation at 20,000 g for 5 minutes, and the phage-containing supernatant collected for determination of phage concentration by measuring absorption at 269 nm and 320 nm. The phage titre (number of phages/mL) is then given by the following equation:

$$Phage\ titre\ = \frac{(A_{269} - A_{320}) \times\ 6 \times 10^{16}}{4900}$$

Purified phages were then used in subsequent rounds of phage display selection.

A3.3. Phage display 1

The first round of phage display utilised Nunc Maxisorp 96-well immunoplates (Merck), with each well incubated overnight with 100 µL 67 nM neutravidin solution (ThermoFisher) to coat wells with neutravidin. Each neutravidin coated well was then blocked for 30 minutes with 250 µL TBS supplemented with 0.5 % (w/v) BSA (TBS + BSA). Purified phages were diluted to a concentration of 10^{12} phages/mL, and 50 nM biotinylated *Pa*MprF was added to diluted phage solutions and incubated for 20 minutes to allow sybody-*Pa*MprF complexes to form. 50 nM of biotinylated AcrB was added to 100 µL of diluted phage as a negative control. 100 µL phage-*Pa*MprF solution was added to 47 wells of the neutravidin plate, and 100 µL of phage-AcrB solution to one well. Plates were incubated for 5 minutes, then washed three times by adding 250 µL TBS supplemented with 0.0261 % (w/v) DDM (TBS + DDM) to each well. 100 µL of phage elution buffer (TBS supplemented with 0.25 mg/mL trypsin) was added to each well and incubated for 10 minutes. The eluate from each *Pa*MprF-containing well was then pooled, and AcrB negative control eluate collected separately. Trypsin was inhibited by addition of aminoethylbenzenesulfonyl fluoride (AEBSF) to 0.25 mM final concentration. Samples of the *Pa*MprF elution and the AcrB negative control elution were then used for quantitative PCR (qPCR) analysis using primers listed in **Appendix 2**. Enriched phages from *Pa*MprF elution were then used to infect 50 mL SS320 *E. coli* for generation and purificaton of phages as described above. These phages were then used for the second round of phage display.

A3.4. Phage display 2

The second round of phage display utilised Dynabeads MyOne Streptavidin C1 (Invitrogen). Phages enriched from the previous round of selection were diluted to $5x10^{12}$ phages/mL in TBS + BSA + DDM. 100 µL of diluted phage solution from each sybody library was mixed with biotinylated *Pa*MprF at 50 nM, and another 100 µL of phage with biotinylated AcrB at 50 nM

as a negative control. Mixtures were incubated on ice for 20 minutes. While incubating, 12 µL Dynabeads for each reaction mixture were washed three times with TBS + BSA + DDM. Phage-protein mixtures were then added to washed Dynabeads and incubated for 5 minutes on ice. Beads were washed with 500 µL TBS + BSA + DDM, and then resuspended in 100 µL TBS + DDM and 5 µM unbiotinylated *Pa*MprF to select for sybodies with slow off rates of binding. Mixtures were incubated for 3 minutes, and then washed twice with 500 µL TBS + DDM. Phages were then eluted as described in **Appendix 3.3**, and samples of each elution for *Pa*MprF and negative control AcrB were used for qPCR analysis using primers listed in **Appendix 2**. Enriched phages from this selection were then subcloned into the expression vector pSB_init (containing an N-terminal pelB sequence for periplasmic expression and a C-terminal Myc and 6x-His affinity tag) by SapI digestion and T4 DNA ligation as described in **Appendix 3.1.** The ligation mixture for each library was transformed into 50 µL MC1061 *E. coli* and plated on LB-Cam. 95 colonies for each sybody library were then grown up individually in 1mL TB cultures and the sybodies expressed by addition of 0.02 % (w/v) L-arabinose. Cultures were grown overnight at 22°C before cells were pelleted at 4,000 g for 20 minutes. Cell pellets were resuspended in periplasmic extraction buffer (50 mM Tris/HCl pH 8.0, 20 % sucrose, 0.5 mM EDTA, 0.5 µg/mL lysozyme) and incubated on ice for 30 minutes. Cell suspensions were then diluted in 20 mL TBS with 1 mM $MgCl_2$, and cells pelleted at 4,000 g for 20 minutes. The supernatant following this spin was the periplasmic cell extract for each colony, which contained the single sybody sequence expressed by the colony. Periplasmic extracts were used to assess binding to *Pa*MprF via enzyme-linked immunosorbent assay (ELISA).

A3.5. ELISA

The ELISA was performed in Nunc Maxisorp immunoplates (Merck) coated overnight by addition of 100 µL Protein A at 5 µg/mL in PBS to each well. Plates were blocked with 250 µL TBS + BSA for 30 minutes. Monoclonal anti-c-Myc antibody (SigmaAldrich) was diluted 1:2,000 in TBS + DDM and incubated for 20 minutes to facilitate binding to Protein A. Plates were washed three times with TBS + DDM. Periplasmic extracts of each colony were diluted 1:5 in TBS + DDM, and 100 µL of each extract was added to two wells on the plate side by side (one well to assess binding to *Pa*MprF, and the other binding to the negative control protein AcrB). Plates were incubated for 20 minutes to facilitate binding of sybodies to anti-c-Myc antibody. Plates were washed three times with 250 µL TBS + DDM, and then 100 µL biotinylated *Pa*MprF or 100 µL biotinylated AcrB was added to the relevant wells. Plates were incubated for 20 minutes to facilitate binding of protein to immobilised sybodies and then washed three times with 250 µL TBS + DDM. 100 µL streptavidin-peroxidase polymer (Merck) diluted 1:5,000 was added to each well and incubated for 20 minutes to facilitate binding to the biotin on the target proteins. Plates were washed three times with 250 µL TBS + DDM and then visualised by addition of 100 µL ELISA developing buffer (51.5 mM Na_2HPO_4, 24.3 mM citric acid, 0.006 % (v/v) H_2O_2, 1mg/mL 3,3′,5,5′-Tetramethylbenzidine (TMB)) to each well. Plates were incubated for 5 minutes and then the absorbance of each well measured at 650 nm. Sybodies that exhibited binding to *Pa*MprF with low background binding to AcrB were selected for small-scale purification.

A3.6. Small-scale sybody purification

Following selection of a range of ELISA hits, each MC1061 strain containing a selected sybody was used to inoculate 50 mL of TB supplemented with 25 µg/mL chloramphenicol. These cultures were grown at 37°C shaking at 160 rpm for 4 hours until OD_{600} = 0.4 – 0.8. Cells were then induced by adding 0.02 % (w/v) L-arabinose and grown overnight at 22°C shaking at 160

rpm. Cells were pelleted at 4,000 g for 20 minutes, resuspended in 5 mL periplasmic extraction buffer (50 mM Tris/HCl pH 8.0, 20 % sucrose, 0.5 mM EDTA, 0.5 µg/mL lysozyme) and incubated on ice for 30 minutes. Cell suspensions were diluted in 20 mL TBS with 1 mM $MgCl_2$, and cells pelleted at 4,000 g for 20 minutes. The supernatant containing the periplasmic extract was collected and incubated with 500 µL Ni affinity resin from a His MultiTrap HP plate (Cytiva) for 1 hour at RT. Resin was washed three times with TBS supplemented with 30 mM imidazole, and then eluted in TBS supplemented with 300 mM imidazole. Sybodies were analysed by size exclusion chromatography on a Sepax SRT-10C SEC100 column equilibrated in TBS. Peak fractions of monomeric sybodies exhibiting limited column interactions were pooled and used for pull-down assays with the truncated *Pa*MprF^{545} to identify sybodies that bound to the membrane domain of *Pa*MprF.

A3.7. *Pa*MprF^{545} pull-down assay

Ni Sepharose 6 FF affinity resin (Cytiva) was equilibrated in Pull-down Buffer (20 mM HEPES pH 7.6, 100 mM KCl, 20 % (w/v) glycerol, 0.0261 % (w/v) DDM), and 5 µL equilibrated resin added to 200 µL of each purified sybody at 25 µM concentration. Samples were incubated on ice for 30 minutes. Affinity resin was washed twice with 1 mL of Pull-Down Buffer + 75 mM imidazole. Purified and 3C proteinase treated *Pa*MprF^{545} was then diluted to 0.15 mg/mL in Pull-down Buffer + 75 mM imidazole and 200 µL added to each affinity resin sample. Samples were incubated on ice for 30 minutes, then washed three times with 1 mL Pull-down Buffer + 75 mM imidazole. Bound sample was then eluted with 5 µL of 4x SDS-PAGE sample buffer, and samples analysed by SDS-PAGE.

A3.8. Sybody29 large-scale expression and purification

The Sybody29 sequence in the plasmid pSB_init was expressed in MC1061 *E. coli.* 100 mL of TB-Cam was inoculated with a single colony of transformed MC1061 cells and grown overnight at 37°C. The overnight culture was used to inoculate 2 L of TB-Cam to a starting OD_{600} of 0.1.

Cells were grown at 37°C to OD_{600} = 0.6 and then induced with 0.02 % (w/v) L-arabinose. Cells were grown overnight at 20°C, before being pelleted at 4,500 g for 20 minutes. Cell pellets were resuspended to 5 mL/g wet cell mass in sybody purification buffer (20 mM Tris pH 7.4, 150 mM NaCl) and lysed by passing twice through a cell disruptor (Constant Systems) at 30 kpsi. Cell lysate was centrifuged at 16,000 g for 1 hour to pellet cell debris, and supernatant collected. 20 mM imidazole was added to the supernatant, which was incubated with 0.5 mL Ni Sepharose 6 FF (Cytiva) for 1 hour at 4°C. Affinity resin was pelleted at 500 g for 5 minutes, and batch washed 3 times with 50 mL sybody purification buffer + 50 mM imidazole. Affinity resin was transferred to a gravity flow column and further washed with 50 mM imidazole sybody purification buffer until the A_{280} of flowthrough was constant. Sybody29 was then eluted with sybody purification buffer + 500 mM imidazole in 500 µL fractions. Peak fractions were pooled and loaded onto a Superdex 200 10/300 increase column equilibrated in sybody purification buffer. Results of this SEC step are shown below in **Figure A3.1:**

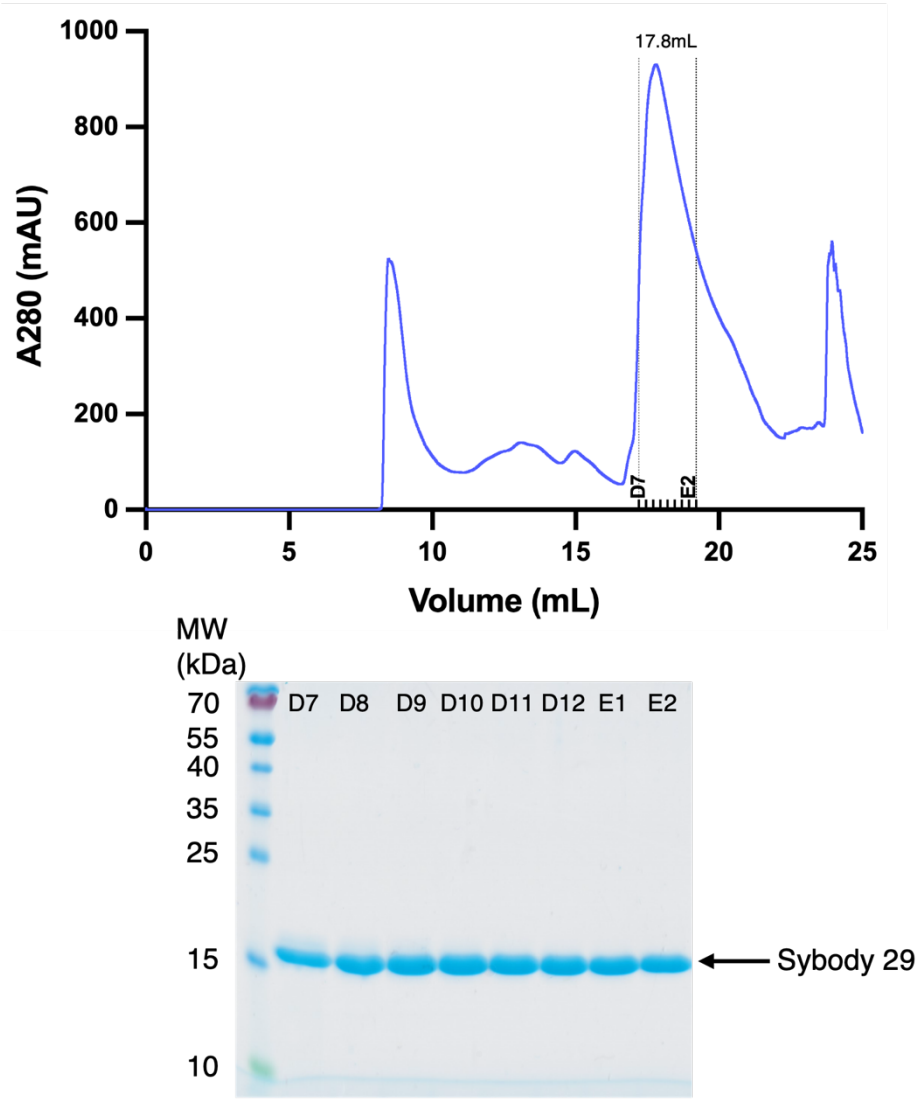

Figure A3.1: Purification of Sybody29. SEC chromatogram of Sybody29 purification with peak fractions highlighted (***Top***) and SDS-PAGE gel (16 %, Coomassie stain) of peak fractions from SEC (***Bottom***).

Sybody29 (MW = 16.5 kDa) elutes at 17.8 mL, and SDS-PAGE demonstrates the high purity of the isolated sybody. Peak fractions from SEC were pooled and flash-frozen in liquid nitrogen for storage at -80°C.

A4. Sybody alignments and phylogenetic tree

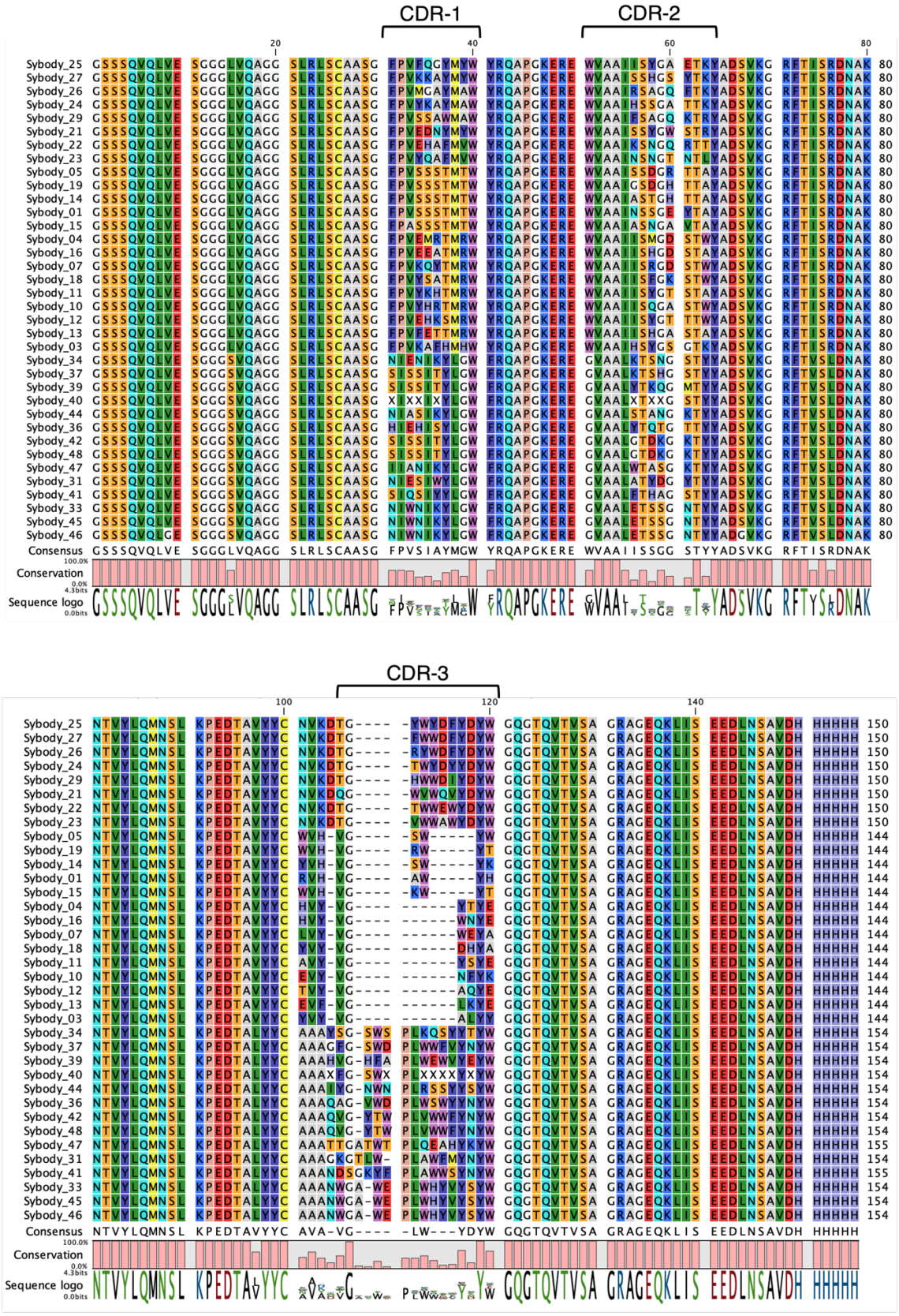

Figure A4.1: Purified sybody alignment. Multiple sequence alignment of the purified *Pa*MprF sybody binders. Residues are coloured by Rasmol colour scheme. CDR regions are highlighted. Alignment generated with CLC sequence viewer (QIAgen).

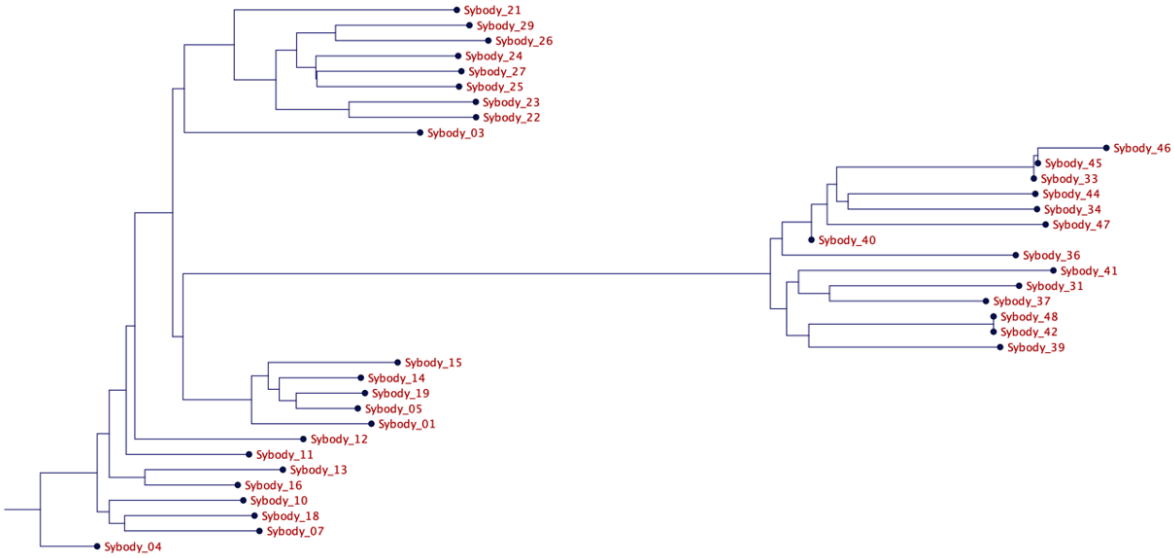

Figure A4.2: Sybody phylogenetic tree. Phylogenetic tree of purified sybodies based on sequence alignment, generated with CLC Workbench (QIAgen).

A5. *Pa*MprF model TM helix fit to map

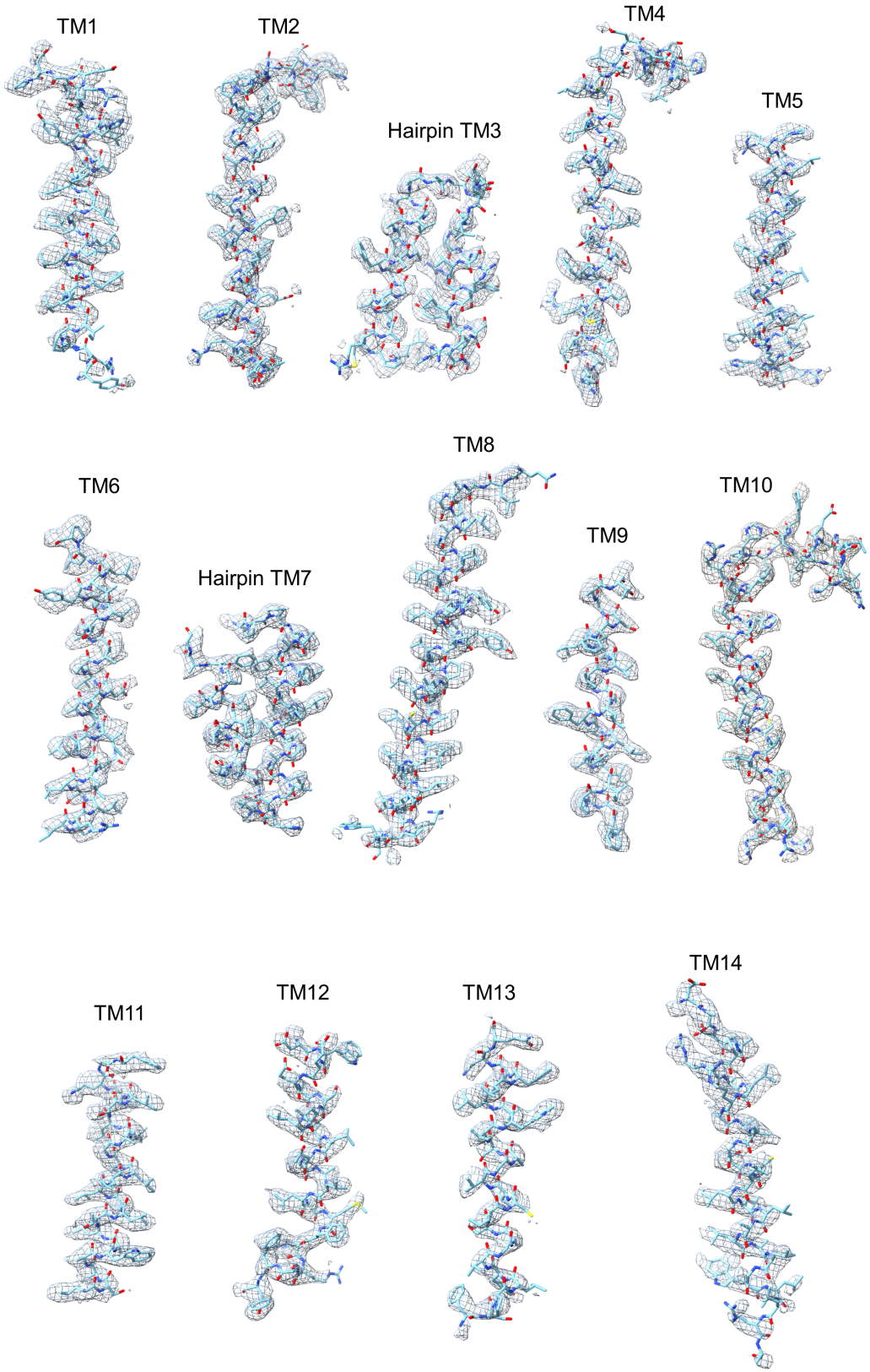

Figure A5.1: *Pa*MprF TM helices fit to cryoEM map. Individual helices from the TM region of *Pa*MprF are shown (blue sticks, coloured by heteroatom) fitted to the corresponding region of the final post-processed cryo-EM map (grey mesh) that was sharpened with a *B*-factor of -85 Å.

A6. Isolation of *P. aeruginosa* PA0919 and assessment of function

The PA0919 gene has been previously identified downstream of the *mprF* gene in *P. aeruginosa* within the same operon (Arendt *et al.* 2013). This gene has been shown to encode a lipid hydrolase that is targeted to the periplasm and anchored to the inner bacterial membrane. Similar hydrolases have been identified in other species (Smith *et al.* 2013) and appear to be involved in controlling the level of aminoacyl lipid produced by MprF following translocation to the bacterial surface; knockout of this hydrolase leads to a significant increase in alanyl-PG in the *P. aeruginosa* inner membrane, but also - interestingly - sees a reduction in the resistance of bacteria to antimicrobials compared to WT. This led to the hypothesis that the level of MprF-modified lipid needs to be tightly regulated to give bacteria increased antimicrobial resistance. As such, it was of interest to purify this hydrolase for use in functional lipid transport assays with *Pa*MprF to determine whether hydrolase activity affects *Pa*MprF lipid transport activity.

A6.1. PA0919 Methods

A6.1.1. PA0919 cloning

The PA0919 sequence was generated from PAO1 genomic DNA using primers in **Appendix 2** to amplify the coding region from residues 35-427; residues 1-34 correspond to *P. aeruginosa* periplasm targeting sequence and anchoring helix and so were excluded. This sequence was cloned via FX cloning into a pBXNPH3 vector which contains an N-terminal 10x-His tag and PelB periplasm targeting sequence.

A6.1.2. PA0919 expression and purification

PA0919 in pBXNPH3 was expressed in MC1061 *E. coli*. 100 mL of TB-Amp was inoculated with a single colony of transformed MC1061 and grown overnight at 37°C. This overnight culture was used to inoculate 2 L of TB to OD_{600} = 0.1. Cells were grown to OD_{600} = 0.6 before induction with 0.01 % (w/v) L-arabinose and further growth overnight at 20°C. Cells were harvested at

4,500 g for 20 minutes and cell pellets resuspended to 5 mL/g wet cell mass in PA0919 lysis buffer (50 mM HEPES pH 8, 150 mM NaCl, DNAse I, EDTA-free protease inhibitors) before cells were lysed for purification.

Cells were lysed by passing the resuspension through a cell disruptor (Constant Systems) twice at 30 kpsi. The lysate was ultracentrifuged at 200,000 g to pellet cell debris and cell membranes. The supernatant containing soluble proteins was collected. 20 mM imidazole was added to the supernatant and then incubated with 1 mL of Ni Sepharose 6 FF (Cytiva) affinity resin for 1.5 hours at 4°C. Resin was batch washed 3 times in 50 mL of PA0919 lysis buffer + 30 mM imidazole, then transferred to a gravity flow column where washing was continued until the A_{280} of flowthrough was constant. Protein was then eluted in 1 mL fractions using PA0919 lysis buffer + 400 mM imidazole. Elution fractions were pooled and dialysed overnight in 10,000 MWCO snakeskin dialysis tubing against 500 mL PA0919 lysis buffer to remove imidazole. Dialysate was collected the next day and concentrated in a Vivaspin 6 30 kDa MWCO concentrator (Sartorius) to 500 µL before being loaded onto a Superdex 200 10/300 increase column equilibrated in PA0919 SEC buffer (50 mM HEPES pH 8, 100 mM NaCl). Peak fractions from SEC were pooled and concentrated in a Vivaspin 6 30 kDa MWCO concentrator down to 5 mg/mL for use in functional assays.

A6.1.3. PA0919 activity assay

PA0919 lipid hydrolase activity was tested with NBD-AlaPG. PA0919 was diluted in buffer (50 mM HEPES pH 8, 100 mM NaCl) to 1 mg/mL (~20 µM) with 10 µg/mL NBD-AlaPG (~10 µM) dissolved in 0.1 % (w/v) DDM. A control tube lacking PA0919, as well as a tube of PA0919 with the addition of the covalent inhibitor phenylmethylsulfonyl fluoride (PMSF) to 1 mM were also included. Reaction mixes were incubated at RT for 1 hour, followed by incubation at 37°C for 30 minutes. Lipids were then extracted as described in **section 2.3.1.** and dried into a film under nitrogen gas. Lipid films were rehydrated in 2:1 (v/v) chloroform:methanol and spotted

onto a silica TLC plate. TLC was run in one dimension in 60:25:4 (v/v/v) chloroform:methanol:water, before NBD lipids were visualised by illumination with blue light.

A6.2. PA0919 results

A6.2.1. Purification of PA0919

The *P. aeruginosa* sequence of PA0919 contains an N-terminal targeting sequence and predicted transmembrane helix for association with the outer leaflet of the inner membrane. Therefore, a PA0919 construct was designed with this helix removed, producing a soluble protein that was expressed recombinantly in the periplasm of *E. coli*. The results of the final SEC step of purification are shown in **Figure A6.1** below:

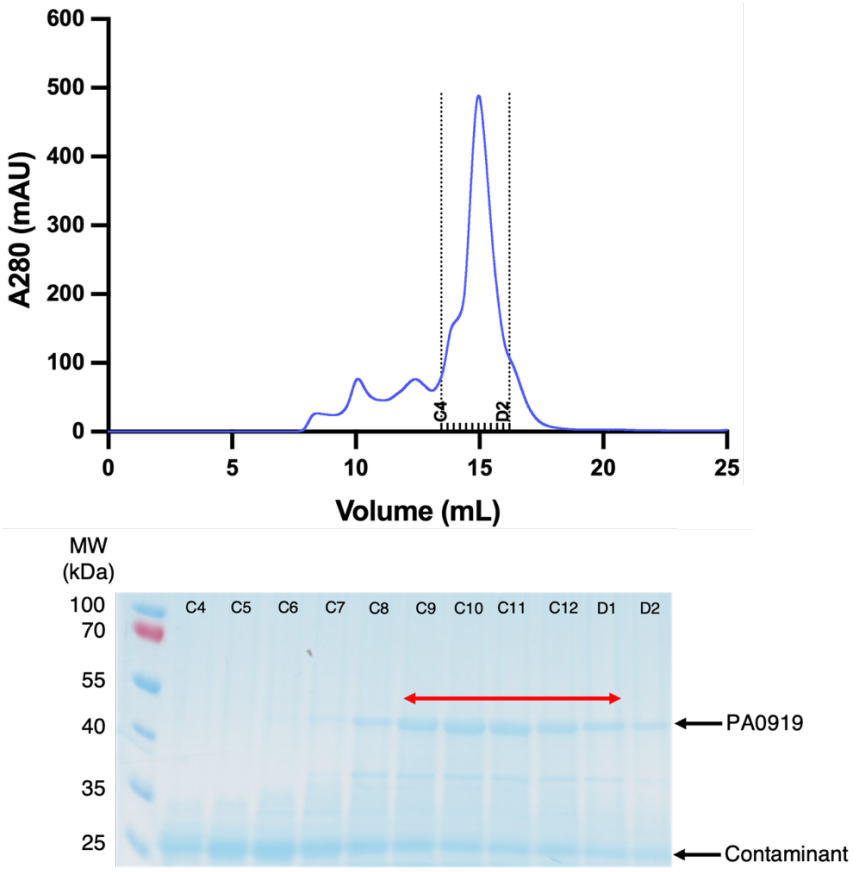

Figure A6.1: SEC of PA0919. *Top:* Chromatogram of SEC purification of PA0919. *Bottom:* SDS-PAGE gel (12 %, Coomassie stain) of peak fractions. The peak fractions pooled corresponding to purified PA0919 are highlighted with a red arrow.

The SEC trace shows PA0919 eluting at 15.0 mL and running to the expected weight for this construct (44 kDa) on SDS-PAGE. There is also a contaminant band present in the elution,

which appears to elute in the shoulder just before the peak at 15.0 mL (~26 kDa). The peak fractions were carefully pooled to avoid the main occurrence of the 26 kDa contaminant. Fractions were concentrated to 5 mg/mL for use in functional assays.

A6.2.2. Lipid hydrolase PA0919 cannot process NBD-labelled lipid substrate

This hydrolase activity of PA0919 was tested via TLC using commercially produced NBD-AlaPG. Briefly, PA0919 was incubated with DDM-solubilised NBD-AlaPG for 2 hours at RT, and then at 37°C for 30 minutes. A control tube without PA0919 and a control tube of PA0919 inactivated with phenylmethylsulfonyl fluoride (PMSF) were also run at the same time. Lipid was then extracted and separated by TLC in one dimension of 60:25:4 (v/v/v) chloroform:methanol:water. The results of this assay are shown in **Figure A6.2:**

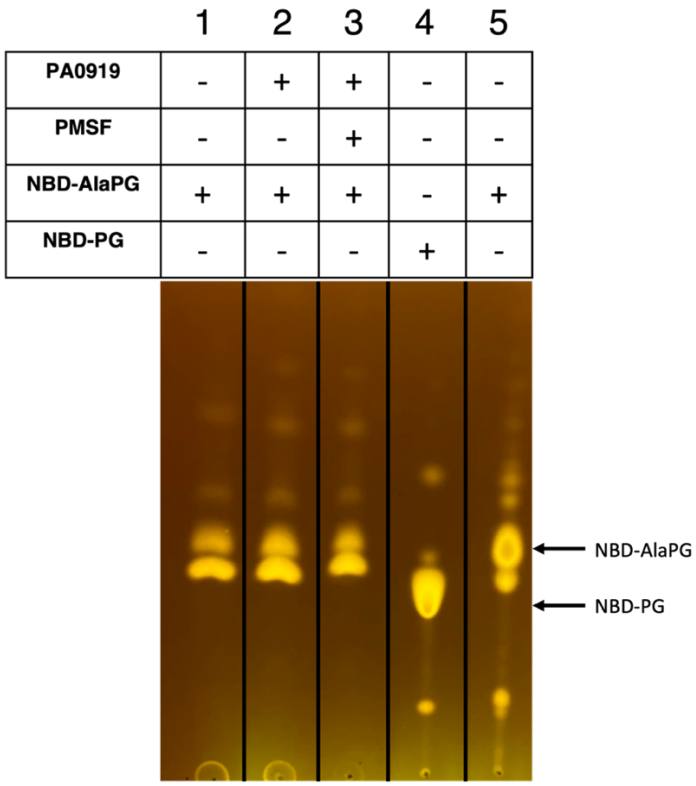

Figure A6.2: PA0919 hydrolase assay. Results of PA0919 hydrolase assay run on 1D TLC, imaged with blue-light. Control lanes of commercially available NBD-PG (lane 4) and NBD-AlaPG (lane 5) are included to demonstrate the expected mobilities of these species.

This assay demonstrates that even in the PA0919 sample not inactivated with PMSF (lane 2), there is no significant shift in the NBD-AlaPG spot to the lower mobility of NBD-PG. This

indicates that the purified PA0919 is unable to hydrolyse the alanine residue attached to the headgroup of NBD-AlaPG. This may be due to the presence of the bulky NBD label, which could interfere with the interaction between PA0919 and AlaPG at the substrate binding site.

As a result of this assay, it was clear that purified PA0919 cannot process the NBD labelled lipid that was used as a reporter in the liposome transport assay of **Chapters 4** and **5**, and so PA0919 was not suitable to probe the effects of an induced concentration gradient on the transport of AlaPG by *Pa*MprF as had been planned.

A7. *Pa*MprF mutant purifications

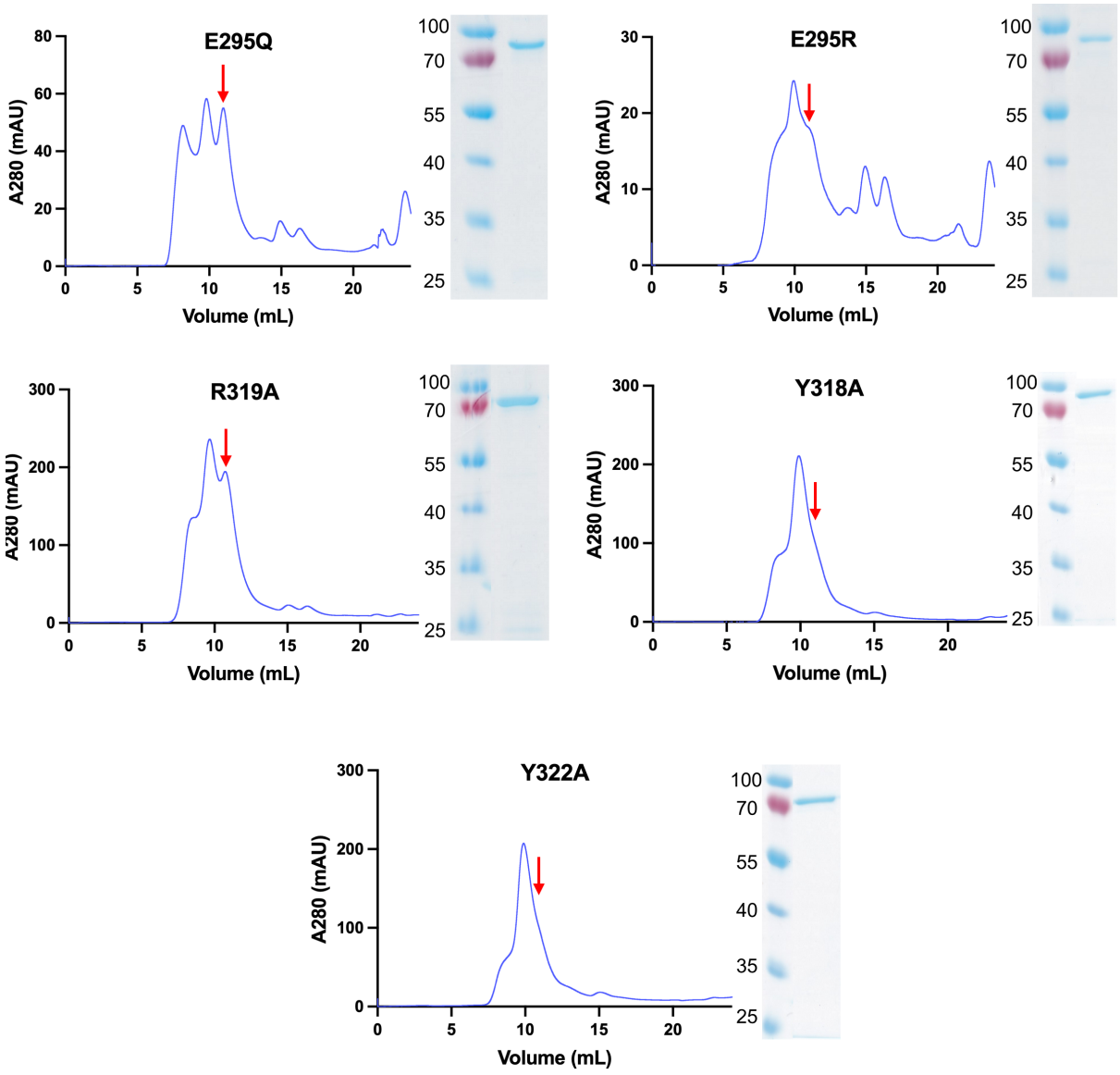

Figure A7.1 Cytoplasmic lipid site mutant purifications. SEC chromatograms and 12 % SDS-PAGE gels of *Pa*MprF mutants discussed in **section 5.4.1.** The 11 mL *Pa*MprF monomer peak used for liposome experiments is highlighted with a red arrow.

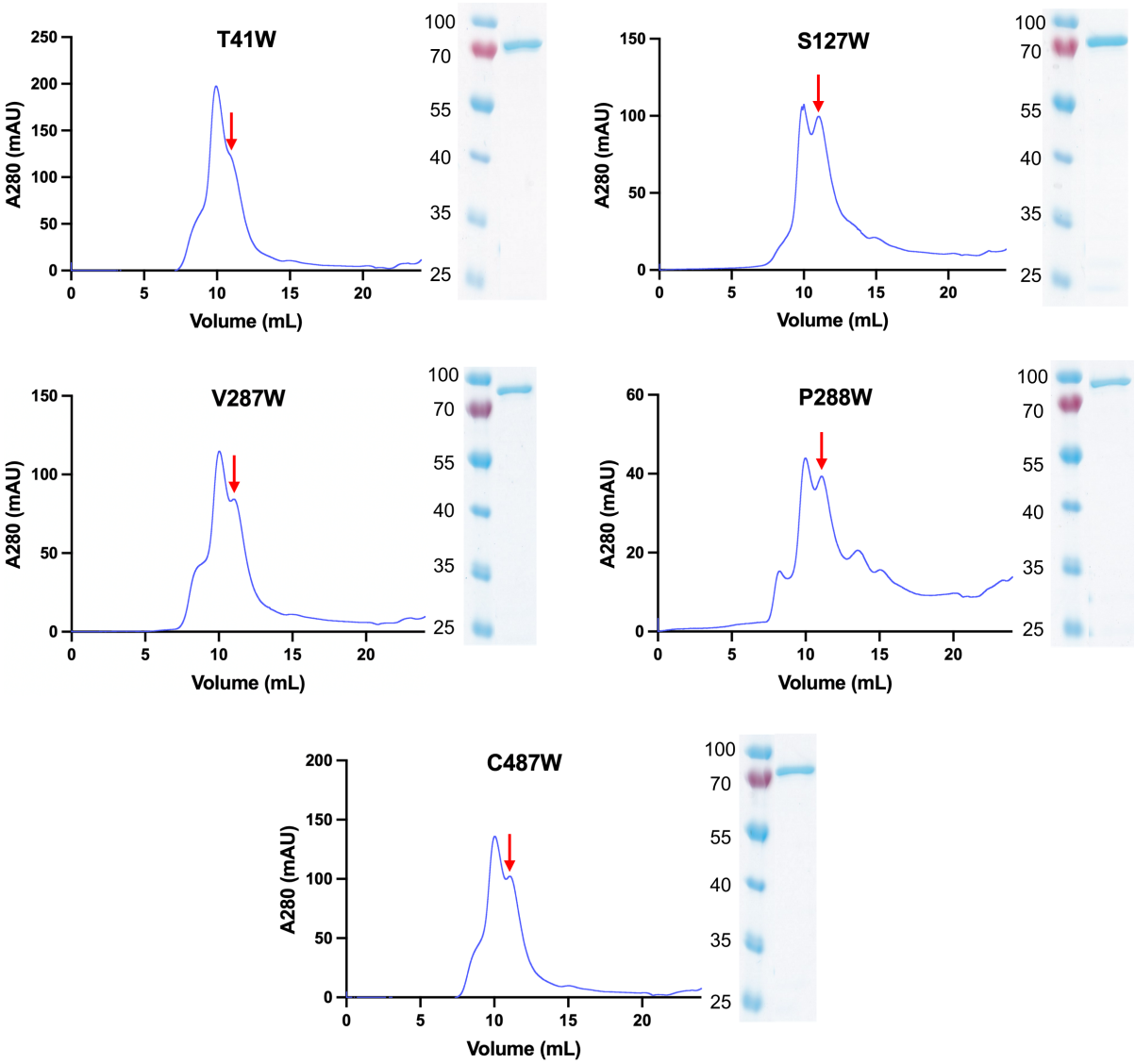

Figure A7.2 TM domain interface mutant purifications. SEC chromatograms and 12 % SDS-PAGE gels of *Pa*MprF mutants discussed in **section 5.4.2.** The 11 mL *Pa*MprF monomer peak used for liposome experiments is highlighted with a red arrow.

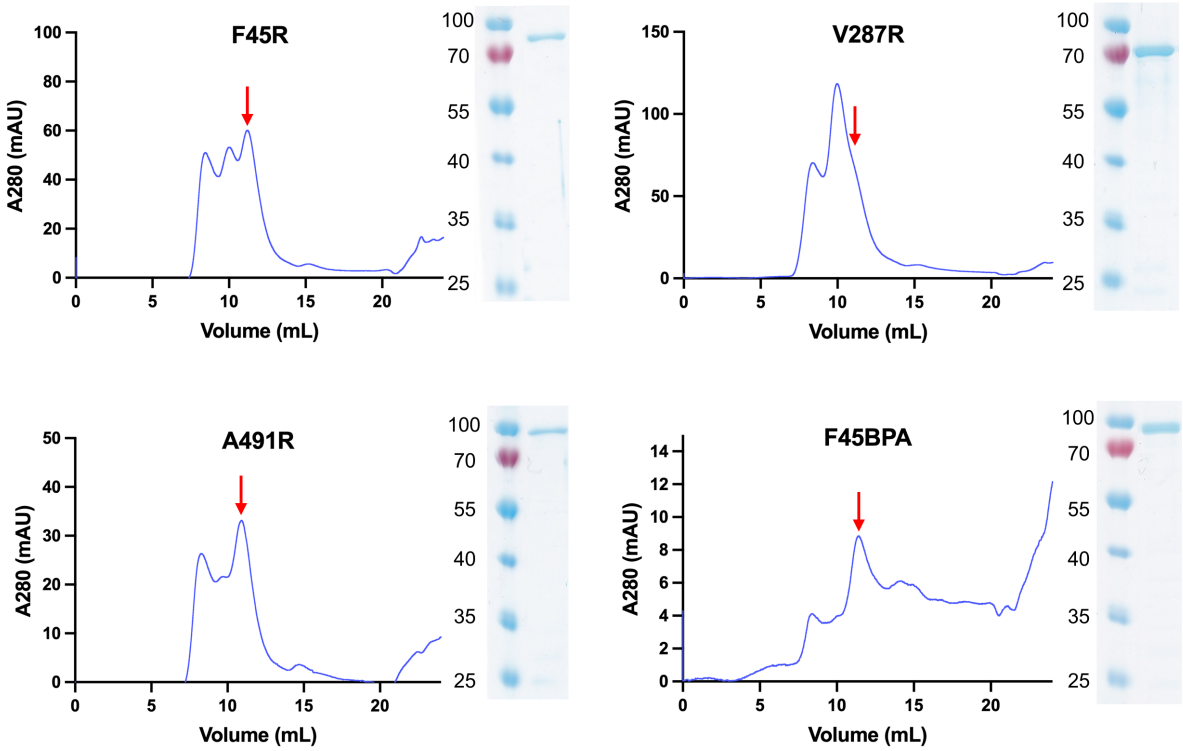

Figure A7.3 Disruptive mutant purifications. SEC chromatograms and 12 % SDS-PAGE gels of *Pa*MprF mutants discussed in **sections 5.4.2** and **5.4.3.** The 11 mL *Pa*MprF monomer peak used for liposome experiments is highlighted with a red arrow.

A8. *Pa*MprF disulfide mutant lipid transport data

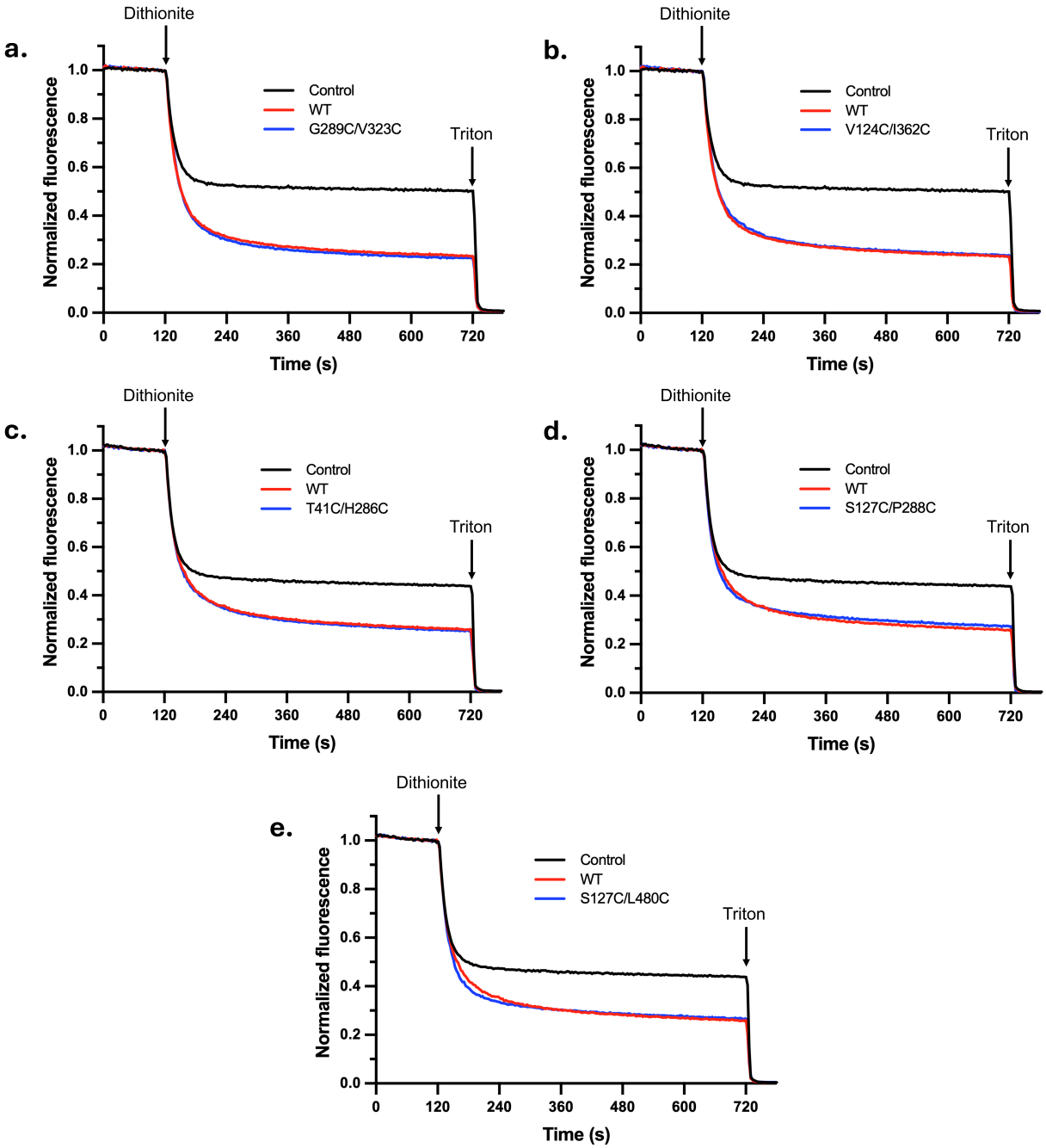

Figure A8.1: Disulfide *Pa*MprF mutant liposome transport data. Normalized fluorescence time-courses assessing *Pa*MprF-mediated transport of NBD-AlaPG in liposomes for disulfide mutants. Disulfide mutants tested were **a.** G289C-V323C, **b.** V124C-I362C, **c.** T41C-H286C, **d.** S127C-P288C, **e.** S127C-L480C. All disulfide pairs gave similar fluorescence decreases to WT *Pa*MprF, indicating that these cysteine mutant pairs either did not form disulfide crosslinks, or crosslinking at these residues does not significantly reduce lipid transport through *Pa*MprF.